POLYTECHNIQUE MONTRÉAL
affiliée à l'Université de Montréal

ET

L'INSTITUT SUPÉRIEUR DE L'AÉRONAUTIQUE ET DE L'ESPACE

Localizability optimization for multi robot systems and applications to ultra-wide band positioning

JUSTIN CANO
Département de génie électrique

Thèse présentée en vue de l'obtention du diplôme de *Philosophiæ Doctor*
Génie électrique

Avril 2023

POLYTECHNIQUE MONTRÉAL
affiliée à l'Université de Montréal

ET

L'INSTITUT SUPÉRIEUR DE L'AÉRONAUTIQUE ET DE L'ESPACE

Cette thèse intitulée :

Localizability optimization for multi robot systems and applications to ultra-wide band positioning

présentée par **Justin CANO**
en vue de l'obtention du diplôme de *Philosophiæ Doctor*
a été dûment acceptée par le jury d'examen constitué de :

David SAUSSIÉ, président
Jérôme LE NY, membre et directeur de recherche
Éric CHAUMETTE, membre et codirecteur de recherche
Gaël PAGÈS, membre et codirecteur de recherche
François POMERLEAU, membre
Juliette MARAIS, membre externe

DEDICATION

Au club du 125,
César, Élisabeth, José & Marie-Thérèse.

ACKNOWLEDGEMENTS

To save my family and friends the trouble of translating, and to spare the rest of the readers from my terrible English, I will exceptionally use my native language for these acknowledgements.

Premièrement, un grand merci à Jérôme Le Ny pour avoir présidé à mon quasi-septennat dans les études supérieures à Polytechnique. Une longue période jonchée d'obstacles que nous avons franchie ensemble: ponctuée de choses "pas claires" qui le devinrent bien souvent grâce à ses remarques. Ensuite, merci à Gaël Pagès, pour avoir été un soutien constant. En particulier, je salue son énergie dans le démarrage de ma thèse en cotutelle et le remercie pour ses nombreux conseils d'implémentation. Enfin, pour les directeurs, je remercie Éric Chaumette de m'avoir introduit au monde des bornes statistiques, aidé dans mes recherches de tous types et épaulé dans des moments particulièrement difficiles.

Mes remerciements les plus sincères vont ensuite au Pr. David Saussié, qui a accepté de présider mon jury de thèse et celui de mon examen de synthèse. Je tiens à souligner que ses conseils en matière d'interaction Sup-Poly m'ont été infiniment précieux. J'adresse ma sincère gratitude aux Prs. Juliette Marais et François Pomerleau pour avoir rejoint le jury en qualité de membres externes et ainsi de faire bénéficier à mes travaux de leurs expertises.

Je tiens à saluer les Prs. Jordi Vilá-Valls et Damien Vivet en France pour leur accueil bienveillant au sein de l'équipe NAVIR^{2}ES du DEOS. Côté canadien, je remercie le Pr. Roland Malhamé pour ses encouragements puis aussi pour les quatre ans d'enseignement de l'automatique passés côte à côte.

Mes salutations vont ensuite aux étudiants au doctorat et à la maîtrise du MRASL de Polytechnique : André, Bugra, Charles, Clémence, Frederick, Lucas, Marc, Mathieu (×3), Mohammed, Narimane, Olivier (×2), Rémi, Sophie et Tien pour leur présence à mes côtés. Je remercie également "mes" chers stagiaires Dean, Malo, et Matthieu pour leur motivation et implication. Je leur souhaite de poursuivre ainsi et leur exprime mes vœux de succès.

Outre-Atlantique, je remercie, empreint d'une grande gratitude pour leur bienveillance à mon égard, les collègues du DEOS pour les moments partagés, souvent en présence de chocolatines, pensées particulières pour Aboubacar, Adrien, Antonío, Asnate, Benjamin, BucketWool[1]*, Colas, Cyril, Émilie, Esteban, Florent, Frédéric, Gaëtan, Gastón, Gilles, Jean-Titouan-Louise-*

[1] Guerrière qui perd ses "u" et la moitié de "Cézaire".

Adrien, Ludwig, Maria, Marie, Matthieu, Mengda, Myriam, Nadia, Nicolas, Nour, Osman, Paul, Pauline, Sami, Sara, Thibaud, Titouan et bien sûr mon cher Yi. Je salue également du groupe technique du DISC pour son support constant, incluant mes demandes farfelues et en particulier Alain, Corentin, Laurent, Louis et Pascal.

Puis, vient le tour de mes amis "civils", autant de soutiens indéfectibles : Anne, Aurélie, Boboy/Cath, Edwige, Émilie, Justine $[2\pi]$*, Laura, Mathilde, Morgane, Valérie; Alexandre, Axel, Brandon, David, Étienne, Fabien, Farid, Gabriel, Gautier (et ses corrections!), (G/J)érémy, Julien, Manuel* ($\times 2$)*, Maxime, Morgan, Paul* ($\times 2$)*, Sylvain* ($\times 2$)*,* $\mathcal{VLC}_+$[2] *et Wissam.*

Évidemment, mes remerciements vont à ma famille, dont les membres, véritables ancres dans le champ de localisabilité de ma vie ne sont pas en reste. Je les remercie tous collectivement car je crains les omissions. Cependant, je décerne des remerciements spéciaux aux cousins du Canada, Annie, Maryse ainsi que Louis pour leur accueil, leur "menoumeries" et leur gentillesse. Également, un salut spécial à celui qui a provoqué (accidentellement?) mon goût pour l'électronique et la robotique, il saura se reconnaître.

Ultimement, vient le carré des braves, merci à "la Mère" pour son sens de l'organisation, à "El Pepe" pour sa culture, à "Tonnée" pour sa soif d'apprendre et à mon regretté "Vorde" pour son courage. Grâce à vous, je suis arrivé en bon état, intègre et à bon port.

Sincèrement,
Justin O. A. Cano.

[2] $\mathcal{VLC}_+ :=$ {Alban, Aline, Arnaud, Elliot, Quentin}.

RÉSUMÉ

Les Systèmes Multi-Robots (SMR) permettent d'effectuer des missions de manière efficace et robuste du fait de leur redondance. Cependant, les robots étant des véhicules autonomes, ils nécessitent un positionnement précis en temps réel. Les techniques de localisation qui utilisent des Mesures Relatives (MR) entre les robots, pouvant être des distances ou des angles, sont particulièrement adaptées puisqu'elles peuvent bénéficier d'algorithmes coopératifs au sein du SMR afin d'améliorer la précision pour l'ensemble des robots.

Dans cette thèse, nous proposons des stratégies pour améliorer la localisabilité des SMR, qui est fonction de deux facteurs. Premièrement, la géométrie du SMR influence fondamentalement la qualité de son positionnement pour des MR bruitées. Deuxièmement, les erreurs de mesures dépendent fortement de la technologie utilisée. Dans nos expériences, nous nous focalisons sur la technologie UWB (*Ultra-Wide Band*), qui est populaire pour le positionnement des robots en environnement intérieur en raison de son coût modéré et sa haute précision. Par conséquent, une partie de notre travail est consacrée à la correction des erreurs de mesure UWB afin de fournir un système de navigation opérationnel. En particulier, nous proposons une méthode de calibration des biais systématiques et un algorithme d'atténuation des trajets multiples pour les mesures de distance en milieu intérieur.

Ensuite, nous proposons des Fonctions de Coût de Localisabilité (FCL) pour caractériser la géométrie du SMR, et sa capacité à se localiser. Pour cela, nous utilisons la Borne Inférieure de Cramér-Rao (BICR) en vue de quantifier les incertitudes de positionnement. Par la suite, nous fournissons des schémas d'optimisation décentralisés pour les FCL sous l'hypothèse de MR gaussiennes ou log-normales. En effet, puisque le SMR peut se déplacer, certains de ses robots peuvent être déployés afin de minimiser la FCL. Cependant, l'optimisation de la localisabilité doit être décentralisée pour être adaptée à des SMRs à grande échelle.

Nous proposons également des extensions des FCL à des scénarios où les robots embarquent plusieurs capteurs, où les mesures se dégradent avec la distance, ou encore où des informations préalables sur la localisation des robots sont disponibles, permettant d'utiliser la BICR bayésienne. Ce dernier résultat est appliqué au placement d'ancres statiques connaissant la distribution statistique des MR et au maintien de la localisabilité des robots qui se localisent par filtrage de Kalman. Les contributions théoriques de notre travail ont été validées à la fois par des simulations à grande échelle et des expériences utilisant des SMR terrestres. Ce manuscrit est rédigé par publication, il est constitué de quatre articles évalués par des pairs et d'un chapitre supplémentaire.

ABSTRACT

Multi-Robot Systems (MRS) are increasingly interesting to perform tasks efficiently and robustly. However, since the robots are autonomous vehicles, they require accurate real-time positioning. Localization techniques that use relative measurements (RMs), i.e., distances or angles, between the robots are particularly suitable because they can take advantage of cooperative schemes within the MRS in order to enhance the precision of its positioning.

In this thesis, we propose strategies to improve the localizability of the SMR, which is a function of two factors. First, the geometry of the MRS fundamentally influences the quality of its positioning under noisy RMs. Second, the measurement errors are strongly influenced by the technology chosen to gather the RMs. In our experiments, we focus on the Ultra-Wide Band (UWB) technology, which is popular for indoor robot positioning because of its moderate cost and high accuracy. Therefore, one part of our work is dedicated to correcting the UWB measurement errors in order to provide an operable navigation system. In particular, we propose a calibration method for systematic biases and a multi-path mitigation algorithm for indoor distance measurements.

Then, we propose Localizability Cost Functions (LCF) to characterize the MRS's geometry, using the Cramér-Rao Lower Bound (CRLB) as a proxy to quantify the positioning uncertainties. Subsequently, we provide decentralized optimization schemes for the LCF under an assumption of Gaussian or Log-Normal RMs. Indeed, since the MRS can move, some of its robots can be deployed in order to decrease the LCF. However, the optimization of the localizability must be decentralized for large-scale MRS.

We also propose extensions of LCFs to scenarios where robots carry multiple sensors, where the RMs deteriorate with distance, and finally, where prior information on the robots' localization is available, allowing the use of the Bayesian CRLB. The latter result is applied to static anchor placement knowing the statistical distribution of the MRS and localizability maintenance of robots using Kalman filtering.

The theoretical contributions of our work have been validated both through large-scale simulations and experiments using ground MRS. This manuscript is written by publication, it contains four peer-reviewed articles and an additional chapter.

TABLE OF CONTENTS

DEDICATION iii

ACKNOWLEDGEMENTS iv

RÉSUMÉ vi

ABSTRACT vii

TABLE OF CONTENTS viii

LIST OF TABLES xii

LIST OF FIGURES xiii

LIST OF SYMBOLS AND ABBREVIATIONS xvi

NOTATION xvii

CHAPTER 1 INTRODUCTION 1
1.1 Localization Methods 2
1.1.1 General Principles 2
1.1.2 Cooperative Relative-Measurement Based Localization 3
1.1.3 The Case of Radio-Frequency Measurements 4
1.2 Localizability of Cooperative Mobile Robot Systems 6
1.2.1 Sources of ToF Measurement Errors 6
1.2.2 Geometric Sources of Errors 7

CHAPTER 2 LITERATURE REVIEW 9
2.1 RF Timestamp-Based Relative Measurements 9
2.1.1 Measurement Protocols 9
2.1.2 Mitigation of UWB Timestamp-based RM Errors 13
2.2 Modeling the MRS' Geometry Impact on Positioning 15
2.2.1 Position Estimators 15
2.2.2 Dilution of Precision 16
2.2.3 Cramér-Rao Lower Bounds 17
2.3 Formation Control 19

2.3.1 Distributed Connectivity Optimization 20
2.3.2 Rigidity Maintenance Problem 22

CHAPTER 3 RESEARCH OBJECTIVES, CONTRIBUTIONS AND DOCUMENT OUTLINE 25
3.1 Research Organization 25
3.1.1 Research Objectives and Hypotheses 25
3.1.2 Project Organization 27
3.2 Contribution 28
3.2.1 Contribution History 28
3.2.2 Manuscript Outline 30

CHAPTER 4 ARTICLE 1 : CLOCK AND POWER-INDUCED BIAS CORRECTION FOR UWB TIME-OF-FLIGHT MEASUREMENTS 32
4.1 Introduction 32
4.2 Time-of-Flight Measurement Model 35
4.3 Clock Offset Correction: the Case of TWR 36
4.4 RxP-Induced Error Correction 38
4.4.1 Most Informative RxP Measurements 38
4.4.2 RxP-Induced Error Estimation Method 39
4.4.3 Experimental Validation 41
4.5 TWR Localization Experiment 43
4.6 Application to Other Localization Schemes 46
4.7 Conclusion 47

CHAPTER 5 ARTICLE 2 : RANGING-BASED LOCALIZABILITY OPTIMIZATION FOR MOBILE ROBOTIC NETWORKS 49
5.1 Introduction 49
5.2 Problem Statement 53
5.3 Localizability Potentials 56
5.3.1 Constrained Cramér-Rao Lower Bound 56
5.3.2 Localizability Potentials and Optimal Design 58
5.4 Properties of the Fisher Information Matrix 59
5.4.1 Infinitesimal Rigidity 60
5.4.2 Relations between the Rigidity Matrix and the FIM 62
5.5 Distributed Gradient Computations for the Localizability Potentials 64
5.5.1 Partial Derivatives of the FIM 65

5.5.2 Decentralized Gradient Computations for the D- and A-Opt Potentials 66
5.5.3 Decentralized Computation of E-Opt Gradient 69
5.6 Localizability Optimization for Rigid Bodies 71
5.6.1 Constrained Localizability Optimization 71
5.6.2 CRLB with Distance Constraints 74
5.6.3 CRLB with Constrained Relative Positions 75
5.7 Simulations 79
5.7.1 Cooperative Structure Inspection 79
5.7.2 Deployment of a UGV Carrying Several Anchors 86
5.8 Experiments 88
5.9 Conclusion and Perspectives 92

CHAPTER 6 ARTICLE 3 : OPTIMAL LOCALIZABILITY CRITERION FOR POSITIONING WITH DISTANCE-DETERIORATED RELATIVE MEASUREMENTS 94
6.1 Introduction 94
6.2 Problem Statement 96
6.2.1 Robot Placement Problem 96
6.2.2 Distance-Deteriorating Measurement Models 97
6.3 Distance-Dependent Variance Model 97
6.3.1 Polynomial Variance Model 98
6.3.2 Application to UWB Two-Way Ranging Measurements 98
6.4 Localizability Cost Function 100
6.5 Computing the FIM 100
6.5.1 Structure of the FIM 101
6.5.2 Distance Measurements 102
6.5.3 Angle Measurements 102
6.6 Localizability Optimization Methods 103
6.6.1 Gradient Descent Strategy 103
6.6.2 Non-Myopic Localizability Improvement Policy 104
6.7 Experimental Validation 104
6.8 Conclusion and Perspectives 107

CHAPTER 7 ARTICLE 4 : MAINTAINING ROBOT LOCALIZABILITY WITH BAYESIAN CRAMÉR-RAO LOWER BOUNDS 109
7.1 Introduction 109
7.2 Problem Statement 111
7.3 Information Modeling 112

7.3.1 Cramér-Rao Lower Bound . . . 112
7.3.2 Computation of the DFIM . . . 113
7.3.3 BFIM Computation with Gaussian Prior . . . 114
7.4 Localizability Potential . . . 115
7.4.1 Localizability Potential . . . 115
7.4.2 An Example of Localizability Enhancement . . . 116
7.5 Motion Planners . . . 118
7.5.1 Deterministic Motion Planner . . . 118
7.5.2 Bayesian Motion Planner . . . 118
7.6 Multi-Robot Deployment . . . 120
7.6.1 DMP implementation with LS estimator . . . 120
7.6.2 BMP implementation with EKF estimator . . . 122
7.7 Conclusion and Perspectives . . . 124

CHAPTER 8 BAYESIAN ANCHOR DEPLOYMENT . . . 125
8.1 Related Work . . . 125
8.2 Problem Statement . . . 126
8.2.1 Notation and Assumptions . . . 126
8.2.2 Anchor Deployment Problem . . . 128
8.3 Design of the Cost Function . . . 129
8.4 Deployment Algorithm . . . 131
8.4.1 Minimal Localizability Coverage Problem Algorithm . . . 131
8.4.2 Local Average Minimization Policy . . . 133
8.5 Simulations . . . 134
8.6 Conclusion and Perspectives . . . 137

CHAPTER 9 GENERAL DISCUSSION . . . 138

CHAPTER 10 CONCLUSION AND RECOMMENDATIONS . . . 142
10.1 Summary of Works . . . 142
10.2 Limitations . . . 143
10.3 Future Research . . . 144

REFERENCES . . . 145

LIST OF TABLES

Table 3.1	List of publications	30
Table 5.1	Monte Carlo Simulation Results	88
Table 6.1	Empirical MSE for initial and final positions	107
Table 9.1	Summary of the contributions of the thesis	141

LIST OF FIGURES

Figure 1.1	Illustration of an MRS	1
Figure 1.2	Illustration of the triangulation principle	2
Figure 1.3	General structure of an estimator	3
Figure 1.4	An example of RM-based localization setup	4
Figure 1.5	Illustration of MP and NLOS phenomena	7
Figure 1.6	Illustration of the DoP concept	7
Figure 2.1	Examples of TWR protocols	10
Figure 2.2	Localization with passive ranging protocols	12
Figure 2.3	Illustration of the AoA measurement principle	13
Figure 2.4	Rigidity graph and rigidity framework	22
Figure 3.1	Thesis timeline	28
Figure 4.1	Custom communication board used in our experiments	33
Figure 4.2	Single-Sided TWR protocol	36
Figure 4.3	An example of computed calibration map	40
Figure 4.4	Robot and sampled position	41
Figure 4.5	Calibration maps for various pairs of modules	42
Figure 4.6	Executed trajectory for the TWR localization test	43
Figure 4.7	Block diagram of the bias correction algorithm	44
Figure 4.8	Plot of raw range errors and biases	44
Figure 4.9	Error histograms after and before compensation	45
Figure 4.10	Error histograms after and before compensation	46
Figure 5.1	Illustration of the setup in 2D	54
Figure 5.2	Setup for two robots, seen as rigid bodies, carrying multiple tags	73
Figure 5.3	Initial system configuration, leaders' waypoints and network sparsity	80
Figure 5.4	Robot and tag configuration for trajectory tracking.	81
Figure 5.5	Tag trajectories in the workspace	83
Figure 5.6	Localizability potential with and without follower deployment	84
Figure 5.7	Plot of the empirical RMSE over the trajectory	85
Figure 5.8	Convergence of the D-Opt and E-Opt gradient estimates	85
Figure 5.9	Robot equipped with two tags	86
Figure 5.10	Deployment results for (D) and (RP) scenarios	87
Figure 5.11	Robots, anchors and tags	89
Figure 5.12	Trajectory $\mathbf{p}_1$ of tag 1 and its estimates $\hat{\mathbf{p}}_1$ in the Cartesian plane	90

Figure 5.13 Empirical MSE obtained by simulation 90
Figure 5.14 Localizability potential and squared errors over the tags' trajectory . 91
Figure 5.15 Anchor and tag 1 trajectories when the anchors are mobile 91
Figure 5.16 Localizability and squared errors during deployment 92
Figure 6.1 Anchor, robot, motion capture system and UWB transceiver 99
Figure 6.2 Empirical variance and fitted polynomial 99
Figure 6.3 2D localizability cost $J(x, y)$ and computed paths for the tag 105
Figure 6.4 Performed trajectory and robot position estimates 106
Figure 6.5 Squared positioning error and localizability cost 107
Figure 7.1 Robots, fixed anchor and UWB sensors used in the experiments . . . 110
Figure 7.2 Estimates $\hat{\mathbf{p}}_{\mathcal{U}}(t)$ and actual trajectory $\mathbf{p}_{\mathcal{U}}(t)$ 117
Figure 7.3 Localizability function and squared errors 117
Figure 7.4 System architecture 120
Figure 7.5 Robots trajectory and estimates (DMP/LS) 121
Figure 7.6 Results with (DMP/LS) 121
Figure 7.7 Robots trajectory and estimates (BMP/EKF) 122
Figure 7.8 Results with (BMP/EKF). 123
Figure 8.1 Example of typical variance model 127
Figure 8.2 Illustration of the placement and operation zones 128
Figure 8.3 Deployment strategy 131
Figure 8.4 Simulated scenario setup 135
Figure 8.5 Simulated annealing algorithm results 136
Figure 8.6 Stochastic gradient algorithm results 136

LIST OF SYMBOLS AND ABBREVIATIONS

AoA Angle of Arrival.

BCRLB Bayesian Cramér-Rao Lower Bound.

CCRLB Constrained Cramér-Rao Lower Bound.

CIR Chanel Impluse Response.

CRLB Cramér-Rao Lower Bound.

DoP Dilution of Precision.

DR Dead Reckoning.

DSTWR Double-Sided Two-Way Ranging.

EKF Extended Kalman Filter.

FIM Fisher Information Matrix.

GNSS Global Navigation Satellite System.

IMU Inertial Measurement Unit.

KF Kalman Filter.

LDE Leading Edge Detector.

LoP Lines of Position.

LoS Line of Sight.

LS Least Squares.

MP Multi Path.

MRS Multi Robot Systems.

MSE Mean Squared Error.

NLoS Non Line of Sight.

OWR One-Way Ranging.

PDF Probability Density Function.

PF Position Fixing.

PTP Precision Time Protocol.

RBCRLB Recursive Bayesian Cramér-Rao Lower Bound.

RF Radio Frequency.

RMs Relative Measurements.

RMSE Root Mean Squared Error.

RSS Received Signal Strength.

RxP Received Power.

SSTWR Single-Sided Two-Way Ranging.

TDoA Time Difference of Arrival.

ToA Time of Arrival.

ToF Time Of Flight.

TWR Two-Way Ranging.

UAV Unmanned Aerial Vehicle.

UGV Unmanned Ground Vehicle.

UWB Ultra-Wide Band.

NOTATION

Set notations	
$\mathbb{N}, \mathbb{Z}, \mathbb{R}, \mathbb{C}$	Scalar sets, respectively : positive integers, relative integers, real numbers and complex numbers. The superscript $*$ denotes that the origin has been removed from the set.
$\mathcal{E} \times \mathcal{F}$	Cartesian product for two sets $\mathcal{E}$ and $\mathcal{F}$.
$1_{\mathcal{A}}(a)$	Indicator function of the set $\mathcal{A}$. Namely, $1_{\mathcal{A}}(a) = 1$ if $a \in \mathcal{A}$ and zero otherwise.
Typography conventions	
$s \in \mathbb{K}$	Scalar quantities are in regular font, for $\mathbb{K} \in \{\mathbb{N}, \mathbb{Z}, \mathbb{R}, \mathbb{C}\}$
$\mathbf{v} = [\dots v_i \dots]^\top \in \mathbb{K}^n$	Vectors are noted in **bold font** for some $n \in \mathbb{N}^*$. The i-th component of the vector $\mathbf{v}$ is denoted v_i for $1 \leq i \leq n$.
$\mathbf{M} = \begin{bmatrix} \ddots & \vdots & \iddots \\ \dots & M_{ij} & \dots \\ \iddots & \vdots & \ddots \end{bmatrix} \in \mathbb{K}^{n \times m}$	Matrices are noted in **CAPITAL BOLD FONT** for $n, m \in \mathbb{N}^*$. The notation M_{ij} denotes coefficient located at the i-th row and j-th column for some $i, j \in [1, n] \times [1, m]$.
$\mathcal{A}$	Sets are denoted in capital $\mathcal{CALLIGRAPHY}$ font.
$\hat{e}$	Estimates are denoted with the hat notation.
$\tilde{m}$	Measurements are represented with the tilde notation.
Statistics Notations See [Kay, 1993] for the definitions.	
$f_r(x)$	Probability Density Function of the random variable r
$\mathbf{r} \sim \mathcal{N}(\boldsymbol{\mu}, \boldsymbol{\Sigma})$	$\mathbf{r}$ is an $n \in \mathbb{N}^*$ dimensional Gaussian vector with its mean $\boldsymbol{\mu} \in \mathbb{R}^n$ and its covariance matrix $\boldsymbol{\Sigma} \in \mathbb{R}^{n \times n}$.
$r \sim \mathcal{U}_{[a,b]}$	r is a random scalar variable following the Uniform law between reals a and b, $a < b$.
$\mathbb{E}\{\mathbf{g}(z)\}$	Expectation, *i.e.*, $\int_z f_z(z)\mathbf{g}(z)\mathrm{d}z$ for a vector function $\mathbf{g} : \mathbb{R} \mapsto \mathbb{R}^n$, $n \in \mathbb{N}^*$.
$\mathbb{E}_z\{\mathbf{g}(\dots, z, \dots)\}$	Expectation over the parameter z, *i.e.*, $\int_z f_z(z) g(\dots, z, \dots)\mathrm{d}z$ for a multivariate vector function $\mathbf{g} : \mathbb{R}^m \mapsto \mathbb{R}^n$, $n, m \in \mathbb{N}^*$.

$\mathsf{cov}(\mathbf{z})$	Covariance matrix of the random vector $\mathbf{z} \in \mathbb{R}^n$, $n \in \mathbb{N}$, *i.e.*, $\mathbb{E}\{(\mathbf{z} - \mathbb{E}\{\mathbf{z}\})(\mathbf{z} - \mathbb{E}\{\mathbf{z}\})^\top\}$
$\mathrm{var}\,(z)$	Variance (scalar case) of $z \in \mathbb{R}$, *i.e.* $\mathbb{E}\{(z - \mathbb{E}\{z\})^2\}$
DERIVATIVES Consider $\mathbf{x} \in \mathbb{R}^n$, $\mathbf{y} \in \mathbb{R}^m$, $z \in \mathbb{R}$, $\mathbf{M} \in \mathbb{R}^{n \times n}$ for some $n, m \in \mathbb{N}^*$, see [Petersen and Pedersen, 2012] for the definitions.	
$\dfrac{\partial \mathbf{x}}{\partial \mathbf{y}}$	Vector $\mathbf{x}$ derivative with respect to vector $\mathbf{y}$: $\dfrac{\partial \mathbf{x}}{\partial \mathbf{y}} \in \mathbb{R}^{n \times m}$, where $\left.\dfrac{\partial \mathbf{x}}{\partial \mathbf{y}}\right\|_{ij} = \dfrac{\partial x_i}{\partial y_j},\ i, j \in [1, n] \times [1, m]$
$\dfrac{\partial \mathbf{M}}{\partial z}$	Matrix derivative $\left.\frac{\partial \mathbf{M}}{\partial z}\right\|_{ij} = \frac{\partial M_{ij}}{\partial z}, \forall i, j \in [1, n]^2$.
$\dfrac{\partial^2 z}{\partial \mathbf{x} \partial \mathbf{x}^\top}$	Hessian matrix $\left.\frac{\partial^2 z}{\partial \mathbf{x} \partial \mathbf{x}^\top}\right\|_{ij} = \frac{\partial z}{\partial x_i \partial x_j}, \forall i, j \in [1, n]^2$.
$\dot{\mathbf{x}}$	First order time derivative vector $\dot{\mathbf{x}} = (\partial \mathbf{x} / \partial t)^\top$.
$\ddot{\mathbf{x}}$	Second order time derivative vector $\ddot{\mathbf{x}} = (\partial \mathbf{x} / \partial^2 t)^\top$.
LINEAR ALGEBRA Consider a square matrix $\mathbf{M} \in \mathbb{R}^{n \times n}$ for $n \in \mathbb{N}^*$, see [Petersen and Pedersen, 2012] for the definitions.	
$\mathrm{Tr}\,\{\mathbf{M}\}$	Trace of $\mathbf{M}$, $\mathrm{Tr}\,\{\mathbf{M}\} = \sum_i M_{ii}$.
$\det\{\mathbf{M}\}$	Determinant of $\mathbf{M}$.
$\lambda(\mathbf{M})$	Spectrum of $\mathbf{M}$, *i.e.*, the set of its n eigenvalues. Moreover if $\mathbf{M} = \mathbf{M}^\top$, that implies a real spectrum, we order the eigenvalue as follows $\lambda_1 \cdots \geq \lambda_i \geq \dots \lambda_n$.
$\mathrm{span}\,\{\mathcal{S}\}$	Vector basis of the set $\mathcal{S}$.
$\ker \mathbf{M}$	Nullspace (or kernel) of $\mathbf{M}$.
$\mathrm{diag}(\mathbf{M}_1 \dots \mathbf{M}_i \dots)$	Block-diagonal concatenation for $\mathbf{M}_i$ square matrices. Note that if all $\mathbf{M}_i$ are scalars then it defines a diagonal matrix.
$\mathrm{col}(\mathbf{x}, \mathbf{y}, z, \dots)$	Column concatenation *i.e.* $\mathrm{col}(\mathbf{x}, \mathbf{y}, z, \dots) = [\mathbf{x}^\top, \mathbf{y}^\top, z, \dots]^\top$
$\mathbf{A} \succ \mathbf{B}$	Matrix strict inequality, *i.e.*, $\mathbf{A} - \mathbf{B}$ is positive definite for $\mathbf{A}, \mathbf{B} \in \mathbb{R}^{n \times n}$ where $n \in \mathbb{N}^*$.
$\mathbf{A} \succeq \mathbf{B}$	Matrix loose inequality, *i.e.*, $\mathbf{A} - \mathbf{B}$ is **semi**-positive definite for $\mathbf{A}, \mathbf{B} \in \mathbb{R}^{n \times n}$ where $n \in \mathbb{N}^*$.
$\|\mathbf{v}\|$	Euclidean norm of $\mathbf{v}$, *i.e.*, $\|\mathbf{v}\| := (\mathbf{v}^\top \mathbf{v})^{1/2}$.

$\mathbf{A} \odot \mathbf{B}$	Hadamard (element-wise) product for $\mathbf{A}, \mathbf{B} \in \mathbb{R}^n$, $n \in \mathbb{N}^*$.
$\mathbf{A} \otimes \mathbf{B}$	Kronecker (tensor) product for $\mathbf{A}, \mathbf{B} \in \mathbb{R}^{n \times m} \times \mathbb{R}^{n' \times m'}$ with $n, m, n', m' \in \mathbb{N}^*$.
$\mathbf{N}^\dagger$	Moore-Penrose pseudo-inverse for $\mathbf{N} \in \mathbb{R}^{n \times m}$ with $n, m \in \mathbb{N}^*$.
$\mathbf{v} \times \mathbf{w}$	Cross product, for $\mathbf{v}, \mathbf{w} \in \mathbb{R}^3$

CHAPTER 1 INTRODUCTION

"Self-education is, I firmly believe, the only kind of education there is."

– Isaac Asimov (1920-1992)

Multi Robot Systems (MRS) become increasingly popular, for their numerous applications and attractive features. Indeed, since a robot is an automated device that is expected to perform tasks safely, quickly and precisely, the redundancy brought by using several robots is a common solution to enforce these requirements. Additional constraints specific to their embedded character such as energy and computational limitation should also be mitigated by an MRS design. For instance, multiple robots can perform a given task quicker than a single one and thus suffer less from charging time.

Figure 1.1 – Illustration of an MRS : Drone100 Light Show, performed by *Ars Electronica Futurelab* in 2015. © *Creative Commons*

In order to be attractive, especially for industrial applications, mobile robots have to remain affordable and replaceable. Thus the mass production of a simple model is often preferred to a single or a small number of more sophisticated robots. Therefore, MRS are increasingly used in various domains : civil engineering, agriculture, military, rescue services, *etc.* To give a more entertaining example, an increase of multiple Unmanned Aerial Vehicle (UAV) air shows has occurred these recent years, as illustrated in Figure 1.1.

Regardless of their assigned tasks, robots must have access to a real-time and reliable positioning system to operate. The position estimates should be precise and refreshed sufficiently often to ensure a safe position control. Moreover, the localization algorithm should take into

account all available information in the MRS, *e.g.*, take into consideration the topology of the network formed by the robots, which could vary over time. In this thesis, we focus on the localization problem and in particular the ways to enhance the position estimates' precision. The following sections of this chapter specify the scope of our work and give a brief overview of the localization problem, in particular when an MRS is involved.

1.1 Localization Methods

1.1.1 General Principles

To determine the position of an object, measurements that are an explicit function of its position are required. For instance, several angle measurements between the object and known reference points can be used to build a position estimate. This technique, mastered by navigators since the Medieval Era [O'Connor and Robertson, 1999], is known as triangulation, see Figure 1.2. In the literature, observations that are extrinsic to an object and that (nonlinearly) depend on its position are called Position Fixing (PF) measurements [Groves, 2013]. Then, the PF data can be used by an estimator, *e.g.*, nonlinear Least Squares (LS) [Kay, 1993, Section 8.9], in order to estimate the position.

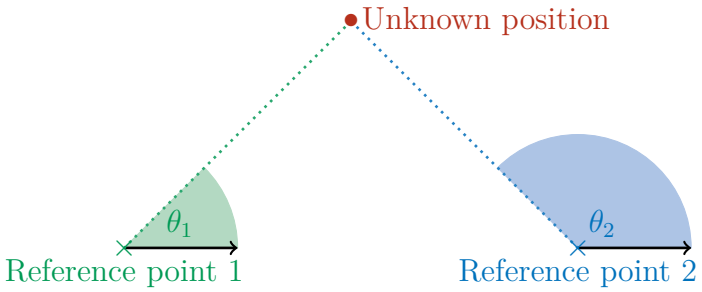

Figure 1.2 – Illustration of the triangulation principle

If the kinematics of the object are known, Dead Reckoning (DR) measurements can be used, which involve the time derivatives of the positions. Typical DR measurements can be provided by accelerometers (acceleration), odometers (velocity), or optical flow sensors (velocity) and require numerical integration in order to retrieve the position. For this reason, DR-based navigation suffers from error drifts [Groves, 2013, Chap. 4], and this fact is exacerbated when the initial states are not perfectly known.

Fused with PF, the information provided by DR sensors can be used to improve the quality of position estimates. This uses a state prediction based on the kinematics and the DR measurements, which allows to build a posterior after incorporating a PF observation. This

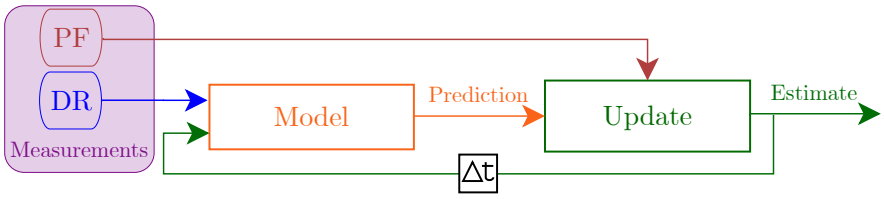

Figure 1.3 – General structure of an estimator model fusing DR and PF measurements

strategy, known as sensor fusion, is widely used in the navigation domain, where complementary measurements are used to produce more reliable estimates [Raol, 2016]. Here, since a kinematic model of the vehicle is assumed, the position estimator has access to prior information, *i.e.*, a prediction, when the measurements are acquired. The estimate can then be constructed recursively using, for example, Kalman filtering techniques [Kay, 1993, Chap. 13]. However, regardless of the availability of prior information, position estimates remain strongly influenced by the quality of the PF, especially if systematic biases occur in these measurements.

1.1.2 Cooperative Relative-Measurement Based Localization

In this thesis, since we aim to enhance the localization precision for an MRS, we focus our study on the Relative Measurements (RMs) between the robots. These observations can be angles or distances between the robots. They are considered as PF measurements since each robot captures extrinsic information from its point of view. This kind of measurement is particularly useful where the Global Navigation Satellite System (GNSS) signals, such as the GPS, are unavailable. A paradigmatic use case of RMs is the navigation inside a building while the GNSS signal is strongly deteriorated and has insufficient resolution to perform position control. However, in order to solve the localization problem in an absolute frame for an MRS aided with RMs , some assumptions have to be made.

First, the connectivity of the graph formed by the RMs (edges) and the sensors (vertices) must be strong enough to determine unambiguously the locations of the robots. In addition, the positions of a sufficient number of sensors must be known in a global reference frame in order to solve the localization problem in that frame. This number depends on the dimension n of the localization problem in $\mathbb{R}^n$ (*e.g.*, for localizing a UAV in $n = 3$ dimensions, or for Unmanned Ground Vehicle (UGV) $n = 2$ on a perfectly flat ground) and the nature of the RMs. In the literature we refer to these known position sensors as *anchors*, while the sensors whose position is unknown and which are carried by the robots are called *tags*. An example of such a setup is shown in Figure 1.4, which presents both fixed and mobile anchors carried

by robots. As shown in the figure, the mobile anchors can be located accurately enough by GNSS, for example. Indeed, Real-Time Kinematics (RTK) positioning systems, which allow sub-meter accuracy, could be used by the mobile anchors, while the other robot tags would not be able to receive this signal and would remain located by RMs.

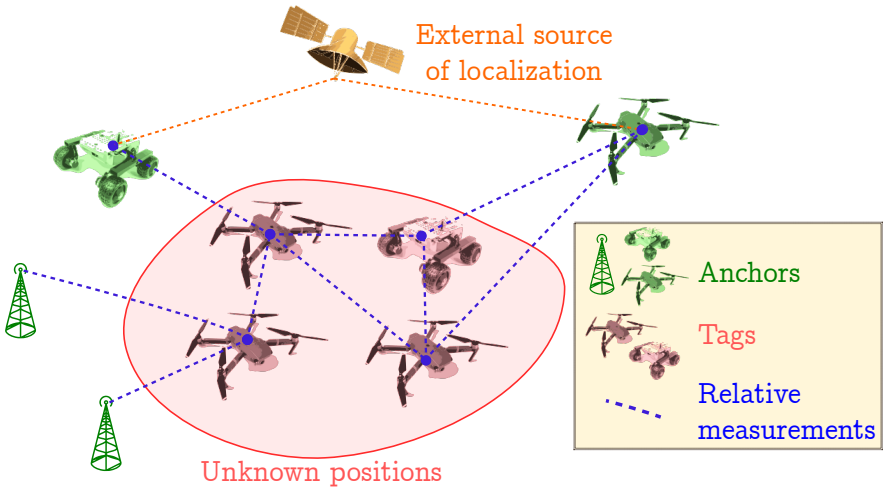

Figure 1.4 – An example of RM-based localization setup

Second, the geometric shape formed by the position of the sensors, the RMs, and the previous graph must be non-degenerate to provide a unique solution to the localization problem. Typically, any position estimator based on distance measurements would do poorly in locating a tag that is aligned with all of its neighbors.

Third, the design of the position estimator should take into account that the graph formed by the RMs is not complete in general *i.e.*, some tags/anchors are not neighbors. As an illustration, the two UAVs shown at the bottom of Figure 1.4 are not connected by RMs. Thus, decentralized positioning algorithms that take into account the sparsity of the graph are required to solve the problem and render the system robust to possible sensor failures.

1.1.3 The Case of Radio-Frequency Measurements

Relative measurement can be provided by different technologies such as visual [Tron et al., 2016], acoustic [Papalia and Leonard, 2020] or Radio Frequency (RF) measurements. Our work focuses on the latter because of its relative robustness to propagation distortions and the enabling of information exchange during RMs. For example, the communication channel can be used as an opportunity signal, considering that knowing a power fading model, the Received Signal Strength (RSS) measurement can be seen as a distance observation.

However, power fading-based techniques require extensive calibration to estimate the specific parameters of the sensors and the environment. Typically, fingerprinting techniques are preferred to determine the accuracy [Xu and Chou, 2017, Vo and De, 2016], but they also require prior calibration to acquire the RSS in the workspace before navigation. Nevertheless, their accuracy may be insufficient for some applications, especially for indoor UAV navigation.

Alternatively, the timestamps of the transmission and reception of the signal between two RF transceivers can be measured instead of the RSS. This technique is more robust to distortions since it uses time correlation between the received signal and a known sequence to estimate the Time of Arrival (ToA), *i.e.*, the reception time of a given signal. In fact, time correlation is known to be a robust parameter estimation technique under noisy observation [Kay, 1993]. For example, we can cite the Gold Codes used in GNSS, which are used as correlation functions to estimate the ToA. [Groves, 2013, Paulin, 2017]. Here we focus on these timestamp-based techniques, which can provide both distance and angle measurements.

For our experiments, we use Ultra-Wide Band (UWB) transceivers as sensors, which are popular in robotics and provide sufficient resolution for indoor localization [Etzlinger and Wymeersch, 2018, Prorok, 2013]. The UWB standard designates signals with an absolute bandwidth of $\Delta f = 500$ MHz or a fractional bandwidth greater than $f_B = 1/5$, according to the US Federal Communication Commission [Sahinoglu et al., 2008, p. 20]. The definition of these quantities is $\Delta f := f_{\max} - f_{min}$ and $\delta_f := \Delta_f / f_c$, where $f_{\max}$ is the maximum frequency of the signal with a tolerance of -3 dB (or $f_{\min}$ for the minimum) and $f_c := (f_{\max} + f_{min})/2$ is the center frequency. This large bandwidth allows a sharp time resolution to estimate signal reception times, which is suitable for precise distance or angle measurements (see (2.6)).

As an example, consider two transceivers i and j exchanging messages by UWB. If we denote T_i the transmission time of the message by i and R_j the reception time by j, then $\tau_{ij} = R_j - T_i$ defines the signal Time Of Flight (ToF). If we assume the signal travels at the speed of light $c \approx 3 \times 10^8$ m/s, then the distance d_{ij} between the two transceivers can be calculated as follows

$$d_{ij} = c\tau_{ij}. \tag{1.1}$$

The equation (1.1) implies that an error of 30 cm in the distance measurement corresponds to a nanosecond error in the time domain. This fact motivates the high time resolution design of ToF based RF sensors and the use of UWB technology. In addition, UWB transceivers are known for their low power consumption, moderate cost, and relative robustness to propagation interference, which explains their popularity for robotic applications [Sahinoglu et al., 2008, Prorok, 2013].

1.2 Localizability of Cooperative Mobile Robot Systems

The main purpose of this thesis is to optimize the **localizability** of the MRS, *i.e.*, their ability to be localized. To do so, we must first analyze the sources of error of the positioning system. In this section, we first discuss the measurement errors induced by a pair of RF sensors, which can significantly degrade the positioning in real experiments. Second, we briefly introduce the dependence between the network topology and the positioning errors, which affects all types of RMs. The mitigation of such phenomena is the main contribution of this thesis.

1.2.1 Sources of ToF Measurement Errors

For ToF-based relative measurement protocols, the first source of error is undoubtedly incorrect timestamps. One of the main factors exacerbating timestamp errors is the clock drift phenomenon: for a given pair of transceivers $\{i, j\}$, the crystal driving the clock of i would oscillate at a different period from that of j. In fact, the crystals are subject to thermodynamic fluctuations that produce significant frequency variations [Frerking, 1978].

Since the RF signals propagate at the speed of light c, this phenomenon can induce significant ranging errors. Therefore, the *clock drift* must be efficiently compensated or estimated over time to ensure an acceptable accuracy for MRS navigation [Prorok, 2013, Etzlinger and Wymeersch, 2018]. Then, modeling the clock drift for ToF-based localization is the very first step to achieve an appropriate positioning accuracy.

Furthermore, the process that estimates ToA, called Leading Edge Detector (LDE), is highly sensitive to Received Power (RxP) for UWB sensors. In particular, RxP variation leads to significant systematic biases (namely $\mathbb{E}\{\hat{\tau}\} \neq \tau$) in ToF estimates [Decawave, 2018]. These biases result from hardware imperfections (amplifiers, antenna gains, inaccurate phase loop) and must be compensated to improve the quality of the RMs.

When the implicit assumption of straight-line signal propagation is not valid, the equation (1.1) no longer holds. First, this can occur when an obstacle between two transceivers deflects the radio signal. The phenomenon is known as Non Line of Sight (NLoS) propagation in both GNSS [Groves, 2013] and UWB [Sahinoglu et al., 2008] literature. In Figure 1.5, we have illustrated the NLoS phenomenon with the blue line. Here, the fixed beacon is hidden from the view of the UGV, which can cause severe distortion of the signal [Yu et al., 2019].

Second, when two transceivers are in Line of Sight (LoS), if a radio-reflecting surface (such as the ground or a wall) is near one of them, the ToA estimator, known as LDE, may detect reflected signals from the surface instead of the received straight-path signal. This

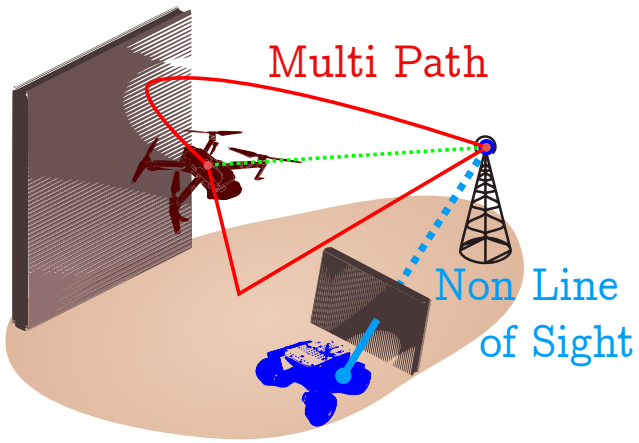

Figure 1.5 – Illustration of MP and NLOS phenomena

phenomenon, called Multi Path (MP) propagation in the RF literature, also introduces significant errors even in the absence of obstacles [Gururaj et al., 2017, Maceraudi et al., 2016]. In Figure 1.5 two MP paths starting from the UAV are shown in red while the staight-path signal is plotted in green. Both NLoS and MP outliers need to be handled in the navigation filter design by detecting or mitigating them to avoid experimental problems.

1.2.2 Geometric Sources of Errors

Even with the aforementioned calibrations, clock synchronization, and perfect LoS propagation, the UWB measurements still have unmodeled error terms. These residual uncertainties can be amplified by poor geometry of the MRS, a phenomenon known in the GNSS literature and quantified with the Dilution of Precision (DoP) [Groves, 2013, Section 9.4].

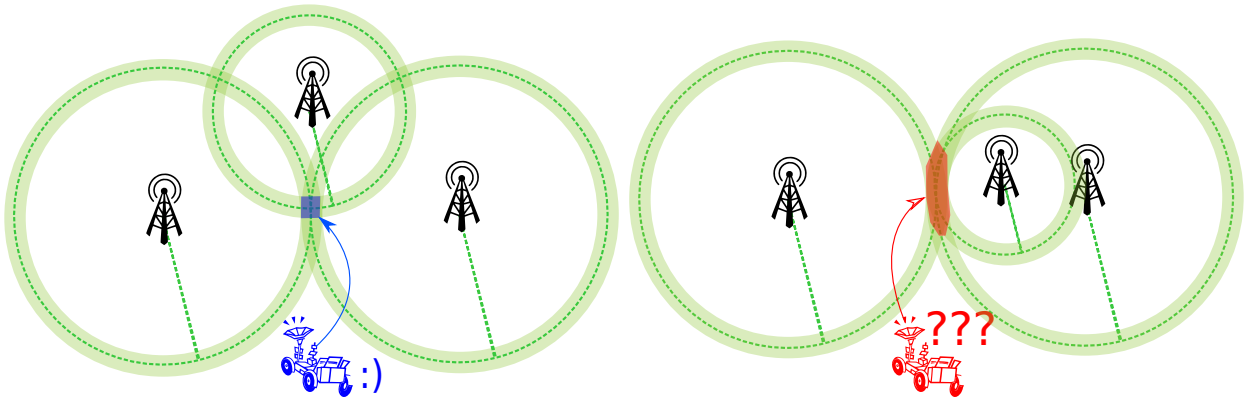

(a) Fair geometry (low DoP)

(b) Poor geometry (high DoP)

Figure 1.6 – Illustration of the DoP concept

To give a concrete example, consider three anchors performing noisy distance measurements with a tag carried by a UGV, as shown in Figure 1.6. The light green *annuli* correspond to the measurement uncertainties and the intersection of three of these *annuli* corresponds to the positioning uncertainty. We can clearly see that the isosceles triangle geometry (Figure 1.6a) gives a better positioning result (in blue) than a quasi-aligned geometry (Figure 1.6b). Thus, this very simple example highlights the dependence between MRS topology and localizability, which remains true for all kinds of noisy RMs.

As Figure 1.4 illustrates, all tags and possibly some anchors are carried by robots that can move and then modify the geometry of the MRS. Thus, through motion planning, it is possible to improve the localizability of some tags by changing the geometry of the network. To do this, we need to model the localization errors, providing the probabilistic distributions of the RMs. Finally, this modeling would allow the formulation of an optimization problem aimed at improving the localizability of the tags.

To use MRS experimentally, the placement problem must be solved in *real time*, in a *decentralized* manner, and using *noisy measurements*. This last point is an additional motivation to track the errors presented in Section 1.2.1, which could lead to erratic behavior. Indeed, since the motion control law depends in practice on the position estimates, we must verify the feasibility of such deployment in practice. The next chapter presents both the theoretical building blocks for solving this motion planing problem and the practical methods to perform prior error elimination on the RMs. Then, Chapter 3 presents the outline of the manuscript and its contributions.

CHAPTER 2 LITERATURE REVIEW

"Science sans conscience n'est que ruine de l'âme."

– François Rabelais (*c.* 1483-1553)

In this chapter, we provide a brief literature review of the concepts used in this thesis. Since the manuscript is *article-based* (see Chapter 3), we focus on a didactic approach to explain the different concepts leveraged in our work, while a more specific discussion of the state of the art is presented at the beginning of each article.

First, we introduce some elementary concepts of the RF timestamp-based protocols that RMs provide. We then discuss the mitigation strategies used in the literature to correct for the measurement errors mentioned in Chapter 1. After that, we define the concept of DoP and introduce covariance bounds as performance indicators of the estimators' precision. Finally, we briefly introduce some notions of MRS formation control related to localizability optimization.

2.1 RF Timestamp-Based Relative Measurements

2.1.1 Measurement Protocols

As seen in (1.1), ToF estimation is equivalent to observing the distances between MRS agents, assuming they are in LoS and without MP phenomena. In order to estimate the ToF τ_{ab} between two beacons a and b, protocols that require the transmission of multiple messages must be designed [Sahinoglu et al., 2008]. We classify these protocols into two categories depending on the configuration of the tags, *i.e.*, whether they are *active* transmitters or simply *passive* receivers.

Active Ranging Protocols (TWR)

To compensate for the clock drift phenomenon introduced in Chapter 1, one idea is to eliminate this quantity by time differences, assuming that the drift remains constant during propagation [Sahinoglu et al., 2008, Section 6.2]. These protocols are referred to as Two-Way Ranging (TWR) in the literature [Prorok, 2013], since both the tags and the anchors are active in the transmission of the messages.

Specifically, let us consider the agent (tag or anchor) a that transmits the message m and the associated timestamp T_m^a that is evaluated by the clock of a. Correspondingly, another agent b receives m at R_m^b, timestamped by its own clock. The ToF is then present in the following difference

$$R_m^b - T_m^a = \tau_{ab} + \delta_m^{ab} \tag{2.1}$$

where $\delta_m^{ab} := T_m^b - T_m^a \cong R_m^b - R_m^a$ is the (assumed constant) clock offset during the transmission of m. Then it is possible to retrieve τ_{ab} by performing multiple time differences similar to (2.1), using multiple messages (constituting a transaction) to eliminate the clock offset.

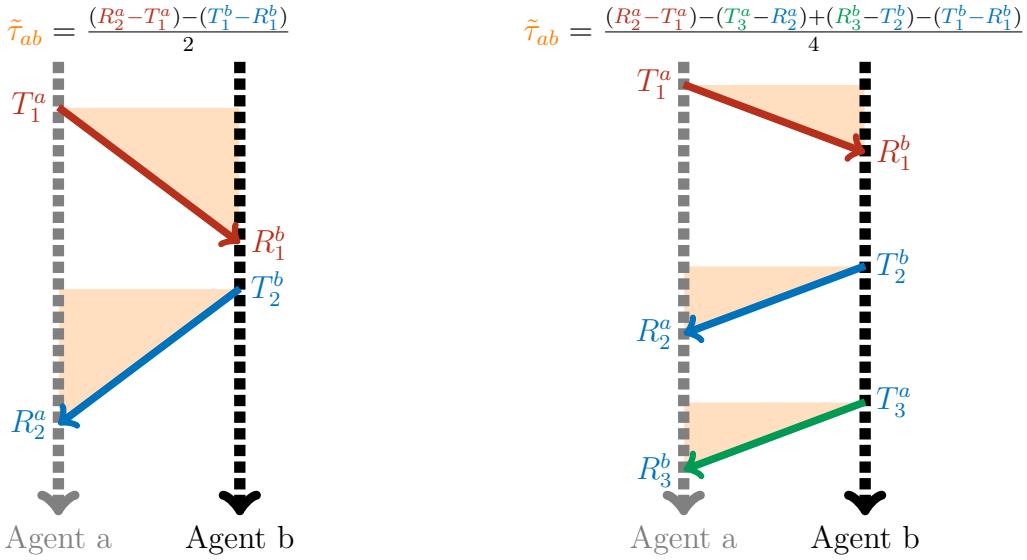

(a) SSTWR [Sahinoglu and Gezici, 2006, 6.2.1] (b) DSTWR [Neirynck et al., 2016]

Figure 2.1 – Examples of TWR protocols

With two messages $m \in \{1, 2\}$, it is possible to perform such compensation [Tewes et al., 2017] as shown in figure 2.1a. This type of protocol is called a Single-Sided Two-Way Ranging (SSTWR). [Sahinoglu and Gezici, 2006, Section 6.2.1]. In fact, calculating the difference and expressing it in the time base of a yields

$$R_1^b - T_1^a + R_2^a - T_2^b = R_1^a + \delta_1^{ab} - T_1^a + R_2^a - (T_2^a + \delta_2^{ab}) = 2\tau_{ab} + \delta_2^{ab} - \delta_1^{ab}, \tag{2.2}$$

assuming that τ_{ab} is the same throughout the transaction, *i.e.*, that the motion between the two agents remains negligible. Another common approximation is to state that the clock offset remains constant over messages in a given transaction [Sahinoglu and Gezici,

2006, Section 6.2.1], *i.e.* $\delta_2^{ab} \approx \delta_1^{ab}$ then (2.2) becomes

$$R_1^b - T_1^a + R_2^a - T_2^b \approx 2\tau_{ab}, \tag{2.3}$$

which allows to observe the ToF τ_{ab} and thus to measure the distance d_{ab}. Once the ToF is measured by such a technique, it can be provided as input to a position estimator such as an Extended Kalman Filter (EKF) [Chui and Chen, 1999, Chap. 8], as implemented in [Mai et al., 2018, Dewberry and Einhorn, 2016] for example.

However, the precision of τ_{ab} may be insufficient due to the variation of clock offset during a transaction. This problem can be solved by using multiple messages to average the noisy ToF observation. Typically, the Double-Sided Two-Way Ranging (DSTWR) protocols use more timestamp measurements [Kim, 2009] in the TWR protocol. To illustrate these techniques, we show the timeline of a DSTWR protocol consisting of three messages in Figure 2.1b presented in [Neirynck et al., 2016]. Alternatively, second-order offset models, *i.e.*, including the *clock skew* $\dot{\delta}^{ab}$, can also be used to improve its compensation in the ToF computation [Jiang and Leung, 2007, Neirynck et al., 2016]. These techniques are strongly inspired by the One-Way Ranging (OWR) literature presented in the next paragraph.

Passive Ranging Protocols (OWR)

In order to perform OWR, *i.e.*, without any communication from the tags, it is necessary to synchronize the anchors [Prorok, 2013, Etzlinger and Wymeersch, 2018] to properly estimate the ToF or, more generally, functions of it. The ToA observable differs from TWR in that it now includes clock offset as an additional state variable. This measurement is called *pseudo-range* and is defined as follows

$$\rho_{ab} := c(\delta^{ab} + \tau_{ab}), \tag{2.4}$$

and clock offset estimation implies that at least $n + 2$ measurements are needed to localize a tag in $\mathbb{R}^n$ [Etzlinger and Wymeersch, 2018, Sahinoglu and Gezici, 2006].

This OWR protocol is used in the GNSS systems, which use an extended model based on (2.4) that adds relativistic, ionospheric, and tropospheric corrections specific to satellite communications [Groves, 2013]. It has also been adapted for indoor localization, in particular using UWB technology, [Alavi and Pahlavan, 2006, Li and Cao, 2014] and can be used for mobile robot navigation [Cano et al., 2019].

Alternatively, localization based on Time Difference of Arrival (TDoA) is also popular in

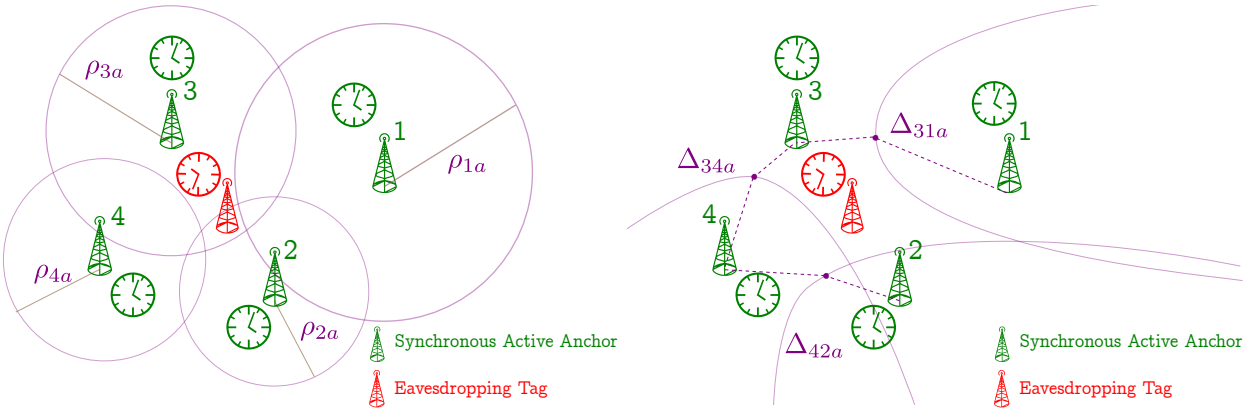

(a) ToA protocol (b) TDoA protocol

Figure 2.2 – Localization with passive ranging protocols

robot navigation [Ledergerber et al., 2015, Angelis et al., 2017, Tiemann et al., 2019, Prorok et al., 2012b]. This protocol leverages the time difference of arrival defined as follows

$$\Delta_{abc} = \rho_{ab} - \rho_{ac} = c\left(\tau_{ab} - \tau_{ac} - \delta^{ab}_{MB} + \delta^{ac}_{MC}\right), \tag{2.5}$$

where ρ_{ab} and ρ_{ac} are pseudoranges computed by tag a thanks to two messages MB and MC sent by anchors b and c. Note that if the anchors are synchronous, their offset with respect to the tag is the same, namely $\delta^{ab}_{MB} = \delta^{ac}_{MB}$. On the other hand, since this offset varies over time due to clock drift, we generally have $\delta^{ab}_{MC} \neq \delta^{ab}_{MB}$, because MB and MC are sent at different times. This motivates tracking the clock offset over time, *i.e.*, assuming a clock drift model as in [Giorgi and Narduzzi, 2011]. Both the ToA and TDoA localization principles are illustrated in Figure 2.2, where again both the position and the drift can be estimated thanks to an EKF as performed in [Wann et al., 2006]. The passive (or eavesdropping) tags are shown in red, the anchors in green, the Lines of Position (LoP) in purple. In the absence of noise and when the system is perfectly synchronized, the intersection of the LoP gives the position of the tags.

Bearing Measurements

In order to obtain Angle of Arrival (AoA) measurements, several receptors on the same tag are required to form a sensor array [Naidu, 2009]. Let us give a simple example adapted from [Sahinoglu et al., 2008, 4.1.2]. Consider a two-dimensional setup with two antennas r_1 and r_2 on a given tag receptor u that has to compute the AoA θ_a of a signal coming from the anchor a. This signal is received by r_1 at R_{r_1} (or R_{r_2} for r_2). In that case, the difference

between the two ToA depends on the bearing, namely, we can express the timestamps and their difference as follows [Sahinoglu et al., 2008, p. 68]

$$\begin{cases} R^u_{r_1} \approx \tau_{ab} + c^{-1} l \sin\theta_a + \delta^{ab}, \\ R^u_{r_2} = \tau_{ab} + \delta^{ab}, \end{cases} \Rightarrow R^u_{r_1} - R^u_{r_2} \approx c^{-1} l \sin\theta_a \tag{2.6}$$

assuming that $d_{ab}/l >> 1$, where l is the distance between the antennas. The geometry of the problem is shown in figure 2.3.

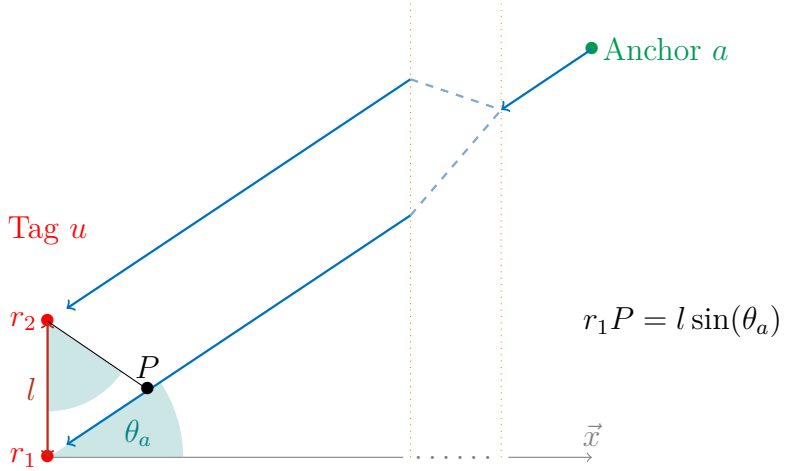

Figure 2.3 – Illustration of the AoA measurement principle

This type of measurement is widely used in UWB positioning systems, for example in [Dotlic et al., 2017] and in the technical report [NASA, 2010]. It can also be used as a complement to ranging techniques such as the TDoA, as presented in [Wann et al., 2006], which provides an improvement in positioning accuracy. We emphasize that since the clock offset is assumed constant in (2.6). Thus, the AoA protocols might also suffer from synchronization problems. Therefore, clock offset must be tracked over time to make accurate measurements [Xu et al., 2008].

2.1.2 Mitigation of UWB Timestamp-based RM Errors

Overall, the methods presented above depend on the ToA accuracy provided by an LDE estimator [Sahinoglu and Gezici, 2006]. As the technical report [Decawave, 2018] suggests, two major sources of error can be identified: synchronization and signal-related errors that degrade LDE performance.

First, the synchronization issue can be addressed by using techniques such as the Precision

Time Protocol (PTP) [Cho et al., 2009]. Then, after observing the clock offset, it can be tracked over time using, for example, a Kalman filter based on a single integrator clock model as in [Giorgi and Narduzzi, 2011]. This kind of implementation has been successfully tested for ToA-based UGV navigation in our work [Cano et al., 2019], where we provided a synchronization method for fixed anchors. This type of tracking has also been validated for UAV localization, for instance in [Hamer and D'Andrea, 2018], which used a more complex clock model to improve precision. Note that a more comprehensive discussion of synchronization and clock modeling can be found in our master's thesis [Cano et al., 2019, Chap. 3].

Second, the ToA estimate provided by the LDE can suffer from systematic biases even under perfect LoS and synchronicity conditions [Decawave, 2018, p.10]. This phenomenon is mainly due to hardware imperfections such as asymmetric radiation patterns of transceivers' antennas or circuitry that causes delays in ToA estimates [González et al., 2009,Savic et al., 2016]. For the popular `DW1000` module manufactured by Qorvo © [Qorvo, 2022], the amplitude of this bias is significant. It can be up to 20 cm, where the expected accuracy of the measurement is 10 cm. As emphasized in the first chapter of this manuscript, PF measurements should not be biased to ensure accurate positioning. Therefore, this bias term must also be tracked in real time to improve the localizability of the MRS.

Finally, as highlighted in Section 1.2.1, in the case of NLoS or MP propagation *scenarii*, the data provided by the LDE may be severely degraded. In this case, a common approach is to remove the contaminated measurement by characterizing the outlier. For this purpose, classification techniques based on the Chanel Impluse Response (CIR) using machine learning are popular to improve the localization [Marano et al., 2010,Bregar and Mohorčič, 2018,Jiang et al., 2020].

Alternatively, instead of simply rejecting the contaminated measurements, one can mitigate their effects using weights that depend on residuals (*e.g.*, for LS) or innovation (*e.g.*, for EKF). For example, the class of M estimators described in [Zoubir et al., 2018] uses weights such as Huber weights [Huber, 1964] to penalize contaminated data. This technique has been used for GNSS in a recent work of our group [Ding et al., 2022] and could then be efficient for indoor navigation systems based on UWB. In addition, sensor fusion can be used to reduce the impact of such outliers. For example, in [Li et al., 2018] a tight coupling of pedestrian DR measurements taken by an Inertial Measurement Unit (IMU) is successfully used to reduce UWB NLoS outliers effects by predicting the motion. However, since the DR measurements introduce drift on the position, this assumes to provide a sufficient quantity of LoS UWB measurements to ensure positioning convergence. To do so, it is necessary to perform outlier filtering on the RF measurements to retrieve the LoS information.

2.2 Modeling the MRS' Geometry Impact on Positioning

As pointed out in section 1.2.2, a poor topology of the MRS agents can affect the localization of tags even with a reasonable noise level. This section gives some basic results to characterize the precision of the position estimator given a certain measurement distribution. These results will then be used to construct cost functions for the deployment of MRS.

2.2.1 Position Estimators

Let us first give a brief overview of the various existing positioning algorithms before establishing a connection between their precision and the geometry of the MRS. Here we are interested in determining the position $\mathbf{p}_u \in \mathbb{R}^n$ of a given tag u thanks to RMs, which is captured in the vector $\tilde{\mathbf{y}} \in \mathbb{R}^M$ for some $M \in \mathbb{N}^*$. We also assume that the generally nonlinear observation model $\mathbf{y}(\mathbf{p}_u)$ is known.

Assuming that $\tilde{\mathbf{y}}$ contains a sufficient amount of non-degenerate RMs, the solution can be determined by the intersection of the LoP as illustrated in Figure 2.2. However, in the presence of measurement errors, these direct approaches cannot be implemented. In practice, the design of the LS problem in order to position u, is widely used in localization systems [Groves, 2013, Sahinoglu et al., 2008, Shen et al., 2008]. It consists in designing an estimator $\hat{\mathbf{p}}_u$ that minimizes the observation residuals [Kay, 1993, Section 8.3]

$$\hat{\mathbf{p}}_u \in \underset{\mathbf{p}_u \in \mathbb{R}^n}{\operatorname{argmin}} \|\tilde{\mathbf{y}} - \mathbf{y}(\mathbf{p}_u)\|^2, \tag{2.7}$$

i.e., solution of a nonlinear LS problem. Because of its nonlinearity, (2.7) must be solved by iterative methods such as Gauss-Newton, Newton-Raphson [Kay, 1993, Section 8.9] or Levenberg-Marquardt [Gavin, 2019]. However, these algorithms can be computationally expensive, *i.e.*, require a large number of iterations, which can be a problem for real-time implementation. Moreover, the measurement $\tilde{\mathbf{y}}$ may be noisy or corrupted (*e.g.*, suffering from NLoS phenomena) and could lead to large estimation errors on $\mathbf{p}_u$. These points motivate a method that recursively considers the motion of the vehicles.

If a dynamic model $\mathbf{p}_u$ is known, then it is now possible to recursively build the estimate $\hat{\mathbf{p}}_u$ using Kalman filtering. The Kalman Filter (KF) filter is the best estimator, in the sense of Mean Squared Error (MSE), for systems admitting linear models of observation and dynamics under additive Gaussian noises [Chui and Chen, 1999, Chap. 9].

Since it is a minimizer of the MSE, the KF can be seen as a form of the recursive weighted LS problem [Chui and Chen, 1999, Section 2.2]. In this paradigm, the covariance of the

processes and the measurement noises play the role of weight matrices that appear in the recursive MSE expression.

However, since the observations $\mathbf{y}(\mathbf{p}_u)$ are generally nonlinear, the KF cannot be applied directly. In practice, the EKF is preferred and requires a linearization of the observation model that includes the Jacobian $\partial\mathbf{y}/\partial\mathbf{p}_u$. This filter is not optimal but remains a standard in the navigation systems, especially when multiple sensor fusion is used [Groves, 2013, Chap. 16] [Raol, 2016]. Moreover, there exists decentralized version of the KF in in the literature, *e.g.*, [Kovvali et al., 2013, Section 4.2]. In particular, this paradigm is transposable to the MRS localization [Roumeliotis and Bekey, 2002], allowing tags' positioning in a complex geometry of the RMs with local information.

In this thesis, we aim to design localizability metrics that are independent of the structure of the estimator in order to quantify the precision provided by the MRS property. However, since LS formulations are common, as mentioned above, we explore this avenue first, before giving an overview of more general criteria.

2.2.2 Dilution of Precision

In GNSS navigation, the DoP is commonly used to characterize localizability [Groves, 2013, Section 7.4]. To define this concept, let $\mathcal{U}$ be the set of the U tags of a given MRS and $\mathcal{K}$ be the set of the K anchors used to localize it. We assume that M distance measurements $\tilde{d}_{ij}$ are captured within the MRS and collected in $\tilde{\mathbf{d}} = [\dots \tilde{d}_{ij} \dots]^\top \in \mathbb{R}^M$ where $i, j \in \mathcal{U} \times (\mathcal{U} \cup \mathcal{K})$, with $i \neq j$. We need to solve the tag positioning problem, *i.e.*, estimate $\mathbf{p}_\mathcal{U} = [\dots \mathbf{p}_u^\top \dots]^\top$ where $\mathbf{p}_u \in \mathbb{R}^n$ for $u \in \mathcal{U}$. To estimate the positions of the tags, assuming a sufficient number of non degenerate ranging measurements [Aspnes et al., 2006], we can solve the following least squares problem

$$\hat{\mathbf{p}}_\mathcal{U} \in \underset{\mathbf{p}_\mathcal{U} \in \mathbb{R}^U}{\operatorname{argmin}} \|\tilde{\mathbf{d}} - \mathbf{d}(\mathbf{p}_\mathcal{U})\|^2, \tag{2.8}$$

with $\mathbf{d}(\mathbf{p}_\mathcal{U}) = [\dots d_{ij}(\mathbf{p}_\mathcal{U}) \dots]^\top \in \mathbb{R}^M$ considering $d_{ij}(\mathbf{p}_\mathcal{U}) = \|\mathbf{p}_i - \mathbf{p}_j\|$ where the pair $i, j \in \mathcal{U} \times (\mathcal{U} \cup \mathcal{K})$, *i.e.*, contains at least a tag. The LS problem (2.8) can be solved by performing the following Gauss-Newton iterations [Kay, 1993]

$$\hat{\mathbf{p}}_\mathcal{U}^k = \hat{\mathbf{p}}_\mathcal{U}^{k-1} - \mathbf{J}_k^\dagger \left(\tilde{\mathbf{d}} - \mathbf{d}(\mathbf{p}_\mathcal{U}^{k-1})\right), \tag{2.9}$$

with $k \in \mathbb{N}^*$ to estimate $\mathbf{p}_\mathcal{U}$, providing an initial estimate $\hat{\mathbf{p}}_\mathcal{U}^0$. In (2.9) we called the measurement Jacobian $\mathbf{J}_k := \partial\mathbf{d}/\partial\mathbf{p}_\mathcal{U}|_{\mathbf{p}_\mathcal{U}=\mathbf{p}_\mathcal{U}^{k-1}} \in \mathbb{R}^{M \times nU}$. Note that in [Groves, 2013, Section 7.4], clock offset is also considered as a state to be estimated. Since we can use TWR, to directly compensate for it in the ToF estimation, we have omitted it for simplicity.

Let us assume a Gaussian independent, uniform and centered distribution of the range measurements $\tilde{\mathbf{d}} \sim \mathcal{N}(\mathbf{d}, \mathbf{I}_M \sigma_r^2)$ for a given noise level $\sigma_r^2 > 0$. Then, at convergence of (2.9), the covariance of the error can be expressed as follows [Groves, 2013, Appendix B.2.1]

$$\mathbf{\Sigma} := \mathbb{E}\{(\hat{\mathbf{p}}_\mathcal{U} - \mathbf{p}_\mathcal{U})(\hat{\mathbf{p}}_\mathcal{U} - \mathbf{p}_\mathcal{U})^\top\} = \mathbf{G}\sigma_r^2 \tag{2.10}$$

where $\mathbf{G} := \left(\mathbf{J}_0^\top \mathbf{J}_0\right)^{-1}$ is the DoP matrix. Overall, $\mathbf{G}$ can be viewed as a noise amplification and used as a model to quantify the quality of the mesh geometry using criteria extracted from the matrix. For example, for a single-tag system ($U = 1$), if $n = 3$, we have the Horizontal, Vertical and Geometric DoPs defined as follows

$$HDoP = \sqrt{G_{11} + G_{22}},\ VDoP = \sqrt{G_{33}} \text{ and } GDoP = \sqrt{G_{11} + G_{22} + G_{33}}. \tag{2.11}$$

These quantities can be seen as localizability cost functions. Indeed, if they increase, then (2.10) implies that the error covariance is amplified, *i.e.*, that the tag localizability is decreased. In the literature, they are used to analyze the localizability of tags located by ToF-based systems [Lv et al., 2010, Xue and Yang, 2017]. More specifically, in GNSS-based navigation, the impact of the $VDoP$ is carefully studied because the satellites do not cover a wide range of altitudes. To mitigate this effect, sensor fusion can be performed, for example using opportunity RF signals as proposed in [Morales et al., 2016]. In wireless sensor networks, especially for UWB-based systems, it is possible to place static sensors to reduce the DoP. This is done by solving optimization problems using the above function as cost functions [Zhao et al., 2020, Khalife and Kassas, 2019].

2.2.3 Cramér-Rao Lower Bounds

The DoP metric is very specific to the resolution of (2.8) and is based on Newton-Gauss iterations in the case of Gaussian noise. For this reason, it is interesting to consider a broader model in order to construct localization cost functions under weaker assumptions.

In our research, we used the Cramér-Rao Lower Bound (CRLB), which can be seen as a generalization of the DoP [Lv et al., 2010]. This tool, introduced in 1945 by the Indian statistician Rao [Rao, 1945] and formalized a year later by the Swedish mathematician Cramér [Cramér, 1946], is historically the first and most popular covariance bound [Ren, 2015, Kay, 1993]. Like the DoP, the CRLB is widely used as a performance tool for the wireless sensor network positioning problem [Patwari et al., 2005, Prorok et al., 2012b, Shi et al., 2020]. Due to its weak assumptions and relative ease of computation, this bound is applied to many use cases involving parameter estimators to characterize their accuracy [Ren, 2015].

Standard CRLB

Consider a parameter vector $\mathbf{p}_{\mathcal{U}} \in \mathbb{R}^{nU}$, $U \in \mathbb{N}$ that we want to estimate and the measurement vector $\tilde{\mathbf{y}} \in \mathbb{R}^M$ with $M \in \mathbb{N}^*$. We define the Probability Density Function (PDF) of $\tilde{\mathbf{y}}$ as follows $f : \mathbb{R}^M \times \mathbb{R}^{nU} \mapsto \mathbb{R}^+, \mathbf{p}_{\mathcal{U}} \to f(\mathbf{p}_{\mathcal{U}})$, which depends on the parameter. We assume that f is twice continuously differentiable with respect to $\mathbf{p}_{\mathcal{U}}$. Let be an unbiased estimator $\hat{\mathbf{p}}_{\mathcal{U}}$ of $\mathbf{p}_{\mathcal{U}}$ (*i.e.*, such that $\mathbb{E}\{\hat{\mathbf{p}}_{\mathcal{U}}\} = \mathbf{p}_{\mathcal{U}}$), that has only access to the measurement $\tilde{\mathbf{y}}$, with a finite covariance $\mathbf{\Sigma}$ (using the definition in (2.10)). Then $\hat{\mathbf{p}}_{\mathcal{U}}$ verifies the following inequality [Kay, 1993, Chap. 3]

$$\mathbf{\Sigma} \succeq \mathbf{F}_{\mathcal{U}}^{-1}(\mathbf{p}_{\mathcal{U}}), \text{ where } \mathbf{F}_{\mathcal{U}} := -\mathbb{E}_{\mathbf{p}_{\mathcal{U}}} \left\{ \frac{\partial^2 \ln f}{\partial \mathbf{p}_{\mathcal{U}} \partial \mathbf{p}_{\mathcal{U}}^\top} \right\}, \tag{2.12}$$

where $\mathbf{F}_{\mathcal{U}}$ is called the Fisher Information Matrix (FIM) and $\mathbf{B}_{\mathcal{U}} = \mathbf{F}_{\mathcal{U}}^{-1}$ is the CRLB. The notation $\mathbf{A} \succeq \mathbf{B}$, given $\mathbf{A}, \mathbf{B} \in \mathbb{R}^{a \times a}$, $a \in \mathbb{N}^*$, means that $\mathbf{A} - \mathbf{B}$ is a positive semi definite matrix.

The result (2.12) can be proved using both the Cauchy-Schwarz inequality and the unbiased assumption as shown in [Kay, 1993, Appendix 3B]. Similar to the DoP matrix $\mathbf{G}$ defined in (2.11), the CRLB can be used to construct localizability cost functions for MRS deployment. In fact, the CRLB is particularly well adapted to the design of deployment policies that need to be computationally efficient and rely on general but realistic precision criteria.

In fact, since (2.12) is a lower bound, we assume that "decreasing" $\mathbf{B}_{\mathcal{U}}$ improves localization accuracy. However, the bound may be far from the actual performance of the estimators, which may have access to more than just a single observation $\tilde{\mathbf{d}}$, *e.g.*, vehicle kinematics model. To solve this problem, we can add some information to the FIM formulation (*i.e.*, obtain a tighter bound), and this motivates a discussion on possible extensions of CRLB.

Extensions of the CRLB

First, we can consider that a robot can carry several tags with known positions in the robot's frame. This design allows to improve the localization by adding information to the estimator, and also the robustness to failures by increasing the number of sensors. In this way, it is possible to estimate the pose (position and attitude) of the robot, which adds constraints to the estimator and improves its precision. Thus, this parameterization of the problem requires that the CRLB be extended to these use cases in order to remain realistic.

In the recent literature, we can cite the FIM extensions to the $SO(3)$ group [Boumal et al., 2014, Chirikjian, 2018], which provides a specific CRLB formulation adapted to the rigid transformations [Bonnabel and Barrau, 2015]. As an alternative to explicit parameter

changes in the CRLB evaluation, it has been proved in [Menni et al., 2014] that the *a posteriori* application of constraints in the FIM derivation is equivalent to a reparameterization. This result then allows the Constrained Cramér-Rao Lower Bound (CCRLB) introduced in [Gorman and Hero, 1990] to be used instead of bounds based on a minimum number of parameters, which require more complex derivations.

On the other hand, we also consider that a prior statistical model may be available to the estimator, *e.g.*, a vehicle dynamics model provided to an EKF. To include this information, the Bayesian Cramér-Rao Lower Bound (BCRLB) defined in [Van Trees and Bell, 2007] can be used. In addition to the measurement PDF f presented in (2.12), this CRLB requires a statistical distribution of the parameter, generally independent of the observation. Typically, for RF-based robot localization, incoming RMs are considered independent of a previous position estimate that can be used as a prior using uncertainty propagation through the vehicle dynamics. The BCRLB has been applied to evaluate the performance of position estimators in wireless sensor network [Fritsche et al., 2013] and is well known for radar applications [Ren, 2015].

Using some relaxing assumptions, the BCRLB can provide a recursive covariance bound [Tichavsky et al., 1998]. This bound, called Recursive Bayesian Cramér-Rao Lower Bound (RBCRLB), is less computationally demanding: the prior distribution can be hard to compute, then, the recursive formula allows to obtain a faster approximation [Galy et al., 2015]. For linear dynamics, the bound takes the form of a Ricatti equation, similar to the Kalman filter covariance recursion [Chui and Chen, 1999]. However, this bound is looser than the BCRLB since it discards some information in its simplifying assumptions [Ren et al., 2015].

Finally, we considered another form of CRLB in our research: the Uniform Cramér-Rao Lower Bound, which was designed for biased estimators [Hero et al., 1996,Eldar, 2007] based on the biased CRLB presented in [Bell and Tian, 1968]. As we pointed out in Section 2.1.2, the UWB-based RMs have a systematic bias that could be mitigated by motion planning. However, the application of this family of bounds requires an explicitly parameter-dependent bias model and seems to apply only to the linear model [Eldar, 2004]. Thus, these bounds are difficult to implement directly in an experimental context. In particular, they require prior calibration of the robot's workspace to identify the bias model.

2.3 Formation Control

Once the modeling of localizability is given by a matrix covariance bound (or a DoP matrix), we need to extract a scalar criterion to solve the MRS placement problem. In other words,

we want to perform formation control for the MRS using a cost function that includes a localizability criterion.

In this section, we present results from the literature that are closely related to localizability optimization. Indeed, in the last decade, as the interest in MRS has grown, the distributed swarm connectivity and then rigidity control have been increasingly studied. We can take advantage of these works in order to generalize some of the algorithms to the localizability optimization problem.

2.3.1 Distributed Connectivity Optimization

The paradigm of formation control is strongly related to graph theory [Bullo et al., 2009] and such is the problem addressed in this thesis. Indeed, the problem of positioning the tags is in general solved distributively, *i.e.*, with local information provided to the tags' neighborhoods. Thus the MRS must at least be connected in order to position it, enabling measurements between agents. For a positioning problem based on RMs, we consider the undirected graph $\mathcal{G} = (\mathcal{E}, \mathcal{U} \cup \mathcal{K})$ as an elementary theoretical model. Let its vertices be the whole set of agents $\mathcal{U} \cup \mathcal{K}$, which is the union of the sets of tags ($\mathcal{U}$) and anchors ($\mathcal{K}$). On the other hand, the edges of the graph $\mathcal{E}$ are defined as the union of the links between the anchor pairs (since they have known position we assume the anchors' sub-graph fully connected) and the communicating pairs with at least one agent being a tag. We also assume that the graph $\mathcal{G}$ is symmetric, *i.e.*, if an agent i is able to communicate with j then the reciprocal is true. Formally, the edge set $\mathcal{E}$ can be written as

$$\mathcal{E} = \{\{k, k'\} \in \mathcal{K} \times \mathcal{K}\} \cup \{\{u, i\} \in \mathcal{U} \times (\mathcal{K} \cup \mathcal{U}), i \in \mathcal{N}_u\}, \tag{2.13}$$

where $\mathcal{N}_u$ is u's neighbor set consisting of the agents communicating with u. With this model it becomes clear that $\mathcal{E}$, which models the RMs, strongly influences the positioning of $\mathcal{U}$, *i.e.* the localizability of the tags. Therefore, the connectivity of the graph, driven by the set $\mathcal{E}$ defined in (2.13), would be the first step to investigate in order to improve the positioning.

If we denote $N = |\mathcal{U} \cup \mathcal{K}|$ as the cardinality of the agents, the graph $\mathcal{G}$ can be characterized by three different matrices. First, the *adjacency matrix* $\mathbf{A} \in \mathbb{N}^{N \times N}$ is defined as

$$A_{ij} := \mathbf{1}_{\mathcal{N}_j}(i);\ i, j \in [1, N]^2,$$

where $\mathbf{1}_{\mathcal{A}}(a)$ is the indicator function of the set $\mathcal{A}$ such that $\mathbf{1}_{\mathcal{A}}(a) = 1$ if $a \in \mathcal{A}$ and zero

otherwise. Second, the *degree (or valency) matrix* $\mathbf{D} \in \mathbb{N}^{N\times N}$ with coefficients

$$D_{ii} = |\mathcal{N}_i| \text{ and } D_{ij} = 0;\ \forall i, j \in [1, N]^2, i \neq j,$$

that stores the number of neighbors for each agent in the network. These two matrices allow to define the following *Laplacian Matrix*

$$\mathbf{L} := \mathbf{D} - \mathbf{A} \in \mathbb{Z}^{N\times N}, \tag{2.14}$$

which contains all the information about the graph connectivity. Therefore, this matrix is used to characterize the connectivity of MRS and in particular for robot formation control [Michael et al., 2009, Ikemoto et al., 2020]. Note that as an alternative to (2.14), $\mathbf{L}$ can also be defined thanks to the directed graph *incidence matrix*. This matrix, denoted $\mathbf{H} \in \mathbb{Z}^{N\times|\mathcal{E}|}$ is defined by first assigning an arbitrary direction $i \to j$ to each edge $\{i, j\}$ of $\mathcal{E}$, and then setting each element as follows:

$$\text{for } \{i, j\} \in \mathcal{E}, k \in \mathcal{U} \cup \mathcal{K}, H_{k,i\to j} = \begin{cases} 1 & \text{if } k = i, \\ -1 & \text{if } k = j, \\ 0 & \text{otherwise.} \end{cases}$$

Therefore, $\mathbf{L}$ can be seen as a generalized square of the incidence matrix, namely $\mathbf{L} = \mathbf{H}\mathbf{H}^\top$.

To perform such a connectivity control, it is common to choose the *Fiedler eigenvalue* λ_2 [Barrière et al., 2013] as the reward function and set up a maximization problem to improve connectivity. λ_2 is defined as the smallest nonzero eigenvalue of $\mathbf{L}$, its subscript 2 indicates that it is, if the graph is connected, the second in ascending order, *i.e.* $\lambda_1 \leq \lambda_2 \leq \cdots \leq \lambda_N$. In fact, $\mathbf{L}$ is by definition rank-degenerate (its kernel has at least one dimension, due to the zero-sum property of its columns and its rows) and has positive eigenvalues, see [Bullo, 2019, Section 6.2]. We emphasize that $\lambda_2 > 0$ implies that $\mathcal{G}$ is connected [Bullo, 2019, Corollary 6.8] and this fact justifies the design of such reward functions.

The optimization of the Fiedler eigenvalue of a graph $\mathcal{G}$ representing a MRS requires a decentralized algorithm for the sake of scalability and robustness to the topology of the system. The work of *Yang et al.* [Yang et al., 2010] proposes a distributed estimator of λ_2 based on the power iteration algorithm. In [Michael et al., 2009], a distributed and topology-responsive control law that penalizes distance constraint violations (modeling the disconnections) was successfully implemented on a multi-UGV system. The more recent journal article [Cai et al., 2017] implements a Fiedler-based control law to improve the connectivity of UAV formations.

Finally [Ikemoto et al., 2020] presents a fast distributed robot position and Laplacian matrix eigenvector estimator that significantly improves distributed computation to increase λ_2 in a swarm of ground robots.

2.3.2 Rigidity Maintenance Problem

In addition to connectivity, which considers abstract communication links between agents, the notion of rigidity includes the geometry of physical edges and vertices. In this paradigm, largely inspired by civil engineering [Tay and Whiteley, 1985], a framework is considered instead of a graph. The framework $(\mathcal{G}, \mathbf{p})$ considers both the communication graph $\mathcal{G}$ and the vector $\mathbf{p}$ containing all agents $j \in \mathcal{U} \cup \mathcal{K}$ positions. Its vertices are the positions $\mathbf{p}_j$ and its edge weights are the distances d_{ij} for $i \in \mathcal{N}_j$ (respectively, for $j \in \mathcal{N}_i$ since the graph are assumed to be symmetric). The difference between $\mathcal{G}$ and $(\mathcal{G}, \mathbf{p})$ is illustrated in Figure 2.4, where a four-agent connectivity graph is shown next to its corresponding three-dimensional rigidity framework.

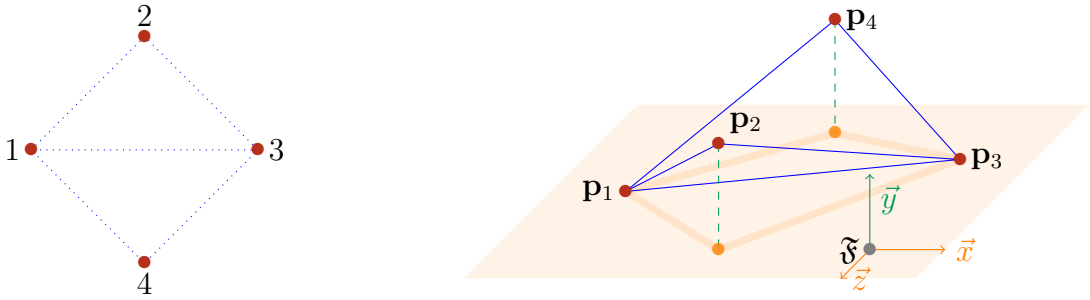

(a) Connectivity graph $\mathcal{G}$

(b) Rigidity framework $(\mathcal{G}, \mathbf{p})$

Figure 2.4 – Rigidity graph and rigidity framework

The notion of rigidity comes in several forms. The $(\mathcal{G}, \mathbf{p})$ framework's *global rigidity* occurs when it is uniquely realized, *i.e.*, given the distances between neighbors, their relative position are uniquely defined [Connelly, 2005, Whiteley, 1996]. For example, the framework shown in Fig. 2.4b is not globally rigid because 2 can be moved around the $[\mathbf{p}_1, \mathbf{p}_3]$ segment without changing d_{12} and d_{23}. Note that in [Aspnes et al., 2006], the notion of rigidity is used to prove the unicity of the solution of the positioning problem.

However, for MRS formation control, *infinitesimal rigidity*, which is a local version of rigidity, is used rather than global rigidity because of its simple algebraic definition [Zelazo et al., 2012]. This type of rigidity uses the *rigidity matrix*, which can be seen as an incidence matrix $\mathbf{H}$ weighted by normalized relative positions $\bar{\mathbf{p}}_{ij} = (\mathbf{p}_i - \mathbf{p}_j)^\top / d_{ij}$ [Tay and Whiteley,

1985]. Note that the DoP matrix defined in (2.10) is related to the $\bar{\mathbf{p}}_{ij}$ coefficients, since $\bar{\mathbf{p}}_{ij} = \partial d_{ij}/\partial \mathbf{p}_i$ is present in the LS Jacobian $\mathbf{J}$. This remark emphasizes the connection between rigidity and localizability optimization. This is not surprising, since the (global) rigidity of $(\mathcal{G}, \mathbf{p})$ implies relative position uniqueness under perfect observation of the distance. The connection between these two notions is made explicitly in Chapter 5.

By definition, the incidence matrix, which is a square root of the Laplacian matrix, is rank deficient [Bullo, 2019, Section 9.2]. The rigidity matrix is also rank deficient, and a Fiedler-like optimization scheme, which discards its nontrivial kernel, can be used to improve the rigidity of the MRS [Zelazo et al., 2012]. This control law has been successfully implemented by *Zelazo et al.* in a multiple-UAV system and has successfully improved the rigidity of the MRS [Zelazo et al., 2015].

Alternative strategies that use other types of rigidity, such as ratio-of-distance rigidity [Cao et al., 2020] can also be used in MRS formation control. Among these strategies we can also mention the *bearing rigidity* theory [Michieletto et al., 2021], which is strongly related to the localizability of systems positioned by AoA (see note 6.2 in Chapter 6). In [Zhao and Zelazo, 2016] the author proposes a control law for MRS based on the bearing Laplacian matrix.

Mathematical Tools for CRLB-Based Localizability Optimization

In our work, we use the CRLB localizability design and exploit the RMs FIM structure presented in [Patwari et al., 2005]. This structure is very similar to a weighted Laplacian matrix [Le Ny and Chauvière, 2018] and this fact is turned into an advantage to design distributed deployment algorithms based on pre-existing rigidity or connectivity related work.

For the design of the localizability cost functions, we mainly use the optimal design of experiments theory [Pukelsheim, 2006], that is widely used in the sensor network domain, to design scalar criteria extracted from a characteristic matrix [Sagnol, 2010]. For example, taking the trace of a covariance matrix (referred as the A-optimality strategy) as penalty is equivalent to set a mean uncertainty minimization problem [Carrillo et al., 2012]. Note that the Fiedler value cost function mentioned above for rigidity maintenance is part of the optimal design of experiments (called E-optimality strategy). Alternative strategies include cost functions based on leveraging the determinant or trace of the matrices to be optimized, those advantages and limitations are discussed extensively throughout Chapter 5.

Then the localizability cost functions can be minimized using local policies, *i.e.*, gradient based motion planning [Khatib, 1986, Lynch and Park, 2017] as in [Zelazo et al., 2015] for rigidity. Alternatively, the localizability of a system can be improved using non-myopic

algorithms, *i.e.*, trajectory generation, as proposed in [Papalia and Leonard, 2020] based on our previous work. However, trajectory generation is beyond the scope of this thesis and is left for future work.

CHAPTER 3 RESEARCH OBJECTIVES, CONTRIBUTIONS AND DOCUMENT OUTLINE

> "You will never reach your destination if you stop and throw stones at every dog that barks."
>
> – Sir. Winston Churchill (1874-1965)

Since this thesis is *article-based*, we provide in this chapter the guideline of our contributions and a description of the investigated research hypotheses. Therefore, we recall the specific research objectives, provide the outline of the manuscript and present the overall organization of the contributed articles in the following sections.

3.1 Research Organization

We outline how our work is structured in terms of goals, research hypotheses, and time constraints in this section.

3.1.1 Research Objectives and Hypotheses

The following research question can be used to summarize the thesis's overall objective:

How to optimize the localizability of an MRS equipped with UWB sensors?

Our research was divided into three different research axes to answer this question:

Theme 1 Mitigation of Errors in UWB Ranging Measurements;

Our goal in this thesis project is to create MRS deployment policies to optimize localizability and test them on real-world robots. For our experiments, we used ground MRSs equipped with UWB sensors performing ranging. However, as mentioned in Chapter 2, it is necessary to improve UWB measurements captured by a pair of sensors before carrying out the deployment that mitigates DoP phenomena. In particular, the assumption of unbiased estimators taken in (2.12) for the CRLB computation is violated if **systematic measurement biases** are not properly calibrated. The LoS hypothesis for measurements that produce near Gaussian RMs PDFs become false when the ranging data is contaminated by NLoS or/and MP outliers, as mentioned in Section 1.2.1.

Hence, the CRLB may be inaccurate in that scenario and result in an inadequate deployment of the MRS. We therefore assume that these effects would be significantly reduced by the estimators. Then, we seek to experimentally verify the following two hypotheses:

Hypothesis 1. *"The bias on UWB ToF-based measurements can be efficiently calibrated"*

Hypothesis 2. *"The corrected range measurements can be approximated with a Gaussian model". In particular, the NLoS and MP outliers in the upcoming MRS deployment can be neglected.*

Theme 2 Cooperative Localizability Optimization;

The mitigation of DoP effects, *i.e.*, the localizability induced by the MRS geometry, is covered in this theme. In this axis we sought to develop **CRLB-based** MRS deployment policies improving tag positioning that are **scalable** and **real-time implementable**. Therefore, is it necessary to design algorithms that enable distributed deployments (*i.e.*, where each agent can only observe its neighbors' estimates). Then, two hypotheses in this theme remain to be validated:

Hypothesis 3. *"The decrease of the CRLB significantly enhances the tags' position estimates in practice." In fact, since it is a* ***lower bound****, there is no assurance that the estimator's performance will be close to the CRLB.*

Hypothesis 4. *"The MRS distributed deployment algorithms can be performed in real-time despite noisy measurements." It is essential to validate this hypothesis because a practical deployment policy relies on noisy position estimates to control the robots.*

With the help of large-scale simulations and physical implementations on smaller MRSs, we wish to verify these hypotheses. Additionally, the deployment of robots carrying multiple tags must be managed, utilizing the CCRLB, and validated in the same way.

Theme 3 Extensions to Localizability.

The Gaussian model of RMs (*i.e.*, Hypothesis 2) may be inaccurate at long range. Namely, the performance of LDE estimators in the UWB chips may decrease significantly if the received power becomes low. We intend to extend the localizability cost functions to range-deteriorated measurement models, in order to address this problem. By adding this distortion model to the CRLB, we aim to design a tighter (*i.e.*, more realistic) bound.

Both the standard CRLB and the DoP characterize the localizability at a given time, *i.e.*, for a fixed MRS configuration $\mathbf{p}$. However, deployment strategies relying on these instantaneous information models might be inefficient for estimators that track positions over time, such as Kalman filters. For instance, once the estimator has converged, if a brief weak DoP configuration occurs, it will result in a significant (and time costly) MRS redeployment for a negligible gain of precision. Then, using the BCRLB, we wish to provide a more realistic localizability cost function than the traditional CRLB, BY leveraging prior information. Additionally, this paradigm enables the theoretical coupling of estimation and deployment in path planning. We aim to propose a method for the EKF, a popular navigation filter.

For both of these extensions, we seek experimental confirmation of the following claim:

Hypothesis 5. *"Enhanced localizability models yield cost functions closer to estimator performance than classical ones."*

The BCRLB allows for fixed anchor placement algorithms where the tags' position are only known through probable operation zones. This makes it possible to place anchors in zones of operation with complex geometries. In these scenario, the tags' positions are probabilistic and only their PDFs remain known, defining its probable zone of operation.

Hypothesis 6. *"BCRLB allows to design computationally effective anchor placement policies when the PDF of their position is known a priori."*

We aim to validate this last hypothesis through simulation.

3.1.2 Project Organization

This thesis project was co-advised between Polytechnique Montréal (Canada) and ISAE-Supaéro (France). It was planned, with 50% of the research being conducted in each laboratory, namely the Mobile Robotics and Autonomous Systems Laboratory (MRASL, Polytechnique) and the Department of Electronics, Optronics, and Signal Processing, respectively (DEOS, ISAE). The timeline of the project is given in Figure 3.1.

This doctoral project is in the continuity of the candidate's *Master of Science* thesis [Cano, 2019], presented in 2019 in the same research group at Polytechnique Montréal. This master's project aimed to develop a localization system based on UWB using a ToA protocol. The network's synchronization, which was essential, as highlighted in Chapter 2, was wireless and performed by the RF beacons. The UWB board used in this project has been again

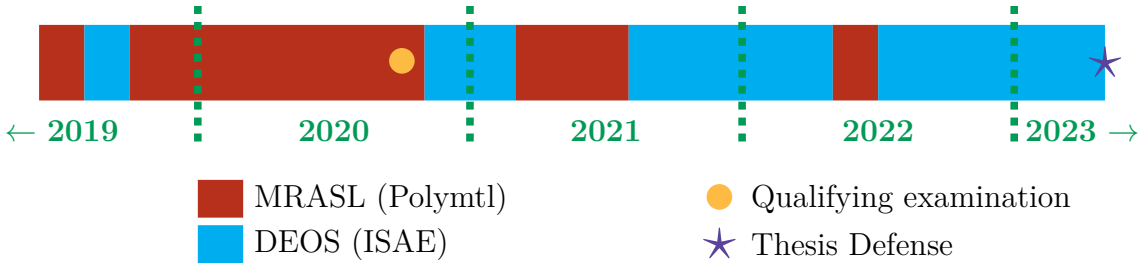

Figure 3.1 – Thesis timeline

used in this thesis and is presented in Figure 4.1. Additionally, the embedded code that implements the SSTWR and is used to validate our deployments is derived from the ToA protocol presented in [Cano et al., 2019], which was the result of the masters' work.

3.2 Contribution

We now list the contributions made in this thesis. The document's outline is presented after a brief overview of the submitted scientific papers.

3.2.1 Contribution History

Our initial objective was to pursue the prior work of our research team, which has been presented at the American Control Conference (ACC) in Milwaukee, USA, in 2018 [Le Ny and Chauvière, 2018]. The design of the localizability cost functions was discussed in this work, along with some connections to rigidity theory and decentralized optimization. In that work, the robots were considered as single points and a gradient descent was applied on the localizability cost function in order to provide the optimal geometry.

We then extended this work in [Cano and Le Ny, 2021] to robots carrying several tags, using distance constraints in the CRLB parameterization. This work was presented at the *2021 IEEE International Conference on Robotics and Automation (ICRA'21)* in Xi'An, China in June 2021. However, the validation of these preliminary results were only simulated, and we aimed to implement the planner on hardware.

In [Cano et al., 2022b] we proposed a method to compensate for clock and RxP induced biases for ToF measurements taken by UWB transceivers. In particular, we validated them for the SSTWR protocol used in the later deployment work. In doing so, we verified the Hypothesis 1 to a reasonable degree, which was a prerequisite for a physical implementation of the planers using CRLBs. This article was published in the *IEEE Robotics and Automation*

Letters (RA-L) in January 2022 and presented at the *2022 IEEE International Conference on Robotics and Automation (ICRA'22)* in Philadelphia, United States, in May 2022.

The article [Cano and Le Ny, 2023], which can be considered as the heart of our work on MRS localizability, builds on [Le Ny and Chauvière, 2018] and [Cano and Le Ny, 2021]. It extended the use of constrained localizability to relative position in three dimensions, allowing the improvement of attitude estimation. Moreover, it allowed to highlight the link between localizability and rigidity theory by studying the structure of the FIM. In particular, theorems guaranteeing the invertibility of the FIM (and thus the existence of the CRLB) have been proposed. These two preliminary theoretical works allowed to propose a decentralized gradient descent of the different localizability cost functions proposed in [Le Ny and Chauvière, 2018]. Then, both simulated and experimental results aimed to validate the Hypotheses 3 and 4. This article was submitted to *IEEE Transactions on Robotics (T-RO)* in February 2022, then revised in October of the same year and conditionally accepted in January 2023.

In [Cano et al., 2022c] we extended the standard CRLB of the previous work, which assumed a constant variance RMs, to distance degraded measurements. In doing so, we allowed the inclusion of power fading effects by fitting the experimental data to the CRLB formulation. In addition, another goal of this paper was to model "smooth" communication losses over large distances, as an alternative to a formal time-varying communication graph, which is more complicated to implement in the MRS deployment algorithm. This RM model adds some information to the CRLB that makes it tighter (and thus more realistic), which validates Hypothesis 5.

In the article [Cano et al., 2022a] we proposed a real-time motion planner tailored to estimators that have access to a Gaussian prior. The main difficulty was to compute the CRLB, which is Bayesian and is only calculable through numerical schemes. In this work, we implemented a BCRLB-based gradient descent method that uses the posterior distribution of an EKF as input to deploy a MRS. Hypothesis 5 was satisfied by this implementation.

These last two articles, [Cano et al., 2022c] and [Cano et al., 2022a], were presented at the *2022 IEEE/RSJ International Conference on Intelligent Robots and Systems (IROS'22)* in Kyoto, Japan in October 2022.

Finally, in [Cano et al., 2023], we proposed an implementation of robust KF based on M-estimation. It presented a method using the Huber function and RxP to mitigate MP outliers for UWB measurements in an obstructed indoor environment. This work, although closely related to the project due to its experimental aspects for UGV navigation in a realistic environment, is distant from the main subject of this thesis since it involves an *a posteriori* filtering method that does not quantify or optimize localizability. Therefore, we considered it

as an additional contribution to the *Axis 1*, *i.e.*, not included in this manuscript. This article has been accepted for presentation at the *2023 IEEE International Conference on Acoustics, Speech and Signal Processing (ICASSP'23)* to be held in Rhodes, Greece, in June 2023.

All of the above contributions and their status are summarized in Table 3.1 in chronological order of their last submission/acceptance and with their corresponding Chapter.

Table 3.1 – List of publications. (Chronological order)
Co-Authors Initials (CAI) : Jérôme Le Ny (JLN), Gaël Pagès (GP), Éric Chaumette (ÉC), Corentin Chauffaut (CC) and Yi Ding (YD).
Theme color code : 1 (red); 2 (green); 3 (blue)

Citation	Title	CAI	Publication
[Cano and Le Ny, 2021]	Improving Ranging-Based Location Estimation with Rigidity-Constrained CRLB-Based Motion Planning	JLN	ICRA'21
[Cano et al., 2022b] **Article 1/Chap. 4**	Clock and Power-Induced Bias Correction for UWB Time-of-Flight Measurements	GP ÉC JLN	RA-L &ICRA'22
[Cano et al., 2022c] **Article 3/Chap. 6**	Optimal Localizability Criterion for Positionning with Distance-Deteriorated Relative Measurements	GP ÉC JLN	IROS'22
[Cano et al., 2022a] **Article 4/Chap. 7**	Maintaining Robot Localizability With Bayesian Cramér-Rao Lower Bounds	CC GP ÉC JLN	IROS'22
[Cano and Le Ny, 2023] **Article 2/Chap. 5**	Ranging-Based Localizability Optimization for Mobile Robotic Networks	JLN	T-RO
[Cano et al., 2023]	A Robust Kalman Filter Based Approach for Indoor Robot Positionning with Multi-Path Contaminated UWB Data	YD GP ÉC JLN	ICASSP'23

3.2.2 Manuscript Outline

The organization of the manuscript, consisting of four selected articles and one additional chapter, is as follows.

First, Chapter 4, [Cano et al., 2022b], allows to present the low-level part of the UWB-based SSTWR protocol used in all our experiments. In particular, it highlights that the range distributions are close to Gaussian in LoS. It also allows to understand the systematic bias phenomena and to provide an original method to calibrate them.

Then, Chapter 5, [Cano and Le Ny, 2023], first presents theoretical results on the MRS localizability and provides optimization problem formulations in order to improve the positioning accuracy of the tags. Then, distributed gradient descent schemes, or Lagrangian in the case of multi-tag robots, are proposed to reduce the localizability cost function. Finally, some illustrative simulation and experiments are provided.

Subsequently, the extension of localizability to range deteriorated measurements is given in Chapter 6, [Cano et al., 2022c], with an experimental example. Bayesian localizability is treated in Chapter 7 , [Cano et al., 2022a], for its integration into the EKF framework and in Chapter 8 as well. The latter chapter presents some additional results on localizability-driven anchor placement considering a prior PDF on the tag positions.

The contributions made by this thesis are then discussed in Chapter 9 and summarized in Table 9.1. Finally, Chapter 10 concludes this thesis.

CHAPTER 4 ARTICLE 1 : CLOCK AND POWER-INDUCED BIAS CORRECTION FOR UWB TIME-OF-FLIGHT MEASUREMENTS

Published in IEEE Robotics and Automation Letters, 9th January 2022.

Coauthors : Justin Cano[1,2], Gaël Pagès[1], Éric Chaumette [1], Jérôme Le Ny[2]

[1] DEOS, ISAE-Supaéro, Toulouse France.

[2] EE Dept., Polytechnique Montréal, QC, Canada & GERAD, Montréal, QC, Canada.

Abstract

Ultra-Wide Band (UWB) communication systems can be used to design low cost, power efficient and precise navigation systems for mobile robots, by measuring the Time of Flight (ToF) of messages traveling between on-board UWB transceivers to infer their locations. Theoretically, decimeter level positioning accuracy or better should be achievable, at least in benign propagation environments where Line-of-Sight (LoS) between the transceivers can be maintained. Yet, in practice, even in such favorable conditions, one often observes significant systematic errors (bias) in the ToF measurements, depending for example on the hardware configuration and relative poses between robots. This paper proposes a ToF error model that includes a standard transceiver clock offset term and an additional term that varies with the received signal power (RxP). We show experimentally that, after fine correction of the clock offset term using clock skew measurements available on modern UWB hardware, much of the remaining pose dependent error in LoS measurements can be captured by the (appropriately defined) RxP-dependent term. This leads us to propose a simple bias compensation scheme that only requires on-board measurements (clock skew and RxP) to remove most of the observed bias in LoS ToF measurements and reliably achieve cm-level ranging accuracy. Because the calibrated ToF bias model does not depend on any extrinsic information such as receiver distances or poses, it can be applied before any additional error correction scheme that requires more information about the robots and their environment.

4.1 Introduction

Mobile robots require accurate position estimates in real-time to operate. Satellite Navigation Systems provide relatively reliable localization but only when the line-of-sight (LoS) between the receiver and sufficiently many satellites can be maintained. Hence, indoor and covered environments require alternative positioning systems, e.g., using machine vision or short-

range radio-frequency (RF) communications [Groves, 2013]. This paper focuses on the latter, more specifically on Ultra-Wide Band (UWB) systems (see Fig. 4.1), which can provide low-cost, low-power, high-accuracy RF-based localization solutions for mobile robots, with a precision of the order of a decimeter in favorable conditions [Sahinoglu et al., 2008, González et al., 2009, Amanda Prorok, 2013, Decawave, 2018, Ledergerber and D'Andrea, 2017, Hamer and D'Andrea, 2018, Mai et al., 2018, Preter et al., 2019, Van Herbruggen et al., 2019] and a refresh rate of the order of 10 to 100 Hz [Cano et al., 2019].

RF-based localization protocols most commonly rely on estimating the Time-of-Flight (ToF) of messages exchanged between transceivers, by comparing the transmission (Tx) and reception (Rx) times of these messages. ToF measurements can then be converted to distance measurements or used to synchronize some of the nodes [Sahinoglu et al., 2008, Cano et al., 2019]. By design, UWB systems are relatively resilient to common sources of errors in ToF measurements [Sahinoglu et al., 2008]. Nonetheless, large positive errors can occur in non line-of-sight (NLoS) configurations, when the direct path between transceivers is blocked by an obstacle and the receiver detects instead a reflected signal. As a result, much of the literature on UWB-based localization focuses on detecting and mitigating the effect of NLoS measurements, see, e.g., [González et al., 2009, Marano et al., 2010, Bregar and Mohorčič, 2018, Zhu and Kia, 2019].

However, even in LoS conditions, ToF measurements are subject to errors due to transceiver clock drift, antenna delays, signal distortion, multipath interference and timestamp triggering uncertainties by the electronic circuits [Decawave, 2018]. The Rx timestamp accuracy is particularly dependent on signal distortion and deteriorates as the received power (RxP) of the direct path signal decreases [Decawave, 2018, p. 10]. These errors should be taken into

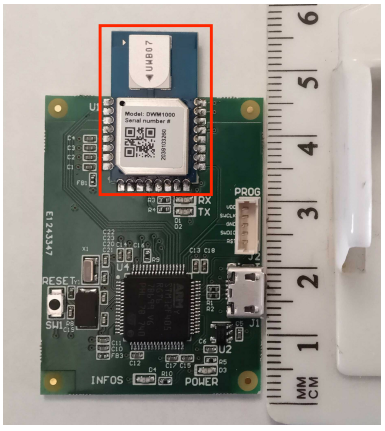

Figure 4.1 – Custom communication board used in our experiments. The UWB transceiver itself (Decawave DWM1000) and its omnidirectional antenna are encircled in red

account for accurate localization, since an offset of just one nanosecond in ToF estimation results in a ranging error of almost thirty centimeters, which is about the maximum tolerable for many indoor operations.

In practice, the systematic errors (bias) in UWB measurements need to be captured by empirical models that are sufficiently simple to be used in real-time positioning algorithms. González et al. [González et al., 2009] fit a model of two-way ranging (TWR) measurement bias in terms of distance between the transceivers, while [Ledergerber and D'Andrea, 2018] and [Zhao et al., 2021] also include the relative antenna orientations in their models, for TWR and time-difference of arrival (TDoA) localization schemes respectively. Unfortunately, such models depend on extrinsic rather than intrinsic measurements, which are in fact often precisely what the higher-level localization schemes aim to estimate. For instance, distance pseudo-measurements are deduced from ToF measurements in various ways depending on the ranging protocol used at the application level (type of TWR scheme, TDoA, Time-of-Arrival (ToA), etc.) and full relative pose measurements between transceivers require additional sensors. Hence, any error in the distance or pose estimation scheme is fed back in the low-level measurement calibration, and these bias models are highly dependent on the specific localization scheme used. These models also do not take advantage of all the information available at the physical layer, in particular the channel impulse response (CIR) at the receiver, as well as the relative clock frequency drift measurements. Because the Rx timestamp is estimated from the CIR, errors can be fundamentally tied to it. Moreover, since the CIR and in particular the RxP is highly dependent on the antenna radiation pattern, it is quite plausible that most of the observed pose dependent bias can be already explained by the CIR features. Calibration models based on CIR features should also be less sensitive to system design choices such as level of transmitted power or type of antenna used, and to environmental characteristics such as multipath propagation.

In this paper, we introduce a simple UWB ToF bias model for LoS measurements, capturing transceiver clock offset and RxP-induced bias, together with a methodology to calibrate such a model.

The application note [Decawave, 2018] mentions a dependency of ToF measurement errors on RxP, but proposes again to calibrate ranging bias models (specifically for TWR) that are based indirectly on distance rather than CIR measurements, as in [González et al., 2009] for example. Savic et al. [Savic et al., 2016] propose a general model for TOA ranging measurements that includes a bias term for LoS measurements, but this term is constant (independent of the channel parameters) and the paper focuses on NLoS error mitigation. Wymeersch et al. [Wymeersch et al., 2012] introduce machine learning-based methods to predict the rang-

ing bias in TWR from the full CIR and a distance estimate, without distinguishing between LoS and NLoS measurements. As we discuss in Section 4.3, their TWR calibration process can benefit from a preliminary clock skew correction step leveraging information available on more recent hardware. Compared to these papers, we focus exclusively on LoS measurements and develop a lightweight model linking ToF measurement bias to a type of RxP measurements. This model does not require extrinsic information such as relative transceiver poses, nor the full CIR but only its samples that are directly used in practice to determine the Rx timestamp. In a TWR localization experiment, we show that this model can capture most of the observed ranging bias. Moreover, this ToF bias model can be used with any type of localization scheme, e.g., TWR, TDoA, or ToA.

The outline of the paper is as follows. Section 4.2 introduces the ToF error model. Section 4.3 proposes a TWR-based clock offset correction scheme, which allows us to isolate the remaining RxP-induced bias in ToF measurements. This RxP-induced bias is modeled in more details in Section 4.4, which also introduces a methodology to calibrate it. Finally, Section 4.5 demonstrates in a TWR experiment that most of the bias in LoS measurements is captured by the model, and discusses further applications.

4.2 Time-of-Flight Measurement Model

Ideally, an UWB transmitter A and receiver B could measure the ToF τ_{AB} of a signal traveling in a direct path between them (LoS conditions) by taking the difference between the message reception time t_R and transmission time t_T, i.e., $\tau_{AB} = t_R - t_T$. This would provide for example a distance measurement $d_{AB} = c\,\tau_{AB}$ between the nodes, with c denoting the speed of light. However, a first difficulty is that each node measures time slightly differently according to its own imperfect clock. Second, even if the nodes were perfectly synchronized, timestamp measurements at each node are imperfect.

As mentioned previously, a dominating factor for the accuracy of t_R measurements is the received signal power (RxP) at B, $\mathcal{P}_R^B$. Indeed, the statistical performance of the algorithm estimating t_R, called the *Leading Edge Detector* (LDE), is known to be dependent on the received *Signal to Noise Ratio* (SNR) [Sharp et al., 2009, Decawave, 2018]. As a result, we can model the timestamp measurement at the receiver as

$$t_R^B \approx t_R + \delta_c^B(t_R) + \delta_p^B(\mathcal{P}_R^B),$$

where $\delta_c^B(t_R)$ captures the clock offset of node B at absolute time t_R and δ_p^B is the RxP-dependent error.

The timestamp measurement t_T^A at the transmitter follows the simpler model

$$t_T^A \approx t_T + \delta_c^A(t_T).$$

Taking the difference, we obtain the following ToF measurement model

$$t_R^B - t_T^A = \tau_{AB} + \delta_c^B(t_R) - \delta_c^A(t_T) + \delta_p^B(\mathcal{P}_R^B) + \nu, \tag{4.1}$$

where ν is a residual unmodeled error. For example, ν could include additional timestamp measurement errors due to imperfect calibration of antenna propagation delays.

For short-range communication systems such as those relying on UWB, the difference between t_R and t_T is of the order of the microsecond at most (which corresponds to a distance between nodes of about 300 m). This duration is too small for the offset δ_c of even low-grade electronic clocks to vary significantly. As a result, it is generally appropriate for short-range systems to use the simplified model

$$t_R^B - t_T^A = \tau_{AB} + \Delta_c^{B/A}(t_{R,T}) + \delta_p^B(\mathcal{P}_R^B) + \nu, \tag{4.2}$$

where one can take for example $t_{R,T} = (t_T + t_R)/2$ and $\Delta_c^{B/A}(t)$ represents the offset of the clock of B with respect to the clock of A at time t. Then, to obtain accurate ToF measurements from the model (4.2) in practice, it is necessary to remove this clock offset as well as the RxP-induced error $\delta_p^B(\mathcal{P}_R^B)$. These topics are discussed in Section 4.3 and 4.4 respectively.

4.3 Clock Offset Correction: the Case of TWR

Clock offset correction is a well studied topic and is strongly dependent on the localization scheme. Hence, our discussion is short and focuses for concreteness on one of the simplest ranging scheme, single-sided TWR (SSTWR), see Fig. 4.2.

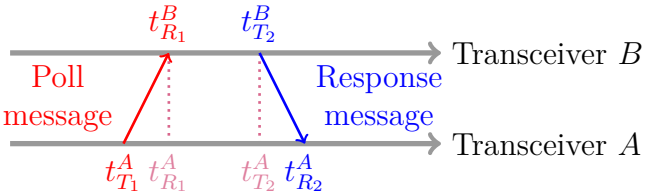

Figure 4.2 – Single-Sided TWR protocol

A SSTWR transaction involves two transceivers A and B. A transmits at time t_{T_1} a message

to B, which is received at time t_{R_1}. B responds at t_{T_2} and this message is received at A at time t_{R_2}. We assume that the duration of the transaction is sufficiently short (of the order of a millisecond) to neglect the relative motion of the nodes. The TWR protocol tries to reduce the clock-offset error without synchronizing the nodes, by performing the following operation

$$\begin{aligned}&(t^B_{R_1} - t^A_{T_1}) + (t^A_{R_2} - t^B_{T_2}) = \\ &2\tau_{AB} + \Delta_c^{B/A}(t_1) - \Delta_c^{B/A}(t_2) + \delta_p^B(\mathcal{P}_R^B) + \delta_p^A(\mathcal{P}_R^A) + \nu,\end{aligned}$$

where ν is another residual error term and $t_1 \approx (t_{T_1} + t_{R_1})/2$, $t_2 \approx (t_{T_2} + t_{R_2})/2$. From this expression, we can approximate the ToF τ_{AB} by $\hat{\tau}_{AB}$ with

$$\begin{aligned}\hat{\tau}_{AB} = \ &\tilde{\tau}_{AB} \\ &+ \frac{\Delta_c^{B/A}(t_2) - \Delta_c^{B/A}(t_1)}{2} - \frac{\delta_p^B(\mathcal{P}_R^B) + \delta_p^A(\mathcal{P}_R^A)}{2}.\end{aligned} \tag{4.3}$$

where $\tilde{\tau}_{AB} := \frac{t^B_{R_1} - t^A_{T_1} + t^A_{R_2} - t^B_{T_2}}{2}$.

Although standard versions of TWR approximate τ_{AB} by the first term and neglect in particular the difference $r_c^{B/A} := (\Delta_c^{B/A}(t_2) - \Delta_c^{B/A}(t_1))/2$ between clock offsets at the first and second messages, this term is often too large for accurate indoor navigation. To illustrate the impact of $r_c^{B/A}$, if we assume a constant typical clock skew of $\gamma := \partial\Delta_c^{B/A}/\partial t = 10^{-6}$ and a transaction time of $t_2 - t_1 = 2$ ms, we obtain $r_c^{B/A} = 1$ ns, which, as we noted before, would correspond to a ranging error of about 30 cm.

To correct this error, as explained in [Cano et al., 2019], we can leverage clock skew measurements $\tilde{\gamma}(t)$ already computed by the receiver of an UWB signal, which are recorded in the register set of current transceivers [Decawave, 2017, p.150]. Indeed, the receiver needs to track the transmitter's oscillator frequency through a process called *timing recovery* [Aldubaikhy, 2012, p.38], [Png et al., 2008] in order to estimate the reception time of an UWB message with the correlation-based LDE algorithm. However, the measured clock skew $\tilde{\gamma}(t)$ is a noisy signal, which needs to be filtered to produce a more reliable estimate $\hat{\gamma}(t)$. The estimated clock skew $\hat{\gamma}$ can then be used to build an estimate of the residual clock error during a given transaction, as follows

$$\hat{r}_c^{B/A} = \frac{1}{2}\int_{t_1}^{t_2} \hat{\gamma}(\tau)d\tau \approx \frac{t_2 - t_1}{2}\hat{\gamma}, \tag{4.4}$$

where $\hat{\gamma}$ is the clock-skew estimate computed at time $t^A_{R_2}$ by agent A, with its own skew measurement $\tilde{\gamma}(t^A_{R_2})$.

The clock skew estimate $\hat{\gamma}$ can be updated at each SSTWR transaction k. Let's denote t_k the timestamp $t^A_{R_2}$ of transaction k. To filter $\tilde{\gamma}(t_k)$ and produce $\hat{\gamma}(t_k)$, we adapt our approach in [Cano et al., 2019] and use a Kalman filter with the following clock skew model

$$\begin{cases} \dot{\gamma} = \zeta_\gamma, \\ \tilde{\gamma}(t_k) = \gamma(t_k) + \nu_\gamma, \end{cases} \tag{4.5}$$

where ζ_γ is a centered Gaussian white noise with power spectral density $\sigma^2_{\gamma\gamma}$ and ν_γ a discrete centered Gaussian random variable with covariance $\sigma^2_{\gamma m}$. The constants $\sigma_{\gamma\gamma}$, $\sigma_{\gamma m}$ are tuned as explained in [Cano et al., 2019].

4.4 RxP-Induced Error Correction

In this section, we present a methodology to estimate and correct the RxP-induced term $\delta^i_p(\mathcal{P}^i_R)$ in the ToF measurement model (4.1) or (4.2). This methodology requires selecting appropriate RxP measurements $\mathcal{P}_R$ at the receiver and then fitting the function $\delta^i_p(\mathcal{P}_R)$.

4.4.1 Most Informative RxP Measurements

The UWB transceivers used in our experiments (Decawave's `DW1000`) directly record two measures of received power in their register set [Decawave, 2017], as follows. Let $\mathfrak{s}(t_i) = r(t_i) + jq(t_i) \in \mathbb{C}$ be the complex-valued CIR sampled at times t_i, $1 \leq i \leq N$, by an UWB module receiving a message. The *Average Received Power* (ARP) is defined as

$$\mathcal{P}_a = 10 \log_{10} \left(\frac{1}{N^2} \sum_{i=1}^{N} |\mathfrak{s}(t_i)|^2 \right) - \mathcal{P}_{ra},$$

with $\mathcal{P}_{ra}$ a reference power level. In constrast, the *First Path Power* (FPP) is defined as

$$\mathcal{P}_f = 10 \log_{10} \left(\frac{1}{3^2} \sum_{i \in \mathcal{L}} |\mathfrak{s}(t_i)|^2 \right) - \mathcal{P}_{rf},$$

where $\mathcal{P}_{rf}$ is another reference power level and $\mathcal{L} = \{i_1, i_2, i_3\}$ is a set of three characteristic amplitudes used by the LDE algorithm to determine the reception time of the message [Decawave, 2017, p.40].

Our experiments lead us to choose the FPP instead of the ARP as a measure of received power to calibrate the function δ_p, since we found a clearer correlation between bias and $\mathcal{P}_f$ compared to $\mathcal{P}_a$. One intuitive explanation is that $\mathcal{P}_f$ is directly used in the LDE algorithm

and hence strongly affects its estimates. Moreover, $\mathcal{P}_a$ is more sensitive to disturbances due to multipath propagation, making the calibrated error model less robust to environmental changes. In practice, we noticed that the behavior of the FPP measured by transceivers in LoS and sufficiently far (beyond 50 cm) from reflective surfaces (walls, ground, etc.) is repeatable at different locations. Hence, in the following we identify $\mathcal{P}_f$ as measure of RxP.

4.4.2 RxP-Induced Error Estimation Method

Based on our experimental results, we *postulate* for a given receiver i an RxP-induced error term of the form

$$\delta_p^i(\mathcal{P}_R^i) = K^i + \delta_p(\mathcal{P}_R^i), \tag{4.6}$$

where K^i is a receiver specific constant and the function δ_p is independent of i. In other words, the RxP-induced error for each UWB receiver (following a particular hardware design) is simply a shifted version of the function δ_p to determine. The constant K^i can be due to fabrication process variations for example.

In this section, we explain how to estimate the function δ_p. This can be done by taking ToF measurements between two transceivers A and B at various level of RxP, provided we can remove first the clock offset error $\Delta_c^{B/A}$ in (4.2). To do so, we can rely on the SSTWR scheme of Section 4.3. From (4.3), we see that after estimating the residual clock error $\hat{r}_c^{B/A}$ from (4.4), we get

$$\frac{\delta_p^A(\mathcal{P}_R^A) + \delta_p^B(\mathcal{P}_R^B)}{2} \approx \tilde{\tau}_{AB} - \frac{d_{AB}}{c} + \hat{r}_c^{B/A}.$$

If we can assume $\mathcal{P}_R^A \approx \mathcal{P}_R^B = \mathcal{P}_R$ during the TWR exchange, then we obtain from (4.6)

$$\delta_p^{A,B}(\mathcal{P}_R) \coloneqq \delta_p(\mathcal{P}_R) + K^{AB} \approx \tilde{\tau}_{AB} - \frac{d_{AB}}{c} + \hat{r}_c^{B/A}, \tag{4.7}$$

where $K^{AB} = \frac{K^A + K^B}{2}$ is an unknown constant depending on the pair (A, B) of transceivers. The assumption of approximately equal RxP at A and B during the SSTWR transaction is reasonable as long as we use omnidirectional antennas and the same transmitted power at A and B.

To estimate δ_p (up to a constant) based on (4.7), we can move a receiver A to different locations in an environment equipped with a precise external localization system, while maintaining LOS with a transmitter B at a fixed location. The goal is to sample sufficiently many values of RxP, covering the range of power values expected in subsequent deployment. At each position of A, the two transceivers perform multiple SSTWR transactions and we

record all the quantities on the right-hand side of (4.7), including the distance d_{AB} measured by external localization. This provides bias measurements $\tilde{\delta}_p$ for the left-hand side of (4.7). We also collect RxP values $\tilde{\mathcal{P}}_R$ in each transaction, by reading the FPP recorded at the transceivers. FPP values $\tilde{\mathcal{P}}_f$ are recorded in dB but we found the logarithmic scale inconvenient to fit δ_p, so we perform a simple transformation and fit the function δ_p with $\tilde{\mathcal{P}}_R = 10^{(\tilde{\mathcal{P}}_f - \alpha_{\text{dB}})/10}$ for some normalization parameter α_{dB} ($\alpha_{\text{dB}} = -82$ dB in our experiments). Since $\tilde{\mathcal{P}}_R^A \approx \tilde{\mathcal{P}}_R^B$ is only approximately true in general during a TWR transaction, we record the average RxP $\tilde{\mathcal{P}}_R = (\tilde{\mathcal{P}}_R^A + \tilde{\mathcal{P}}_R^B)/2$.

The resulting calibration dataset contains a large number of pairs $(\tilde{P}_R, \tilde{\delta}_p)$, one for each TWR transaction. To fit δ_p (up to the constant K^{AB}), we quantize the RxP into L values $\{\mathcal{P}_{R,i}\}_{i=1}^L$ uniformly spread between the minimum and maximum values observed for $\tilde{\mathcal{P}}_R$. The RxP-induced offset $\delta_p(\mathcal{P}_{R,i})$ for a given level $\mathcal{P}_{R,i}$ on the discretized grid is estimated by taking the empirical average of the observed bias $\tilde{\delta}_p$ for all corresponding RxP measurements $\tilde{\mathcal{P}}_R$ that are quantized to $\mathcal{P}_{R,i}$. We then store in a lookup table the L bias values $\{\delta_p(\mathcal{P}_{R,i})\}_{i=1}^L$ and compute any other value $\delta_p(\mathcal{P}_R)$ by linear interpolation. Fig. 4.3 shows an example of calibration dataset and fitted bias model.

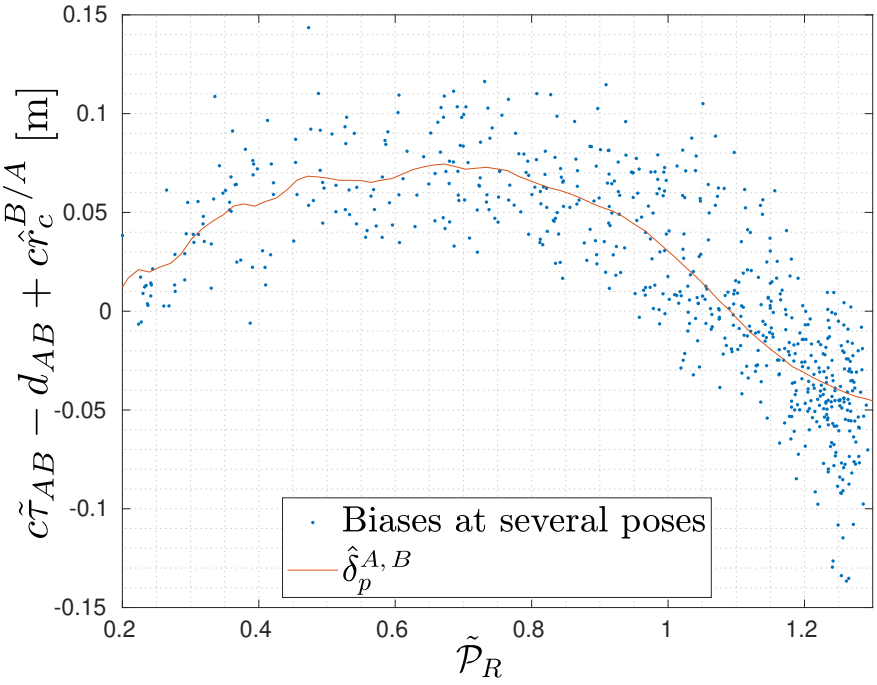

Figure 4.3 – An example of computed calibration map and RxP/bias data taken at several poses in the Polytechnique Montreal laboratory

For one-way ranging protocols (ToA, TDoA), the identification of the receiver dependent constant K^i in (4.6) is generally not needed, see Section 4.6. For TWR, the constant K^{AB} in

(4.7) for a given pair of transceivers can be obtained by a short initialization phase, once δ_p is known. For this, we separate the transceivers by a known distance and let them perform a few SSTWR transactions. We then correct the ToF measurement for $\delta_p(\mathcal{P}_R)$ and $\hat{r}_c^{B/A}$, so that the remaining systematic bias in the measurements can be used to estimate K^{AB} from (4.7).

4.4.3 Experimental Validation

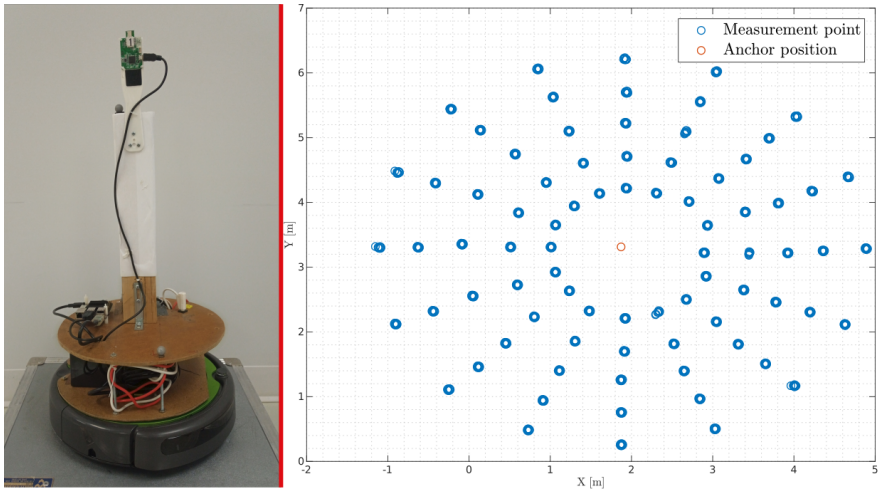

Figure 4.4 – Left: Robot used for our experiments. Right: Sampled positions of the tag around the anchor

To validate the modeling assumptions and methodology presented in the previous section, in particular (4.7), we performed experiments at two different laboratories, in Montreal, Canada and Toulouse, France. FPP and RxP-induced bias measurements $(\tilde{P}_R, \tilde{\delta}_p)$ were obtained through SSTWR transactions with clock skew correction as described above, in multiple experiments with a fixed UWB transceiver B (anchor) and a mobile one A (tag) carried by an omnidirectional ground robot, see Fig. 4.4. Each laboratory is equipped with a motion capture system, providing the required distance measurements d_{AB} with mm-level accuracy.

The mobile node moved to different locations in the environment as illustrated on Fig. 4.4 and performed at each location a full rotation to sample 8 different headings $\theta = k\pi/4, k \in [0, 7]$. The robot stops for 0.5 s at each pose to perform SSTWR with a refresh rate of 100 Hz. Therefore, we obtain about 50 measurements in each pose. Overall, this allows us to observe a sufficiently diverse set of RxP values. The data is recorded by an onboard computer running ROS and the function δ_p is fitted in a post-processing step after the complete dataset is collected. The results shown on Fig. 4.3 were obtained during one such experiment in Montreal.

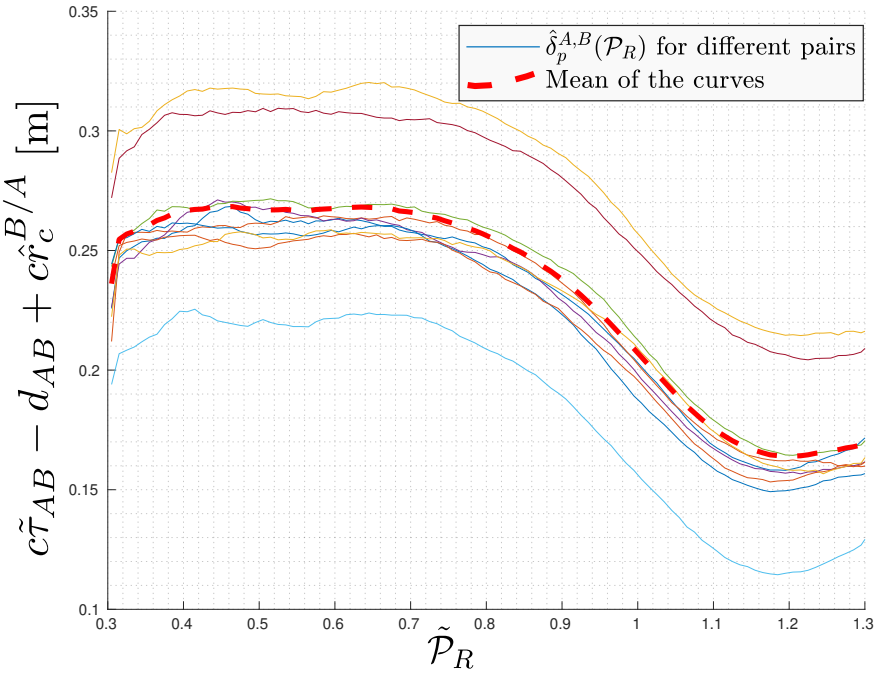

Figure 4.5 – Calibration maps for various pairs of modules (acquired at the ISAE laboratory in Toulouse)

Fig. 4.5 shows calibration curves $c\,\delta_p^{A,B}(\mathcal{P}_R)$ (see (4.7)) obtained by fitting the datasets of measurements $(\tilde{\mathcal{P}}_R, \tilde{\delta}_p)$ for ten different pairs (A, B) of UWB transceivers similar to the one shown on Fig. 4.1. These experiments were carried out in Toulouse and we used $L = 100$ quantization levels for the RxP. We observe that the curves indeed have a similar profile and mainly differ by their offset, i.e., they satisfy the model anticipated in (4.7). We noticed that the offset K^{AB} appears to be constant over time. We also plotted on Fig. 4.5 the calibration curve averaged over the previous 10 pairs of transceivers. This curve can serve as function δ_p to calibrate new pairs (A', B') of similar transceivers performing TWR transactions, which only requires estimating the offset $K^{A'B'}$, as explained at the end of Section 4.4.2.

Figs 4.3 and 4.5 show that the calibration curves acquired in Toulouse and Montreal have a similar shape. This indicates that the estimated function $\delta_p^{AB}(\tilde{\mathcal{P}}_R)$ can be used to remove RxP-induced bias in LOS conditions in different environments. Indeed, the localization experiment presented in Section 4.5 has been repeated with calibration curves obtained in the other laboratory, which still provide a significant bias reduction. The main differences in the two sets of curves are observable at low RxP ($\tilde{\mathcal{P}}_R < 0.4$), where some environments more sensitive to multipath outliers degrade the accuracy of the calibration curves, and close to saturation ($\tilde{\mathcal{P}}_R > 1.2$). The latter differences could be explained by the fact that we used two different versions of the UWB modules (DWM1000) at the two locations, which may differ in their amplifier circuits and antennas.

4.5 TWR Localization Experiment

To evaluate the usefulness of performing a correction for clock skew and RxP-induced error, we carried out a localization experiment in 2D with a mobile UWB tag (playing the role of transceiver A in Fig. 4.2) performing SSTWR with two fixed UWB anchors B_1 and B_2 at known locations, see Fig. 4.6.

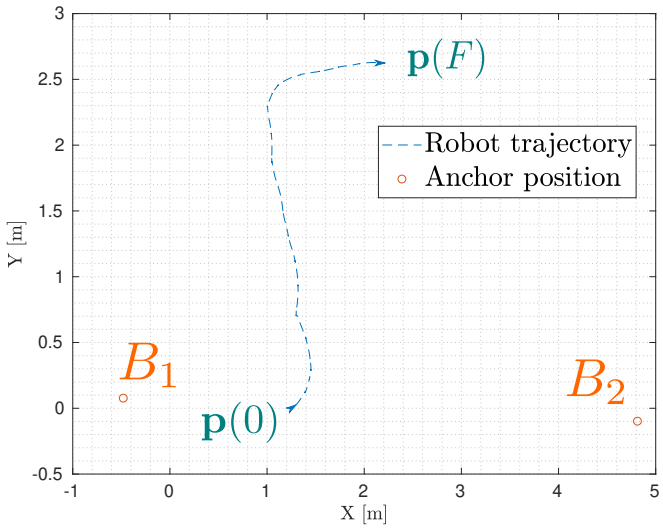

Figure 4.6 – Executed trajectory for the TWR localization test

The block diagram of the ranging algorithm implemented at the tag is shown on Fig. 4.7. The inputs of this algorithm are the measured timestamps $\tilde{\mathcal{T}} := \{t^A_{T_1}, t^{B_i}_{R_1}, t^{B_i}_{T_2}, t^A_{R_2}\}$, the clock skew measurements $\tilde{\gamma}$ and RxP $\tilde{\mathcal{P}}_R$ (derived from FPP measurements $\tilde{P}_f$). Note that all these inputs are directly provided by the UWB transceivers (the anchors can send their timestamps to the tag in their messages). The estimated range $\hat{d}_{AB}$ is obtained by elementary operations: i) time-related processing (in blue) consists of scalar elementary operations and a single state Kalman filter (estimator $\hat{r}^{B/A}_c$); ii) power-related processing (in purple) performs a simple linear interpolation using a lookup table containing just 100 RxP-induced bias values. The bias model δ_p used by the algorithm is the one previously estimated independently from the dataset presented in Section 4.4.3. The initialization phase described at the end of Section 4.4.2 is performed for each pair (anchor, tag) in order to estimate the constants K^{AB}. The algorithm can provide corrected range estimates between the tag and anchors with an update frequency of 100 Hz.

Fig. 4.6 shows the two anchors at coordinates $\mathbf{B}_1 = [-0.48, 0.08, 1.69]^\top$ and $\mathbf{B}_2 = [4.81, -0.10, 1.69]^\top$ and the trajectory of the mobile tag from the initial position $\mathbf{p}(0)$

to the final position $\mathbf{p}(F)$. This trajectory, measured by the motion capture system, is produced by the *D-Opt* motion planner presented in [Le Ny and Chauvière, 2018], which aims to compute positions that reduce the ranging-based localization error for the robot. We denote d_i the true distance between the anchor B_i and the tag, measured by the motion capture system. The raw UWB range measurements between the tag and anchor $i \in \{1, 2\}$ are denoted $\tilde{d}_i = c\,\tilde{\tau}_{AB_i}$, while $\hat{d}_i$ are the corrected range estimates produced by the algorithm of Fig. 4.7.

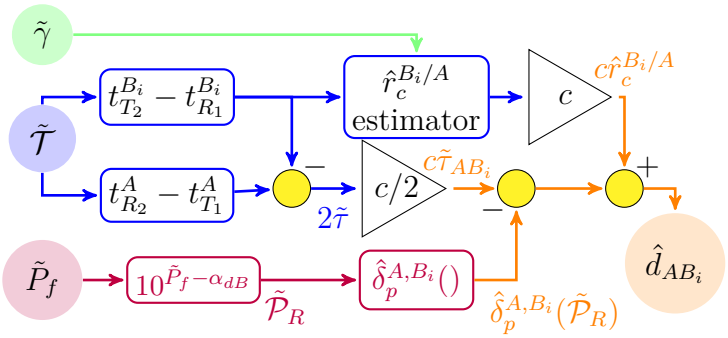

Figure 4.7 – Block diagram of the bias correction algorithm for each pair of transceivers A, B_i

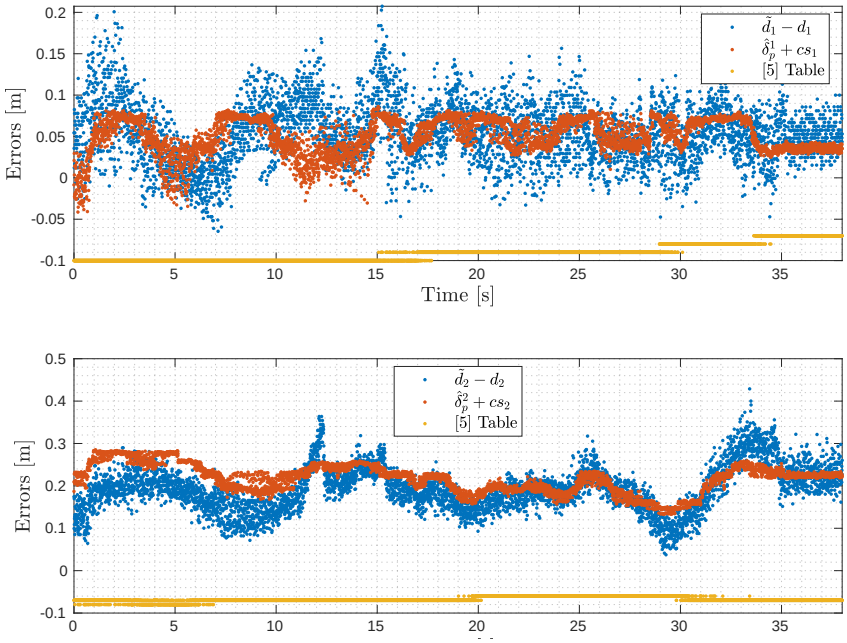

Figure 4.8 – Plot of raw range errors (blue), biases estimated by our method (orange) and biases predicted by the lookup table of [Decawave, 2018] (yellow)

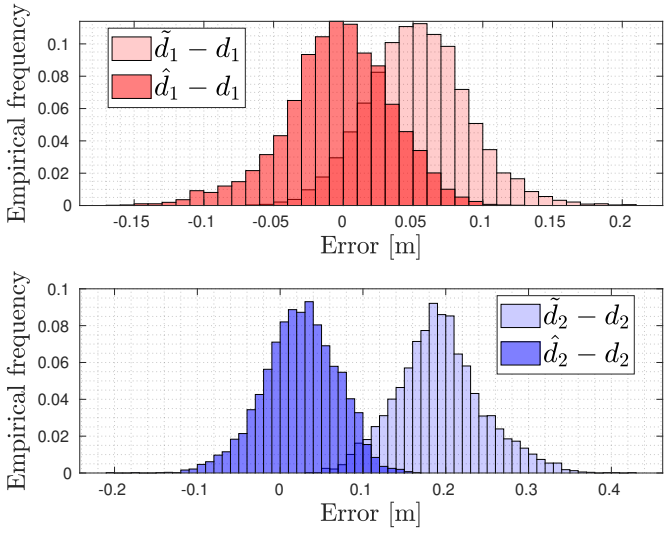

Figure 4.9 – Error histograms after and before compensation (calibrated with Montreal dataset)

Fig. 4.9 shows the histograms of error values for raw and corrected UWB range measurements. The time series of these experiments, presenting raw errors and biases estimated by the algorithm, are plotted in Fig. 4.8. The apparent offset at the beginning of the trajectory might be due to the time it takes for the clock offset estimate $\hat{r}_c^{B/A}$ to converge. Note that large range measurement outliers, presumably due to reflected signals, where removed from the dataset, since we focus on LoS conditions. Overall, the corrected range measurements present a residual bias below two centimeters, while this bias was typically close to 20 cm for the range to anchor 2 before correction. Since the residual noise after bias correction shows a standard deviation of 3 to 5 cm, we see that it is crucial for accurate range measurements to correct the bias error. Fig. 4.8 also provides a comparison with the bias predicted by the lookup table of the application note [Decawave, 2018, Table 1] (our implementation sets the PRF to 64 MHz and uses channel 2). This table attempts to correct the bias based on the uncorrected distance estimates obtained from TWR, but it clearly fails here to track the bias, possibly because of the significant differences in hardware.

We repeated the calibration process for the experiment presented on Fig. 4.6, which took place in Montreal, using the mean calibration map acquired in Toulouse, plotted on Fig. 4.5. The accuracy of the bias correction, illustrated in Fig. 4.10, slightly deteriorated compared to that of Fig. 4.9, but the average ranging error remained below 3 cm for both anchors. Finally, in a video accompanying this article, we illustrate the calibration process and the validation on the previously presented trajectory with dynamic plots.

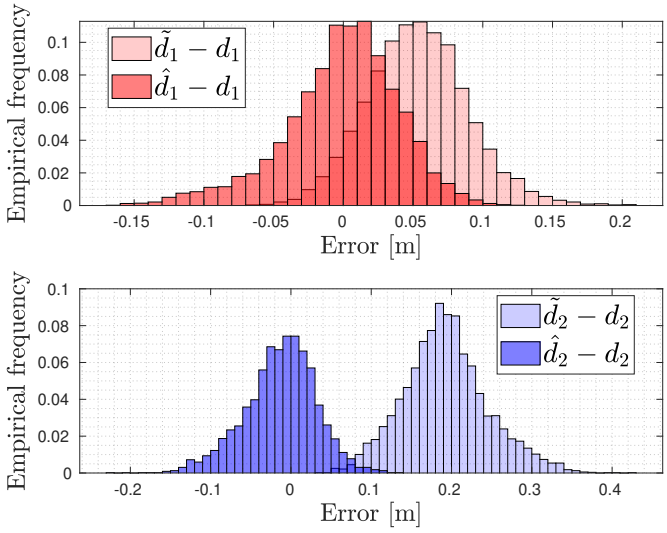

Figure 4.10 – Error histograms after and before compensation (calibrated with Toulouse dataset)

4.6 Application to Other Localization Schemes

In this section, we briefly discuss how the ToF model (4.2) with RxP-induced bias model (4.6) is useful to correct errors in different RF-based localization schemes, such as ToA and TDoA [Groves, 2013]. Both ToA and TDoA systems require multiple *synchronized* UWB anchors $A_1, \ldots, A_M$ placed at known locations $\mathbf{p}_{A_i}$ and broadcasting localization messages, while any number of UWB-equipped tags can determine their location by listening to these messages.

Consider a tag B receiving a message from anchor A_i. For ToA, we can write from (4.2) and (4.6)

$$\begin{aligned} \rho_i &:= c(t^B_{R_i} - t^{A_i}_{T_i}) \\ &\approx d_{A_iB} + c\Delta^{B/A}_c + c\delta^B_p(\mathcal{P}^B_{R,i}) \\ &\approx d_{A_iB} + D + c\delta_p(\mathcal{P}^B_{R,i}), \end{aligned} \tag{4.8}$$

where $D = \Delta^{B/A}_c + K^B$ is independent of the index i of anchor A_i because the anchors are synchronized (and we neglect here the time variation of the clock offset $\Delta^{B/A}_c$) and K^B only depends on the receiver B. To determine its position, the tag records the M pseudo-range

measurements ρ_i and corresponding FPP values $\mathcal{P}_{R,i}$ to solve the least-squares problem

$$\min_{\mathbf{p},D} \sum_{i=1}^{M} \left| \rho_i - \|\mathbf{p} - \mathbf{p}_{A_i}\| - c\delta_p(\mathcal{P}_{R,i}^B) - D \right|^2. \tag{4.9}$$

A well-posed problem requires at least $M = d + 1$ anchors for localization in d dimensions. A minimizer $(\mathbf{p}, D)$ of (4.9) produces an estimate $\mathbf{p}_B$ of the position of B and an estimate of the constant D, which is discarded. Hence, we see that the constant K^B does not need to be calibrated separately, the knowledge of the function δ_p is enough to correct the RxP-induced error in ToA.

Similarly, for TDoA, a tag B receiving messages from two anchors A_i and A_j computes the double difference

$$\begin{aligned} \Delta_{ij} &:= c(t_{R_i}^B - t_{T_i}^{A_i}) - c(t_{R_j}^B - t_{T_j}^{A_j}) \\ &\approx d_{A_iB} - d_{A_jB} + c(\delta_p(\mathcal{P}_{R,i}^B) - \delta_p(\mathcal{P}_{R,j}^B)). \end{aligned}$$

The clock offsets cancel out because the anchors are synchronized (and we neglect the offset time variations). So does the constant K^B, which does not depend on the anchor. To determine its position, tag B records the Δ_{ij} for all pairs of anchors, as well as the FPP $\mathcal{P}_{R,i}^B$ for all messages. It then solves the least-squares problem

$$\begin{aligned} \min_{\mathbf{p}} \sum_{i \neq j} \Big| \Delta_{ij} - \|\mathbf{p} - \mathbf{p}_{A_i}\| + \|\mathbf{p} - \mathbf{p}_{A_j}\| \\ - c\delta_p(\mathcal{P}_{R,i}^B) + c\delta_p(\mathcal{P}_{R,j}^B) \Big|^2. \end{aligned} \tag{4.10}$$

Again, correction of RxP-induced errors for TDoA depends only on identifying the function δ_p and not the constant K^B.

4.7 Conclusion

We developed an empirical bias model for UWB ToF measurements in LoS conditions. The input variable of the model is the received power (RxP), which can be measured directly by UWB receivers from the channel impulse response. We proposed a methodology based on a TWR protocol to calibrate the RxP-induced bias model, which leverages relative clock skew measurements available on current receivers to first correct residual clock offsets. We verified empirically that the identified bias model is relatively robust to changing environmental conditions and that it can be used to significantly improve localization accuracy in practice.

An important advantage of the bias correction method is that it does not require external measurements nor a complex model that depends on estimating the robot or environment parameters. If more is known about those parameters, additional corrections could be applied as a second step, for example to identify NLoS measurements. Future work will apply the bias correction method to other localization protocols and consider more complex signal propagation scenarios.

Acknowledgments

The authors thank Corentin Chauffaut and Louis Treton from ISAE for their availability and their assistance.

CHAPTER 5 ARTICLE 2 : RANGING-BASED LOCALIZABILITY OPTIMIZATION FOR MOBILE ROBOTIC NETWORKS

Published in IEEE Transactions on Robotics, April 1st, 2023.

Coauthors : Justin Cano[1,2], Jérôme Le Ny[2]

[1] DEOS, ISAE-Supaéro, Toulouse France.

[2] EE Dept., Polytechnique Montréal, QC, Canada & GERAD, Montréal, QC, Canada.

Abstract

In robotic networks relying on noisy range measurements between agents for cooperative localization, the achievable positioning accuracy strongly depends on the network geometry. This motivates the problem of planning robot trajectories in such multi-robot systems in a way that maintains high localization accuracy. We present potential-based planning methods, where localizability potentials are introduced to characterize the quality of the network geometry for cooperative position estimation. These potentials are based on Cramér Rao Lower Bounds (CRLB) and provide a theoretical lower bound on the error covariance achievable by any unbiased position estimator. In the process, we establish connections between CRLBs and the theory of graph rigidity, which has been previously used to plan the motion of robotic networks. We develop decentralized deployment algorithms appropriate for large networks, and we use equality-constrained CRLBs to extend the concept of localizability to scenarios where additional information about the relative positions of the ranging sensors is known. We illustrate the resulting robot deployment methodology through simulated examples and an experiment.

5.1 Introduction

Mobile robots require accurate, computationally efficient and low power localization systems to navigate their environment and perform their assigned tasks. Positioning can rely on various technologies, e.g., wheel odometry, computer vision or long- and short-range radio frequency (RF) systems, each with distinct advantages and drawbacks, depending on the environment and requirements. For example, the most common methods of terrestrial localization rely on RF signals from Global Navigation Satellite Systems (GNSS) to achieve meter- to centimeter-level accuracy, but these systems do not operate indoors or when the line of sight to the satellites is obstructed, and are sensitive to interference.

Multiple robots can collaborate to improve the accuracy and coverage of their individual localization solution [Sheu et al., 2010, Prorok et al., 2012a]. In particular, they can leverage information about their proximity to other location-aware nodes [Sheu et al., 2010] or use relative position [Prorok et al., 2012a], bearing [Xu et al., 2008] or distance measurements [Wei et al., 2015, Carlino et al., 2019] between them to estimate their individual positions in a common reference frame. Relative bearing measurements can be provided by monocular cameras for example, range measurements by short-range RF systems, and relative position measurements by LiDARs or stereo cameras. In this paper, we focus on collaborative localization in Multi-Robot Systems (MRS) *using only range measurements*. This is motivated by the fact that accurate distance measurements can be deduced from Time-of-Flight (ToF) measurements obtained from inexpensive short-range RF communication systems, e.g., Ultra-Wide Band (UWB) transceivers [Sahinoglu et al., 2008, Mueller et al., 2015, Cano et al., 2019]. In particular, such systems associate distance measurements unambiguously with pairs of robots, simply by having the robots broadcast their IDs.

Once the robots have measured their relative distances, many algorithms exist to compute from these measurements an estimate of the robot positions, see, e.g., [Buehrer et al., 2018] for a recent survey. These algorithms can be centralized or decentralized, applicable to static or mobile networks, appropriate or not for real-time localization, etc. Two major factors determine the ability of these algorithms to solve the position estimation problem and their accuracy. First, enough relative distance measurements should be available, which links the feasibility of the location estimation problem to the concept of *rigidity* [Tay and Whiteley, 1985, Cao et al., 2020, Aspnes et al., 2006] of the *ranging graph* corresponding to these measurements. Second, satisfying the graph-theoretic condition of rigidity is still insufficient to guarantee accurate localization of the individual agents, when measurement noise is inevitably present. For example, a group of robots that are almost aligned can form a rigid formation if enough range measurements are available, but can only achieve poor localization accuracy in practice. Indeed, the spatial *geometry* of the network strongly influences the accuracy of position estimates in the presence of measurement noise [Patwari et al., 2005], a phenomenon known as Dilution of Precision (DOP) in the navigation literature [Groves, 2013, Chap. 7]. We call here *localizability* the ability to accurately estimate the positions of the individual robots of an MRS in a given geometric configuration, using relative measurements.

In contrast to static sensor networks or GNSS, an MRS can actively adjust its geometry, *e.g.*, some of the robot positions and orientations, in order to improve its overall localizability. This results in a coupling between the motion planning and localization problem for the group. Maintaining the rigidity of the ranging graph during the motion of an MRS is a

stronger condition than maintaining its connectivity, but similar techniques can be used to address both problems. In particular, we can capture the degree of connectivity or rigidity of the graph using a function of the first non-zero eigenvalue of a type of Laplacian matrix, and guide the MRS along paths or configure its nodes in ways that increase this function. This is the approach adopted for example in [Kim and Mesbahi, 2006, Michael et al., 2009, Yang et al., 2010] for improving connectivity and in [Shames et al., 2009, Zelazo et al., 2012, Zelazo et al., 2015, Sun et al., 2015] for improving rigidity. This article builds on this principle to optimize localizability. Following an approach that we initially proposed in [Le Ny and Chauvière, 2018, Cano and Le Ny, 2021], we leverage Cramér Rao Lower Bounds (CRLBs) [Haug, 2012, Chap. 14] to construct localizability potentials, which can then be used as artificial potentials [Choset et al., 2005] to drive the motion of an MRS toward geometric configurations promoting good localization.

The CRLB provides a lower bound on the covariance of any unbiased position estimate constructed from the relative range measurements available in the robot network. Tighter covariance lower bounds exist, such as Barankin bounds [McAulay and Hofstetter, 1971], but an advantage of the CRLB is that it is relatively easy to compute and admits a closed-form expression for the problem considered here, assuming Gaussian noise [Patwari et al., 2005]. Moreover, as we show in Section 5.4, the CRLB for Gaussian noise is in fact closely related to the so-called *rigidity matrix* of the ranging graph. This does not come as a surprise, since the Gaussian CRLB is known to correspond to DOP expressions for least-squares estimators, which are implicitly derived in [Shames et al., 2009] for example and also linked to the rigidity matrix. The CRLB only provides a lower bound on estimation performance and there is generally no guarantee that a position estimator actually achieves it. Nonetheless, using this bound as a proxy to optimize sensor placement is a well accepted approach [Uciński, 2004]. An important advantage of this approach is that the motion planning strategy becomes independent of the choice of position estimator implemented in the network.

Contributions: First, this paper formulates a novel motion planning problem allowing an MRS to optimize its localizability, by minimizing appropriate cost functions based on the Fisher Information Matrix (FIM) appearing in the CRLB. Second, we establish an explicit connection between localizability and the weighted rigidity matrices introduced in [Zelazo et al., 2015, Sun et al., 2015]. One of the benefits of establishing this connection is to see that various artificial potentials can be constructed from the FIM to capture localizability, as discussed in the literature on optimal experimental design [Pukelsheim, 2006] or optimal sensing with mobile robots, see, e.g., [Uciński, 2004, Le Ny and Pappas, 2009, Carrillo et al., 2012]. Some of these functions may be more conveniently optimized than the smallest nonzero eigenvalue, which is the standard potential used for connectivity and rigidity maintenance.

Third, by leveraging the structure of the FIM matrix, we propose new distributed algorithms enabling the deployment of groups of robots carrying ranging sensors in a scalable and robust manner. Fourth, we extend the results to robots carrying multiple ranging sensors, using the theory of *constrained* CRLBs [Gorman and Hero, 1990] to account for the presence of additional rigidity constraints. This can be viewed as an alternative and simpler approach to deriving intrinsic CRLBs on the manifold of rigid motions [Bonnabel and Barrau, 2015, Chirikjian, 2018].

The structure of the paper is as follows. First, we define the deployment problem in Section 5.2, including localizability potentials further discussed in Section 5.3. Then, we derive in Section 5.4 the closed-form expression for the FIM and analyze its structure, which allows us to introduce in Section 5.5 decentralized methods to estimate the gradients of the localizability potentials. Section 5.6 extends the analysis to the case of robots carrying multiple ranging sensors. The deployment algorithms are validated in two simulated scenarios in Section 5.7, and experimental results using RF range measurements from UWB transceivers are described in Section 5.8.

This article builds on the conference paper [Le Ny and Chauvière, 2018], which introduced the concept of localizability potentials for the deployment of MRS in two dimensions. Here we extend the methodology to three dimensions, introduce new distributed optimization schemes, discuss useful properties on the FIM and make a clearer connection with rigidity theory. We also generalize the conference paper [Cano and Le Ny, 2021], which considered robots carrying multiple sensors, by developing the results in three dimensions and integrating the full relative position information in the CRLB rather than just relative distances, which is significantly more challenging. We demonstrate in simulation the improvement achievable with this extension.

Notation: We write vectors and matrices with a bold font. The all-one vector of size p is denoted $\mathbf{1}_p$. The notation $\mathbf{x} = \mathrm{col}(\mathbf{x}_1, \dots, \mathbf{x}_n)$ means that the vectors or matrices $\mathbf{x}_i$ are stacked on top of each other, and $\mathrm{diag}(\mathbf{A}_1, \dots, \mathbf{A}_k)$ denotes a block diagonal matrix with the matrices $\mathbf{A}_i$ on the diagonal. The nullspace of a matrix $\mathbf{A}$ is denoted $\ker \mathbf{A}$. For $\mathbf{A}$ and $\mathbf{B}$ symmetric matrices of the same dimensions, $\mathbf{A} \succeq \mathbf{B}$ means that $\mathbf{A} - \mathbf{B}$ is positive semidefinite and $\mathbf{A} \succ \mathbf{B}$ that it is positive definite. If $\mathbf{A}$ is a symmetric matrix, $\lambda_{\min}(\mathbf{A})$ and $\lambda_{\max}(\mathbf{A})$ denote its minimum and maximum eigenvalues. The time derivative of a vector-valued function $t \mapsto \mathbf{x}(t)$ is denoted $\dot{\mathbf{x}}$. The expectation of a random vector $\mathbf{x}$ is denoted $\mathbb{E}[\mathbf{x}]$ and its covariance matrix $\mathsf{cov}[\mathbf{x}] = \mathbb{E}\left[(\mathbf{x} - \mathbb{E}[\mathbf{x}])(\mathbf{x} - \mathbb{E}[\mathbf{x}])^\top\right]$. For a differentiable function $f : \mathbb{R}^p \to \mathbb{R}^q$, $\frac{\partial f(\mathbf{p})}{\partial \mathbf{p}}$ represents the $q \times p$ Jacobian matrix of f, with components $\partial f_i(\mathbf{p})/\partial p_j$ for $1 \leq i \leq q$, $1 \leq j \leq p$. When $q = 1$, $\partial^2 f(\mathbf{p})/\partial \mathbf{p} \partial \mathbf{p}^\top$ denotes the Hessian, i.e., the square

matrix with components $\partial^2 f(\mathbf{p})/\partial p_i \partial p_j$. Finally, $\mathsf{1}_\mathsf{e}$ is equal to 1 if the logical expression e is true and 0 otherwise, and for a set $\mathcal{S}$ we also use the alternative notation $\mathsf{1}_\mathcal{S}(i) \coloneqq \mathsf{1}_{i\in\mathcal{S}}$.

5.2 Problem Statement

Consider a set of N nodes in the n-dimensional Euclidean space, where $n = 2$ or $n = 3$. We fix a global reference frame denoted $\mathfrak{F} = (O, \vec{x}, \vec{y}, \vec{z})$ if $n = 3$ or $\mathfrak{F} = (O, \vec{x}, \vec{y})$ if $n = 2$. For $1 \leq i \leq N$, we write the coordinates of node i in that frame $\mathbf{p}_i \coloneqq [x_i, y_i, z_i]^\top$ if $n = 3$ or $\mathbf{p}_i \coloneqq [x_i, y_i]^\top$ if $n = 2$, and we let $\mathbf{p} \coloneqq \mathrm{col}(\mathbf{p}_1, \dots, \mathbf{p}_N) \in \mathbb{R}^{nN}$ denote the global spatial configuration of the nodes, which can vary with time.

As illustrated on Fig. 5.1, some of these nodes are carried by mobile robots, while others could remain at fixed locations. We suppose that the coordinates of a subset $\mathcal{K}$ of the nodes are perfectly known in $\mathfrak{F}$, for $1 < |\mathcal{K}| \coloneqq K < N$, and refer to these nodes as *anchors*. The anchors could be placed at fixed locations or they could be mobile, as long as we can precisely localize them via external means, e.g., using accurate GNSS receivers. The other nodes, also mobile or fixed and whose positions are unknown and need to be estimated, are called *tags* in the following. They form a set denoted $\mathcal{U}$, with $|\mathcal{U}| \coloneqq U = N - K$. Next, we assume that P pairs of nodes, called ranging pairs, can measure their distance (with each such pair containing at least one tag).

For a ranging pair of nodes (i, j), we denote d_{ij} the true distance between the nodes and $\tilde{d}_{ij}$ a corresponding measurement, to which both nodes i and j have access. In the following, we consider measurement models assuming either additive Gaussian noise

$$\tilde{d}_{ij} = d_{ij} + \nu_{ij},\ \nu_{ij} \sim \mathcal{N}(0, \sigma^2), \tag{5.1}$$

or multiplicative log-normal noise

$$\tilde{d}_{ij} = d_{ij}\, e^{\mu_{ij}},\ \mu_{ij} \sim \mathcal{N}(0, \bar{\sigma}^2), \tag{5.2}$$

where the noise realizations ν_{ij} or μ_{ij} are independent for all i, j and $\sigma^2, \bar{\sigma}^2 \in \mathbb{R}^+$ are given covariances. We collect all the measured distances $\tilde{d}_{ij}$ at a given time in the vector $\tilde{\mathbf{d}} = [\dots, \tilde{d}_{ij}, \dots]^\top \in \mathbb{R}^P$. We also define an undirected graph $\mathcal{G} = (\mathcal{E}, \mathcal{V})$, called the *ranging graph*, whose vertices $\mathcal{V}$ are the N nodes and with an edge in $\mathcal{E}$ for each ranging pair and for each pair of anchors. In particular, the subgraph of $\mathcal{G}$ formed by the anchors is a complete graph, which is consistent with the fact that the distances between anchors are implicitly known from their coordinates. Two nodes linked by an edge in $\mathcal{G}$ are called neighbors and we

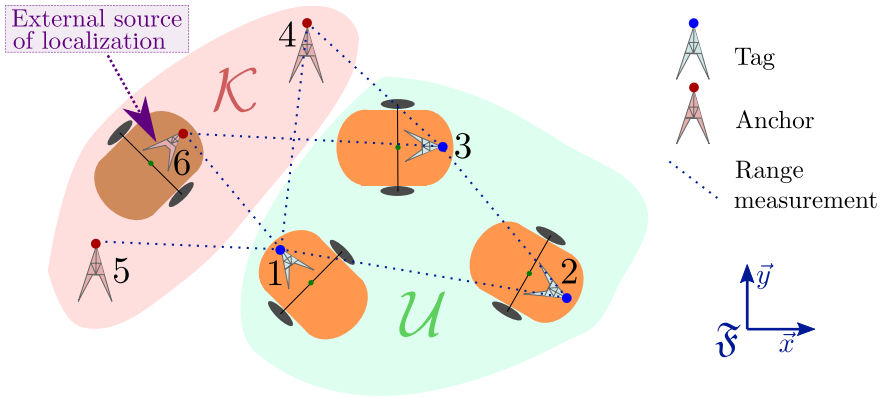

Figure 5.1 – Illustration of the setup in 2D with 3 mobile tags and 3 anchors, 2 of whom are fixed. The links for the ranging pairs are shown. The ranging graph includes 3 additional implicit links between the anchors, not shown

denote by $\mathcal{N}_i$ the set of neighbors of i or *neighborhood* of i, for $1 \leq i \leq N$. Let $E = P + \frac{K(K-1)}{2}$ be the total number of edges in $\mathcal{G}$.

A concrete implementation of the previous system is as follows. The nodes could correspond to RF transceivers capable of measuring their distance with respect to other nodes within their communication radius. Radiolocation protocols such as Two-Way Ranging (TWR), Time of Arrival (ToA) or Time Difference of Arrival (TDoA) [Sahinoglu et al., 2008, Bensky, 2016] use the timestamps of messages exchanged by the transceivers to estimate the ToF of these messages and deduce distance measurements, which can be assumed to be of the form (5.1), at least under line-of-sight signal propagation conditions. Another ranging method consists in measuring the strength of a received signal (RSS) to deduce the distance to the transmitter using a path loss propagation model [Bensky, 2016]. This method typically leads to a distance measurement model of the form (5.2), assuming again a simple radio propagation environment [Coulson et al., 1998, Patwari et al., 2005].

We assume that the nodes implement a cooperative localization scheme, in order to jointly produce an estimate $\hat{\mathbf{p}}$ of all their coordinates $\mathbf{p}$ in $\mathfrak{F}$, based on the noisy measurements $\tilde{\mathbf{d}}$ and the knowledge of the anchor coordinates. As we explain in Section 5.3, the value of $\mathbf{p}$ itself strongly influences the achievable accuracy of its estimate. Hence, we introduce in that section some real-valued functions $J_{\text{loc}} : \mathbb{R}^{nN} \to \mathbb{R}$ that can serve as *localizability potentials*, i.e., such that a low value (resp. high value) for $J_{\text{loc}}(\mathbf{p})$ means that the performance of an estimator at configuration $\mathbf{p}$ is expected to be good (resp. bad). A localizability potential can then serve as an artificial potential for motion planning [Choset et al., 2005], to guide or constrain the motion of an MRS to configurations that are favorable for accurate cooperative localization. Concretely, consider a potential function $J(\mathbf{p}) = \alpha J_1(\mathbf{p}) + (1-\alpha) J_{\text{loc}}(\mathbf{p})$, for $\alpha \in (0,1)$, where J_1 may include attractive and repulsive potentials to steer robots toward

desired locations [Khatib, 1986] and away from obstacles [Choset et al., 2005], to maintain network connectivity [Yang et al., 2010], to cover an area [Bullo et al., 2009], etc. One can then generate a sequence of configurations $\mathbf{p}(0), \mathbf{p}(1), \ldots$, for the MRS by following the gradient descent scheme

$$\mathbf{p}_{i,k+1} = \mathbf{p}_{i,k} - \gamma_k \left(\frac{\partial J(\mathbf{p}_k)}{\partial \mathbf{p}_i} \right)^\top, \tag{5.3}$$

for each mobile node i, with $\{\gamma_k\}_{k\geq 0}$ a sequence of appropriate stepsizes. The presence of J_{loc} in the overall potential favours configurations that have higher localizability, and this effect becomes more pronounced as α increases. Alternatively, one can also minimize J_1 subject to a constraint on the maximum tolerable value of J_{loc}. Note however that as in most cases where artificial potentials are used to plan the motion of an MRS, the gradient descent scheme (5.3) typically only leads to locally optimal configurations.

A key issue when relying on artificial potentials to provide goal configurations to an MRS is to ensure that each mobile node i can compute the gradient $(\partial J_{\text{loc}}(\mathbf{p}(k))/\partial \mathbf{p}_i)^\top$ with respect to its coordinates in (5.3) by exchanging information only with its immediate neighbors in the communication network, *which we assume here to coincide with the ranging graph* (although in general the anchors will not need to communicate with each other). This ensures scalability to large networks and improves the robustness of the network against the loss of nodes. The design of distributed gradient descent schemes for the localizability potentials is discussed in Section 5.5.

In summary, the problem considered in this paper is to first define appropriate functions that can serve as localizability potentials and then design distributed gradient descent algorithms for these potentials in order to deploy an MRS with ranging sensors while ensuring that its cooperative localization scheme remains precise. In addition, we show in Section 5.6 how to adapt the definition of the localizability potentials and the gradient descent scheme to a more complex situation where multiple tags can be carried by the same robot. This introduces additional constraints on the positions $\mathbf{p}$, which should be taken into account by localization and motion planning algorithms. These constraints can be used in practice to provide more accurate full pose estimates for the robots.

Remark 5.1. *In practice, the tags have access to their position* $\mathbf{p}$ *only through their estimates* $\hat{\mathbf{p}}$. *As a result, when using artificial potentials for motion planning, the gradient descent scheme* (5.3) *cannot be directly implemented, and the standard approach is to compute and follow the gradient at the current estimate, i.e., use* $\partial J(\hat{\mathbf{p}}_k)/\partial \mathbf{p}_i$ *in* (5.3). *Since including a localizability potential aims to improve the accuracy of the position estimates along the robots' paths, it contributes to making this approximation of ignoring position uncertainty*

less problematic. Alternatively, (5.3) *can also be used to compute a sequence of steps, i.e., plan a future trajectory for the MRS, in which case we assume at the planning stage that the agents will be able to track that trajectory perfectly. Moreover, we empirically study the behavior of the scheme* (5.3) *with gradients evaluated at the imperfect position estimates, both in simulations in Section 5.7 and through experiments in Section 5.8. In particular, our experiment confirms the intuitive fact that enhancing the localizability is important to ensure that the robots are able to reliably follow their desired trajectories.*

Remark 5.2. *In general, the ranging graph $\mathcal{G}$ could change over time as nodes move in their environment. In this case, the algorithms presented later could still be implemented at each period over the current ranging graph, but localizability could become poor if critical ranging pairs become disconnected. To address this issue, ranging between specific pairs can be maintained by adding connectivity potentials to the function J_1 above. Alternatively, when we use the model* (5.2) *or alternative models where the variance degrades with distance [Cano et al., 2022c], then J_{loc} increases when the links become longer, a consequence of the result* (5.5) *stated in the next section. Hence, in a manner similar to the use weighted graph models for connectivity [Kim and Mesbahi, 2006] and rigidity [Zelazo et al., 2015], maintaining ranging distance between nodes can be promoted directly through the localizability potential.*

5.3 Localizability Potentials

This section is concerned with defining artificial potentials that can be used as localizability potentials. The proposed definitions require that we first recall some notions from estimation theory related to the CRLB.

5.3.1 Constrained Cramér-Rao Lower Bound

We assume that the position estimator implemented by the MRS is unbiased, i.e., satisfies $\mathbb{E}[\hat{\mathbf{p}}] = \mathbf{p}$. We then focus on finding configurations $\mathbf{p}$ for which the error covariance matrix $\mathbb{E}\left[(\hat{\mathbf{p}} - \mathbf{p})(\hat{\mathbf{p}} - \mathbf{p})^\top\right]$ for $\hat{\mathbf{p}}$, which is then also the covariance matrix $\mathsf{cov}[\hat{\mathbf{p}}]$, is "small" in some sense. More precisely, since the error covariance depends on the specific estimator used and can be difficult to predict analytically, we use the CRLB, a lower bound on the covariance of any unbiased estimator, to quantify the quality of a configuration $\mathbf{p}$. Although this implicitly assumes that an estimator can be constructed to achieve or approach this lower bound, this methodology is commonly used in optimal experiment design and sensor placement [Pukelsheim, 2006,Uciński, 2004]. In general, the CRLB corresponds to the inverse of the Fisher Information Matrix (FIM), which we define below.

Definition 5.1 (FIM)**.** *Let* $\mathbf{x} \in \mathbb{R}^p$ *be a deterministic parameter vector and* $\mathbf{y} \in \mathbb{R}^q$ *a random observation vector, for some positive integers* p, q*. Define* $f : \mathbb{R}^q \times \mathbb{R}^p \to \mathbb{R}^+$ *the Probability Density Function (PDF) of* $\mathbf{y}$*, which depends on the parameter* $\mathbf{x}$*, so that we write* $f(\mathbf{y}; \mathbf{x})$*. Under some regularity assumptions on* f *(see [Haug, 2012, Chap. 14]), the* $p \times p$ *Fisher Information Matrix (FIM) of this PDF is defined as*

$$\mathbf{F}(\mathbf{x}) = -\mathbb{E}_{\mathbf{y}}\left[\frac{\partial^2 \ln f(\mathbf{y}; \mathbf{x})}{\partial \mathbf{x} \partial \mathbf{x}^\top}\right]. \tag{5.4}$$

The matrix $\mathbf{F}(\mathbf{x})$ *is symmetric and positive semi-definite.*

In the position estimation problem, the parameters of interest are the node coordinates in the vector $\mathbf{p} \in \mathbb{R}^{nN}$, whereas the random observations are contained in the vector $\tilde{\mathbf{d}}$. As computed in [Patwari et al., 2005], the FIM of the PDF $f(\tilde{\mathbf{d}}; \mathbf{p})$ is an $nN \times nN$ matrix that depends on $\mathbf{p}$ and can be decomposed into $n \times n$ blocks $\mathbf{F}_{ij}$ such that

$$\begin{aligned} \mathbf{F}_{ij}(\mathbf{p}) &= \mathbf{F}_{ij}(\mathbf{p}_{ij}) = -\frac{1}{d_{ij}^{2\kappa}\sigma^2}\mathbf{p}_{ij}\mathbf{p}_{ij}^\top \mathbf{1}_{\mathcal{N}_i}(j), \text{ if } i \neq j, \\ \mathbf{F}_{ii}(\mathbf{p}) &= -\sum_{j \neq i} \mathbf{F}_{ij}, \end{aligned} \tag{5.5}$$

where $\mathbf{p}_{ij} \coloneqq \mathbf{p}_i - \mathbf{p}_j$, and $\kappa = 1$ for the additive noise model (5.1) or $\kappa = 2$ for the multiplicative noise model (5.2). The result (5.5) can be obtained using the Slepian-Bangs formula [Kay, 1993, Section 3.9] or by direct calculation.

Note however that estimating the anchor positions is not needed, since the locations of these nodes are known. The fact that $\hat{\mathbf{p}}_i := \mathbf{p}_i$ for all $i \in \mathcal{K}$, with $\mathbf{p}_i$ known, should be taken into account by an estimator of the tag positions, and hence should also be taken into account when bounding the covariance of these estimators. We can rely on the theory of CRLBs with equality constraints on the estimated parameters in order to include these trivial constraints on the anchor positions and later in Section 5.6 also additional rigid constraints on the tag positions.

Theorem 5.1 (Equality constrained CRLB [Gorman and Hero, 1990])**.** *Let* $\mathbf{x} \in \mathbb{R}^p$ *be a deterministic parameter vector and* $\mathbf{y} \in \mathbb{R}^q$ *a random observation vector, for some positive integers* p, q*. Let* $\mathbf{h} : \mathbb{R}^p \to \mathbb{R}^c$*, for* $c \leq p$*, be a differentiable function such that* $\mathbf{h}(\mathbf{x}) = \mathbf{0}$*. Let* $\hat{\mathbf{x}}$ *be an unbiased estimate of* $\mathbf{x}$ *also satisfying* $\mathbf{h}(\hat{\mathbf{x}}) = \mathbf{0}$ *and with finite covariance matrix. Define* $\mathbf{F}_c \coloneqq \mathbf{A}^\top \mathbf{F} \mathbf{A}$*, the* constrained Fisher Information Matrix*, where* $\mathbf{A}$ *is any matrix whose columns span* $\ker \frac{\partial \mathbf{h}}{\partial \mathbf{x}}$*, and* $\mathbf{F}$ *is the FIM defined in* (5.4)*.*

Then, the following inequality holds

$$\mathsf{cov}[\hat{\mathbf{x}}] \succeq \mathbf{A}\,(\mathbf{F}_c)^{\dagger}\,\mathbf{A}^{\top} =: \mathbf{B}_c \tag{5.6}$$

where † denotes the Moore-Penrose pseudo-inverse [Petersen and Pedersen, 2012, p. 21].

Consider now the problem of estimating the vector of tag coordinates $\mathbf{p}_{\mathcal{U}} \in \mathbb{R}^{nU}$ based on the distance measurements $\tilde{\mathbf{d}}$ and knowledge of the anchor coordinates $\mathbf{p}_{\mathcal{K}} \in \mathbb{R}^{nK}$. Order the nodes so that $\mathbf{p} = \mathrm{col}(\mathbf{p}_{\mathcal{U}}, \mathbf{p}_{\mathcal{K}})$, and partition the FIM defined in (5.5) accordingly as

$$\mathbf{F} = \begin{bmatrix} \mathbf{F}_{\mathcal{U}} & \mathbf{F}_{\mathcal{U}\mathcal{K}} \\ \mathbf{F}_{\mathcal{U}\mathcal{K}}^{\top} & \mathbf{F}_{\mathcal{K}} \end{bmatrix}, \tag{5.7}$$

with in particular $\mathbf{F}_{\mathcal{U}}$ a symmetric positive semi-definite matrix of size $nU \times nU$. We then have the following result.

Proposition 5.1. *Let $\hat{\mathbf{p}}_{\mathcal{U}}$ be an unbiased estimate of the tag positions $\mathbf{p}_{\mathcal{U}}$, based on the measurements $\tilde{\mathbf{d}}$ and the knowledge of the anchor positions $\mathbf{p}_{\mathcal{K}}$. Then*

$$\mathsf{cov}[\hat{\mathbf{p}}_{\mathcal{U}}] \succeq \mathbf{F}_{\mathcal{U}}^{\dagger}(\mathbf{p}). \tag{5.8}$$

Proof. This result is a corollary of Proposition 5.5 stated below, with $\mathbf{f}_c \equiv \mathbf{0}$ in (5.28) and so $\mathbf{A}_{\mathcal{U}} = \mathbf{I}_{nU}$. □

5.3.2 Localizability Potentials and Optimal Design

Given (5.8), the following functions are possible candidates to define potential functions that penalize configurations of the ranging network leading to poor localizability

$$J_A(\mathbf{p}) = \mathrm{Tr}\left\{\mathbf{F}_{\mathcal{U}}^{-1}(\mathbf{p})\right\} \quad \text{(A-Optimal Design)}, \tag{5.9}$$

$$J_D(\mathbf{p}) = -\ln\det\{\mathbf{F}_{\mathcal{U}}(\mathbf{p})\} \quad \text{(D-Optimal Design)}, \tag{5.10}$$

$$J_E(\mathbf{p}) = -\lambda_{\min}\{\mathbf{F}_{\mathcal{U}}(\mathbf{p})\} \quad \text{(E-Optimal Design)}, \tag{5.11}$$

assuming in the first two cases that $\mathbf{F}_{\mathcal{U}}(\mathbf{p})$ is invertible. In the following, we refer to the functions J_A, J_D and J_E as the A-Opt, D-Opt and E-Opt potentials respectively, using standard terminology from optimal experiment design [Pukelsheim, 2006].

In each case, configurations $\mathbf{p}$ for which $J(\mathbf{p})$ takes large values correspond to geometries for which the error covariance matrix of an unbiased position estimator will necessarily be "large"

in a sense defined by the choice of potential. Hence, for (5.9), we have from (5.8) that $J_A(\mathbf{p})$ is a lower bound on $\mathrm{Tr}\left\{\mathsf{cov}[\hat{\mathbf{p}}_{\mathcal{U}}]\right\}$, which represents the total mean-squared error (MSE) of the unbiased estimator $\hat{\mathbf{p}}_{\mathcal{U}}$. Similarly, (5.10) corresponds to a lower bound on $\ln\det(\mathsf{cov}[\hat{\mathbf{p}}_{\mathcal{U}}])$, which would be equal (up to a constant) to the statistical entropy of $\hat{\mathbf{p}}_{\mathcal{U}}$, if this estimate were to follow a normal distribution. Finally, still assuming $\mathbf{F}_{\mathcal{U}} \succ 0$, minimizing J_E in (5.11) aims to minimize the maximum eigenvalue of $\mathbf{F}_{\mathcal{U}}^{-1}$ (equal to $1/\lambda_{\min}(\mathbf{F}_{\mathcal{U}})$), which is a lower bound on the maximum eigenvalue or induced 2-norm of $\mathsf{cov}[\hat{\mathbf{p}}_{\mathcal{U}}]$. Potentials like J_E are often used to maintain the connectivity [Kim and Mesbahi, 2006, Yang et al., 2010, Michael et al., 2009] or rigidity [Zelazo et al., 2015, Sun et al., 2015] of an MRS, which are closely related problems.

Once a potential has been chosen, it can be used to move the nodes to configurations of low potential values, where the localization accuracy is expected to be high. This can be done for example by descending the gradient of the potential, as discussed in Sections 5.5 and 5.6.

Remark 5.3. *Another a priori possible potential is*

$$J_T(\mathbf{p}) = -\mathrm{Tr}\left\{\mathbf{F}_{\mathcal{U}}(\mathbf{p})\right\}.$$

Configurations $\mathbf{p}$ *that minimize this potential are called T-optimal designs [Pukelsheim, 2006]. However, in our case we can compute*

$$J_T(\mathbf{p}) = -\alpha \sum_{\{i,j\}\in\mathcal{E}} d_{ij}^{2-2\kappa},$$

with α *a positive constant. In the case of additive Gaussian noise* (5.1)*,* $\kappa = 1$ *and* J_T *is constant, so that it cannot be used to optimize* $\mathbf{p}$*. In the case of multiplicative noise* (5.2)*, we have* $\kappa = 2$ *so* $J_T(\mathbf{p}) = -\alpha \sum_{\{i,j\}\in\mathcal{E}} d_{ij}^{-2}$ *becomes a simple attractive potential. In this case,* J_T *cannot be used alone as a potential, since its global minimum is trivially achieved when all agents occupy the same position. In view of these remarks,* J_T *is not considered further in the following.*

5.4 Properties of the Fisher Information Matrix

In this section, we study certain algebraic properties of the FIM that are useful for the design of algorithms in the next sections. In particular, we establish connections between the FIM and rigidity theory.

5.4.1 Infinitesimal Rigidity

For the ranging graph $\mathcal{G} = (\mathcal{E}, \mathcal{V})$, the incidence matrix $\mathbf{H} \in \mathbb{Z}^{E \times N}$ is defined by first assigning an arbitrary direction $i \to j$ to each edge $\{i, j\}$ of $\mathcal{E}$, and then setting each element as follows:

$$\text{for } \{i,j\} \in \mathcal{E}, k \in \mathcal{V}, H_{i\to j,k} = \begin{cases} 1 & \text{if } k = i, \\ -1 & \text{if } k = j, \\ 0 & \text{otherwise.} \end{cases}$$

We use throughout the paper the lexicographic ordering to order the edges $i \to j$ and hence the rows of $\mathbf{H}$. As a result, the rows of $\mathbf{H}$ corresponding to pairs of tags (in $\mathcal{U} \times \mathcal{U}$) appear first, followed by pairs in $\mathcal{U} \times \mathcal{K}$ and finally by pairs of anchors, in $\mathcal{K} \times \mathcal{K}$.

Remark 5.4. *Some references define* $\mathbf{H}$ *as an* $N \times E$ *matrix, transposing the* $E \times N$ *matrix above. Our choice of convention is motivated by the fact that it makes the connection to the rigidity matrix and the FIM clearer below.*

Given a ranging graph $\mathcal{G}$, a *framework* is a pair $(\mathcal{G}, \mathbf{p})$, where the vector $\mathbf{p} \in \mathbb{R}^{nN}$ contains the positions of all agents. The *rigidity function* $\mathbf{r} : \mathbb{R}^{nN} \to \mathbb{R}^E$ of a framework $(\mathcal{G}, \mathbf{p})$ is defined componentwise by

$$[\mathbf{r}(\mathcal{G}, \mathbf{p})]_{i\to j} = \frac{1}{2}\|\mathbf{p}_{ij}\|^2, \;\; \forall \{i,j\} \in \mathcal{E}, \tag{5.12}$$

and its *rigidity matrix* $\mathbf{R}(\mathcal{G}, \mathbf{p}) \in \mathbb{R}^{E \times nN}$ is the Jacobian $\partial \mathbf{r}/\partial \mathbf{p}$ of the rigidity function [Tay and Whiteley, 1985, Zelazo et al., 2015], which can be written explicitly as

$$\mathbf{R}(\mathcal{G}, \mathbf{p}) = \text{diag}(\dots, \mathbf{p}_{ij}^\top, \dots)\,[\mathbf{H} \otimes \mathbf{I}_n]. \tag{5.13}$$

In other words, the row $i \to j$ of $\mathbf{R}(\mathcal{G}, \mathbf{p})$ is

$$\begin{bmatrix} \mathbf{0} & \dots & \mathbf{0} & \mathbf{p}_{ij}^\top & \mathbf{0} & \dots & \mathbf{0} & -\mathbf{p}_{ij}^\top & \mathbf{0} \dots & \mathbf{0} \end{bmatrix}$$

with $\mathbf{p}_{ij}^\top$ occupying the i^{th} block of n coordinates and $-\mathbf{p}_{ij}^\top$ the j^{th} block. Next, when the node positions vary with time, consider motions that do not change the distances between nodes in ranging pairs, in other words, motions that keep the rigidity function constant. These motions must then satisfy

$$\frac{d\mathbf{r}(\mathcal{G}, \mathbf{p})}{dt} = \mathbf{R}(\mathcal{G}, \mathbf{p})\frac{d\mathbf{p}}{dt} = \mathbf{0},$$

i.e., the corresponding velocity vectors $d\mathbf{p}/dt$ must lie in the kernel of $\mathbf{R}(\mathcal{G}, \mathbf{p})$. This constraint is rewritten more explicitly in the following definition.

Definition 5.2 (Infinitesimal motion of a framework)**.** *An infinitesimal motion of a framework $(\mathcal{G}, \mathbf{p})$ is any vector $\mathbf{v} = \mathrm{col}(\mathbf{v}_1, \ldots, \mathbf{v}_N)$ in $\mathbb{R}^{nN}$, such that $\mathbf{v} \in \ker \mathbf{R}(\mathcal{G}, \mathbf{p})$. Equivalently, for each edge $\{i, j\} \in \mathcal{E}$, we have $\mathbf{p}_{ij}^\top(\mathbf{v}_i - \mathbf{v}_j) = \mathbf{0}$.*

Any framework admits a basic set of infinitesimal motions, namely, the *Euclidean* infinitesimal motions of the framework [Tay and Whiteley, 1985, Whiteley, 1996], which can be defined for $n = 3$ as

$$\mathrm{Eucl}^3_{\mathbf{p}} = \left\{ \mathrm{col}(\mathbf{v} + \boldsymbol{\omega} \times \mathbf{p}_1, \ldots, \mathbf{v} + \boldsymbol{\omega} \times \mathbf{p}_N) \,|\, \mathbf{v}, \boldsymbol{\omega} \in \mathbb{R}^3 \right\},$$

and for $n = 2$, with the notation $\mathbf{p}_i = [x_i, y_i]^\top$,

$$\mathrm{Eucl}^2_{\mathbf{p}} = \left\{ \mathrm{col}\left(\mathbf{v} + \omega \begin{bmatrix} y_1 \\ -x_1 \end{bmatrix}, \ldots, \mathbf{v} + \omega \begin{bmatrix} y_N \\ -x_N \end{bmatrix} \right) \,\Big|\, \mathbf{v} \in \mathbb{R}^2, \omega \in \mathbb{R} \right\}.$$

These infinitesimal motions correspond to the global rigid translations and rotations of the whole framework, and it is immediate to verify that the subspace $\mathrm{Eucl}_{\mathbf{p}}$ is always contained in $\ker \mathbf{R}(\mathcal{G}, \mathbf{p})$. Infinitesimally rigid frameworks do not admit other infinitesimal motions, which would correspond to internal deformations.

Definition 5.3 (Infinitesimal rigidity)**.** *A framework $(\mathcal{G}, \mathbf{p})$ in $\mathbb{R}^{nN}$ is called infinitesimally rigid if all its infinitesimal motions are Euclidean, i.e., if $\ker \mathbf{R}(\mathcal{G}, \mathbf{p}) = \mathrm{Eucl}^n_{\mathbf{p}}$.*

The following result provides a basis of $\mathrm{Eucl}^n_{\mathbf{p}}$ and is used in Section 5.6. When $n = 3$, with $\mathbf{e}_x$, $\mathbf{e}_y$, $\mathbf{e}_z$ the standard unit vectors in $\mathbb{R}^3$, define $\mathbf{v}_{T_\xi} = \mathbf{1}_N \otimes \mathbf{e}_\xi$ as well as $\mathbf{v}_{R_\xi} = \mathrm{col}(\mathbf{e}_\xi \times \mathbf{p}_1, \ldots, \mathbf{e}_\xi \times \mathbf{p}_N)$, for $\xi \in \{x, y, z\}$. Similarly, if $n = 2$ and $\mathbf{e}_x$, $\mathbf{e}_y$ are the standard unit vectors in $\mathbb{R}^2$, define $\mathbf{v}_{T_x} = \mathbf{1}_N \otimes \mathbf{e}_x$, $\mathbf{v}_{T_y} = \mathbf{1}_N \otimes \mathbf{e}_y$ and

$$\mathbf{v}_{R_z} = \mathrm{col}\left(\begin{bmatrix} -y_1 \\ x_1 \end{bmatrix}, \ldots, \begin{bmatrix} -y_N \\ x_N \end{bmatrix} \right).$$

Proposition 5.2. *Suppose that $N \geq n$. If $n = 2$ and at least 2 nodes are at distinct locations, the dimension of $\mathrm{Eucl}^2_{\mathbf{p}}$ is 3 and a basis of this subspace is given by $(\mathbf{v}_{T_x}, \mathbf{v}_{T_y}, \mathbf{v}_{R_z})$. If $n = 3$ and we have at least 3 nodes that are not aligned, the dimension of $\mathrm{Eucl}^3_{\mathbf{p}}$ is 6 and a basis of this subspace is given by $(\mathbf{v}_{T_x}, \mathbf{v}_{T_y}, \mathbf{v}_{T_z}, \mathbf{v}_{R_x}, \mathbf{v}_{R_y}, \mathbf{v}_{R_z})$.*

Proof. We provide a proof for $n = 3$, the case $n = 2$ is similar. The fact that the vectors in the proposition span $\mathrm{Eucl}^3_{\mathbf{p}}$ is clear by definition, so it is sufficient to prove their independence. Consider a linear combination equal to zero

$$\begin{aligned}&\alpha_1\mathbf{v}_{T_x} + \alpha_2\mathbf{v}_{T_y} + \alpha_3\mathbf{v}_{T_z} + \alpha_4\mathbf{v}_{R_x} + \alpha_5\mathbf{v}_{R_y} + \alpha_6\mathbf{v}_{R_z}\\ &= \mathrm{col}(\mathbf{v} + \boldsymbol{\omega} \times \mathbf{p}_1, \ldots, \mathbf{v} + \boldsymbol{\omega} \times \mathbf{p}_n) = \mathbf{0},\end{aligned}$$

where $\mathbf{v} = [\alpha_1, \alpha_2, \alpha_3]^\top$ and $\boldsymbol{\omega} = [\alpha_4, \alpha_5, \alpha_6]^\top$. Suppose that the nodes indexed by i, j and k are not aligned. We have from the equation above $\mathbf{v} = -\boldsymbol{\omega} \times \mathbf{p}_i$, and so

$$\boldsymbol{\omega} \times (\mathbf{p}_j - \mathbf{p}_i) = \boldsymbol{\omega} \times (\mathbf{p}_k - \mathbf{p}_i) = \mathbf{0}.$$

Since $(\mathbf{p}_j - \mathbf{p}_i)$ and $(\mathbf{p}_k - \mathbf{p}_i)$ are by assumption independent, this gives $\boldsymbol{\omega} = \mathbf{0}$ and hence $\mathbf{v} = \mathbf{0}$. This proves the independence of the vectors in the proposition, which therefore form a basis of $\mathrm{Eucl}^3_{\mathbf{p}}$. □

5.4.2 Relations between the Rigidity Matrix and the FIM

Throughout this section, we consider the set of nodes (tags and anchors) to be at positions $\mathbf{p}$, with corresponding ranging graph $\mathcal{G}$. This defines a framework $(\mathcal{G}, \mathbf{p})$, as discussed in the previous section. The FIM $\mathbf{F}$ is given by (5.5), whereas the rigidity matrix $\mathbf{R} \coloneqq \mathbf{R}(\mathcal{G}, \mathbf{p})$ is given by (5.13).

Proposition 5.3. *We have* $\mathbf{F} = \mathbf{R}^\top\mathbf{Q}\mathbf{R}$*, where* $\mathbf{Q} = \mathrm{diag}\left(\ldots, 1/(d_{ij}^{2\kappa}\sigma^2), \ldots\right) \in \mathbb{R}^{E\times E}$*, and* $\kappa \in \{1, 2\}$ *is the parameter appearing in* (5.5)*.*

To explain this result, remark that $\mathbf{F}$ in (5.5) has a structure similar to the Laplacian matrix $\mathbf{L}$ of the graph $\mathcal{G}$ [Godsil and Royle, 2001, Chapter 12]. The expression of Proposition 5.3 then corresponds to the standard relationship $\mathbf{L} = \mathbf{H}^\top\mathbf{H}$ between the incidence matrix and the usual Laplacian matrix of an undirected graph. Hence, the FIM $\mathbf{F}$ can be considered as a weighted Laplacian matrix, noting the relation (5.13) between $\mathbf{H}$ and $\mathbf{R}$. In [Zelazo et al., 2015], matrices of the form $\mathbf{R}^\top\mathbf{Q}\mathbf{R}$, for any diagonal matrix $\mathbf{Q}$, are called (weighted) "symmetric rigidity matrices". Hence, with this terminology, Proposition 5.3 says that the FIM is a symmetric rigidity matrix, for a specific set of weights in $\mathbf{Q}$ determined by the properties of the measurement noise model. In particular, these weights depend inversely on the (true) distances between ranging nodes.

Proof. Starting from (5.13), we have

$$\mathbf{R}^\top \mathbf{Q}\mathbf{R} = (\mathbf{H}^\top \otimes \mathbf{I}_n)\,\mathrm{diag}\left(\ldots, \frac{\mathbf{p}_{ij}\mathbf{p}_{ij}^\top}{d_{ij}^{2\kappa}\sigma^2}, \ldots\right)(\mathbf{H}\otimes \mathbf{I}_n).$$

Hence, for $i \neq j$, the block i,j of $\mathbf{R}^\top\mathbf{Q}\mathbf{R}$ is

$$[\mathbf{R}^\top\mathbf{Q}\mathbf{R}]_{ij} = \sum_{e\in\mathcal{E}} H_{ei}H_{ej}\mathbf{Q}_{ee} = -\frac{\mathbf{p}_{ij}\mathbf{p}_{ij}^\top}{d_{ij}^{2\kappa}\sigma^2}\mathbf{1}_{\mathcal{N}_i}(j) = \mathbf{F}_{ij},$$

using the fact that $H_{ei}H_{ej} = -1$ if e is $i \to j$ and 0 otherwise. Similarly, for all i

$$[\mathbf{R}^\top\mathbf{Q}\mathbf{R}]_{ii} = \sum_{e\in\mathcal{E}} H_{ei}H_{ei}\mathbf{Q}_{ee} = \sum_{j\in\mathcal{N}_i} \frac{\mathbf{p}_{ij}\mathbf{p}_{ij}^\top}{d_{ij}^{2\kappa}\sigma^2} = \mathbf{F}_{ii}.$$

□

The following result then follows immediately from the fact that $\mathbf{Q} \succ \mathbf{0}$ in Proposition 5.3.

Corollary 5.1. *We have* $\ker \mathbf{F} = \ker \mathbf{R}$.

The following result states that infinitesimal rigidity provides a sufficient condition for the invertibility of the symmetric positive semi-definite matrix $\mathbf{F}_\mathcal{U}$ appearing in (5.7).

Theorem 5.2. *Suppose that the framework* $(\mathcal{G}, \mathbf{p})$ *is infinitesimally rigid and contains at least* n *anchors at distinct locations. Moreover, when* $n = 3$*, suppose that at least* 3 *of these anchors are not aligned. Then* $\mathbf{F}_\mathcal{U}$ *is invertible.*

Proof. We give the proof in the more involved case $n = 3$. With the assumed ordering of nodes and edges, the rigidity matrix has the following block structure

$$\mathbf{R} = \begin{bmatrix} \mathbf{R}_1 & \mathbf{R}_2 \\ \mathbf{0} & \mathbf{R}_3 \end{bmatrix}, \text{ with } \mathbf{R}_1 \in \mathbb{R}^{P\times U}, \mathbf{R}_3 \in \mathbb{R}^{\frac{K(K-1)}{2}\times K}.$$

In other words, the rows of the matrix $\mathbf{R}_1$ correspond to the edges internal to $\mathcal{U}$ and between $\mathcal{U}$ and $\mathcal{K}$, whereas $\mathbf{R}_3$ is the rigidity matrix of the complete subgraph formed by the anchors and the links between them. Now, we have $\mathbf{F}_\mathcal{U} = \mathbf{R}_1^\top\mathbf{Q}_1\mathbf{R}_1$, with $\mathbf{Q}_1$ diagonal and invertible, as in Proposition 5.3, so $\ker \mathbf{F}_\mathcal{U} = \ker \mathbf{R}_1$. Consider some vector $\mathbf{x}_1 \in \mathbb{R}^U$ with $\mathbf{x}_1 \in \ker \mathbf{R}_1$. Then,

$$\mathbf{R}\begin{bmatrix}\mathbf{x}_1 \\ \mathbf{0}\end{bmatrix} = \begin{bmatrix} \mathbf{R}_1 & \mathbf{R}_2 \\ \mathbf{0} & \mathbf{R}_3 \end{bmatrix}\begin{bmatrix}\mathbf{x}_1 \\ \mathbf{0}\end{bmatrix} = \mathbf{0}, \tag{5.14}$$

hence $\mathrm{col}(\mathbf{x}_1, \mathbf{0})$ is in $\ker \mathbf{R}$. Since $\mathcal{G}$ is infinitesimally rigid, there must exist $\mathbf{v}$, $\boldsymbol{\omega}$ in $\mathbb{R}^3$ such that

$$\begin{bmatrix} \mathbf{x}_1 \\ \mathbf{0} \end{bmatrix} = \mathrm{col}(\mathbf{v} + \boldsymbol{\omega} \times \mathbf{p}_1, \ldots, \mathbf{v} + \boldsymbol{\omega} \times \mathbf{p}_N).$$

In particular, for the 3 anchors that are not aligned, indexed by i, j and k, we must have

$$\mathbf{v} + \boldsymbol{\omega} \times \mathbf{p}_i = \mathbf{v} + \boldsymbol{\omega} \times \mathbf{p}_j = \mathbf{v} + \boldsymbol{\omega} \times \mathbf{p}_k = \mathbf{0}.$$

From this, we conclude as in the proof of Proposition 5.2 that $\mathbf{v} = \boldsymbol{\omega} = \mathbf{0}$, which in turns implies $\mathbf{x}_1 = \mathbf{0}$. Hence $\ker \mathbf{F}_{\mathcal{U}} = \{\mathbf{0}\}$, i.e., $\mathbf{F}_{\mathcal{U}} \succ \mathbf{0}$. □

Remark 5.5. *If we have only one tag, then one can show that $\mathbf{F}_{\mathcal{U}}$ is invertible if and only if we have at least n anchors and the nodes' locations span an affine space of full dimension n (i.e., we have 3 non aligned nodes if $n = 2$, and 4 non coplanar nodes if $n = 3$). Note that if we have only n anchors, we cannot localize uniquely the tag in general, even with perfect measurements, because the intersection of n spheres in $\mathbb{R}^n$ gives two possible locations. Hence, even when $\mathbf{F}_{\mathcal{U}}$ is invertible, the localization problem might not be uniquely solvable. Unicity of the localization solution can be characterized by the stronger notion of global rigidity [Aspnes et al., 2006], which however is more complex to check if $n = 2$ and for which no exact test is currently known if $n = 3$.*

Theorem 5.2 can be used to produce an initial node placement and choose ranging links to guarantee that $\mathbf{F}_{\mathcal{U}}$ is already invertible at the start of the deployment. For this, we should ensure that $(\mathcal{G}, \mathbf{p})$ is infinitesimally rigid. One convenient way to satisfy this condition (in fact, the stronger condition of global rigidity) is to construct a *triangulation graph* [Aspnes et al., 2006,Moore et al., 2004]: starting from a set of at least $n+1$ anchors, we add tags one by one, with each new tag connected to at least $n+1$ previous nodes that are in general position (3 non-aligned nodes if $n = 2$, 4 non-coplanar nodes if $n = 3$). Although this construction requires more anchors and links than the strict minimum necessary for the invertibility of $\mathbf{F}_{\mathcal{U}}$, the resulting network supports efficient distributed localization algorithms that are robust to measurement noise [Moore et al., 2004].

5.5 Distributed Gradient Computations for the Localizability Potentials

In order to implement the gradient descent scheme (5.3), in Section 5.5.1 we provide analytical forms for the gradients of the localizability potentials (5.9), (5.10) and (5.11). Then, in Sections 5.5.2 and 5.5.3, we describe decentralized deployment algorithms by showing how each agent can compute its components of the gradient of the chosen localizability potential,

using its own local information as well as data obtained from its neighbors in the ranging graph.

5.5.1 Partial Derivatives of the FIM

Irrespective to the potential considered, we need to evaluate the derivative of the FIM $\mathbf{F}_{\mathcal{U}}$ in (5.7) with respect to any coordinate $\xi_i \in \{x_i, y_i, z_i\}$ of a mobile agent i (anchor or tag) located at $\mathbf{p}_i = [x_i, y_i, z_i]^\top$. We provide formulas for the case $n = 3$, the case $n = 2$ being similar. Define the notation $\xi_{ij} = \xi_i - \xi_j$ and $\gamma_{ij} = \frac{\kappa}{\sigma^2 d_{ij}^{2(\kappa+1)}} 1_{\mathcal{N}_i}(j)$. For $\mathbf{F}_{ij}$, $i \neq j$, the 3×3 blocks introduced in (5.5), we find

$$\frac{\partial \mathbf{F}_{ij}}{\partial x_i} = \gamma_{ij} \begin{bmatrix} x_{ij}^3 - \frac{d_{ij}^2 x_{ij}}{\kappa} & x_{ij}^2 y_{ij} - \frac{d_{ij}^2 y_{ij}}{2\kappa} & x_{ij}^2 z_{ij} - \frac{d_{ij}^2 z_{ij}}{2\kappa} \\ \star & x_{ij} y_{ij}^2 & x_{ij} y_{ij} z_{ij} \\ \star & \star & x_{ij} z_{ij}^2 \end{bmatrix}$$

$$\frac{\partial \mathbf{F}_{ij}}{\partial y_i} = \gamma_{ij} \begin{bmatrix} x_{ij}^2 y_{ij} & x_{ij} y_{ij}^2 - \frac{d_{ij}^2 x_{ij}}{2\kappa} & x_{ij} y_{ij} z_{ij} \\ \star & y_{ij}^3 - \frac{d_{ij}^2 y_{ij}}{\kappa} & y_{ij}^2 z_{ij} - \frac{d_{ij}^2 z_{ij}}{2\kappa} \\ \star & \star & y_{ij} z_{ij}^2 \end{bmatrix},$$

$$\frac{\partial \mathbf{F}_{ij}}{\partial z_i} = \gamma_{ij} \begin{bmatrix} x_{ij}^2 z_{ij} & x_{ij} y_{ij} z_{ij} & x_{ij} z_{ij}^2 - \frac{d_{ij}^2 x_{ij}}{2\kappa} \\ \star & y_{ij}^2 z_{ij} & y_{ij} z_{ij}^2 - \frac{d_{ij}^2 y_{ij}}{2\kappa} \\ \star & \star & z_{ij}^3 - \frac{d_{ij}^2 z_{ij}}{\kappa} \end{bmatrix}, \tag{5.15}$$

where the symbol $\star$ replaces symmetric terms. These expressions are sufficient to compute the whole matrix $\partial \mathbf{F}_{\mathcal{U}} / \partial \xi_i$, because $\mathbf{F}_{ji} = \mathbf{F}_{ij}$, $\mathbf{F}_{aa} = -\sum_{b \in \mathcal{N}_a} \mathbf{F}_{ab}$, and $\partial \mathbf{F}_{ab} / \partial \xi_i = \mathbf{0}$ if $a \neq b$ and $i \notin \{a, b\}$.

Using standard differentiation rules [Petersen and Pedersen, 2012], the partial derivatives of the A-Opt potential (5.9) are

$$\frac{\partial J_A(\mathbf{p})}{\partial \xi_i} = \frac{\partial \mathrm{Tr}\left\{\mathbf{F}_{\mathcal{U}}^{-1}\right\}}{\partial \xi_i} = -\mathrm{Tr}\left\{\mathbf{F}_{\mathcal{U}}^{-2} \frac{\partial \mathbf{F}_{\mathcal{U}}}{\partial \xi_i}\right\}. \tag{5.16}$$

Similarly, we can compute the derivatives of the D-Opt potential (5.10) as

$$\frac{\partial J_D(\mathbf{p})}{\partial \xi_i} = -\frac{\partial \ln \det \mathbf{F}_{\mathcal{U}}}{\partial \xi_i} = -\mathrm{Tr}\left\{\mathbf{F}_{\mathcal{U}}^{-1} \frac{\partial \mathbf{F}_{\mathcal{U}}}{\partial \xi_i}\right\}. \tag{5.17}$$

Finally, if $\lambda_{\min}(\mathbf{F}_{\mathcal{U}})$ is a non-repeated eigenvalue with associated unit norm eigenvector $\mathbf{v}$, we

can compute the derivative of the E-Opt potential (5.11) as [Harville, 1997, p. 565]

$$\frac{\partial J_E(\mathbf{p})}{\partial \xi_i} = -\frac{\partial \lambda_{\min}(\mathbf{p})}{\partial \xi_i} = -\mathbf{v}^\top \frac{\partial \mathbf{F}_\mathcal{U}}{\partial \xi_i}\mathbf{v}. \tag{5.18}$$

Hence, we can in principle compute the gradient of the chosen localizability potential, using the expressions for the FIM and its derivatives. However, in practice we would also like to be able to implement these computations in a distributed manner, in order to obtain deployment strategies that can be used by an MRS with incomplete ranging graph $\mathcal{G}$, assuming communication over this ranging graph is also possible.

5.5.2 Decentralized Gradient Computations for the D- and A-Opt Potentials

We propose now a new method to estimate in a distributed way the gradient of the D- and A-Opt potentials at a given configuration $\mathbf{p}$, which have similar expressions, see (5.16) and (5.17). As mentioned in Remark 5.1, we assume that each node i has access to its position $\mathbf{p}_i$, which could be its true position (e.g., for anchors) or an estimate obtained after executing a localization algorithm such as the one in [Moore et al., 2004]. In the latter case, the algorithms presented here will simply produce the gradient of J_{loc} at the estimated position.

In the following, we omit $\mathbf{p}$ from the notation, writing $\mathbf{F}_\mathcal{U}$ instead of $\mathbf{F}_\mathcal{U}(\mathbf{p})$. The method essentially relies on inverting $\mathbf{F}_\mathcal{U}$ in a decentralized manner, which we discuss first.

Auxiliary Problem

Suppose that each tag $i \in \mathcal{U}$ knows initially a matrix $\mathbf{E}_i \in \mathbb{R}^{n\times m}$, for some integer m, and the tags need to compute $\mathbf{F}_\mathcal{U}^{-1}\mathbf{E}$ in a distributed manner over the network $\mathcal{G}$, where $\mathbf{E} = \text{col}(\mathbf{E}_1, \ldots, \mathbf{E}_U) \in \mathbb{R}^{nU\times m}$. This is equivalent to solving in a decentralized manner the linear system $\mathbf{F}_\mathcal{U}\mathbf{X} = \mathbf{E}$, with the matrix variable $\mathbf{X} \in \mathbb{R}^{nU\times m}$. A special case of this problem is to compute $\mathbf{F}_\mathcal{U}^{-1}$, when $\mathbf{E} = \mathbf{I}_{nU}$.

Consider the following system of differential equations

$$\dot{\mathbf{X}}(t) = -\mathbf{F}_\mathcal{U}\mathbf{X}(t) + \mathbf{E},\ \mathbf{X}(0) = \mathbf{X}_0. \tag{5.19}$$

If $\mathbf{F}_\mathcal{U} \succ \mathbf{0}$, as guaranteed by Theorem 5.2, then $-\mathbf{F}_\mathcal{U}$ has strictly negative eigenvalues, i.e., is stable, so the solution $\mathbf{X}(t)$ to the system (5.19) converges to the solution $\mathbf{F}_\mathcal{U}^{-1}\mathbf{E}$ of the linear system as $t \to \infty$, no matter the choice of initial condition $\mathbf{X}_0$. A discrete-time version of

the flow (5.19) can be implemented for $l \geq 0$ as

$$\mathbf{X}_{l+1} = \mathbf{X}_l - \eta_l \left(\mathbf{F}_{\mathcal{U}} \mathbf{X}_l - \mathbf{E}\right),$$

for some stepsizes η_l, which reads more explicitly for each tag $1 \leq i \leq U$

$$\begin{aligned} \mathbf{X}_{i,l+1} = & \eta_l \sum_{j \in \mathcal{N}_i \cap \mathcal{U}} \mathbf{F}_{ij} (\mathbf{X}_{i,l} - \mathbf{X}_{j,l}) \\ & + \left(\mathbf{I}_n + \eta_l \sum_{j \in \mathcal{N}_i \cap \mathcal{K}} \mathbf{F}_{ij} \right) \mathbf{X}_{i,l} + \eta_l \mathbf{E}_i. \end{aligned} \tag{5.20}$$

Again, the iterates $\mathbf{X}_k$ converge to the desired solution $\mathbf{F}_{\mathcal{U}}^{-1}\mathbf{E}$ if we choose for example $\eta_l = \eta$ constant and sufficiently small (namely, as long as $\eta < 2/\lambda_{\max}(\mathbf{F}_{\mathcal{U}})$). The iterations (5.20) can be implemented in a decentralized manner by the tags, i.e., at each step l tag i only needs to exchange its matrix $\mathbf{X}_i$ with its neighboring tags. This also requires that tag i knows $\mathbf{F}_{ij}$ for $j \in \mathcal{N}_i$, which is the case if prior to the iterations, the nodes (tags and anchors) broadcast their position (estimates) to their neighbors. When the iterations have converged, the $n \times m$ matrix $\mathbf{X}_i$ at tag i represents the i^{th} block of rows of $\mathbf{F}_{\mathcal{U}}^{-1}\mathbf{E}$, i.e., $\mathbf{F}_{\mathcal{U}}^{-1}\mathbf{E} = \text{col}(\mathbf{X}_1, \ldots, \mathbf{X}_U)$.

Remark 5.6. *The iterations* (5.20) *correspond to Richardson iterations to solve the linear system* $\mathbf{F}_{\mathcal{U}}\mathbf{X} = \mathbf{E}$ *in a decentralized way [Bertsekas and Tsitsiklis, 2015]. Other distributed iterative methods could be used, such as the Jacobi over-relaxation iterations*

$$\mathbf{X}_{i,l+1} = (1-\eta)\, \mathbf{X}_{i,l} + \eta\, \mathbf{F}_{ii}^{-1} \left(\mathbf{E}_i - \sum_{j \in \mathcal{N}_i \cap \mathcal{U}} \mathbf{F}_{ij} \mathbf{X}_{j,l} \right),$$

with potentially better convergence properties, but a detailed discussion of such alternatives, which can be found in [Bertsekas and Tsitsiklis, 2015, Chapter 2], is outside of the scope of this paper.

Application to compute $\partial J_D / \partial \xi_i$

To implement the gradient descent scheme (5.3) for D-optimization, each mobile node i (tag or anchor) needs to compute $\partial J_D / \partial \xi_i$ for $\xi_i \in \{x_i, y_i, z_i\}$, which is given by (5.17). Denote $\mathbf{M} = \mathbf{F}_{\mathcal{U}}^{-1} \in \mathbb{R}^{nU \times nU}$ and its $n \times n$ blocks $\mathbf{M}_{ij}$, for $1 \leq i, j \leq U$. First, the tags run the iterations (5.20), with the matrix $\mathbf{E} = \mathbf{I}_{nU}$. That is, tag j uses the matrix $\mathbf{E}_j = \mathbf{e}_j^\top \otimes \mathbf{I}_n$, where $\mathbf{e}_j$ is the j^{th} unit vector in $\mathbb{R}^U$. After convergence, tag j stores an approximation of the matrix $\mathbf{M}_j = [\mathbf{M}_{j1}, \ldots, \mathbf{M}_{jU}] \in \mathbb{R}^{n \times nU}$. A stopping condition $\max_{i \in \mathcal{N}_j} \|\mathbf{X}_{i,l+1} - \mathbf{X}_{i,l}\| / \|\mathbf{X}_{i,l}\| < \epsilon$ can be implemented at each node j, for a threshold $\epsilon > 0$.

Next, note from (5.15) that the only $n \times n$ non-zero blocks $\partial \mathbf{F}_{ab}/\partial \xi_i$, with $0 \leq a, b \leq U$, are those for which: i) $a = b$ and $a \in \mathcal{N}_i$; ii) $a = b = i$; iii) $a = i$ and $b \in \mathcal{N}_i$; or iv) $b = i$ and $a \in \mathcal{N}_i$. Moreover, if i is a mobile anchor (so $i \geq U + 1$), only case i) can occur. From this remark, we can derive the following expressions. If $i \in \mathcal{U}$

$$\frac{\partial J_D(\mathbf{p})}{\partial \xi_i} = \sum_{j \in \mathcal{N}_i \cap \mathcal{U}} \operatorname{Tr}\left\{ \left(\mathbf{M}_{jj} + \mathbf{M}_{ii} - 2\mathbf{M}_{ij}\right) \frac{\partial \mathbf{F}_{ij}}{\partial \xi_i} \right\} + \sum_{j \in \mathcal{N}_i \cap \mathcal{K}} \operatorname{Tr}\left\{ \mathbf{M}_{ii} \frac{\partial \mathbf{F}_{ij}}{\partial \xi_i} \right\}, \tag{5.21}$$

and if $i \in \mathcal{K}$

$$\frac{\partial J_D(\mathbf{p})}{\partial \xi_i} = \sum_{j \in \mathcal{N}_i \cap \mathcal{U}} \operatorname{Tr}\left\{ \mathbf{M}_{jj} \frac{\partial \mathbf{F}_{ij}}{\partial \xi_i} \right\}. \tag{5.22}$$

Assuming that each node knows an estimate of its coordinates and of its neighbors' coordinates, node i can obtain from its neighbor tags j the terms $\operatorname{Tr}\{\mathbf{M}_{jj}\partial \mathbf{F}_{ij}/\partial \xi_i\}$, and also compute the terms $\operatorname{Tr}\{\mathbf{M}_{ii}\partial \mathbf{F}_{ij}/\partial \xi_i\}$ and $\operatorname{Tr}\{\mathbf{M}_{ij}\partial \mathbf{F}_{ij}/\partial \xi_i\}$ if $i \in \mathcal{U}$. Hence, overall this provides a method allowing each mobile node i to compute $\partial J_D/\partial \xi_i$ by communicating only with its neighbors. Nevertheless, it requires significant data exchanges between the agents (exchanges to reach the convergence in (5.20) and sending of the approximations of $\mathbf{M}_j$, of size $n \times nU$, to the neighbors), which can limit its scalability to large MRS. Algorithm 5.1 summarizes the distributed gradient computation procedure for D-optimization.

Algorithm 5.1: D-Opt distributed gradient computation

Data: Each node i knows an estimate of its $\mathbf{p}_i$ from a localization algorithm, or exactly if $i \in \mathcal{K}$

Result: Each mobile node i knows $\partial J_D(\mathbf{p})/\partial \mathbf{p}_i$

1 Each node $i \in \mathcal{U} \cup \mathcal{K}$ broadcasts $\mathbf{p}_i$ to its neighbors;

2 The tags run the iterations (5.20) until convergence, with $\mathbf{E}_j = \mathbf{e}_j^\top \otimes \mathbf{I}_n$ for tag j, and each tag j stores the resulting matrix $\mathbf{M}_j$;

3 Each mobile tag i computes $\sum_{j \in \mathcal{N}_i} \operatorname{Tr}\left\{ \left(\mathbf{M}_{ii} - 2\mathbf{M}_{ij} 1_{\mathcal{K}}(j)\right) \frac{\partial \mathbf{F}_{ij}}{\partial \xi_i} \right\}$;

4 Each tag j computes and sends $\operatorname{Tr}\left\{ \mathbf{M}_{jj} \frac{\partial \mathbf{F}_{ij}}{\partial \xi_i} \right\}$ to each of its mobile neighbors $i \in \mathcal{N}_j$ (i tag or anchor);

5 Each mobile node i computes its gradient using (5.21) or (5.22);

The same steps can be used to compute the gradient (5.16) at each mobile node for A-optimization. The only difference is that the matrices $\mathbf{M}_i$ above should represent rows of $\mathbf{F}_{\mathcal{U}}^{-2}$ instead of $\mathbf{F}_{\mathcal{U}}^{-1}$. For this, the tags first compute the rows $\tilde{\mathbf{M}}_i$ of $\mathbf{F}_{\mathcal{U}}^{-1}$ using the iterations (5.20). Then, we restart these iterations but now replacing the matrices $\mathbf{E}_i = \mathbf{e}_i^\top \otimes \mathbf{I}_n$ by $\tilde{\mathbf{M}}_i$. This computes an approximation of $\mathbf{F}_{\mathcal{U}}^{-1}\mathbf{F}_{\mathcal{U}}^{-1} = \mathbf{F}_{\mathcal{U}}^{-2}$, as desired. However, the resulting distributed

A-Opt scheme requires more computational resources and communication exchanges and is thus less applicable for large MRS.

5.5.3 Decentralized Computation of E-Opt Gradient

The decentralized computation of the gradient of the E-Opt potential can be done using the methodology developed in [Yang et al., 2010] for the standard Laplacian, also used in [Zelazo et al., 2015] for the symmetric rigidity matrix. Hence, our presentation is brief and focuses on adapting this methodology to $\mathbf{F}_{\mathcal{U}}(\mathbf{p})$.

Using the sparsity of $\mathbf{F}_{\mathcal{U}}$, if $i \in \mathcal{U}$, we can rewrite (5.18) as

$$\frac{\partial J_E(\mathbf{p})}{\partial \xi_i} = \sum_{j \in \mathcal{N}_i \cap \mathcal{U}} (\mathbf{v}_i - \mathbf{v}_j)^\top \frac{\partial \mathbf{F}_{ij}}{\partial \xi_i} (\mathbf{v}_i - \mathbf{v}_j)^\top + \mathbf{v}_i^\top \left(\sum_{j \in \mathcal{N}_i \cap \mathcal{K}} \frac{\partial \mathbf{F}_{ij}}{\partial \xi_i} \right) \mathbf{v}_i, \tag{5.23}$$

and if $i \in \mathcal{K}$

$$\frac{\partial J_E(\mathbf{p})}{\partial \xi_i} = \sum_{j \in \mathcal{N}_i \cap \mathcal{U}} \mathbf{v}_j^\top \frac{\partial \mathbf{F}_{ij}}{\partial \xi_i} \mathbf{v}_j, \tag{5.24}$$

where $\mathbf{v} = \mathrm{col}(\mathbf{v}_1, \ldots, \mathbf{v}_U) \in \mathbb{R}^{nU}$. Computing these expressions requires a decentralized algorithm to estimate the components of $\mathbf{v}$, a unit norm eigenvector associated with $\lambda_1 := \lambda_{\min}(\mathbf{F}_{\mathcal{U}})$.

Power-iteration eigenvector estimator

To compute $\mathbf{v}$ in a decentralized manner, consider the solution $t \mapsto \mathbf{w}(t) \in \mathbb{R}^{nU}$ to the following differential equation, adapted from [Yang et al., 2010],

$$\dot{\mathbf{w}} = -[\beta \mathbf{F}_{\mathcal{U}} + \mu((nU)^{-1}\|\mathbf{w}(t)\|^2 - 1)\mathbf{I}_{nU}]\mathbf{w}(t), \tag{5.25}$$

with an initial condition $\mathbf{w}_0 := \mathbf{w}(0)$ and $\beta, \mu > 0$.

Proposition 5.4. *If $\mu > \lambda_1 \beta$ and $\mathbf{w}_0^\top \mathbf{v} \neq 0$, then the solution $\mathbf{w}(t)$ to (5.25) converges to an eigenvector $\mathbf{w}_\infty$ of $\mathbf{F}_{\mathcal{U}}$, associated with λ_1 and proportional to $\mathbf{v}$.*

Proof. This follows from the argument in the appendix of [Yang et al., 2010]. □

In practice, we can choose $\mathbf{w}_0$ randomly to fulfill the condition $\mathbf{w}_0^\top \mathbf{v} \neq 0$ with probability one. To set the gains β, μ, note that $\mathrm{Tr}\{\mathbf{F}_{\mathcal{U}}\} > \lambda_1$ since $\mathbf{F}_{\mathcal{U}} \succ 0$. Then, for the additive

measurement noise model (5.1), we have $\mathrm{Tr}\{\mathbf{F}_{\mathcal{U}}\} \leq \frac{2P}{\sigma^2}$. So, if we choose $\beta \geq \sigma^2/(2P)$ and $\mu > 1$, the condition of Proposition 5.4 is satisfied. For the log-normal model (5.2), we have $\mathrm{Tr}\{\mathbf{F}_{\mathcal{U}}\} \leq \frac{2}{\sigma^2}\sum_{\{i,j\}\in\mathcal{E}, i\in\mathcal{U}} d_{ij}^{-2}$. Hence, if we set again $\beta \geq \sigma^2/(2P)$ and now $\mu > 1/d_{min}^2$, such that $d_{ij} \geq d_{\min}$ for all i, j, then the condition of Proposition 5.4 is satisfied. The minimum distance $d_{\min}$ between robots could be enforced as part of a collision avoidance scheme.

An estimation algorithm for $\mathbf{v}$ is obtained by discretizing (5.25), leading to the following iterations for each agent $i \in \mathcal{U}$

$$\begin{aligned}\mathbf{w}_{i,l+1} =& \mathbf{w}_{i,l} - \eta_l\Big(\mu(s_l - 1)\mathbf{w}_{i,l} \\ &+ \beta \sum_{a\in(\mathcal{N}_i\cup\{i\})\cap\mathcal{U}} \mathbf{F}_{il}\mathbf{w}_{a,l}\Big),\end{aligned} \tag{5.26}$$

where $\eta_l > 0$ is a sufficiently small step-size and $s_l := \|\mathbf{w}_l\|^2/nU$. All the terms in (5.26) can be obtained locally by node i using one-hop communication with its neighbors, except for the global average s_l, which can be computed by a consensus algorithm as described next. The last step is to normalize $\mathbf{w}_\infty$, obtained after convergence in (5.26). This can again be done by each individual agent, since $\mathbf{v} := \mathbf{w}_\infty/\sqrt{nUs_\infty}$ is a unit-norm vector.

Estimation of s_l via a consensus algorithm

Since $s_l = \|\mathbf{w}_l\|^2/(nU) = \frac{1}{U}\sum_{i=1}^{U}(\|\mathbf{w}_{i,l}\|^2/n)$, this term can be computed by the tags using a decentralized averaging consensus algorithm. We assume for simplicity that the graph of the tags $\mathcal{G}_{\mathcal{U}}$ is connected. To solve the averaging problem, each tag i initializes a variable $\hat{s}_{i,l,0} := \|\mathbf{w}_{i,l}\|^2/n$. Then, they execute in a distributed manner the iterations

$$\hat{\mathbf{s}}_{l,m+1} = \mathbf{G}\,\hat{\mathbf{s}}_{l,m}, \forall m \geq 0, \tag{5.27}$$

where $\hat{\mathbf{s}}_{l,m} = \mathrm{col}(\hat{s}_{1,l,m}, \ldots, \hat{s}_{U,l,m})$, and $\mathbf{G}$ is a doubly stochastic matrix of weights G_{ij} associated with the edges of $\mathcal{G}_{\mathcal{U}}$ (i.e., $\sum_{u=1}^{U} G_{iu} = \sum_{u=1}^{U} G_{ui} = 1$, for $1 \leq i \leq U$, and $G_{ij} = 0$ if $j \notin \mathcal{N}_i$), for instance the Metropolis-Hastings weights

$$\begin{cases} G_{ij} = \mathbf{1}_{\mathcal{N}_i\cap\mathcal{U}}(j)(1 + \max(|\mathcal{N}_i|, |\mathcal{N}_j|))^{-1}, \forall i \neq j, \\ G_{ii} = 1 - \sum_{u=1}^{U} G_{iu}. \end{cases}$$

We then have $\hat{\mathbf{s}}_{l,m} \to s_l\mathbf{1}_U$ [Bullo et al., 2009, p. 58], so that each tag knows after convergence the scalar value s_l needed for (5.26).

Remark 5.7. *Since s_l is time varying and we need to track its value at each period l, dynamic*

consensus methods [Kia et al., 2019] may converge faster than the solution presented here. We leave the exploration of such schemes for future work.

Algorithm 5.2 summarizes the decentralized computation of the estimate $\hat{\mathbf{v}}_i$ of the i-th component of $\mathbf{v}$ by a given tag $i \in \mathcal{U}$. After decentralized estimation of $\mathbf{v}$ by the tags, each mobile agent i can compute its components of the gradient of J_E from (5.23) or (5.24) by communicating with its neighbors.

Algorithm 5.2: Estimation of $\mathbf{v}_i$ by tag $i \in \mathcal{U}$.

Data: $\mathbf{w}_{i,0}$ random, $\mathbf{G}$, $\mu, \beta, n_{\text{iter}}, \tilde{n}_{\text{iter}}$

for $0 \leq l \leq n_{iter}$ **do**
  $\hat{s}_{i,l,0} = \|\mathbf{w}_{i,l}\|^2/n$;
  for $0 \leq m \leq \tilde{n}_{iter}$ **do**
    $\hat{s}_{i,l,m+1} = G_{ii}\hat{s}_{i,l,m} + \sum_{j \in \mathcal{N}_i \cap \mathcal{U}} G_{ij}\hat{s}_{j,l,m}$;
  end
  compute $\mathbf{w}_{i,l+1}$, setting $s_l := \hat{s}_{i,\tilde{n}_{\text{iter}}}$ in (5.26).
end
transmit $\hat{\mathbf{v}}_i := \frac{\mathbf{w}_{i,n_{\text{iter}}}}{\sqrt{nU\hat{s}_{\tilde{n}_{i,\text{iter}}}}}$ to the neighborhood;

Remark 5.8. *When the subgraph of $\mathcal{G}$ with only the tags is not connected, it is still possible to distributively compute the gradient of J_E. In this case, there exists a $U \times U$ permutation matrix $\mathbf{P}$ such that $\check{\mathbf{F}}_{\mathcal{U}} = (\mathbf{P} \otimes \mathbf{I}_n)^{-1}\mathbf{F}_{\mathcal{U}}(\mathbf{P} \otimes \mathbf{I}_n) = \text{diag}(\mathbf{F}_{\mathcal{S}_1} \dots \mathbf{F}_{\mathcal{S}_l} \dots)$ is block diagonal, where each $\mathcal{S}_l$ represents a subset of connected tags. Hence, the minimal eigenvalue λ of $\mathbf{F}_{\mathcal{U}}$ is among the minimal eigenvalues $\lambda_{\mathcal{S}_l}$ of the blocks $\mathbf{F}_{\mathcal{S}_l}$. Therefore, each subset $\mathcal{S}_l$ can use Algorithm 5.2 to compute its eigenvector $\mathbf{v}_{\mathcal{S}_l}$ associated to $\lambda_{\mathcal{S}_l} := \mathbf{v}_{\mathcal{S}_l}^\top \mathbf{F}_{\mathcal{S}_l}\mathbf{v}_{\mathcal{S}_l}$. On the other hand, the graph $\mathcal{G}$ with all nodes is assumed rigid and hence fully connected. This allows comparing the $\lambda_{\mathcal{S}_l}$ through the network $\mathcal{K}$ formed by the anchors in order to find $\lambda := \min_{\mathcal{S}_l} \lambda_{\mathcal{S}_l}$ corresponding to the subset $\mathcal{S}^*$. Since $\check{\mathbf{F}}_{\mathcal{U}}$ is block diagonal, its eigenvector associated with λ is $\text{col}(0, \dots, \mathbf{v}_{\mathcal{S}^*}, \dots 0)$, which then yields $\mathbf{v} = (\mathbf{P} \otimes \mathbf{I}_n)\,\text{col}(0, \dots, \mathbf{v}_{\mathcal{S}^*}, \dots 0)$ for $\mathbf{F}_{\mathcal{U}}$. Then, $\mathbf{v}$ gives the gradient of J_E using* (5.23) *and* (5.24).

5.6 Localizability Optimization for Rigid Bodies

5.6.1 Constrained Localizability Optimization

In this section, we consider scenarios where mobile robots can carry several tags, see Fig. 5.2. Hence, the relative motion and position of some tags are constrained by the fact that they are attached to the same rigid body. More generally, let $\mathbf{f}_c : \mathbf{R}^{nU} \to \mathbf{R}^C$ be a known

function defining C constraints $\mathbf{f}_c(\mathbf{p}_\mathcal{U}) = \mathbf{0}$ that the tag positions must satisfy, and define the feasible set

$$\mathcal{C} \coloneqq \left\{ \mathbf{p} = \mathrm{col}(\mathbf{p}_\mathcal{U}, \mathbf{p}_\mathcal{K}) \in \mathbb{R}^{nN} \middle| \mathbf{f}_c(\mathbf{p}_\mathcal{U}) = \mathbf{0} \right\}. \tag{5.28}$$

To use the CRLB as localizability potential, the bound should now reflect the fact that localization algorithms can leverage the information provided by the constraints to improve their performance. We use the following result generalizing Proposition 5.1.

Proposition 5.5. *Assume that the tag positions are subject to the constraints* (5.28)*. Let* $\mathbf{A}_\mathcal{U}(\mathbf{p}_\mathcal{U})$ *be a matrix whose columns span* $\ker \partial \mathbf{f}_c / \partial \mathbf{p}_\mathcal{U}$ *(which depends on* $\mathbf{p}_\mathcal{U}$ *in general). Let* $\hat{\mathbf{p}}_\mathcal{U}$ *be an unbiased estimate of the tag positions* $\mathbf{p}_\mathcal{U}$*, based on the measurements* $\tilde{\mathbf{d}}$*, the knowledge of the anchor positions* $\mathbf{p}_\mathcal{K}$*, and the knowledge of the constraints* (5.28)*. Then*

$$\mathsf{cov}[\hat{\mathbf{p}}_\mathcal{U}] \succeq \mathbf{B}_\mathcal{U}(\mathbf{p}), \tag{5.29}$$

where

$$\mathbf{B}_\mathcal{U}(\mathbf{p}) := \mathbf{A}_\mathcal{U} [\mathbf{A}_\mathcal{U}^\top \mathbf{F}_\mathcal{U} \mathbf{A}_\mathcal{U}]^\dagger \mathbf{A}_\mathcal{U}^\top. \tag{5.30}$$

Proof. We have both the trivial constraint $\mathbf{f}_t(\mathbf{p}_\mathcal{U}) = \mathbf{p}_\mathcal{K} - \mathbf{p}_\mathcal{K}^* = \mathbf{0}$ with $\mathbf{p}_\mathcal{K}^*$ the known positions of the anchors, and the equality constraint $\mathbf{f}_c(\mathbf{p}_\mathcal{U}) = \mathbf{0}$. Define $\mathbf{h}(\mathbf{p}) = \mathrm{col}(\mathbf{f}_c(\mathbf{p}_\mathcal{U}), \mathbf{f}_t(\mathbf{p}_\mathcal{K}))$. We then have :

$$\frac{\partial \mathbf{h}}{\partial \mathbf{p}} = \begin{bmatrix} \frac{\partial \mathbf{f}_c}{\partial \mathbf{p}_\mathcal{U}} & \mathbf{0} \\ \mathbf{0} & \mathbf{I}_{nK} \end{bmatrix}.$$

We apply the result of Theorem 5.1, with the matrix $\mathbf{A}$ in (5.6)

$$\mathbf{A} = \begin{bmatrix} \mathbf{A}_\mathcal{U} \\ \mathbf{0} \end{bmatrix} \text{ so } \mathbf{F}_c = \mathbf{A}_\mathcal{U}^\top \mathbf{F}_\mathcal{U} \mathbf{A}_\mathcal{U},\ \mathbf{B}_c = \begin{bmatrix} \mathbf{A}_\mathcal{U} \mathbf{F}_c^\dagger \mathbf{A}_\mathcal{U}^\top & \mathbf{0} \\ \mathbf{0} & \mathbf{0} \end{bmatrix}.$$

In (5.6), the $nU \times nU$ top-left corner of the matrix inequality gives (5.29) for the covariance of $\hat{\mathbf{p}}_\mathcal{U}$. The other parts of the bound (5.6) are trivial ($\mathbf{0} \succeq \mathbf{0}$) and correspond to the fact that a reasonable estimate $\hat{\mathbf{p}} = \mathrm{col}(\hat{\mathbf{p}}_\mathcal{U}, \hat{\mathbf{p}}_\mathcal{K})$ should set $\hat{\mathbf{p}}_\mathcal{K} = \mathbf{p}_\mathcal{K}$, so that $\hat{\mathbf{p}}_\mathcal{K}$ will have zero covariance. □

Note that to simplify the notation, we have omitted in (5.30) to state the dependencies $\mathbf{A}_\mathcal{U}(\mathbf{p}_\mathcal{U})$ and $\mathbf{F}_\mathcal{U}(\mathbf{p})$. From the matrix-valued bound (5.30), we can define constrained localizability potentials as in Section 5.3.2. Here, for conciseness, we only consider the A-Opt potential

$$J_c(\mathbf{p}) := \mathrm{Tr}\left\{ \mathbf{B}_\mathcal{U}(\mathbf{p}) \right\}. \tag{5.31}$$

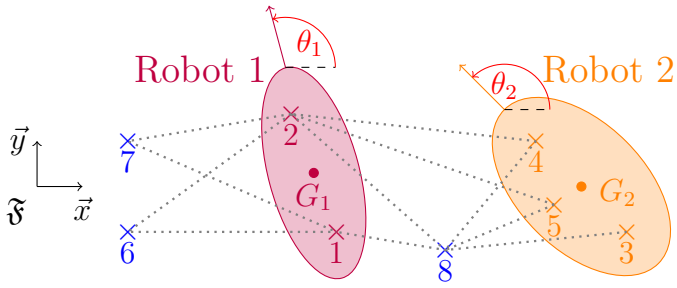

Figure 5.2 – Setup for two robots, seen as rigid bodies, carrying multiple tags

Moreover, the desired tag positions should also respect the constraints specified by (5.28). In other words, we aim to adjust the positions of the mobile nodes (anchors or tags) in order to minimize, at least locally, the overall potential J, which includes the localizability potential J_c in (5.31), subject to the constraints (5.28). For this, we can replace the gradient-descent method (5.3) by the following first-order primal-dual method [Bertsekas, 2016, p. 528]:

$$\begin{cases} \mathbf{p}_{k+1} = \mathbf{p}_k - \eta_k \left(\frac{\partial J(\mathbf{p}_k)}{\partial \mathbf{p}} + \boldsymbol{\lambda}_k^\top \frac{\partial \mathbf{f}_c(\mathbf{p}_{\mathcal{U},k})}{\partial \mathbf{p}} \right)^\top, \\ \boldsymbol{\lambda}_{k+1} = \boldsymbol{\lambda}_k + \delta\, \mathbf{f}_c(\mathbf{p}_{\mathcal{U},k}), \end{cases} \tag{5.32}$$

where $\eta_k \in \mathbb{R}$ is a sequence of stepsizes, δ a fixed parameter and $\boldsymbol{\lambda}_k$ are dual variable iterates. The scheme (5.32) provides a sequence of configurations $\mathbf{p}_k$, $k \geq 0$. Feasibility of the constraints (5.28) is not maintained during the iterations (5.32), but the algorithm contributes to keeping $\mathbf{p}_{k+1}$ close to $\mathcal{C}$. In addition, for each iterate $\mathbf{p}_k$ that we actually want to use as waypoint for motion planning (some iterates could be skipped), since (5.28) represents rigidity constraints, we can enforce feasibility by computing for each robot the pose minimizing the distance between the desired and achievable tag locations, in a least-squares sense (this corresponds to a standard pose estimation problem [Barfoot, 2017, Section 8.1]).

A *local* convergence result for the iterations (5.32) to a local constrained minimum $\mathbf{p}^*$ and Lagrange multiplier $\boldsymbol{\lambda}^*$ is stated in [Bertsekas, 2016, Proposition 5.4.2], for constant stepsizes $\eta_k = \delta$, $k \geq 0$, and δ sufficiently small. Note that this method is not guaranteed to converge starting from any initial configuration $\mathbf{p}_0$. Hence, it may need to be combined with or replaced by other optimization methods with global convergence guarantees, such as multiplier methods, as discussed in [Bertsekas, 2016, Section 5.2]. We refer the reader to the literature on nonlinear programming for further discussion and comparison of available iterative methods, and focus instead in the rest of this section on the computation of the derivatives $\partial J_c/\partial \mathbf{p}$ and $\partial \mathbf{f}_c/\partial \mathbf{p}$ appearing in (5.32), which are required for the implementation of all such methods. We specialize the discussion above to the deployment problem where some some

robots carry multiple tags, which requires evaluating the cost function (5.31) and its gradient. First, we only take into account in the CRLB the constraints on the distances between the intra-robot tags, since this leads to somewhat simpler expressions and computations. In Section 5.6.3, we include in the CRLB the full information about the relative positions of these tags.

5.6.2 CRLB with Distance Constraints

Considering Fig. 5.2, as robots carrying multiple tags move, their tags' relative positions must satisfy rigid displacement constraints. We partition the set of tags $\mathcal{U}$ into R groups $\mathcal{U}_1, \ldots \mathcal{U}_R$, with $\sum_{r=1}^{R} |\mathcal{U}_r| = U$, such that the tags in group $\mathcal{U}_r$ are rigidly connected (mounted on the same robot). To simplify the discussion in the following, we assume that each group has $|\mathcal{U}_r| \geq n$ tags in dimension n and that these tags are in general position (no 3 tags aligned, and no 4 tags coplanar in dimension 3). As a result, each group of tags forms an infinitesimally rigid framework for the complete graph (note that all pairwise distances within a group $\mathcal{U}_r$ are known). For example, we can simply have 2 tags on each robot if $n = 2$, or 3 non-aligned tags if $n = 3$. We also ignore the possibility of having known rigid constraints between anchors and tags. The analysis can be extended to mixed networks of robots carrying a single or multiple tags, or both anchors and tags, in a straightforward manner.

Since we know the relative positions of the tags in $\mathcal{U}_r$ in the robot's frame of reference (by carefully placing them on the robot), this information should in principle be included in the CRLB. First, however, we only include the information about relative *distances* between tags in each group, as this leads to simpler algorithms. In this case, in the framework of Section 5.6.1, $\mathbf{f}_c$ has one component for each pair of tags $\{i, j\}$ in the same group $\mathcal{U}_r$, of the form

$$\mathbf{f}_c^{\{i,j\}}(\mathbf{p}_\mathcal{U}) = ||\mathbf{p}_{ij}||^2 - d_{ij}^2,$$

where d_{ij} is perfectly known. If we order these components by listing all pairs of tags in the same set $\mathcal{U}_1$, $\mathcal{U}_2$, $\ldots$, $\mathcal{U}_R$, then we obtain for the Jacobian matrix

$$\frac{\partial \mathbf{f}_c(\mathbf{p}_\mathcal{U})}{\partial \mathbf{p}_\mathcal{U}} = \mathrm{diag}(\mathbf{R}_1, \ldots, \mathbf{R}_R), \tag{5.33}$$

where $\mathbf{R}_r$ is the rigidity matrix defined in Section 5.4.1, for the framework formed by a complete graph among the tags in group $\mathcal{U}_r$. Because the framework within each group is infinitesimally rigid, the kernel of each matrix $\mathbf{R}_r$ is spanned by three explicitly known vectors if $n = 2$, or six if $n = 3$, as described in Proposition 5.2. Then we can compute the matrix

$\mathbf{A}_\mathcal{U} = \begin{bmatrix}\mathbf{A}_1 & \dots & \mathbf{A}_R\end{bmatrix}$ with nU rows and $3R$ (if $n=2$) or $6R$ (if $n=3$) columns spanning the kernel of (5.33). For example, based on the discussion above Proposition 5.2, if $n=2$ we can take $\mathbf{A}_r = \begin{bmatrix}\mathbf{v}^r_{T_x} & \mathbf{v}^r_{T_y} & \mathbf{v}^r_{R_z}\end{bmatrix}$, with $[\mathbf{v}^r_{T_x}]_{2i-1} = 1$, $[\mathbf{v}^r_{T_y}]_{2i} = 1$, $[\mathbf{v}^r_{R_z}]_{2i-1} = -y_i$ and $[\mathbf{v}^r_{R_z}]_{2i} = x_i$ for all $i \in \mathcal{U}_r$ and zeros everywhere else. From these explicit expressions of $\mathbf{A}_\mathcal{U}$, we can also immediately compute the derivatives $\partial\mathbf{A}_\mathcal{U}/\partial\xi_i$, for $\xi_i \in \{x_i, y_i, z_i\}$.

Since determining $\mathbf{A}_\mathcal{U}(\mathbf{p}_\mathcal{U})$ allows us to compute $J_c(\mathbf{p}_\mathcal{U})$ using (5.30), the only missing element to execute the iterations (5.32) is the gradient of J_c. For simplicity, suppose that $\mathbf{F}_c \coloneqq \mathbf{A}_\mathcal{U}^\top \mathbf{F}_\mathcal{U} \mathbf{A}_\mathcal{U}$ is invertible. Since $\mathbf{A}_\mathcal{U}$ can be taken to be full column rank, this can be ensured by fulfilling the assumptions of Theorem 5.2, guaranteeing that $\mathbf{F}_\mathcal{U}$ is invertible. Then, we have

$$\begin{aligned}\frac{\partial J_c}{\partial \xi_i} &= \frac{\partial}{\partial \xi_i}\mathrm{Tr}\left\{\mathbf{A}_\mathcal{U}{\mathbf{F}_c}^{-1}\mathbf{A}_\mathcal{U}^\top\right\} \\ &= 2\mathrm{Tr}\left\{\mathbf{F}_c^{-1}\mathbf{A}_\mathcal{U}^\top\frac{\partial \mathbf{A}_\mathcal{U}}{\partial \xi_i}\right\} - \mathrm{Tr}\left\{\mathbf{A}_\mathcal{U}\mathbf{F}_c^{-1}\frac{\partial \mathbf{F}_c}{\partial \xi_i}{\mathbf{F}_c}^{-1}{\mathbf{A}_\mathcal{U}}^\top\right\} \\ &= 2\mathrm{Tr}\left\{\mathbf{F}_c^{-1}\mathbf{A}_\mathcal{U}^\top(\mathbf{I} - \mathbf{B}_\mathcal{U}\mathbf{F}_\mathcal{U})\frac{\partial \mathbf{A}_\mathcal{U}}{\partial \xi_i}\right\} - \mathrm{Tr}\left\{\mathbf{B}_\mathcal{U}^2\frac{\partial \mathbf{F}_\mathcal{U}}{\partial \xi_i}\right\}.\end{aligned} \tag{5.34}$$

5.6.3 CRLB with Constrained Relative Positions

When we place two tags i and j on a robot r, we can in fact know the relative positions (RP) $\mathbf{p}^r_{ij}$ of these tags in the frame of robot r, not just their distance. Since a position estimator can leverage this information to improve its accuracy, we derive in this section the corresponding CRLB. To simplify the presentation, we assume here that each robot carries at least two tags.

To obtain the CRLB, let us first introduce R new parameters $\boldsymbol{\theta} \coloneqq \mathrm{col}(\boldsymbol{\theta}_1, \dots, \boldsymbol{\theta}_R)$, one for each robot, where $\boldsymbol{\theta}_i \in \mathbb{R}^q$, with $q=1$ if $n=2$ and $q=3$ if $n=3$. Then, for the extended set of parameters $\tilde{\mathbf{p}}_\mathcal{U} = (\mathbf{p}_\mathcal{U}, \boldsymbol{\theta})$ and the measurements (5.1) or (5.2), we denote the extended FIM

$$\tilde{\mathbf{F}}_\mathcal{U} = -\mathbb{E}\{\frac{\partial^2 \ln f(\tilde{\mathbf{d}}; \tilde{\mathbf{p}}_\mathcal{U})}{\partial \tilde{\mathbf{p}}_\mathcal{U} \partial \tilde{\mathbf{p}}_\mathcal{U}^\top}\} = \begin{bmatrix}\mathbf{F}_\mathcal{U} & \mathbf{0}_{nU,qR} \\ \mathbf{0}_{qR,nU} & \mathbf{0}_{qR,qR}\end{bmatrix}. \tag{5.35}$$

In the following, we add constraints between the tag positions and the parameters $\boldsymbol{\theta}$, in such a way that the latter represent the robot orientations in exponential coordinates. Then, we compute the constrained FIM from $\tilde{\mathbf{F}}_\mathcal{U}$ using Theorem 5.1 to obtain the final CRLB on position estimates.

It is convenient to number and order the tags as follows. Consider robot $r \in \{1, \dots, R\}$ and associated tags $\mathcal{U}_r$, using the notation of Section 5.6.2. Pick one tag in $\mathcal{U}_r$, denoted in the

following 1^r. The other tags of $\mathcal{U}_r$ are denoted $2^r, \ldots, U_r^r$, with $U_r = |\mathcal{U}_r|$. We group these latter tags by robot and list them in the order

$$\mathbf{p}_o \coloneqq \mathrm{col}(\mathbf{p}_{2^1}, \ldots \mathbf{p}_{U_1^1}, \ldots, \mathbf{p}_{2^R}, \ldots \mathbf{p}_{U_R^R}) \in \mathbb{R}^{n(U-R)}, \tag{5.36}$$

from robot 1 to robot R. The positions of the R tags 1^r are also grouped in the vector

$$\mathbf{p}_c \coloneqq \mathrm{col}(\mathbf{p}_{1^1}, \ldots, \mathbf{p}_{1^R}) \in \mathbb{R}^{nR}.$$

Then, we have $\tilde{\mathbf{p}}_{\mathcal{U}} = \mathrm{col}(\mathbf{p}_o, \mathbf{p}_c, \boldsymbol{\theta})$.

Next, for each tag $j^r \in \mathcal{U}_r$ other than 1^r, we add the constraint $\mathbf{f}^{(r,j^r)}(\mathbf{p}_{1^r}, \mathbf{p}_{j^r}, \boldsymbol{\theta}_r) = \mathbf{0} \in \mathbb{R}^n$, where

$$\mathbf{f}^{(r,j^r)}(\mathbf{p}_{1^r}, \mathbf{p}_{j^r}, \boldsymbol{\theta}_r) = \mathbf{p}_{j^r} - \mathbf{p}_{1^r} - \exp([\boldsymbol{\theta}_r]_\times)\mathbf{p}^r_{j^r 1^r}, \tag{5.37}$$

with the notation (depending if $n = 2$ or $n = 3$)

$$[\theta]_\times = \begin{bmatrix} 0 & -\theta \\ \theta & 0 \end{bmatrix}, \text{ if } \theta \in \mathbb{R},$$
$$[\boldsymbol{\theta}]_\times = \begin{bmatrix} 0 & -\theta_z & \theta_y \\ \theta_z & 0 & -\theta_x \\ -\theta_y & \theta_x & 0 \end{bmatrix}, \text{ if } \boldsymbol{\theta} = [\theta_x, \theta_y, \theta_z]^\top \in \mathbb{R}^3.$$

There are $U_r - 1$ constraints of the form (5.37) for robot r, each of dimension n, which represent a change from the known coordinates $\mathbf{p}^r_{j^r 1^r}$ in the robot frame to the (unknown) coordinates $\mathbf{p}_{j^r 1^r}$ in the world frame $\mathfrak{F}$, with the matrix $\exp([\boldsymbol{\theta}_r]_\times)$ representing the rotation matrix from $\mathfrak{F}$ to the frame of robot r, using the exponential coordinate representation [Lynch and Park, 2017]. Define in the following the notation $\exp([\boldsymbol{\theta}_r]_\times) \coloneqq \mathbf{R}_{\boldsymbol{\theta}_r}$ and

$$\boldsymbol{\Phi}^{(r,j^r)}_{\boldsymbol{\theta}_r} \coloneqq \mathbf{R}_{\boldsymbol{\theta}_r}\, \mathbf{p}^r_{j^r 1^r}, \quad \text{for } j^r \in \mathcal{U}_r, 1 \le r \le R.$$

Remark 5.9. *Recall that when $n = 2$, we have simply*

$$\exp([\theta]_\times) = \begin{bmatrix} \cos(\theta) & -\sin(\theta) \\ \sin(\theta) & \cos(\theta) \end{bmatrix},$$

and when $n = 3$, $\exp([\boldsymbol{\theta}]_\times)$ can be computed efficiently using Rodrigues' formula [Lynch and Park, 2017, Proposition 3.1].

Considering (5.37) for all R robots, we obtain $U - R$ constraints on the parameters $\tilde{\mathbf{p}}_{\mathcal{U}}$, each

of dimension n. We list these constraints in the same order as for $\mathbf{p}_o$ in (5.36) and denote them $\mathbf{f}_{\mathrm{RP}}(\mathbf{p}_o, \mathbf{p}_c, \boldsymbol{\theta}) = \mathbf{0}$. For the constrained CRLB, we are interested in the kernel of the Jacobian matrix of $\mathbf{f}_{\mathrm{RP}}$. Remark that with the chosen ordering of tags and constraints, we have $\frac{\partial \mathbf{f}_{\mathrm{RP}}}{\partial \mathbf{p}_o} = \mathbf{I}_{n(U-R)}$. If we define

$$\mathbf{N} \coloneqq \begin{bmatrix} \frac{\partial \mathbf{f}_{\mathrm{RP}}}{\partial \mathbf{p}_c} & \frac{\partial \mathbf{f}_{\mathrm{RP}}}{\partial \boldsymbol{\theta}} \end{bmatrix}, \tag{5.38}$$

and $\mathbf{A}_{\mathrm{RP}} \coloneqq \operatorname{span}\left\{\ker \frac{\partial \mathbf{f}_{\mathrm{RP}}}{\partial \tilde{\mathbf{p}}_{\mathcal{U}}}\right\}$, then immediately

$$\begin{aligned} \mathbf{A}_{\mathrm{RP}} &= \operatorname{span}\left\{\ker \begin{bmatrix} \mathbf{I}_{n(U-R)} & \mathbf{N} \end{bmatrix}\right\} \\ &= \operatorname{col}\left(-\mathbf{N}, \mathbf{I}_{(n+q)R}\right). \end{aligned} \tag{5.39}$$

Indeed, $\frac{\partial \mathbf{f}_{\mathrm{RP}}}{\partial \tilde{\mathbf{p}}_{\mathcal{U}}}$ is of rank $n(U-R)$, so $\mathbf{A}_{RP}$ should have $nU + qR - n(U-R) = (n+q)R$ independent columns, and clearly

$$\frac{\partial \mathbf{f}_{\mathrm{RP}}}{\partial \tilde{\mathbf{p}}_{\mathcal{U}}} \mathbf{A}_{\mathrm{RP}} = -\mathbf{N} + \mathbf{N} = \mathbf{0}.$$

Hence, it is sufficient to compute $\mathbf{N}$ to obtain $\mathbf{A}_{\mathrm{RP}}$.

Proposition 5.6. *The matrix* $\mathbf{N}$ *in* (5.38) *is defined by*

$$\mathbf{N} = \operatorname{col}\left(\{\mathbf{N}^{(r,j^r)}\}_{1 \le r \le R, 2^r \le j^r \le U_r^r}\right) \in \mathbb{R}^{n(U-R)\times(n+q)R}.$$

where the blocks $\mathbf{N}^{(r,j^r)} \in \mathbb{R}^{n\times(n+q)R}$ *are stacked in the same order as* $\mathbf{p}_o$ *in* (5.36) *and are of the form*

$$\mathbf{N}^{(r,j^r)} = -\begin{bmatrix} \mathbf{0}_{n,n(r-1)} & \mathbf{I}_n & \mathbf{0}_{n,s} & \mathbf{N}_{\boldsymbol{\theta}_r}^{(r,j^r)} & \mathbf{0}_{n,(R-r)q} \end{bmatrix}$$

with $s = (R-r)n + (r-1)q$, *where*

$$\mathbf{N}_{\boldsymbol{\theta}_r}^{(r,j^r)} = \begin{cases} [1]_\times \boldsymbol{\Phi}_{\boldsymbol{\theta}_r}^{(r,j^r)} \in \mathbb{R}^2 \text{ if } n = 2, \\ \left[\boldsymbol{\Phi}_{\boldsymbol{\theta}_r}^{(r,j^r)}\right]_\times \boldsymbol{\Omega}_{\boldsymbol{\theta}_r} \in \mathbb{R}^{3\times 3} \text{ if } n = 3, \end{cases} \tag{5.40}$$

with $\boldsymbol{\Omega}_{\boldsymbol{\theta}_r} \coloneqq (\boldsymbol{\theta}_r \boldsymbol{\theta}_r^\top + (\mathbf{I}_3 - \mathbf{R}_{\boldsymbol{\theta}_r})[\boldsymbol{\theta}_r]_\times)\|\boldsymbol{\theta}_r\|^{-2}$.

Proof. Decompose $\mathbf{N}^{(r,j^r)}$ by blocks

$$\mathbf{N}^{(r,j^r)} = \begin{bmatrix} \mathbf{G}_1 & \dots \mathbf{G}_R & \mathbf{H}_1 & \dots & \mathbf{H}_R \end{bmatrix}$$

with $\mathbf{G}_i \in \mathbb{R}^{n\times n}$ and $\mathbf{H}_i \in \mathbb{R}^{n\times q}$. The matrix $\mathbf{N}^{(r,j^r)}$ is obtained by taking the partial

derivatives of $\mathbf{f}^{(r,j^r)}$ in (5.37) with respect to the coordinates of $\mathbf{p}_{1^r}$, which gives the block $\mathbf{G}_r = -\mathbf{I}_n$, and with respect to the coordinates of $\boldsymbol{\theta}_r$, which gives the block $\mathbf{H}_r = -\mathbf{N}_{\boldsymbol{\theta}_r}^{(r,j^r)} \in \mathbb{R}^{n\times q}$. All other blocks are zero. The expression of $\mathbf{H}_r$ comes from the fact that $[\boldsymbol{\theta}_r]_\times = \theta_r\,[1]_\times$ when $n = 2$, whereas when $n = 3$, we have

$$\frac{\partial \boldsymbol{\Phi}_{\boldsymbol{\theta}_r}^{(r,j^r)}}{\partial \boldsymbol{\theta}_r} = -\mathbf{R}_{\boldsymbol{\theta}_r}[\mathbf{p}_{j^r 1^r}^r]_\times \frac{\boldsymbol{\theta}_r\boldsymbol{\theta}_r^\top + (\mathbf{R}_{\boldsymbol{\theta}_r}^\top - \mathbf{I}_3)[\boldsymbol{\theta}_r]_\times}{\|\boldsymbol{\theta}_r\|^2}$$

from [Gallego and Yezzi, 2015, Result 1]. This expression is further reduced to the one in (5.40) using elementary properties of rotation matrices. □

With the matrices $\tilde{\mathbf{F}}_\mathcal{U}$ and $\mathbf{A}_{\mathrm{RP}}$ defined in (5.35) and (5.39), we can follow the discussion of Section 5.6.1 and define $\mathbf{B}_{\mathrm{RP}} := \mathbf{A}_{\mathrm{RP}}[\mathbf{A}_{\mathrm{RP}}^\top \tilde{\mathbf{F}}_\mathcal{U} \mathbf{A}_{\mathrm{RP}}]^\dagger \mathbf{A}_{\mathrm{RP}}^\top$ to obtain a CRLB taking the RP constraints into account. We can build a cost function providing a lower bound on MSE of the tag positions as

$$J_c(\mathbf{p}) = \mathrm{Tr}\left\{\mathbf{C}\mathbf{B}_{\mathrm{RP}}\mathbf{C}^\top\right\}, \tag{5.41}$$

similarly to (5.31), where $\mathbf{C} = [\mathbf{I}_{nU}\ \mathbf{0}_{nU,qR}]$ is introduced here to select the $nU \times nU$ first block of $\mathbf{B}_{\mathrm{RP}}$ and hence consider only the uncertainty in the estimate $\hat{\mathbf{p}}_\mathcal{U}$. Alternatively, the uncertainty in the estimate of the whole extended state $\tilde{\mathbf{p}}_\mathcal{U}$ can be considered by using the matrix $\mathbf{C} = \mathrm{diag}(\mathbf{I}_{nU}, w_\theta \mathbf{I}_{qR})$, with w_θ a weight to select. To compute the gradient with respect to $\mathbf{p}$ for (5.32), similarly to (5.34), we have, for $\xi \in \{x, y, z\}$:

$$\frac{\partial J_c}{\partial \xi_i} = 2\mathrm{Tr}\left\{\mathbf{C}\frac{\partial \mathbf{A}_{\mathrm{RP}}}{\partial \xi_i}\mathbf{D}^\top\right\} - \mathrm{Tr}\left\{\mathbf{D}\frac{\partial \mathbf{F}_c}{\partial \xi_i}\mathbf{D}^\top\right\}, \tag{5.42}$$

with $\mathbf{D} := \mathbf{C}\mathbf{A}_{\mathrm{RP}}\mathbf{F}_c^{-1}$, assuming $\mathbf{F}_c = \mathbf{A}_{\mathrm{RP}}^\top \tilde{\mathbf{F}}_\mathcal{U} \mathbf{A}_{\mathrm{RP}}$ to be invertible. To compute the derivative $\partial \mathbf{A}_{\mathrm{RP}}/\partial \xi_i$, it is sufficient to know how to compute the terms $\partial \mathbf{N}_{\boldsymbol{\theta}_r}^{(r,j^r)}/\partial \xi_i$. Then, noting that $\boldsymbol{\Phi}_{\boldsymbol{\theta}_r}^{(r,j^r)} = \mathbf{p}_{j^r} - \mathbf{p}_{1^r}$, the differentiation of (5.40) yields

$$\frac{\partial \mathbf{N}_{\boldsymbol{\theta}_r}^{(r,j^r)}}{\partial \xi_i} = \begin{cases} [1]_\times\, \mathbf{e}_\xi\, \psi_{j^r}(i) \text{ if } n = 2; \\ [\mathbf{e}_\xi]_\times\, \boldsymbol{\Omega}_{\boldsymbol{\theta}_r}\, \psi_{j^r}(i) \text{ if } n = 3, \end{cases}$$

for $\xi \in \{x, y, z\}$, where $\mathbf{e}_x, \mathbf{e}_y, \mathbf{e}_z$ forms the canonical basis of $\mathbb{R}^3$, and we introduced the notation $\psi_{j^r}(i)$ equals to 1 if $i = j^r$, to -1 if $i = 1^r$ and to zero otherwise.

5.7 Simulations

In this section, we present simulation results for two deployment scenarios. The first scenario is a structure inspection problem by a multi-robot network maintaining localizability while the task is performed. The second concerns the deployment of an Unmanned Ground Vehicle (UGV) carrying several tags, where we include the distance and relative position constraints in the CRLB-based potential.

5.7.1 Cooperative Structure Inspection

Consider a system composed of $N = 16$ agents, with $U = 12$ tags carried by mobile robots (*i.e.*, $\mathcal{U} = \{1, \dots, 12\}$) and $K = 4$ fixed anchors with known positions (*i.e.*, $\mathcal{K} = \{13, \dots, 16\}$). Each robot carries an UWB transceiver to communicate and take ranging measurements with any other robot or UWB anchor, following the model (5.1), via a Two Way Ranging (TWR) protocol [Mai et al., 2018, Prorok, 2013].

We assign an inspection task to the two first robot-tags 1 and 2, called "leaders", while the remaining robot-tags $\mathcal{U}_F = \{i \in \mathcal{U}, i > 2\}$ are called "followers" and deploy to support accurate localization. The leaders are required to visit ten waypoints each, underneath a 50 m $\times$ 10 m rectangular structure represented in blue in Fig. 5.3, in order to inspect it. The links in the ranging/communication network are represented on Fig. 5.3 by the sparsity pattern of the network adjacency matrix, i.e., showing its non-zero entries. In particular, we stress that the leaders cannot communicate directly with the anchors.

Motion Planner for the Follower Robots

We follow the motion planning framework based on artificial potentials presented in Section 5.2. To enhance the localizability of the robots, we chose to include in the overall potential the cost $J_D(\mathbf{p}) = -\log\det \mathbf{F}_{\mathcal{U}}$ introduced in Section 5.3. This choice is motivated in particular by the fact that in a decentralized system, computing the gradient of J_D via Algorithm 5.1 requires a single distributed matrix inversion. We add safety margins between robots by introducing a collision avoidance potential

$$J_{\text{avd}}(\mathbf{p}) = \frac{1}{2}\sum_{i\in\mathcal{U}}\sum_{j\in\mathcal{U}\cup\mathcal{K}} \left(d_{ij}^{-1} - {d_a}^{-1}\right)^2 \mathbf{1}_{d_{ij}<d_a}.$$

We also encourage ranging tags to maintain proximity, in order to limit the potential deterioration of ranging measurements at long distances, e.g., due to power fading. To do so, we

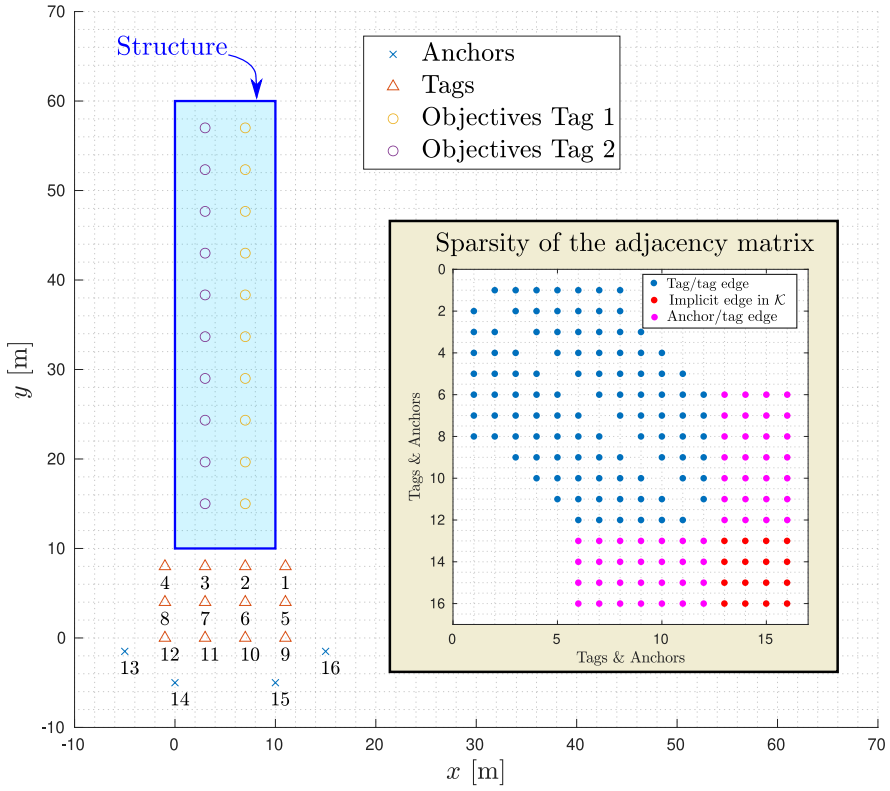

Figure 5.3 – Initial system configuration, waypoints for the leaders 1 et 2 and ranging network sparsity

use the potential

$$J_{\text{con}}(\mathbf{p}) = \frac{1}{2}\sum_{i\in\mathcal{U}}\sum_{j\in\mathcal{N}_i}(d_{ij}-d_c)^2\,\mathbf{1}_{d_{ij}>d_c}.$$

In our simulations, we set $d_a = 2$ m and $d_c = 50$ m.

Therefore, the overall potential is defined as $J(\mathbf{p}) := K_l J_D(\mathbf{p}) + K_c J_{con}(\mathbf{p}) + K_a J_{\text{avd}}(\mathbf{p})$ where $K_l, K_a, K_c > 0$ are constant parameters. The leaders travel directly to their prespecified waypoints. Meanwhile, each follower $i \in \mathcal{U}_F$ implements the following gradient descent scheme

$$\mathbf{p}^d_{i,k+1} = \hat{\mathbf{p}}_{i,k} - \frac{\partial J(\hat{\mathbf{p}}_{\mathcal{U},k})}{\partial \mathbf{p}_{i,k}} \times \min\left\{1, \frac{\Delta_{\text{vel}}}{\|\partial J/\partial \mathbf{p}_{i,k}\|}\right\}, \tag{5.43}$$

i.e., with robot i at its current position $\mathbf{p}_{i,k}$ at period $k \geq 0$, a gradient step provides the next desired position $\mathbf{p}^d_{i,k+1}$. The min term bounds the stepsizes so that $\|\mathbf{p}^d_{i,k+1} - \mathbf{p}_{i,k}\| \leq \Delta_{\text{vel}}$, for some specified value of Δ_{vel}. For $\xi_i \in \{x_i, y_i\}$, we compute $\partial J_D/\partial \xi_i$ by (5.17), possibly using Richardson iterations presented in Algorithm 5.1 for a decentralized implementation. The expressions of the derivatives $\partial J_{\text{con}}/\partial \xi_i$ and $\partial J_{\text{avd}}/\partial \xi_i$ of the other potentials are standard [Lynch and Park, 2017] and can be distributively computed since they only depend on

each tag's neighborhood. Note that in (5.43) we do not assume that the true positions are accessible but compute the gradients at the estimates $\hat{\mathbf{p}}_{i,k}$ (see (5.46)).

The gradient descent scheme is used to obtain desired waypoints for the tags, which we can track using controllers on the robots. For concreteness, assume that all robots are identical with unicycle kinematics [Corke, 2011, Chap. 4]

$$\dot{x}_M = v\cos(\theta), \quad \dot{y}_M = v\sin(\theta), \quad \dot{\theta} = \omega \tag{5.44}$$

where ω and v are the rotational and translational velocities and θ is the robot's heading with respect to $\mathfrak{F}$. The coordinates of the tag in the robot's frame (for any i) are $\mathbf{p}_i^r = [a, b]^\top$, with $a \neq 0$, see Fig. 5.4. With $\dot{\mathbf{p}}_i \in \mathbb{R}^2$ the velocity of tag i in $\mathfrak{F}$, implementing the following Proportional-Integral (PI) controller

$$\dot{\mathbf{p}}_i = K_P(\mathbf{p}_i^d(t) - \mathbf{p}_i(t)) + K_I \int_{\tau=0}^{\top} (\mathbf{p}_i^d(\tau) - \mathbf{p}_i(\tau))d\tau, \tag{5.45}$$

with $K_P, K_I > 0$, allows the tags to track the desired (piecewise constant) trajectory $\mathbf{p}^d$. This corresponds to a velocity command $\mathbf{u}_i := [v_i, \omega_i]^\top$ for robot i, since $\mathbf{u}_i = \mathbf{T}(\theta_i)\dot{\mathbf{p}}_i$ [Lynch and Park, 2017, Section 13.3.1.4] with

$$\mathbf{T}(\theta) = \frac{1}{a}\begin{bmatrix} a\cos\theta - b\sin\theta & a\sin\theta + b\cos\theta \\ -\sin\theta & \cos\theta \end{bmatrix}.$$

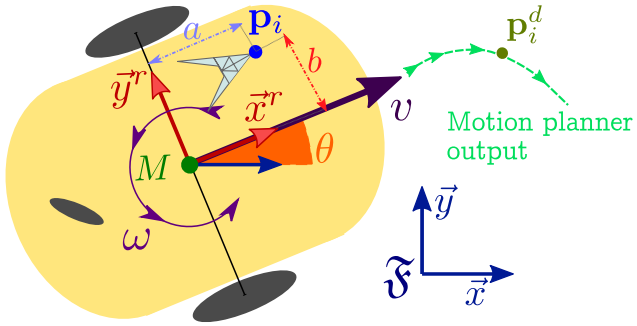

Figure 5.4 – Robot and tag configuration for trajectory tracking. $(M, \vec{x}^r, \vec{y}^r)$ is the robot frame

Simulation and Performance Analysis

We choose the weights in the potential J as $K_l = 5 \times 10^4$, $K_a = K_c = 1 \times 10^3$ and the maximal step length $\Delta_{vel} = 2$ m. When the leaders reach their o-th waypoint, we repeat the iterations (5.43) $N_{\text{iter}} = 30$ times to compute sufficiently distant waypoints for the followers. Then, we only transmit the desired position $\mathbf{p}^d_{i,oN_{\text{iter}}}$ to the controller of each follower $i \in \mathcal{U}_F$ in order to enhance the tags' localizability. The tags are positioned on the robots so that $a = b = 0.5$ m, and the PI controller gains are $K_p = 3$, $K_i = 0.5$. The controller (5.45) follows the trajectory computed from (5.43) with a maximum tracking error of about 10 cm.

To illustrate the performance of our deployment scheme we perform $M = 1000$ Monte Carlo simulations, using the measurement model (5.1) with $\sigma = 5$ cm. At simulation ρ, the position estimates $\hat{\mathbf{p}}^\rho_{\mathcal{U},k}$ used in (5.43) are obtained by solving the least-squares problem

$$\begin{aligned} \hat{\mathbf{p}}^\rho_{\mathcal{U},k} &= \underset{\mathbf{p}_\mathcal{U} \in \mathbb{R}^{2U}}{\operatorname{argmin}} \, Q(\mathbf{p}_\mathcal{U}), \\ \text{with } Q(\mathbf{p}_\mathcal{U}) &\coloneqq \sum_{i \in \mathcal{U}} \sum_{j \in \mathcal{N}_i} (\|\mathbf{p}_{i,k} - \mathbf{p}_{j,k}\| - \tilde{d}^\rho_{ij,k})^2, \end{aligned} \tag{5.46}$$

where $\mathbf{p}_{j,k}$ is the anchor position in (5.46) if $j \in \mathcal{K}$ and $\tilde{d}^\rho_{ij,k}$ are the range measurements.

As shown by the trajectories on Fig. 5.5, the leaders follow their assigned paths and the followers maintain the network's localizability. Initially, all robots are aligned, a geometry with poor localizability. On Fig. 5.6, we plot the empirical average $\bar{J}_D$ and 3σ confidence bounds (CBs) for the potential J_D over the M simulations. Initially, the localizability potential decreases as the followers deploy. The following step increases occur when the leaders move to their next waypoints and the network extends, while the anchors remain fixed and far away, see Fig. 5.5. Overall however, the followers manage to keep the localizability at a low value. For comparison, we plot in blue on Fig. 5.6 the evolution of the localizability potential without deployment of the followers. We also plot the empirical statistical entropy $\ln \det \tilde{\Sigma}_k$ and its CBs, with $\tilde{\Sigma}_k$ the empirical covariance of the estimates $\hat{\mathbf{p}}_{\mathcal{U},k}$ obtained by solving (5.46). The plot highlights that the entropy remains close to the theoretical lower bound provided by J_D, as discussed in Section 5.3.2.

Even though the deployment is performed here using J_D to measure localizability, which is related to entropy, Fig. 5.7 shows that other localization accuracy measures are improved as well. In this case, we plot the empirical Root Mean Squared Error (RMSE) for the location estimate of the first leader tag, the plot for the second leader being similar. Namely, at each iteration k of (5.43), we compute the empirical MSE $\widetilde{MSE}_{1,k} \coloneqq \frac{1}{M} \sum_{\rho=1}^{M} \|\hat{\mathbf{p}}^\rho_{1,k} - \mathbf{p}_{1,k}\|^2$, with $\hat{\mathbf{p}}^\rho_{1,k}$ the estimate of $\mathbf{p}_{1,k}$ for simulation ρ. Then $\widetilde{RMSE}_1 \coloneqq (\widetilde{MSE}_{1,k})^{1/2}$. The CBs shown

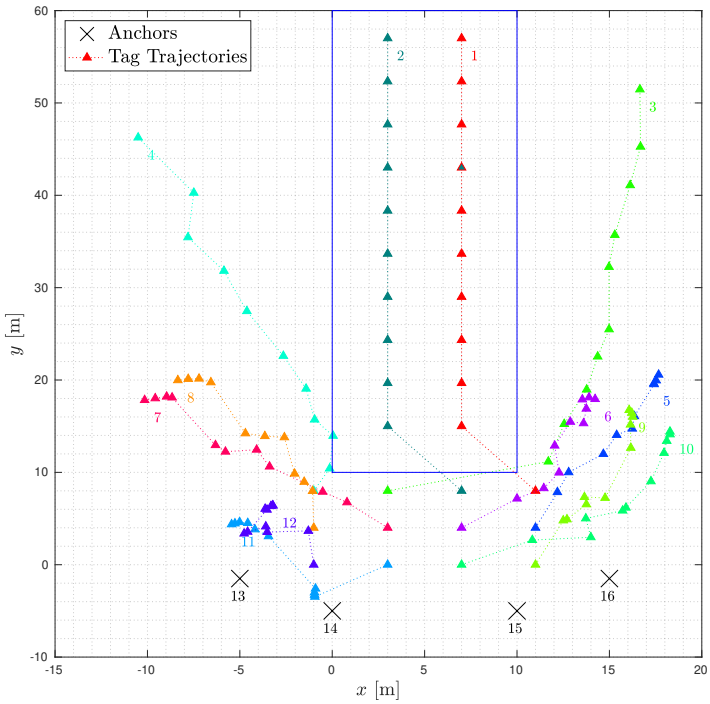

Figure 5.5 – Tag trajectories in the workspace

on Fig. 5.7 are defined by $b_{\pm,k} = s_{\pm,k}^{1/2}$, where $s_{\pm,k} = \widetilde{MSE}_{1,k} \pm 3\widetilde{\sigma}_{1,k}/\sqrt{M}$, with $\widetilde{\sigma}_{1,k}^2 = \frac{1}{M-1}\sum_{\rho=1}^{M}[\|\hat{\mathbf{p}}_{1,k}^{\rho} - \mathbf{p}_{1,k}\|^2 - \widetilde{MSE}_{1,k}]^2$ the empirical variance of the samples. For comparison, we also plot $\widetilde{RMSE}_1$ without deployment. The empirical RMSE is significantly reduced by the motion of the followers, remaining below 12 cm even when the leader 1 is at its farthest waypoint.

Distributed Gradient Computations

Here we illustrate the convergence of the distributed algorithms of Section 5.5 estimating the gradients of the localizability potentials, more specifically Algorithm 5.1 (D-Opt) and Algorithm 5.2 (E-Opt). Define the relative error ϵ_{S_l} on the gradients at the l-th iteration as follows

$$\epsilon_{S,l} = \frac{\|[\widehat{\partial J_S/\partial \mathbf{p}_{\mathcal{U}}}]_l - \partial J_S/\partial \mathbf{p}_{\mathcal{U}}\|_2}{\|\partial J_S/\partial \mathbf{p}_{\mathcal{U}}\|_2}$$

for each scheme $S \in \{D, E\}$ producing the estimates $[\widehat{\partial J_S/\partial \mathbf{p}_{\mathcal{U}}}]_l$. On Fig. 5.8 we plot the errors $\epsilon_{E,l}$ and $\epsilon_{D,l}$ for increasing values of l at the last (fixed) configuration $\mathbf{p}_{\mathcal{U}}$ of the trajectory shown on Fig. 5.5. For the D-Opt scheme, we arbitrarily choose the initial

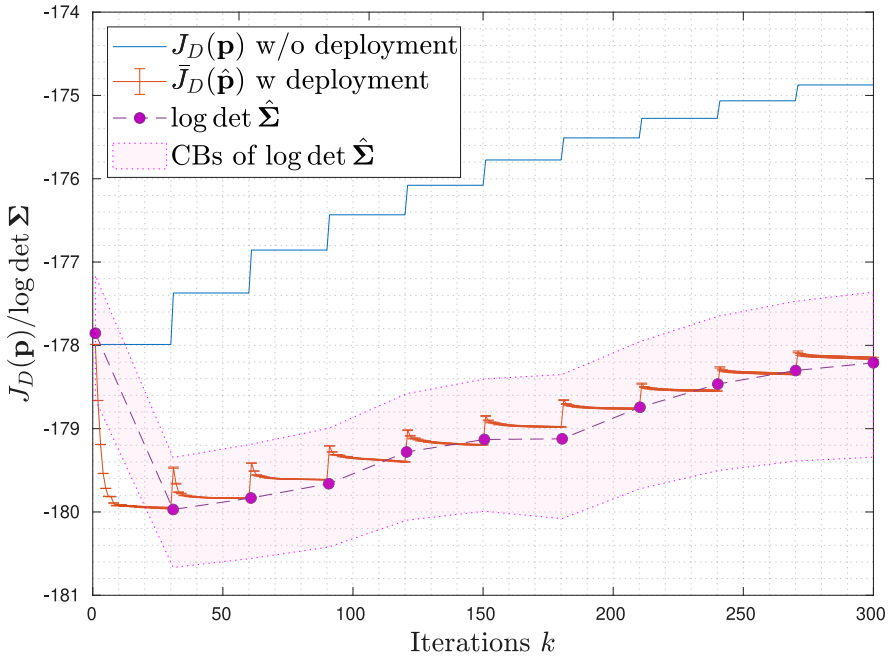

Figure 5.6 – Localizability potential with and without follower deployment, empirical entropy and 3σ confidence bounds obtained from the Monte-Carlo simulations. The leaders' waypoints are updated every $N_{\text{iter}} = 30$ iterations of the gradient descent scheme

condition $\mathbf{x}_0 = \mathbf{I}_{n\times u}$ in Algorithm 5.1, which is far from the ideal value $\mathbf{F}_{\mathcal{U}}^{-1}$. Nonetheless, an error of 10% on the gradient is obtained after about 120 iterations. To estimate the gradient of J_E, we arbitrarily set $\mathbf{w}(0) = \mathbf{1}_{nU}$ in Algorithm 5.2. In this case a relative error of 10% is obtained after 50 iterations, with the inner loop to compute the squared norm of the eigenvector set to $\tilde{n}_{\text{iter}} = 10$.

The convergence speed of both algorithm depends on the structure of $\mathbf{F}_{\mathcal{U}}$ and the chosen initial condition. In practice, for $k = 0$ we can initialize the decentralized gradient estimation schemes with arbitrary values and wait for a sufficient number of iterations, until some stopping condition of the form $\max_{i\in\mathcal{U}} \|[\widehat{\partial J_S/\partial \mathbf{p}_i}]_l - [\widehat{\partial J_S/\partial \mathbf{p}_i}]_{l-1}\| < \epsilon$ is reached, for some tolerance threshold $\epsilon > 0$. Then, for the next periods $k > 0$ of the trajectory, we can use for initialization the values obtained after convergence at the end of the previous period $k - 1$, which should lead to faster convergence.

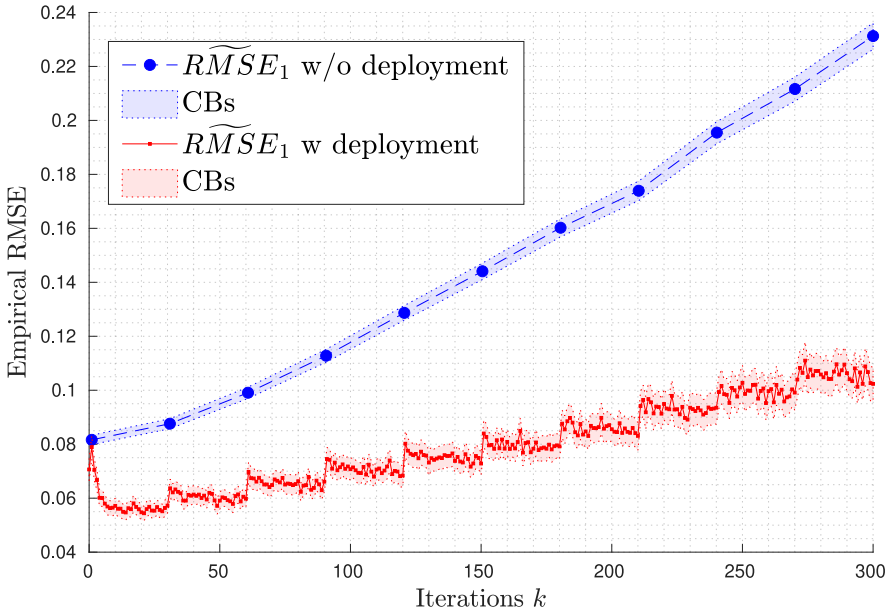

Figure 5.7 – Plot of the empirical RMSE over the trajectory

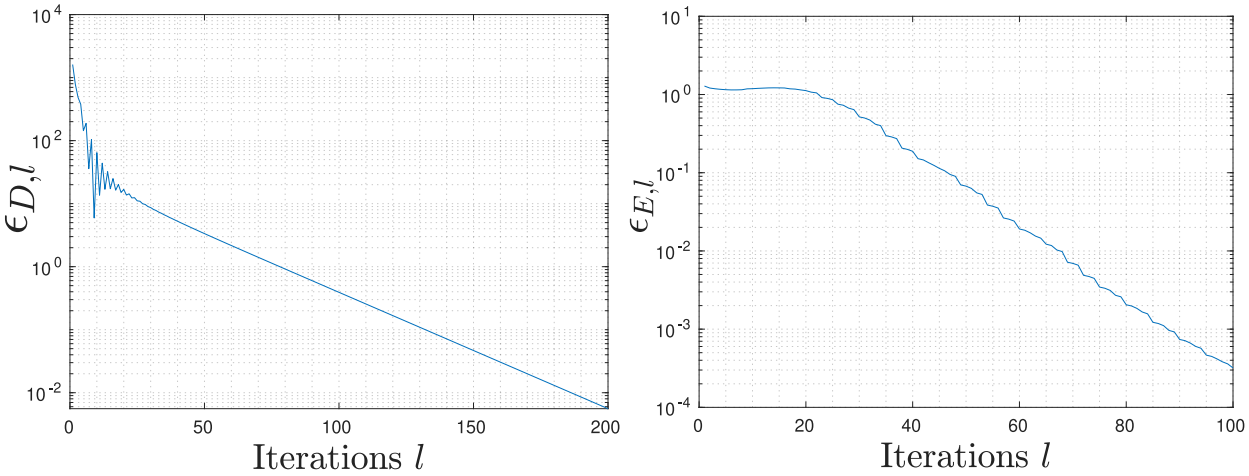

(a) Errors on D-Opt gradient.

(b) Errors on E-Opt gradient.

Figure 5.8 – Convergence of the D-Opt and E-Opt gradient estimates for the last configuration in the trajectory

5.7.2 Deployment of a UGV Carrying Several Anchors

Here we illustrate the results of Section 5.6 and the performance difference between leveraging information only on relative distances or on the full relative positions. Consider the robot shown in Fig. 5.9, following the kinematic model (5.44) and carrying two tags $\mathcal{U} = \{1, 2\}$ placed at positions $\mathbf{p}_1^r = [1, 0]^\top$ and $\mathbf{p}_2^r = [-1, 0]^\top$ in the robot frame, centered at $\mathbf{p}_M = \frac{1}{2}(\mathbf{p}_1 + \mathbf{p}_2)$. Three fixed anchors $\mathcal{K} = \{3, 4, 5\}$ are placed at the coordinates $\mathbf{p}_3 = [-5, 5]^\top$, $\mathbf{p}_4 = [5, -5]^\top$ and $\mathbf{p}_5 = [5, 5]^\top$ in the absolute frame. All nodes communicate and obtain range measurements with each other, following the Gaussian additive model (5.1) with $\sigma = 0.1$ m. The heading of the robot is θ and $\exp[\theta]_\times$ is the rotation matrix between $\mathcal{F}$ and the robot frame.

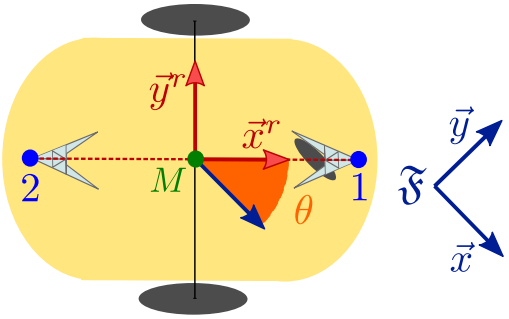

Figure 5.9 – Robot equipped with two tags

In scenario (D), we include the constraint $d_{12} = 2$ m as in Section 5.6.2, and define the cost function as (5.31). In scenario (RP), we include the constraint $\mathbf{p}_{12}^r = [2, 0]^\top$ as in Section 5.6.3 and define the cost function as (5.41), so that it can be compared to the previous one. We compute the potentials and their derivatives with the results of Section 5.6 and implement the scheme (5.32) to compute a sequence of desired poses. The robot reaches them by using the pose controller presented in [Astolfi, 1999], which includes heading control, in contrast to (5.45). At $k = 0$, the initial configuration of the robot in both cases is given by $\mathbf{p}_M(0) = [-15, -4]^\top$ and $\theta(0) = -\pi/8$. The cost and robot trajectories are shown in Fig. 5.10, denoting $F = 5000$ the last iteration index of (5.32). Thanks to the dual penalization of the rigidity constraint, the steady state configuration of the tags provided by (5.32) is feasible for the robot.

The following constrained least-squares estimators $\hat{\mathbf{p}}_\mathcal{U}^\mathrm{D}$ and $\hat{\mathbf{p}}_\mathcal{U}^\mathrm{RP}$ of $\mathbf{p}_\mathcal{U}$ are implemented in

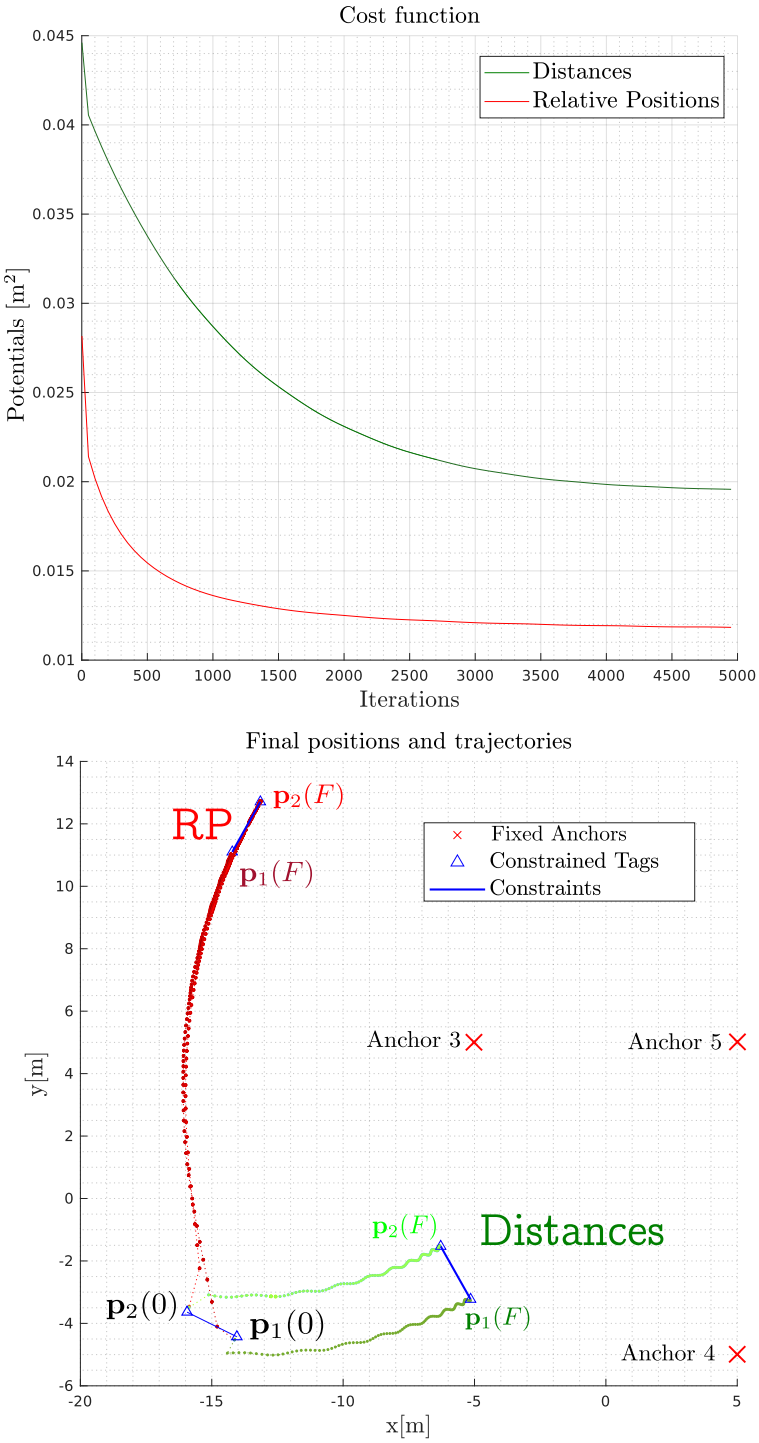

Figure 5.10 – Deployment results for (D) and (RP) scenarios. The cost functions are plotted as well as the positions during the trajectory

scenarios (D) and (RP)

$$\begin{cases} \hat{\mathbf{p}}_{\mathcal{U}}^{\mathrm{D}} = \underset{\hat{\mathbf{p}}_{\mathcal{U}}}{\operatorname{argmin}}\ Q(\hat{\mathbf{p}}_{\mathcal{U}}), \\ \text{s.t } \hat{d}_{12} - d_{12} = 0 \end{cases} \quad \text{and} \quad \begin{cases} \hat{\mathbf{p}}_{\mathcal{U}}^{\mathrm{RP}} = \underset{\hat{\mathbf{p}}_{\mathcal{U}}}{\operatorname{argmin}}\ Q(\hat{\mathbf{p}}_{\mathcal{U}}), \\ \text{s.t } \hat{\mathbf{p}}_{21} - \exp\left[\hat{\theta}\right]_{\times} \mathbf{p}_{12}^{r} = \mathbf{0} \end{cases}$$

where $\hat{\theta} := \operatorname{atan2}(\hat{y}_{21}, \hat{x}_{21})$ and $Q(\mathbf{p}_{\mathcal{U}})$ is defined in (5.46). We evaluate the localization performance by computing the empirical MSE $\widetilde{MSE}_{\mathcal{U},k} := \frac{1}{2}[\widetilde{MSE}_{1,k} + \widetilde{MSE}_{2,k}]$ for the two tag positions, using the same process as in Section 5.7.1, with $M = 500$ simulations.

Table 5.1 – Monte Carlo Simulation Results. Empirical MSE at the initial and terminal point, with 3σ confidence bounds

	$\widetilde{MSE}_{\mathcal{U},0}$	Confidence	$\widetilde{MSE}_{\mathcal{U},F}$	Confidence	ET
(D)	4.28 m^2	$\pm$0.03 m^2	0.93 m^2	$\pm$0.02 m^2	1.70 s
(RP)	2.97 m^2	$\pm$0.04 m^2	0.63 m^2	$\pm$0.002 m^2	1.89 s

The results shown in Table 5.1 indicate that the motion significantly improves the estimate accuracy in both cases: around 78% for (D) and 79% for (RP). Moreover, the relative position constraints provides a clear improvement to the MSE compared to only using the relative distance information. Table 5.1 also provides the Execution Times (ET) of the deployment algorithms for all the steps shown in Fig. 5.10. The simulation is coded in `Matlab R2018b` and runs on a computer equipped with an `Intel I7` processor. The ET for the (RP) scenario is about 10% larger than for (D), due to the increased complexity to evaluate $\mathbf{A}$ and its derivative. In summary, compared to (D), deployment using (RP) leads to a significant improvement of the precision and a moderate increase of the ET.

5.8 Experiments

To validate experimentally some of the ideas presented in this paper, we placed two tags $\mathcal{U} = \{1, 2\}$ on the *same* ground robot R_1 and two anchors $\mathcal{K} = \{3, 4\}$ on two other robots R_3 and R_4, as shown on Fig. 5.11. The anchors are externally positioned with a motion capture system, which is also used in the following to provide the true positions of the tags and evaluate the accuracy of position estimates. The anchors and tags are based on Qorvo's `DW1000` UWB modules [Qorvo, 2022]. Each tag-anchor pair $(u, k) \in \mathcal{U} \times \mathcal{K}$ is measuring its distance d_{uk} using a bias-compensated single-sided two-way ranging protocol described in [Cano et al., 2022b]. The modules are placed at known height on masts, to limit signal reflections on the ground.

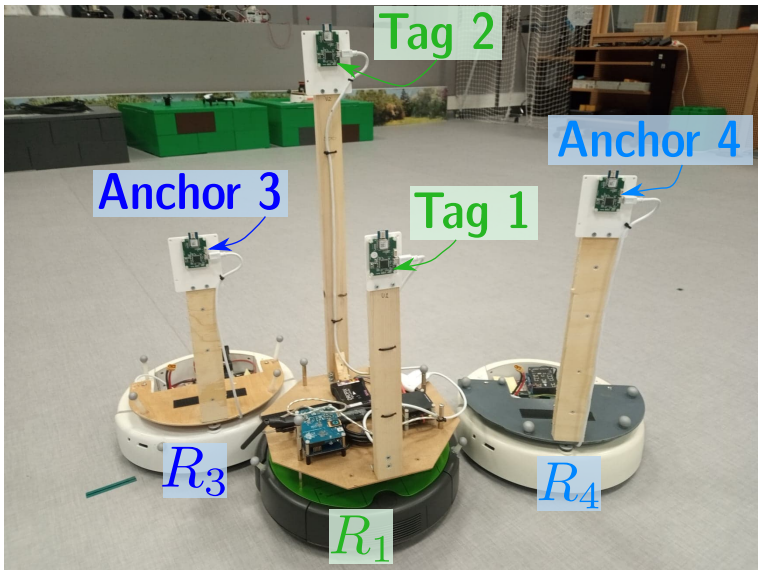

Figure 5.11 – Robots, anchors and tags

Robot R_1 is initially placed at location $[-3, 0]^\top$ in the world frame and is expected to follow the x-axis of that frame until reaching the neighborhood of the final location at coordinates $[3, 0]^\top$, see Fig. 5.12 and 5.15. To do so, the robot's position is controlled by the low-level trajectory tracking controller described in Section 5.7.1, using estimates $\hat{\mathbf{p}}_\mathcal{U}$ of the tags' locations. These estimates are computed by collecting the four UWB-based ranging measurements $\tilde{d}_{uk}$ between tags and anchors and solving the least-squares problem

$$\hat{\mathbf{p}}_\mathcal{U} = \underset{\mathbf{p}_\mathcal{U} \in \mathcal{C}}{\operatorname{argmin}} \sum_{k \in \mathcal{K}} \sum_{u \in \mathcal{U}} \left(||\mathbf{p}_u - \mathbf{p}_k|| - \tilde{d}_{uk} \right)^2, \tag{5.47}$$

where $\mathcal{C} := \{\text{col}(\mathbf{p}_1, \mathbf{p}_2) \in \mathbb{R}^4 | \mathbf{p}_{21} = \exp([\theta]_\times)\mathbf{p}_{21}^1\}$ captures constraint (5.37), with the relative position $\mathbf{p}_{21}^1 = [0.3, 0]^\top$ of the tags in the robot frame centered at $\mathbf{p}_1$ known. Here θ is the heading of R_1. Note that we do not attempt to improve the location estimates (5.47) by filtering them, in order to emphasize the effect of the network geometry on the localizability from the distance measurements alone.

First, R_1 attempts to follow its path while the anchors remain fixed at $[-3.3, \pm 0.3]^\top$ in the Cartesian plane, as shown on Fig. 5.12. After each small motion, R_1 stops and repeatedly computes estimates of $\hat{\mathbf{p}}_\mathcal{U}$ using (5.47), each time using fresh measurements. The resulting estimates for tag 1 are shown by orange dots on Fig. 5.12. The position estimates are increasingly noisy as R_1 moves toward the positive x-axis, with the y-coordinate in particular becoming increasingly uncertain. This is intuitive because the inter-anchor distance d_{34} becomes small compared to the measured anchor-tag distances. The trajectory of the robot

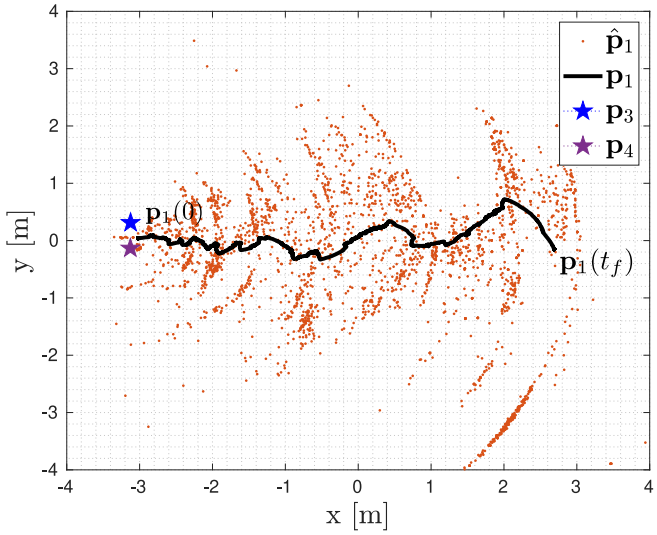

Figure 5.12 – Trajectory $\mathbf{p}_1$ of tag 1 and its estimates $\hat{\mathbf{p}}_1$ in the Cartesian plane while the anchors remain fixed

becomes increasingly erratic as a result of using poor estimates, which motivates improving the localizability. Although the estimates could be filtered over time to improve their accuracy and better track the desired path, this would lead to a slower system.

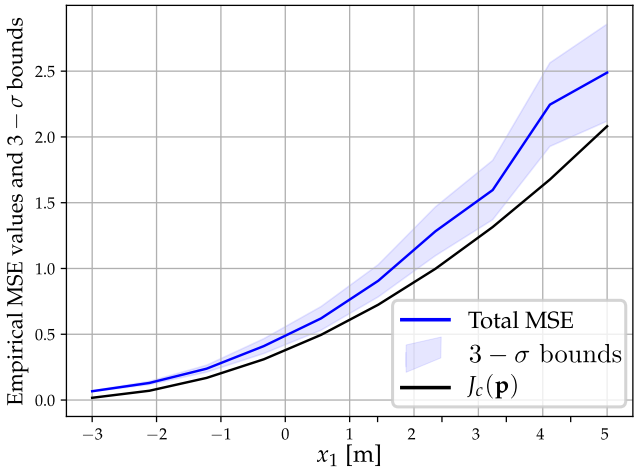

Figure 5.13 – Motion of robot R_1 with static anchors: empirical MSE of $\hat{\mathbf{p}}_{\mathcal{U}}$ obtained from solving (5.47) 500 times at each location, and localizability potential (5.41) for an ideal trajectory of R_1 with $y_1 = 0$

Fig. 5.13 shows in blue the empirical average MSE obtained after solving (5.47) 500 times, together with the 3σ confidence bounds on this MSE value. It also shows the localizability potential J_c defined in (5.41), which is a theoretical lower bound on the MSE. We see that

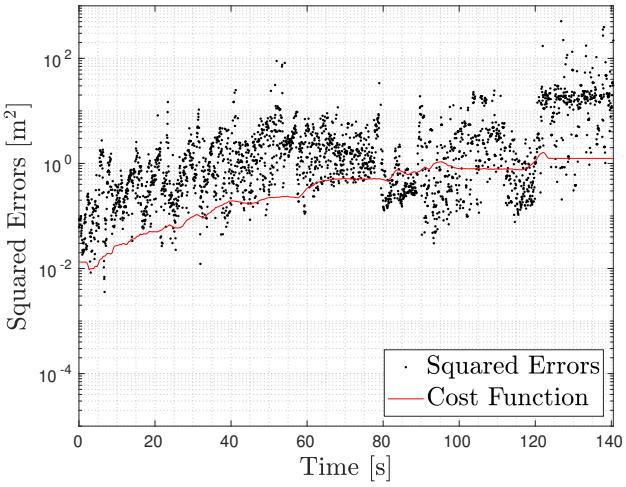

Figure 5.14 – Localizability potential and squared errors over the tags' trajectory, with fixed anchors

J_c predicts an increasingly poor localizability as the robot moves toward the positive x-axis, which is confirmed by the empirical MSE measurements.

Fig. 5.14 shows the squared errors $||\hat{\mathbf{p}}_{\mathcal{U}} - \mathbf{p}_{\mathcal{U}}||^2$ and the potential J_c over the tags' trajectory, on a semi-logarithmic plot. We note that J_c is generally a good indicator of the order of magnitude of the expected uncertainties, which however are amplified in practice by other effects such as multipath and non-line of sight measurements [Cano et al., 2019, Sahinoglu et al., 2008].

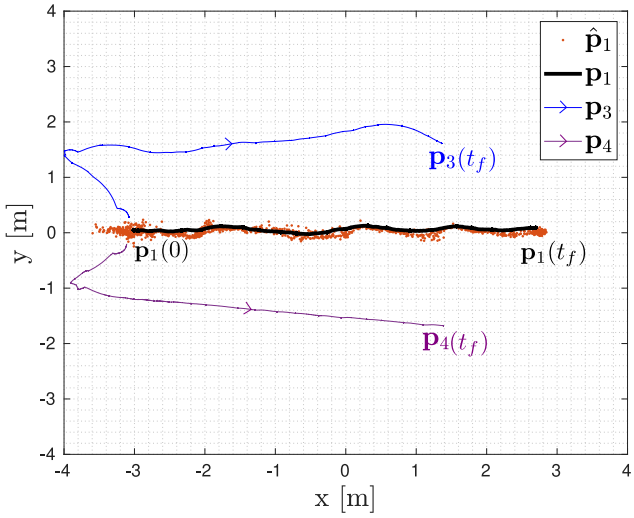

Figure 5.15 – Anchor and tag 1 trajectories when the anchors are mobile

Next, we illustrate on Fig. 5.15 the trajectory tracking results when the anchors are deployed simultaneously with R_1, using the gradient descent scheme described in Section 5.6.3, with the gradient expression (5.42). In this case, the position estimates produced by (5.47) exhibit much less variance, which is confirmed also by Fig. 5.16. This figure also shows that the localizability potential J_c is kept at a much lower value during the motion. The reduced variance allows us to efficiently reject measurement outliers and maintain an empirical MSE of about 12 cm along the trajectory, which is appropriate for indoor navigation. Hence, this experiment highlights that localizability can be improved automatically in real-time, even when using the position estimates to replace the true position in the gradient-based deployment algorithm.

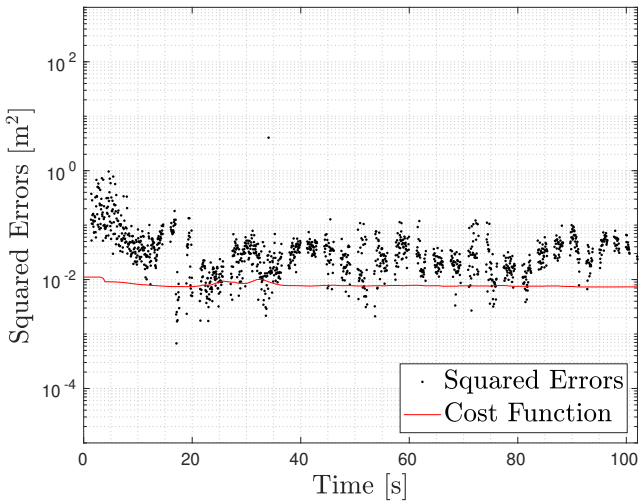

Figure 5.16 – Localizability and squared errors during deployment

5.9 Conclusion and Perspectives

This paper presents deployment methods applicable to Multi Robots Systems (MRS) with relative distance measurements, which maximize localizability. Constrained Cramér-Rao Lower Bounds (CRLB) are used to predict the localization error of a given configuration, assuming Gaussian ranging measurement models. A connection between Fisher information matrices and rigidity matrices is highlighted, which yields useful invertibility properties, e.g., for initial MRS placement.

The CRLB is used to design artificial potentials, so that gradient descent schemes can be developed to plan robot motions that enhance the overall localizability of the network. Moreover, we show how to distribute the execution of the gradient estimation algorithms among

the robots, so that they only need to communicate with their neighbors in the ranging graph. Finally, we extend the methodology to MRS with robots carrying multiple tags, again leveraging the theory of equality-constrained CRLBs. Future work could consider also optimizing the network topology, since maintaining ranging links typically entails a cost (consuming bandwidth, computation resources, etc.). Developing formal closed-loop stability properties for the gradient-based control law with noisy position estimates is also of interest.

Acknowledgements

The authors thank Drs. Éric Chaumette, Gaël Pagès and Ali Naouri from ISAE-Supaéro (France) for helpful discussions.

CHAPTER 6 ARTICLE 3 : OPTIMAL LOCALIZABILITY CRITERION FOR POSITIONING WITH DISTANCE-DETERIORATED RELATIVE MEASUREMENTS

Published in IEEE/RSJ International Conference on Intelligent Robots and Systems, October, 20th 2022.

Coauthors : Justin Cano[1,2], Gaël Pagès[1], Éric Chaumette [1], Jérôme Le Ny[2]

[1] DEOS, ISAE-Supaéro, Toulouse France.

[2] EE Dept., Polytechnique Montréal, QC, Canada & GERAD, Montréal, QC, Canada.

Abstract

Position estimation in Multi-Robot Systems (MRS) relies on relative angle or distance measurements between the robots, which generally deteriorate as distances increase. Moreover, the localization accuracy is strongly influenced both by the quality of the raw measurements but also by the overall geometry of the network. In this paper, we design a cost function that accounts for these two issues and can be used to develop motion planning algorithms that optimize the localizability in MRS, i.e., the ability of individual robots to localize themselves accurately. This cost function is based on computing new Cramér Rao Lower Bounds characterizing the achievable positioning performance with range and angle measurements that deteriorate with increasing distances. We describe a gradient-based motion-planning algorithm for MRS deployment that can be implemented in a distributed manner, as well as a non-myopic strategy to escape local minima. Finally, we test the proposed methodology experimentally for range measurements obtained using ultra-wide band transceivers and illustrate the improvements resulting from leveraging the more accurate measurement model in the robot placement algorithms.

6.1 Introduction

Reliable and accurate localization systems are critical for mobile robots to autonomously perform tasks in their environment. Various positioning technologies, e.g., short- and long-range radio-frequency (RF) systems, camera- or Lidar-based systems, offer different trade-offs in terms of performance, cost or applicability in various environments [Groves, 2013, Corke, 2011]. Generally however, these technologies provide different modalities to obtain range or angle measurements between a robot and environmental features or between different robots in a Multi-Robot System (MRS).

The quality of the position estimates produced for an MRS based on relative range or angle measurements depends on the geometry of the network, a phenomenon known as *dilution of precision* [Groves, 2013, Chap. 7]. The relationship between network geometry and the ability of the robots to localize themselves can be captured through a *localizability cost function* [Le Ny and Chauvière, 2018], and the robots can then move to optimize this cost function and thus their positioning performance [Le Ny and Chauvière, 2018,Irani et al., 2019,Papalia et al., 2021, Cano and Le Ny, 2021]. Localizability can be quantified independently of the localization scheme by using Cramér Rao Lower Bounds (CRLB), which provide a bound on the error covariance matrix of any unbiased position estimator one may implement in the MRS.

The CRLB depends on the specific stochastic error model considered for the raw distance or angle measurements. Although explicit CRLBs have been developed for measurement noise with constant variance [Patwari et al., 2005, Cano and Le Ny, 2021], in practice we observe for many systems that the quality of measurements degrades with distance. To address this issue, connectivity constraints can be added to maintain the robots sufficiently close [Michael et al., 2009, Yang et al., 2010]. However, such constraints increase the complexity of the motion planning problems, and moreover this approach captures the issue of measurement quality only indirectly, leading to suboptimal geometries. Hence, in this paper we propose a measurement variance model with polynomial dependence on the robot inter-distances and derive the corresponding CRLB to be used to quantify localizability and develop MRS deployment algorithms.

To illustrate the usefulness of deriving more refined CRLBs and localizability measures, we focus on localization using Ultra-Wide Band (UWB) transceivers [Sahinoglu et al., 2008]. This technology can provide distance measurements with decimeter to centimeter-level accuracy [Decawave, 2017] while being relatively inexpensive and energy efficient, which makes it particularly attractive for robotics applications [Ledergerber et al., 2015,Mai et al., 2018,Cano et al., 2022b], especially indoors. We consider the problem of localizing multiple robots equipped with UWB transceivers, called *tags*, communicating with each other and with other transceivers, called *anchors*, the location of the latter being known. Anchors can also be carried by mobile robots having access to an external source of localization. With enough relative distance or angle measurements obtained between the transceivers, the robot positions can be estimated for example using least-squares or filtering techniques [Etzlinger and Wymeersch, 2018, Sahinoglu et al., 2008]. UWB sensors can acquire relative range [Ledergerber et al., 2015, Cano et al., 2022b] or angle [Peng and Sichitiu, 2006, Dotlic et al., 2017] measurements, using a variety of protocols transmitting signals between nodes. The accuracy of these protocols deteriorates with the distance between transceivers because the received

signal power decreases and errors due to fading and multi-path increase. In particular, the received signal power directly influences the *Leading Edge Detection* (LDE) algorithm used to estimate the signals' time-of-flight [Sahinoglu et al., 2008, Cano et al., 2022b]. Therefore, using a localizability criterion relying on the network's geometry without taking into account a realistic measurement error distribution can lead to misleading predictions about the tags' localization accuracy.

The rest of the paper is organized as follows. After a description of the problem in Section 6.2, Section 6.3 presents the distance-dependent variance model for relative measurements and illustrates how to fit such a model experimentally for UWB range sensors. For this general polynomial variable model, the new localizability criterion is derived in Section 6.4, based on Fisher Information Matrices defining the CRLB, computed in Section 6.5. Then, we present optimization algorithms in Section 6.6, which include gradient-descent based algorithms as well as non-myopic strategies to escape local minima. Finally, Section 6.7 validates the methodology experimentally and illustrates the benefits of incorporating the refined model with distance deteriorated measurements to predict localization accuracy.

6.2 Problem Statement

Consider the problem of localizing in a given reference frame in dimension n, with $n = 2$ or 3, a set $\mathcal{U}$ of U tags with unknown positions, while relying on a set $\mathcal{K}$ of K anchors with known positions. Relative angle or range measurements $\mu_{ij} \in \mathbb{R}$ are available between a subset $\mathcal{E}$ of the tags and anchors, with $i \in \mathcal{U}$ and $j \in \mathcal{U} \cup \mathcal{K}$. Note that these measurements can involve either tag-tag or tag-anchor pairs, i.e., $\mathcal{E} \subset \mathcal{U} \times (\mathcal{U} \cup \mathcal{K})$. The coordinates $\mathbf{p}_i \in \mathbb{R}^n$ of node $i \in \mathcal{U} \cup \mathcal{K}$ in the reference frame are denoted $\mathbf{p}_i = [x_i, y_i, z_i]^\top$ if $n = 3$ or $\mathbf{p}_i = [x_i, y_i]^\top$ if $n = 2$. Each tag is assumed to be carried by a robot, and a subset $\mathcal{K}_M \subseteq \mathcal{K}$ of the anchors can also be mobile. Let $\mathbf{p} := [\dots \mathbf{p}_i^\top \dots]^\top \in \mathbb{R}^{nN}$ denote the positions of the $N := U + K$ nodes (anchors or tags).

6.2.1 Robot Placement Problem

We aim to move the robots to enhance the *localizability* of the tags, which is some measure of the accuracy with which we can compute an estimate $\hat{\mathbf{p}}_\mathcal{U}$ of the vector of tag positions $\mathbf{p}_\mathcal{U} := [\dots \mathbf{p}_i^\top \dots]^\top \in \mathbb{R}^{nU}$, $i \in \mathcal{U}$. Since the localizability depends on the network geometry $\mathbf{p}$, we introduce a *localizability function* $J(\mathbf{p})$, which takes smaller values when the achievable accuracy for $\hat{\mathbf{p}}_\mathcal{U}$ increases. We then aim to find the optimal geometry $\mathbf{p}^*$, solution to the

following placement problem for the mobile nodes

$$\mathbf{p}^* = \underset{\{\mathbf{p}_j\}_{j\in\mathcal{K}_M\cup\mathcal{U}}}{\operatorname{argmin}} \; J(\mathbf{p}) + J_{\text{task}}(\mathbf{p}_\mathcal{U}), \tag{6.1}$$

where $J_{\text{task}}(\mathbf{p}_\mathcal{U})$ is an additional cost function that represents the tasks to be achieved by the robots carrying the tags. Indeed, from the tags' point of view, J can be seen as a constraint (*e.g.,* avoid configurations with poor localizability) as they must achieve tasks while been accurately localized. The function J should take into account both the geometry and the quality of the relative measurements μ_{ij}.

6.2.2 Distance-Deteriorating Measurement Models

The localizability depends on the assumed relative measurement model. In this paper, we consider the following Gaussian model

$$\mu_{ij} \sim \mathcal{N}\left(\bar{\mu}_{ij}(\mathbf{p}_{ij}), \sigma_{ij}^2(d_{ij})\right). \tag{6.2}$$

where $\bar{\mu}_{ij}$ is a mean function that depends on the relative positions $\mathbf{p}_{ij} := \mathbf{p}_i - \mathbf{p}_j$ of the pairs of agents $(i,j)\in\mathcal{E}$. The variance $\sigma_{ij}^2(d_{ij})$ of these measurements is a function of the inter-node distance $d_{ij} := ||\mathbf{p}_{ij}||$. Moreover, we assume that the measurements are independent for distinct pairs (i,j). This type of measurement model is standard for example for RF sensors estimating distances from Time-of-Flight (ToF) measurements [Patwari et al., 2005,Mai et al., 2018]. It is also used in 2D to model noise in Angle of Arrival (AoA) measurements [Peng and Sichitiu, 2006, Patwari et al., 2005]. However, σ_{ij}^2 is generally assumed to be a constant, independent of the position, although in practice it is generally the case that the quality of the measurements decreases as the distance increases [Patwari et al., 2005], especially as we approach the maximum range of a given technology. Hence, we propose to use variance functions $\sigma_{ij}^2(d_{ij})$ that model the degradation in measurement accuracy with distance, in order to improve the ability of the function $J(\mathbf{p})$ to accurately predict the localizability. It is important however to keep the computation of the function J and of its derivatives sufficiently simple in order to develop tractable motion planning algorithms.

6.3 Distance-Dependent Variance Model

In this section, we introduce a general polynomial model of the measurement variance $\sigma_{ij}^2(d_{ij})$ in (6.2). As an application, we calibrate a model of distance measurements with UWB transceivers.

6.3.1 Polynomial Variance Model

The proposed polynomial variance model is

$$\sigma_{ij}^2(d_{ij};\boldsymbol{\alpha}) = \alpha_0 + \sum_{l=1}^{P} \alpha_l (d_{ij} - \delta_l)^l \mathbf{1}_{\delta_l < d_{ij}}. \tag{6.3}$$

where $P \in \mathbb{N}$ is the chosen degree of the polynomial and $\boldsymbol{\alpha} = [\alpha_0, \alpha_1, \delta_0, \ldots, \alpha_P, \delta_P]^\top \in \mathbb{R}_+^{2P+1}$ is a vector of parameters. The l-th order term of the polynomial activates at the distance δ_l. We assume that $\alpha_0 > 0$ because measurements are uncertain even at close range, and $\alpha_l \geq 0$ and $\delta_l \geq 0$, $\forall l \in [1, P]$, to keep $\sigma_{ij}^2(d_{ij}) > 0$ and increasing with distance. CRLBs are derived in [Patwari et al., 2005] for the constant variance case where $P = 0$. The model (6.3) offers additional flexibility at long range while still allowing closed form expressions for the localizability function.

The parameter vector $\boldsymbol{\alpha}$ in (6.3) for a specific system and environment can be identified by collecting M measurements $\{\mu_{ij}^k(\mathbf{p}_{ij})\}_{k=1}^M$ at a set $\mathcal{M}$ of relative positions $\mathbf{p}_{ij}$, i.e., a total of $M \times |\mathcal{M}|$ measurements. We can then compute the empirical means $\hat{\bar{\mu}}_{ij}(\mathbf{p}_{ij}) = \frac{1}{M}\sum_{k=1}^M \mu_{ij}^k(\mathbf{p}_{ij})$ and variances $\hat{\sigma}_{ij}^2(\mathbf{p}_{ij}) = \frac{1}{M-1}\sum_{k=1}^M (\mu_{ij}^k(\mathbf{p}_{ij}) - \hat{\bar{\mu}}_{ij}(\mathbf{p}_{ij}))^2$, and finally obtain $\boldsymbol{\alpha}$ by solving the least squares problem

$$\boldsymbol{\alpha} = \underset{\check{\boldsymbol{\alpha}} \in \mathbb{R}_+^{2P+1}}{\operatorname{argmin}} \sum_{\mathbf{p}_{ij} \in \mathcal{M}} \left[\sigma_{ij}^2(||\mathbf{p}_{ij}||;\check{\boldsymbol{\alpha}}) - \hat{\sigma}_{ij}^2(\mathbf{p}_{ij})\right]^2. \tag{6.4}$$

6.3.2 Application to UWB Two-Way Ranging Measurements

To illustrate the model (6.3), we consider relative distance measurements acquired by two `Decawave DW1000` © UWB sensors [Decawave, 2017] performing Single-Sided Two Way Ranging (SSTWR). The exact protocol to deduce distance measurements from signal time-of-flight measurements, including clock and power correction, is detailed in [Cano et al., 2022b]. The UWB transceiver j is carried by a mobile robot as shown on Fig. 6.1, and the transceiver i is fixed on a tripod. The robot moves to different positions while a motion capture system provides exact measurements of $\mathbf{p}_{ij}$. We compute empirical variances $\hat{\sigma}_{ij}^2(\mathbf{p}_{ij})$ using $M = 150$ measurement samples at each relative positions $\mathbf{p}_{ij}$. The results are plotted in Fig. 6.2 for a straight line trajectory, as a function of d_{ij}. A polynomial fit of the empirical variance is performed for $P = 3$ in (6.4) and shown in red.

At close range in Line-of-Sight (LoS) conditions, the received power is saturated, which can explain that the variance remains relatively constant. At longer range, the fact that received power theoretically decreases proportionally to the square of the distance could explain the

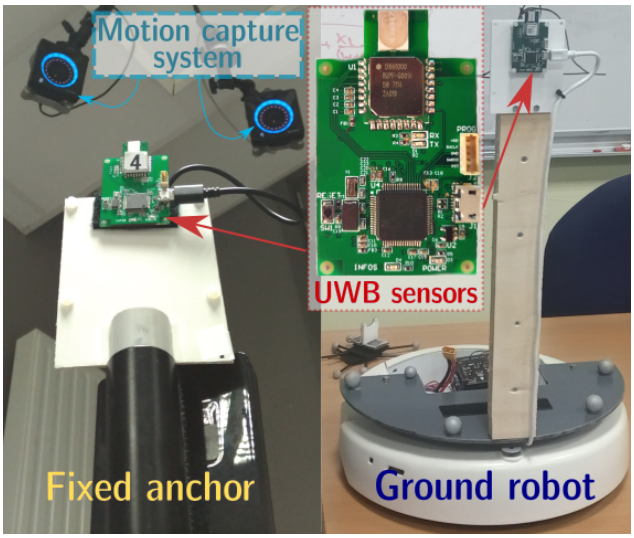

Figure 6.1 – Anchor, robot, motion capture system and UWB transceiver used for the variance model calibration

parabolic shape of σ_{ij}^2 when $d_{ij} > 6.5$ m. Moreover, even in LoS, outlier measurements can also be caused by multi-path propagation [Etzlinger and Wymeersch, 2018, Sahinoglu et al., 2008], when reflected signals with significant power are detected by the LDE algorithm instead of the wave on the direct path. For our set-up using a wheeled robot and isotropic antennas, the planar ground leads to a higher chance of multi-path propagation as the distance increases. Note that the data collected to fit the model using (6.4) should include these outlier measurements, in order to capture such trends.

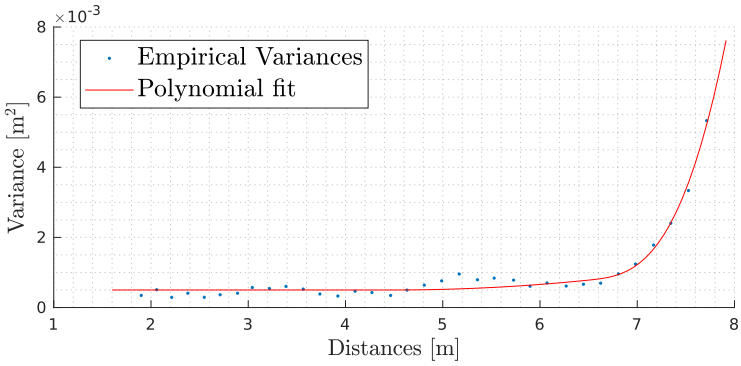

Figure 6.2 – Empirical variance and fitted polynomial

6.4 Localizability Cost Function

As in [Le Ny and Chauvière, 2018], the cost function penalizing network geometries leading to poor localizability, i.e., poor accuracy of the estimator $\hat{\mathbf{p}}_{\mathcal{U}}$ of $\mathbf{p}_{\mathcal{U}}$, can be constructed from the CRLB. To define it, denote $f(\boldsymbol{\mu}; \mathbf{p})$ the joint probability density function of the random measurement vector $\boldsymbol{\mu} = [\dots \mu_{ij} \dots]^\top$, which depends on the positions $\mathbf{p}$ of the tags and anchors. Moreover, assume that the estimator $\hat{\mathbf{p}}_{\mathcal{U}}$ is unbiased, *i.e.*, $\mathbb{E}\{\hat{\mathbf{p}}_{\mathcal{U}}\} = \mathbf{p}_{\mathcal{U}}$. Then, the covariance matrix $\Sigma_{\hat{\mathbf{p}}_{\mathcal{U}}, \hat{\mathbf{p}}_{\mathcal{U}}}$ of $\hat{\mathbf{p}}_{\mathcal{U}}$ satisfies the CRLB [Kay, 1993, 3.3]

$$\Sigma_{\hat{\mathbf{p}}_{\mathcal{U}}, \hat{\mathbf{p}}_{\mathcal{U}}} := \mathbb{E}\{(\hat{\mathbf{p}}_{\mathcal{U}} - \mathbf{p}_{\mathcal{U}})(\hat{\mathbf{p}}_{\mathcal{U}} - \mathbf{p}_{\mathcal{U}})^\top\} \succeq \mathbf{F}_{\mathcal{U}}^{-1}, \tag{6.5}$$

where $\mathbf{A} \succeq \mathbf{B}$ for symmetric matrices $\mathbf{A}, \mathbf{B}$ means that $\mathbf{A} - \mathbf{B}$ is positive semi-definite, and $\mathbf{F}_{\mathcal{U}} \in \mathbb{R}^{nU \times nU}$ is the Fisher Information Matrix (FIM), defined as follows [Kay, 1993, 3.7]

$$\mathbf{F}_{\mathcal{U}}(\mathbf{p}) = -\mathbb{E}_{\boldsymbol{\mu}} \left\{ \frac{\partial^2 \ln f(\boldsymbol{\mu}; \mathbf{p})}{\partial \mathbf{p}_{\mathcal{U}} \partial \mathbf{p}_{\mathcal{U}}^\top} \right\}. \tag{6.6}$$

Note that the FIM depends on the global geometry $\mathbf{p}$ and also on the specific distribution f of $\boldsymbol{\mu}$.

One can then define the localizability cost function to minimize as

$$J(\mathbf{p}) := \mathrm{Tr}\left\{ \mathbf{F}_{\mathcal{U}}^{-1}(\mathbf{p}) \right\}, \tag{6.7}$$

which is a lower bound on $\mathbb{E}\{\|\hat{\mathbf{p}}_{\mathcal{U}} - \mathbf{p}_{\mathcal{U}}\|^2\}$, the Mean Square Error (MSE) of $\hat{\mathbf{p}}_{\mathcal{U}}$. Using the CRLB has the advantage of providing a localizability measure that is independent of the specific estimator $\hat{\mathbf{p}}_{\mathcal{U}}$ implemented in the MRS. The function (6.7) corresponds to the A-Opt optimal design strategy [Pukelsheim, 2006, p.137], other functions can be used, such as $J_D(\mathbf{p}) = \log\det \mathbf{F}_{\mathcal{U}}^{-1}$ (D-Opt design) or $J_E(\mathbf{p}) = -\lambda_{\min}(\mathbf{F}_{\mathcal{U}})$ (E-Opt design, to maximize the minimum eigenvalue of $\mathbf{F}_{\mathcal{U}}$), as discussed in more detail in [Cano and Le Ny, 2023, III].

6.5 Computing the FIM

In this section we derive a closed form expression of the FIM $\mathbf{F}_{\mathcal{U}}$ for the measurement model introduced in sections 6.2 and 6.3, which is required to evaluate the localizability function J in (6.7).

6.5.1 Structure of the FIM

The $nU \times nU$ FIM matrix $\mathbf{F}_{\mathcal{U}}$ can be decomposed into $n \times n$ blocks $\mathbf{F}_{ij}$, $1 \leq i, j \leq U$, written as

$$\mathbf{F}_{ij} = \begin{bmatrix} F_{ij}^{xx} & F_{ij}^{xy} & F_{ij}^{xz} \\ \star & F_{ij}^{yy} & F_{ij}^{yz} \\ \star & \star & F_{ij}^{zz} \end{bmatrix} \text{ or } \mathbf{F}_{ij} = \begin{bmatrix} F_{ij}^{xx} & F_{ij}^{xy} \\ \star & F_{ij}^{yy} \end{bmatrix}, \tag{6.8}$$

depending if $n = 3$ or $n = 2$, where $\star$ denotes symmetric terms. From the assumption that the measurements μ_{ij} are independent and only available for $(i, j) \in \mathcal{E}$, i.e., $f(\boldsymbol{\mu}; \mathbf{p}) = \prod_{(i,j)\in\mathcal{E}} f_{ij}(\mu_{ij}; \mathbf{p}_{ij})$, we deduce that $\mathbf{F}_{ij} = \mathbf{0}$ for $(i, j) \notin \mathcal{E}$, whereas for (i, j) pairs of tags in $\mathcal{E}$

$$F_{ij}^{\xi\eta} := -\mathbb{E}_{\mu_{ij}}\{\partial^2 \ln f_{ij}(\mu_{ij}; \mathbf{p}_{ij})/\partial\xi_i \partial\eta_j\}, \tag{6.9}$$

where we denote pairs of Cartesian coordinates $\xi, \eta \in \{x, y, z\}^2$ if $n = 3$ or $\xi, \eta \in \{x, y\}^2$ if $n = 2$. We extend the expression (6.9) to tag-anchor pairs, so that $\mathbf{F}_{ij}$ is defined for all $(i, j) \in \mathcal{E}$. Then, we find that

$$\mathbf{F}_{ii} = -\sum_{j\in\mathcal{N}_i} \mathbf{F}_{ij},$$

where $\mathcal{N}_i = \{j \in \mathcal{U} \cup \mathcal{K}, (i, j) \in \mathcal{E}\}$, by using the fact that

$$\partial f_{ij}(\mu_{ij}; \mathbf{p}_{ij})/\partial\mathbf{p}_i = -\partial f_{ij}(\mu_{ij}; \mathbf{p}_{ij})/\partial\mathbf{p}_j.$$

Note that $\mathbf{F}_{ii}$ can require blocks $\mathbf{F}_{ij}$ outside $\mathbf{F}_{\mathcal{U}}$, *i.e.*, when $j \in \mathcal{K}$. Hence, it is sufficient to obtain $\mathbf{F}_{\mathcal{U}}$ to compute the terms of (6.9) for all $(i, j) \in \mathcal{E}$. For the Gaussian measurement model (6.2), this can be done using the Slepian-Bangs Formula (SBF) [Kay, 1993, 3.9], which gives for $(i, j) \in \mathcal{E}$

$$F_{ij}^{\xi\eta} = \frac{\partial\bar{\mu}_{ij}}{\partial\xi_i}\frac{\partial\bar{\mu}_{ij}}{\partial\eta_j}\sigma_{ij}^{-2} + \frac{1}{2}\frac{\partial\sigma_{ij}^2}{\partial\xi_i}\frac{\partial\sigma_{ij}^2}{\partial\eta_j}\sigma_{ij}^{-4}. \tag{6.10}$$

We see that (6.10) involves the derivatives of the function σ_{ij}^2 defined in (6.3). For any $(i, j) \in \mathcal{E}$, coordinates $\xi_i \in \{x_i, y_i, z_i\}$, $\xi_j \in \{x_j, y_j, z_j\}$, and $\xi_{ij} = \xi_i - \xi_j$, we have

$$\frac{\partial\sigma_{ij}^2}{\partial\xi_i} = \partial\sigma_{ij}^2 := \sum_{l=1}^{P} \alpha_l \, l \, \frac{\xi_{ij}}{d_{ij}}(d_{ij} - \delta_l)^{l-1}\mathbb{1}_{\delta_l < d_{ij}}, \tag{6.11}$$

and $\partial\sigma_{ij}^2/\partial\xi_j = -\partial\sigma_{ij}^2/\partial\xi_i$. The expression $\partial\sigma_{ij}^2$ defined in (6.11) is zero if $P = 0$, i.e., if σ_{ij}^2 is constant. Note that at points such that $d_{ij} = \delta_l$, depending on the values of the constants α_l, (6.11) may only provide one-sided derivatives.

6.5.2 Distance Measurements

Suppose that the measurements are distances $\mu_{ij} = \tilde{d}_{ij}$ given by the model (6.2) with mean $\bar{\mu}_{ij} := ||\mathbf{p}_{ij}|| = d_{ij}$, so that $\partial\bar{\mu}_{ij}/\partial\xi_i = \xi_{ij}/d_{ij} = -\partial\bar{\mu}_{ij}/\partial\xi_j$. Starting from the SBF (6.10), using identity (6.11) and differentiation rules, we obtained for $(i,j) \in \mathcal{E}$

$$F_{ij}^{\xi,\eta} = -\frac{\xi_{ij}}{d_{ij}}\frac{\eta_{ij}}{d_{ij}}\sigma_{ij}^{-2}\left[1 + \frac{1}{2}\left(\partial\sigma_{ij}^2\right)^2\sigma_{ij}^{-2}\right]. \tag{6.12}$$

with σ_{ij}^2 defined in (6.3) (we omitted the dependence on d_{ij} for conciseness), and the same notation for the coordinate $\eta \in \{x, y, z\}$ as for ξ. Alternatively, we can write for $(i,j) \in \mathcal{E}$

$$\mathbf{F}_{ij} = -\frac{w_{ij}}{\sigma_{ij}^2}\frac{\mathbf{p}_{ij}\,\mathbf{p}_{ij}^\top}{d_{ij}^2}, \tag{6.13}$$

where $w_{ij} := 1 + \frac{1}{2}\left(\partial\sigma_{ij}^2\right)^2\sigma_{ij}^{-2}$.

Remark 6.1. *The formulas in [Patwari et al., 2005] correspond to* (6.13) *for a constant variance Gaussian model, i.e., $w_{ij} = 1$. As in [Cano and Le Ny, 2023],* (6.13) *can be used to establish a connection between the FIM and a weighted version of the* infinitesimal rigidity matrix *[Tay and Whiteley, 1985], which can be used to provide conditions guaranteeing the invertibility of $\mathbf{F}_\mathcal{U}$ [Cano and Le Ny, 2023, Theorem 2].*

6.5.3 Angle Measurements

Suppose now that $n = 2$ and we have angle measurement $\mu_{ij} := \tilde{\theta}_{ij}$ between nodes $(i,j) \in \mathcal{E}$, with mean $\bar{\mu}_{ij} := \theta_{ij} := \angle(\vec{x}, \mathbf{p}_{ij})$, where $\vec{x}$ is a know reference direction. Without loss of generality, we choose $\vec{x} = [1,0]^\top$, so that $\theta_{ij} = \text{atan2}(y_{ij}, x_{ij})$. For a coordinate variable $\xi \in \{x, y\}$, we denote by $\bar{\xi}$ the other coordinate. We also introduce the symbol $\mathsf{s}_{\xi,\eta}$, which is equals to 1 if $\eta = \xi$ and -1 if $\xi \neq \eta$. Finally, the SBF (6.10) yields directly the following formula, if $i \neq j$

$$F_{ij}^{\xi\eta} = -\frac{\bar{\xi}_{ij}}{d_{ij}}\frac{\bar{\eta}_{ij}}{d_{ij}}\sigma_{ij}^{-2}\left[\frac{\mathsf{s}_{\xi,\eta}}{d_{ij}^2} + \frac{1}{2}\left(\partial\sigma_{ij}^2\right)^2\sigma_{ij}^{-2}\right]. \tag{6.14}$$

Alternatively, we can write for $(i,j) \in \mathcal{E}$

$$\mathbf{F}_{ij} = \sigma_{ij}^{-2}\left[-\frac{1}{2}\left(\partial\sigma_{ij}^2\right)^2\sigma_{ij}^{-2}\frac{\mathbf{p}_{ij}\,\mathbf{p}_{ij}^\top}{d_{ij}^2} + \frac{\mathbf{B}_{ij}}{d_{ij}}\right], \tag{6.15}$$

where $\mathbf{B}_{ij} := d_{ij}^{-1}(\mathbf{I}_2 - \mathbf{p}_{ij}\mathbf{p}_{ij}^\top d_{ij}^{-2})$.

Remark 6.2. *The matrices* $\mathbf{B}_{ij}$ *are* 2×2 *blocks of the bearing rigidity matrix as defined in [Zhao and Zelazo, 2015, Theorem 8]. As in Remark 6.1, this link can be used to provide conditions guaranteeing the invertibility of* $\mathbf{F}_{\mathcal{U}}$.

6.6 Localizability Optimization Methods

In this section we discuss two motion strategies for the mobile nodes in $\mathcal{U}$ and $\mathcal{K}_M$ that improve localizability by minimizing the cost function J in (6.7).

6.6.1 Gradient Descent Strategy

To quickly improve the localizability of $\mathcal{U}$, we can use a gradient descent strategy starting from the initial configuration $\mathbf{p}^0$ of the network. For each agent $i \in \mathcal{U} \cup \mathcal{K}_M$, the successive desired positions are computed as follows

$$\mathbf{p}_i^{k+1} = \mathbf{p}_i^k - \eta \min\left\{1, \frac{\eta_{\max}}{||\partial J/\partial \mathbf{p}_i||}\right\} \frac{\partial J}{\partial \mathbf{p}_i}^\top \Bigg|_{\mathbf{p}_i = \mathbf{p}_i^k}, \tag{6.16}$$

where k denotes a step index, using a normalized stepsize rule [Bertsekas, 2016]. The step size η is a given positive constant and $\eta_{\max}$ is a parameter adjusting the maximum distance $\eta_{\max}\eta$ between two iterations. The gradient $(\partial J/\partial \mathbf{p}_i)^\top$ can be computed using standard matrix differentiation rules [Petersen and Pedersen, 2012], which give for each coordinate $\zeta_i \in \{x_i, y_i, z_i\}$, $i \in \mathcal{U} \cup \mathcal{K}_M$,

$$\frac{\partial J}{\partial \zeta_i} = -\mathrm{Tr}\left\{\mathbf{F}_{\mathcal{U}}^{-2} \frac{\partial \mathbf{F}_{\mathcal{U}}}{\partial \zeta_i}\right\}. \tag{6.17}$$

In the Appendix, we provide an analytic formula for $\partial \mathbf{F}_{\mathcal{U}}/\partial \zeta_i$, which can also be used to evaluate gradients for cost functions J_D and J_E, from other optimal design strategies, see [Le Ny and Chauvière, 2018].

Suppose that the scheme (6.16) converges after l iterations to a configuration $\mathbf{p}^l$ in the neighborhood of a local minimum, i.e., $||\mathbf{p}_i^l - \mathbf{p}_i^{l-1}|| < \epsilon$ for each mobile node i and some threshold ϵ. The sequence of configurations $\{\mathbf{p}^k\}_{k=0}^l$ can be computed offline and used to provide a reference trajectory for a lower-level trajectory tracking controller. If used in real-time in a feedback loop however, the gradients in the scheme (6.16) can only be evaluated at the current estimates $\hat{\mathbf{p}}$, which are supposed unbiased.

The gradient descent scheme can also be implemented in a distributed manner by the nodes, i.e., it is possible for each node i to compute its local gradient $(\partial J/\partial \mathbf{p}_i)^\top$ in (6.16) by communicating only with its ranging neighbors. Indeed, the FIM has the same sparse structure

as in [Cano and Le Ny, 2023], so that the distributed algorithms presented in Section V.B in that reference can be implemented.

6.6.2 Non-Myopic Localizability Improvement Policy

The gradient descent strategy can quickly improve the localizability of the MRS by finding a local minimum $\mathbf{p}^l$ of the function J. However, as we illustrate in Section 5.8, there may exist other configurations relatively close to $\mathbf{p}^l$ with significantly better localizability. Hence, we propose a search strategy to attempt to discover such configurations.

To do so, we introduce a regular grid of $\mathbb{R}^n$ around each $\mathbf{p}_i^l$, for $i \in \mathcal{U} \cup \mathcal{K}_M$. Starting from $\mathbf{p}^l$, we recursively construct the grid by allowing at each stage k motion vectors $\mathbf{u}_i^k \in \mathbb{R}^n$ for each mobile robot i, with components $\pm\delta$ for some step size δ, up to a maximum number of moves D. We associate a stage cost to a motion $\mathbf{u}_i^k$, which can penalize odometry drift, energy spent, etc. If we stop the robots in some configuration $\mathbf{p}^k$ at stage k, the terminal cost is $J(\mathbf{p}^k)$. We then compute via dynamic programming [Bertsekas, 2012] trajectories for the robots that minimize the sum of the stage costs and the terminal cost, up to the maximum horizon D. The optimal trajectory found balances potential improvement in localizability with the total cost of the additional motions from $\mathbf{p}^l$.

Note that the complexity of the dynamic programming algorithm is polynomial in D, but exponential in the number of robots. It is also possible to reduce the size of the search space by removing from the grid the configurations $\mathbf{p}$ such that $J(\mathbf{p}) > (1+\gamma)J(\mathbf{p}^l)$ for some parameter $\gamma > 0$, which prevents trajectories to go through configurations for the MRS that deteriorate the localizability too much.

6.7 Experimental Validation

To test the models and methods developed in this paper, we consider a simple scenario with 3 fixed UWB anchors $\mathcal{K} = \{K_1, K_2, K_3\}$, located at $\mathbf{p}_1 = [3.0, 2.0, 1.5]^\top$, $\mathbf{p}_2 = [3.0, -2.0, 1.5]^\top$ and $\mathbf{p}_3 = [-4, 0.1, 2.0]^\top$, and a unique UWB tag T carried by the robot shown on Fig. 6.1. The position of the tag is $\mathbf{p}_T = [x, y, z]^\top$ where $z = 0.43$ m is a fixed constant and $\mathbf{p}_\mathcal{U} := [x, y]^\top$ has to be determined. The tag T acquires distance measurements with the anchors using the SSTWR protocol described in [Cano et al., 2022b], and we aim to find a position that optimizes its localizability.

The following model for the distance measurement variance is identified empirically in the

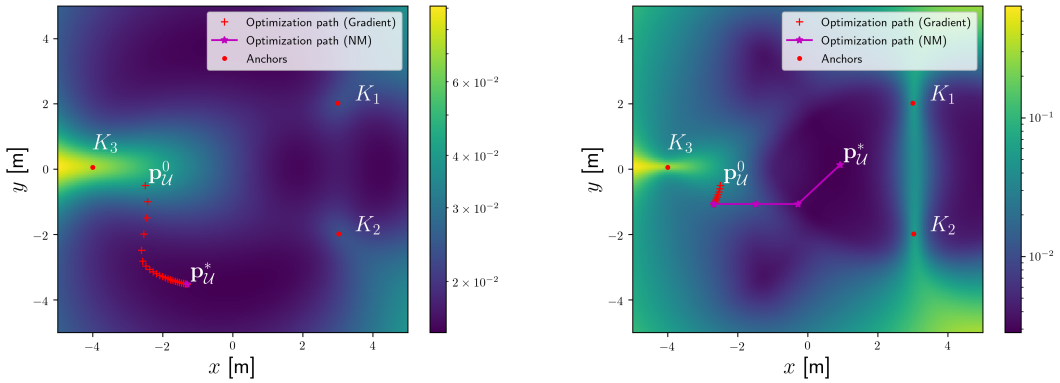

(a) CV model (b) QV model

Figure 6.3 – 2D localizability cost $J(x, y)$ and computed paths for the tag, with the CV and QV models

area where the experiment is held, as explained in Section 6.3

$$\sigma_{Tj}^2 = \alpha_0 + \alpha_2 (d_{Tj} - \delta_2)^2 1_{\delta_2 < d_{Tj}}, \quad j \in \mathcal{K}, \tag{6.18}$$

where $\alpha_0 = 0.038^2$ m^2, $\alpha_2 = 5 \times 10^{-3}$ and $\delta_2 = 4.5$ m. To stress the benefits of using the model (6.18) for localizability optimization, we consider two deployment scenarios: first, using a Constant Variance (CV) model, as in [Cano and Le Ny, 2023], with $\alpha_0 = 0.1^2$ m^2, $\alpha_2 = 0$, and second using the Quadratic Variance (QV) model (6.18). Then, we compare the actual positioning performances and the localizability potential values for both trajectories to stress the benefits of the refined model.

The values of the cost $J(\mathbf{p}_{\mathcal{U}}) = \mathrm{Tr}\left\{\mathbf{F}_{\mathcal{U}}^{-1}(\mathbf{p}_{\mathcal{U}})\right\}$ for the CV and QV models are plotted on a logarithmic color scale on Fig. 6.3. Note that $\mathbf{F}_{\mathcal{U}}$ corresponds to the information on x and y coordinates but involves distance measurements in $\mathbb{R}^3$. The initial tag position is $\mathbf{p}_{\mathcal{U}}(0) = [-2.5, 0.5]^\top$. For the CV model, the cost presents minima that are quite far from the anchors, which ignores the deterioration of the the measurements with the distance. In contrast, the cost for the QV model has its global minimum inside the triangle formed by the anchors, which is an intuitive placement solution.

To move the tag and optimize the localizability cost J, for both scenarios we first use the gradient descent scheme (6.16). We set $\mathbf{p}_{\mathcal{U}}^0 := \mathbf{p}_{\mathcal{U}}(0)$, $\eta = 200$ and $\eta\eta_{\max} = 0.5$ m, and plot the computed paths in red on Fig. 6.3. After convergence, which is detected using a tolerance parameter $\epsilon = 0.1$ m, we apply the Non-Myopic (NM) optimization strategy of Section 6.6.2. We use a step size $\delta = 1.2$ m, a depth $D = 4$ and a stage cost equal to $2.0 \times 10^{-4} \times \|\mathbf{u}_T\|^2$. The

NM strategy returns a path from $\mathbf{p}_{\mathcal{U}}^{l}$ to a potentially new point $\mathbf{p}_{\mathcal{U}}^{*}$ with better localizability, plotted in magenta on Fig. 6.3. However, in the CV case it turns out that $\mathbf{p}_{\mathcal{U}}^{l}$ was already a global minimum of the cost function, so that the NM optimization has no effect for that model.

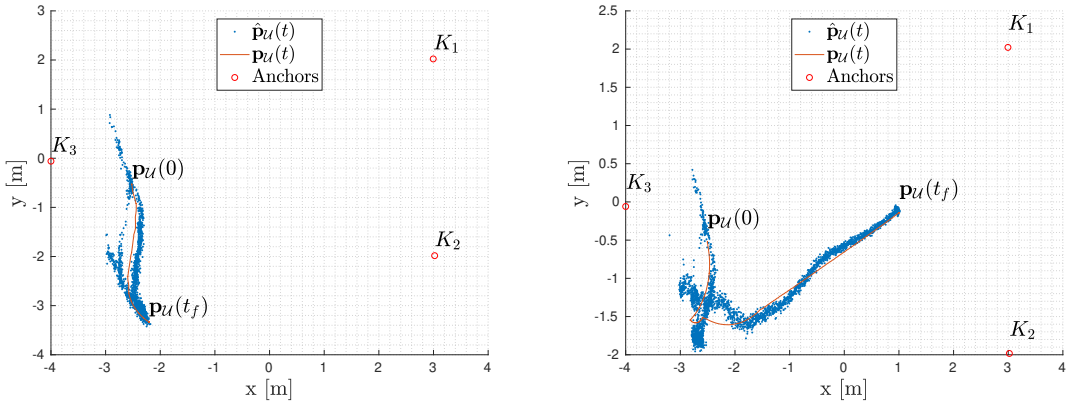

(a) CV model. (b) QV model.

Figure 6.4 – Performed trajectory and robot position estimates

Then, the robot follows pre-computed trajectories joining the waypoints $\{\mathbf{p}_{\mathcal{U}}^{0}, \ldots, \mathbf{p}_{\mathcal{U}}^{l}, \ldots, \mathbf{p}_{\mathcal{U}}^{*}\}$ and acquires along them UWB range measurements with the anchors. At each position $\mathbf{p}_{\mathcal{U}}(t)$, it measures distances $\tilde{d}_{Tj}$, $j \in \mathcal{K}$, and computes its position estimate by solving the least squares problem

$$\hat{\mathbf{p}}_{\mathcal{U}}(t) = \underset{\mathbf{p}\in\mathbb{R}^2}{\operatorname{argmin}} \sum_{j\in\mathcal{K}} \left(\tilde{d}_{Tj}(t) - ||\mathbf{p} - \mathbf{p}_j(t)||\right)^2,$$

using the Gauss-Newton method [Bertsekas, 2016]. A motion capture system records the true trajectory $\mathbf{p}_{\mathcal{U}}(t)$ of the robot. Since we are only interested here in characterizing the localization error, we use $\mathbf{p}_{\mathcal{U}}(t)$ directly to control the motion of the robot and follow the preplanned trajectory, instead of $\hat{\mathbf{p}}_{\mathcal{U}}(t)$. Finally, we compute the Squared Error (SE) $SE(t) = ||\mathbf{p}_{\mathcal{U}}(t) - \hat{\mathbf{p}}_{\mathcal{U}}(t)||^2$ and the potential $J(\mathbf{p}_{\mathcal{U}}(t))$. We plot the results on Figs. 6.4 and 6.5 for one trajectory. We also summarize in Table 6.1 the empirical MSE and 3σ confidence bounds for the initial and final position estimates in both scenarios over five trajectories.

During the first 3 seconds of each run, we observe large SE values, as shown on Fig. 6.5 and by the empirical MSE for $\mathbf{p}_{\mathcal{U}}(0)$ in Table 6.1. The cost $J(\mathbf{p}_{\mathcal{U}})$ is correspondingly high, *i.e.*, the localizability is poor. Indeed, the cost function is a theoretical lower bound on the MSE, which is highlighted along the trajectories by the superposition of $J(\mathbf{p}_{\mathcal{U}}(t))$ and $SE(t)$ on Fig. 6.5. After about 4 seconds for both scenarios the localization error decreases as the robot moves. However, range measurement errors presumably due to multi-path are

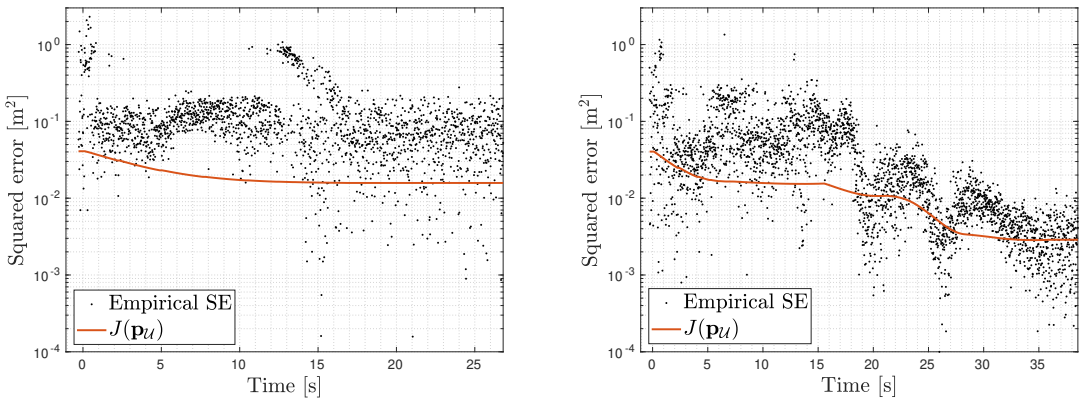

(a) CV scenario.

(b) QV scenario.

Figure 6.5 – Squared positioning error and localizability cost

observed when the robot is moving and is far from the anchors K_1 and K_2 (see Fig. 6.5a after about 13 s for example), which yields a significant loss of precision. These distance-dependent deterioration issues with the measurements are ignored by the CV model, while using the QV model for deployment leads to a significant improvement of the MSE when the final position $\mathbf{p}^*_\mathcal{U}$ computed by the NM strategy is reached after 35 seconds.

Table 6.1 – Empirical MSE for initial and final positions

$[\mathrm{m}^2]$	$\mathbf{p}_\mathcal{U}(0)$	$\mathbf{p}_\mathcal{U}(t_f)$ (CV)	$\mathbf{p}_\mathcal{U}(t_f)$ (QV)
MSE	0.38	0.23	8.3×10^{-3}
3σ	± 0.09	± 0.01	$\pm 0.46 \times 10^{-3}$

6.8 Conclusion and Perspectives

In this paper, we developed a localizability criterion taking into account relative measurement distortion at long range, which provides a tighter bound on the covariance of position estimates compared to constant measurement error variance models. To use this criterion for robot deployment, we described gradient-based and non-myopic optimization schemes. The possible improvements in positioning accuracy have been illustrated experimentally. Future work includes developing tractable non-myopic policies to search for optimal configurations over a larger area.

Acknowledgments

The authors thank Corentin Chauffaut and Louis Treton from ISAE for their availability and their assistance.

Appendix : Derivatives of the FIM

Here we give the expressions of $\partial \mathbf{F}_{ij}/\partial \mathbf{p}_l$ required to evaluate $\partial J/\partial \mathbf{p}_l$ in (6.16) via (6.17). Consider a coordinate $\zeta_l \in \{x_l, y_l, z_l\}$. If $i \neq j$, $\partial F_{ij}^{\xi\eta}/\partial \zeta_l = 0$ for all $l \notin \{i, j\}$. Next, if $i = j$ we have $\partial F_{ii}^{\xi\eta}/\partial \zeta_l = -\sum_{j \in \mathcal{N}_i \cap \mathcal{N}_l} \partial F_{ij}^{\xi\eta}/\partial \zeta_l$. Finally, since the FIM $\mathbf{F}_{\mathcal{U}}$ is symmetric, we have $\partial F_{ij}^{\xi\eta}/\partial \zeta_l = \partial F_{ji}^{\xi\eta}/\partial \zeta_l$. Therefore, to determine all the terms $\partial F_{ij}^{\xi\eta}/\partial \zeta_l$ of $\partial \mathbf{F}_{\mathcal{U}}/\partial \zeta_l$ it is sufficient to compute $\partial F_{lj}^{\xi\eta}/\partial \zeta_l$ for $j \in \mathcal{N}_l$. We find

$$\frac{\partial F_{lj}^{\xi\eta}}{\partial \zeta_l} = -\frac{\partial r_{ij}}{\partial \zeta_l}\sigma_{lj}^{-2} q_{lj} + r_{ij}\zeta_{lj}(\partial \sigma_{lj}^2)\sigma_{ij}^{-4} q_{lj} - r_{ij}\sigma_{lj}^{-2}\frac{\partial q_{lj}}{\partial \zeta_l}, \tag{6.19}$$

where $r_{ij} = \xi_{lj}\eta_{lj} d_{lj}^{-2}$ and $q_{lj} = w_{lj} = 1 + \frac{1}{2}\left(\partial \sigma_{lj}^2\right)^2 \sigma_{lj}^{-2}$ if we consider distance measurements or $q_{lj} = \frac{\mathsf{s}_{\xi,\eta}}{d_{ij}^2} + w_{ij} - 1$ for angle measurements. We then compute the two remaining derivatives $\partial r_{ij}/\partial \zeta_l$ and $\partial q_{lj}/\partial \zeta_l$. First, we have

$$\frac{\partial r_{ij}}{\partial \zeta_l} = d_{lj}^{-2}\gamma_{lj} - 2\xi_{lj}\eta_{lj}\zeta_{lj} d_{lj}^{-4},$$

where

$$\gamma_{lj} = \begin{cases} \xi_{lj} \text{ if } \zeta = \eta \text{ and } \xi \neq \eta, \\ \eta_{lj} \text{ if } \zeta = \xi \text{ and } \xi \neq \eta, \\ 2\zeta_{lj} \text{ if } \zeta \in \{\eta, \xi\} \text{ and } \xi = \eta, \\ 0 \text{ if } \zeta \notin \{\eta, \xi\}. \end{cases}$$

Second, if we consider distances measurement, we have

$$\frac{\partial q_{lj}}{\partial \zeta_l} = \frac{\partial w_{lj}}{\partial \zeta_l} = \frac{\zeta_{lj}}{2d_{lj}}\left(2(\partial^2 \sigma_{lj}^2)(\partial \sigma_{lj}^2)\sigma_{lj}^{-2} - (\partial \sigma_{lj}^2)^3 \sigma_{ij}^{-4}\right),$$

where

$$\partial^2 \sigma_{lj}^2 = \sum_{l=2}^{P} \alpha_l \, l \, (l-1)(d_{lj} - d_{0,l})^{l-2} \, \mathbf{1}_{d_{0,l} < d_{ij}},$$

and for angle measurements

$$\frac{\partial q_{lj}}{\partial \zeta_l} = -2\zeta_{lj}\frac{\mathsf{s}_{\xi,\eta}}{d_{ij}^3} + \frac{\partial w_{lj}}{\partial \zeta_l}.$$

CHAPTER 7 ARTICLE 4 : MAINTAINING ROBOT LOCALIZABILITY WITH BAYESIAN CRAMÉR-RAO LOWER BOUNDS

Published in IEEE/RSJ International Conference on Intelligent Robots and Systems, October 20th, 2022.

Coauthors : Justin Cano[1,3], Corentin Chauffaut[2] Gaël Pagès[1], Éric Chaumette [1], Jérôme Le Ny[3]

[1] DEOS, ISAE-Supaéro, Toulouse France.

[2] DISC, ISAE-Supaéro, Toulouse France.

[3] EE Dept., Polytechnique Montréal, QC, Canada & GERAD, Montréal, QC, Canada.

Abstract

Accurate and real-time position estimates are crucial for mobile robots. This work focuses on ranging-based positioning systems, which rely on distance measurements between known points, called anchors, and a tag to localize. The topology of the network formed by the anchors strongly influences the tag's localizability, *i.e.,* its ability to be accurately localized. Here, the tag and some anchors are supposed to be carried by robots, which allows enhancing the positioning accuracy by planning the anchors' motions. We leverage Bayesian Cramér-Rao Lower Bounds (CRLBs) on the estimates' covariance in order to quantify the tag's localizability. This class of CRLBs can capture prior information on the tag's position and take it into account when deploying the anchors. We propose a method to decrease a potential function based on the Bayesian CRLB in order to maintain the localizability of the tag while having some prior knowledge about its position distribution. Then, we present a new experiment highlighting the link between the localizability potential and the precision expected in practice. Finally, two real-time anchor motion planners are demonstrated with ranging measurements in the presence or absence of prior information about the tag's position.

7.1 Introduction

Mobile robots require reliable, energy-efficient and real-time positioning systems to operate. Various technologies can be used to estimate the position of a robot : computer vision [Corke, 2011] or Global Navigation Satellite Systems (GNSS) [Groves, 2013] are among the leading ones. However, irrespective of the positioning system, an extrinsic measurement is required

to determine the bodies' locations in a given frame [Groves, 2013, Sahinoglu et al., 2008].

We focus on ranging-based localization, which determines positions thanks to distance measurements between the robot to locate, called *tag*, and known reference points, called *anchors*. For our experiments we use Ultra-Wide Band (UWB) sensors, which are increasingly popular in mobile robotics, due to their low cost and energy consumption [Amanda Prorok, 2013, Mai et al., 2018]. In particular, signal Time-of-Flight (ToF) estimation techniques applied to UWB allows up-to-decimeter ranging accuracy [Cano et al., 2022b, Sahinoglu et al., 2008, Etzlinger and Wymeersch, 2018, Decawave, 2017], which makes the technology suitable for indoor navigation.

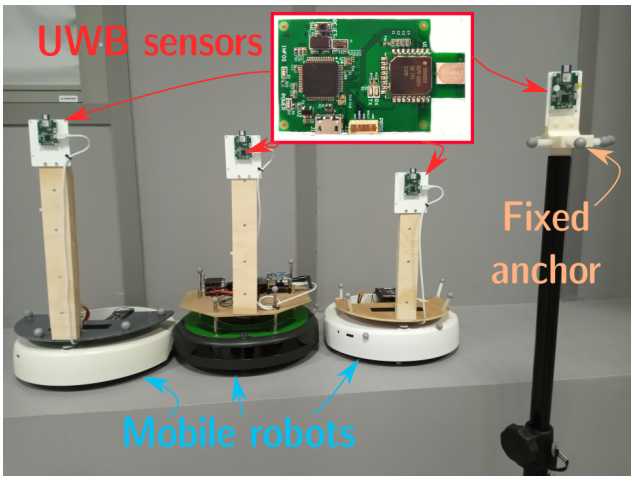

Figure 7.1 – Robots, fixed anchor and UWB sensors used in the experiments

Even with small ranging uncertainties, the geometry of the anchors' network strongly influences the *localizability* of the tags, i.e., their ability to be accurately localized [Patwari et al., 2005]. This phenomenon is known as *Dilution of Precision* (DoP) in the GNSS literature [Groves, 2013, Lv et al., 2010, Chap. 7] and transferable to mobile robotics. To quantify these uncertainties over the tag's location, the *Cramér-Rao Lower Bound* (CRLB), is commonly used as a performance metric for localization systems [Liu et al., 2012, Patwari et al., 2005, Papalia et al., 2021]. The CRLB is a lower bound on covariance that permits computing optimal theoretical performance of estimators independently of their implementation [Kay, 1993, Van Trees and Bell, 2007].

We assume that some anchors are carried by robots and can be deployed to enhance the tag's *localizability*. This property can be used to design motion planning algorithms, defining a CRLB-based localizability *potential* (*i.e.*, cost function) to decrease in order to improve the tag's positioning accuracy [Le Ny and Chauvière, 2018]. In previous work [Cano and Le Ny, 2023], we proposed decentralized techniques to optimize localizability in Multi-Robots

Systems (MRS) and for robots carrying several tags [Cano and Le Ny, 2021]. The recent work [Papalia et al., 2021] proposes to implement localizability constraints in graph-based planners to enhance the MRS positioning performance. However, these methods requires tag positions that can only been available through estimates.

In this paper, we present an experimental implementation of a motion planner proposed in [Cano and Le Ny, 2023] for an MRS that uses tag position estimates as input. Moreover, we define a novel criterion of localizability, taking into account prior information on the tag's position. Indeed, information on the position distribution can be obtained during the estimation of the tag's position, *e.g.*, using Kalman Filtering. This additional information is considered when modeling localizability, since it directly relates to the estimates' accuracy. To do so, we leverage Bayesian Cramér-Rao Lower Bounds [Van Trees and Bell, 2007]. We also propose a motion planner to improve this bound in real-time and test it in an MRS deployment experiment.

7.2 Problem Statement

Consider a set $\mathcal{K}$ of K *anchors*, with known positions. The anchors aim to localize a *tag* T, which is a sensor carried by a robot with unknown position $\mathbf{p}_\mathcal{U} \in \mathbb{R}^n$, where $n \in \{2, 3\}$. The tag performs with each anchor $i \in \mathcal{K}$ noisy distance measurements $\tilde{d}_i$ of $d_i = ||\mathbf{p}_\mathcal{U} - \mathbf{p}_i||$ where $\mathbf{p}_i \in \mathbb{R}^n$ denotes i's position. Then an estimate of $\hat{\mathbf{p}}_\mathcal{U}$ is computed using the information brought by these measurements. We assume that there exists a subset $\mathcal{K}_M \subseteq \mathcal{K}$ of K_M *mobile anchors* in $\mathbb{R}^n$, each carried by a different robot.

Since the geometry of $\mathcal{K}$ strongly influences the quality of $\hat{\mathbf{p}}_\mathcal{U}$, our goal is to design motion planners for $\mathcal{K}_M$ in order to maintain an adequate localizability of T while its carrier performs tasks. First, we model the amount of information brought by the observations $\tilde{\mathbf{d}}$ used to build $\hat{\mathbf{p}}_\mathcal{U}$. This approach leverages *Fisher Information Matrices* (FIM) for deterministic parameter $\mathbf{p}_\mathcal{U}$ estimation as seen in [Patwari et al., 2005]. Second, we consider that prior information on $\mathbf{p}_\mathcal{U}$ is available and used in the estimation process. We assume that the prior on the position is actualized by its estimator that gathers range measurements during the tag trajectory. In particular, we focus on the case of the popular *Kalman Filter* (KF) that dynamically provides a Gaussian model to quantify its estimates' uncertainties. Here, we propose to incorporate this new information in the localizability evaluation thanks to the *Bayesian Fisher Information Matrix* (BFIM). In Section 7.3, we give its definition and a methodology to compute it.

In order to deploy $\mathcal{K}_M$, we design in Section 7.4 a *localizability potential* $J_C(\mathbf{p}_{\mathcal{K}_M}, \mathbf{p}_\mathcal{U})$, where

$\mathbf{p}_{\mathcal{K}_M} \in \mathbb{R}^{nK_M}$ contains all the positions of $\mathcal{K}_M$. Based on the the BFIM, this potential models the expected precision of the estimates, *i.e.*, J_C increases when the quality of $\hat{\mathbf{p}}_\mathcal{U}$ decreases. This yields a minimization problem to deploy $\mathcal{K}_M$ towards an optimal configuration $\mathbf{p}^*_{\mathcal{K}_M}$ that minimizes J_C for a given $\mathbf{p}_\mathcal{U}$. We also provide an experiment that highlights the relation between $\hat{\mathbf{p}}_\mathcal{U}$ precision and this potential.

Section 7.5 presents motion planners for $\mathcal{K}_M$ that maintain dynamically tag's localizability in deterministic (*i.e.*, without prior) or Bayesian contexts. We stress that since the tag is moving to perform tasks, each $\mathbf{p}^k_\mathcal{U}$ at time k yields generally a different optimal anchor placement $\mathbf{p}^{k*}_{\mathcal{K}_M}$. For the Bayesian case, a methodology is provided to decrease J_C if the prior density at time k is Gaussian. These algorithms are then tested on an MRS in Section 7.6. In these experiments, the tag is being located with the Least Squares (LS) algorithm and the KF respectively, using the estimates $\hat{\mathbf{p}}_\mathcal{U}$ in the motion planning process.

7.3 Information Modeling

We aim to quantify the information provided by the measurements and a (possible) prior on $\mathbf{p}_\mathcal{U}$. First, we define the FIM and relate it to the uncertainty on $\hat{\mathbf{p}}_\mathcal{U}$. Then, we propose methods to evaluate it numerically.

7.3.1 Cramér-Rao Lower Bound

Consider the Probability Density Function (PDF) of the prior $\mathbf{p}_\mathcal{U}$ on $\mathbf{p}_\mathcal{U}$ denoted $f_\pi : \mathbb{R}^n \mapsto \mathbb{R}^+, \mathbf{p}_\mathcal{U} \to f_\pi(\mathbf{p}_\mathcal{U})$. We have $f_\mu : \mathbb{R}^{Kn} \mapsto \mathbb{R}^+, \tilde{\mathbf{d}} \to f_\mu(\tilde{\mathbf{d}}; \mathbf{p})$ the measurements' PDF, considering the vector $\tilde{\mathbf{d}} = [\dots \tilde{d}_i \dots]^\top$ with $i \in \mathcal{K}$ gathering the observations and the vector $\mathbf{p} = [\dots \mathbf{p}_i^\top \dots \mathbf{p}_\mathcal{U}^\top]^\top$ containing the sensors' positions. We assume that these PDFs are twice continuously differentiable. Under these assumptions the *Bayesian Fisher Information Matrix* (BFIM) [Van Trees and Bell, 2007] of $\mathbf{p}_\mathcal{U}$ is defined as follows

$$\mathbf{F}_B(\mathbf{p}) = -\mathbb{E}_{\mathbf{p}_\mathcal{U},\tilde{\mathbf{d}}} \left\{ \frac{\partial^2 \ln f_\mu(\tilde{\mathbf{d}}; \mathbf{p})}{\partial \mathbf{p}_\mathcal{U} \partial \mathbf{p}_\mathcal{U}^\top} \right\} - \mathbb{E}_{\mathbf{p}_\mathcal{U}} \left\{ \frac{\partial^2 \ln f_\pi(\mathbf{p}_\mathcal{U})}{\partial \mathbf{p}_\mathcal{U} \partial \mathbf{p}_\mathcal{U}^\top} \right\} \tag{7.1}$$

where $\partial^2 f_\bullet / \left(\partial \mathbf{p}_\mathcal{U} \partial \mathbf{p}_\mathcal{U}^\top \right)$ defines the Hessian matrix of $f_\bullet$ with respect to $\mathbf{p}_\mathcal{U}$. If f_π is unknown, (7.1) is simplified and yields the *Deterministic Fisher Information Matrix* (DFIM)

$$\mathbf{F}_D(\mathbf{p}) := -\mathbb{E}_{\tilde{\mathbf{d}}} \left\{ \frac{\partial^2 \ln f_\mu(\tilde{\mathbf{d}}; \mathbf{p})}{\partial \mathbf{p}_\mathcal{U} \partial \mathbf{p}_\mathcal{U}^\top} \right\}, \tag{7.2}$$

that only depends on the range measurements distribution.

Theorem 7.1 (Cramér-Rao Lower Bound [Van Trees and Bell, 2007])**.** *If the BFIM is invertible then the estimator's covariance satisfies*

$$\Sigma_{\hat{\mathbf{p}}_\mathcal{U}} := \mathbb{E}\{(\hat{\mathbf{p}}_\mathcal{U} - \mathbf{p}_\mathcal{U})(\hat{\mathbf{p}}_\mathcal{U} - \mathbf{p}_\mathcal{U})^\top\} \succeq \mathbf{F}_B^{-1}(\mathbf{p}),$$

where the notation $\mathbf{A} \succeq \mathbf{B}$ *denotes that* $\mathbf{A} - \mathbf{B}$ *is positive semi-definite for* $\mathbf{A}$ *and* $\mathbf{B}$ *symmetric. In the case of an invertible DFIM* $\mathbf{F}_D$*, if* $\mathbb{E}\{\hat{\mathbf{p}}_\mathcal{U}\} = \mathbf{p}_\mathcal{U}$*, then* $\Sigma_{\hat{\mathbf{p}}_\mathcal{U}} \succeq \mathbf{F}_D^{-1}$*.*

This result is known as the *Cramér-Rao Lower Bound* (CRLB) and we use it as a proxy to quantify the tag's localizability. This performance bound has the advantage to be an explicit function of $\mathbf{p}$. It can be decreased by moving $\mathcal{K}_M$ and is quickly calculable, as shown in the rest of this section.

7.3.2 Computation of the DFIM

We assume that the distance observations $\tilde{\mathbf{d}}$ are Gaussian and independent which is common when modeling ToF-based range measurements [Patwari et al., 2005, Sahinoglu et al., 2008]. Thus we have $\tilde{\mathbf{d}} \sim \mathcal{N}(\mathbf{d}, \mathbf{\Sigma}_d)$, denoting $\mathbf{d} = [\dots d_i^\top \dots] \in \mathbb{R}^K$ and $\mathbf{\Sigma}_d = \mathrm{diag}(\dots \sigma_i^2 \dots) \in \mathbb{R}^{K\times K}$. To compute the DFIM, we use the Slepian Bangs Formula (SBF) for real Gaussian distributions.

Proposition 7.1 (Slepian-Bangs Formula [Kay, 1993])**.** *Consider a position vector* $\mathbf{p}_\mathcal{U} = [x, y, z]^\top$ *(resp.* $\mathbf{p}_\mathcal{U} = [x, y]^\top$*) that parameterizes the PDF* f_g *of a Gaussian random vector* $\mathbf{g} \sim \mathcal{N}(\bar{\mathbf{g}}(\mathbf{p}_\mathcal{U}), \mathbf{\Sigma}_g(\mathbf{p}_\mathcal{U}))$*, with* $\bar{\mathbf{g}} \in \mathbb{R}^K$ *and* $\mathbf{\Sigma}_g \in \mathbb{R}^{K\times K}$ *for some* $K \in \mathbb{N}$*. Then, the coefficients* $F^{\xi,\eta} = -\mathbb{E}_\mathbf{g}\{\partial^2 \ln f_g / \partial\xi\partial\eta\}$ *of the DFIM* $\mathbf{F}_g \in \mathbb{R}^{n\times n}$ *of* $\mathbf{g}$ *with respect to* $\mathbf{p}_\mathcal{U}$ *coordinates are given as follows*

$$F_g^{\xi,\eta} = \frac{\partial \bar{\mathbf{g}}}{\partial \xi} \mathbf{\Sigma}_g^{-1} \frac{\partial \bar{\mathbf{g}}}{\partial \eta} + \frac{1}{2}\mathrm{Tr}\left\{\mathbf{\Sigma}_g^{-1}\frac{\partial \mathbf{\Sigma}_g}{\partial \xi}\mathbf{\Sigma}_g^{-1}\frac{\partial \mathbf{\Sigma}_g}{\partial \eta}\right\},$$

where $\eta, \xi \in \{x, y, z\}$ *if* $n = 3$ *(and* $\eta, \xi \in \{x, y\}$ *if* $n = 2$*).*

Since $\partial d_i / \partial \xi = (\xi - \xi_i)/d_i$ for a given coordinate $\xi \in \{x, y, z\}$ and $\mathbf{\Sigma}_d$ is assumed independent of the position, the application of the SBF yields [Patwari et al., 2005]

$$\mathbf{F}_D(\mathbf{p}_\mathcal{K}, \mathbf{p}_\mathcal{U}) = \sum_{i\in\mathcal{K}} \frac{1}{d_i^2 \sigma_i^2}(\mathbf{p}_\mathcal{U} - \mathbf{p}_i)(\mathbf{p}_\mathcal{U} - \mathbf{p}_i)^\top, \tag{7.3}$$

where $\mathbf{p}_\mathcal{K} = [\dots \mathbf{p}_i^\top \dots]^\top$ contains the anchors' i positions. The equation (7.3) clearly indicates that the estimates' quality depends on the tag's *relative positions* (RP) $\mathbf{e}_i := \mathbf{p}_\mathcal{U} - \mathbf{p}_i$

with respect to the anchors i. The CRLB exists over a simple condition on the RPs presented below.

Proposition 7.2. *$\mathbf{F}_D$ is invertible if and only if n relative position vectors $\mathbf{e}_i$, $i \in \mathcal{K}$ span $\mathbb{R}^n$.*

Proof. We gather the RPs $\mathbf{e}_i$ in $\mathbf{E} = [\dots \mathbf{e}_i \dots] \in \mathbb{R}^{n \times K}$ from (7.3) and note that $\mathbf{F}_D = \mathbf{E}\mathbf{Q}\mathbf{E}^\top$, with $\mathbf{Q} = \operatorname{diag}(\dots d_i^{-2}\sigma_i^{-2} \dots)$ a invertible diagonal matrix. Then, noting that $\operatorname{rank}(\mathbf{F}_D) = \operatorname{rank}(\mathbf{E})$ fulfills the proof. □

7.3.3 BFIM Computation with Gaussian Prior

Before deployment, the tag might know with some uncertainty its initial position, *e.g.*, we assume that it lies in the operating zone. However, the tag moves to fulfill its task and the prior uncertainty can be propagated through time while updating the distance measurements. Here, we suppose that a distribution is provided by the estimator of $\mathbf{p}_\mathcal{U}$ and can be used in order to compute the BFIM over time. Typically, if a KF estimator is used to locate the tag, it yields at each time k the estimate $\hat{\mathbf{p}}_\mathcal{U}^k$ and its estimated covariance matrix $\hat{\mathbf{\Sigma}}_{\mathbf{p}_\mathcal{U}}^k$ [Kay, 1993]. We assume that the PDF f_π of the prior on $\mathbf{p}_\mathcal{U}$ is the Gaussian distribution $\mathcal{N}(\mathbf{p}_\mathcal{U}, \mathbf{\Sigma})$ with $\mathbf{\Sigma}$ a given definite positive matrix. Thanks to the SBF, we compute $\mathbb{E}_{\mathbf{p}_\mathcal{U}}\left\{\partial^2 \ln f_\pi(\mathbf{p}_\mathcal{U}) / \left(\partial \mathbf{p}_\mathcal{U} \partial \mathbf{p}_\mathcal{U}^\top\right)\right\} = -\mathbf{\Sigma}^{-1}$ and finally (7.1) becomes

$$\mathbf{F}_B(\mathbf{p}) = \mathbb{E}_{\mathbf{p}_\mathcal{U}}\left\{\mathbf{F}_D(\mathbf{p}_\mathcal{K}, \mathbf{p}_\mathcal{U})\right\} + \mathbf{\Sigma}^{-1}. \tag{7.4}$$

Then, we need to evaluate $\mathbb{E}_{\mathbf{p}_\mathcal{U}}\left\{\mathbf{F}_D(\mathbf{p}_\mathcal{K}, \mathbf{p}_\mathcal{U})\right\}$ which is not analytically possible in general. However, we can approximately evaluate it thanks to the *unscented transform algorithm* [Sarkka, 2013, Chap. 5], which is a standard approach to sample random Gaussian distributions. To do so, we compute $\mathbf{R} := [\mathbf{r}_1 \dots \mathbf{r}_n]$ the generalized square root of $\mathbf{\Sigma}$ *i.e.*, which fulfills $\mathbf{\Sigma} = \mathbf{R}^\top \mathbf{R}$. Then, we form the set of sampling points

$$\mathcal{S} = \{\mathbf{p}_\mathcal{U}\} \cup_{i=1}^n \left\{\mathbf{p}_\mathcal{U} + \delta \mathbf{r}_i, \mathbf{p}_\mathcal{U} - \delta \mathbf{r}_i\right\},$$

where $\eta = \delta\sqrt{n + \beta}$ is parameterized with some constants $\alpha, \beta > 0$. Finally, this expectation can be approximated with

$$\mathbb{E}_{\mathbf{p}_\mathcal{U}}\left\{\mathbf{F}_D(\mathbf{p}_\mathcal{K}, \mathbf{p}_\mathcal{U})\right\} \approx \sum_{\mathbf{y}_j \in \mathcal{S}} w_\pi(\mathbf{y}_j) \mathbf{F}_D(\mathbf{p}_\mathcal{K}, \mathbf{y}_j) \tag{7.5}$$

where $w(\mathbf{y}_j) = f_\pi(\mathbf{y}_j) / \sum_{l \in \mathcal{S}} f_\pi(\mathbf{y}_l)$. The scheme (7.5) provides a computationally efficient estimate $\hat{\mathbf{F}}_B$ of $\mathbf{F}_B$, which can be implemented in real-time.

7.4 Localizability Potential

Here, we design a localizability potential that permits $\mathcal{K}_M$ deployment. Then an experiment that illustrates the link between empirical localizability and its potential is provided.

7.4.1 Localizability Potential

We aim to design motion planners that enhance the quality of $\hat{\mathbf{p}}_{\mathcal{U}}$. We use LS and the KF estimators to compute these estimates. These algorithms are designed to minimize the total Mean Square Error (MSE) of $\hat{\mathbf{p}}_{\mathcal{U}}$, defined as follows

$$MSE(\hat{\mathbf{p}}_{\mathcal{U}}) := \mathbb{E}\{||\hat{\mathbf{p}}_{\mathcal{U}} - \mathbf{p}_{\mathcal{U}}||^2\} = \mathrm{Tr}\left\{\Sigma_{\hat{\mathbf{p}}_{\mathcal{U}}}\right\}.$$

Thus, we choose the MSE as performance criterion on the estimates to quantify the tag's localizability. The CRLB, defined in the Theorem 7.1, yields the following result for each considered FIM, $C \in \{D, B\}$ depending with respect to which information we condition

$$J_C(\mathbf{p}_{\mathcal{K}_M}, \mathbf{p}_{\mathcal{U}}) := \mathrm{Tr}\left\{\mathbf{F}_C^{-1}(\mathbf{p})\right\} \leq MSE(\hat{\mathbf{p}}_{\mathcal{U}}), \tag{7.6}$$

where $J_C(\mathbf{p}_{\mathcal{K}_M}, \mathbf{p}_{\mathcal{U}})$ is the *localizability potential* and with $\mathbf{p}_{\mathcal{K}_M} := [\dots, \mathbf{p}_i^\top, \dots]^\top$ for $i \in \mathcal{K}_M$. Then, *we assume* that decreasing J_C yields a better MSE for the estimator $\hat{\mathbf{p}}_{\mathcal{U}}$ in practice [Patwari et al., 2005, Papalia et al., 2021]. Hence, we define the following placement problem for the mobile anchors

$$\mathbf{p}^*_{\mathcal{K}_M} = \underset{\mathbf{p}_{\mathcal{K}_M} \in \mathbb{R}^{nK_M}}{\mathrm{argmin}} \; J_C(\mathbf{p}_{\mathcal{K}_M}, \mathbf{p}_{\mathcal{U}}) \tag{7.7}$$

where $\mathbf{p}^*_{\mathcal{K}_M}$ depends on the tag's position. We propose to solve (7.7) locally in real-time by descending the potential gradient, which is a common approach for mobile robot motion planning [Choset et al., 2005]. We compute the partial derivatives of J_C, with respect to $\xi_i \in \{x_i, y_i, z_i\}$ a given coordinate of $i \in \mathcal{K}$, thanks to the following formula [Le Ny and Chauvière, 2018]

$$\frac{\partial J_C(\mathbf{p}_{\mathcal{K}_M}, \mathbf{p}_{\mathcal{U}})}{\partial \xi_i} = -\mathrm{Tr}\left\{\mathbf{F}_C^{-2} \frac{\partial \mathbf{F}_C}{\partial \xi_i}\right\}, C \in \{D, B\}. \tag{7.8}$$

Then, the results of (7.8) are gathered in gradient vectors

$$\nabla_i J_C(\mathbf{p}_{\mathcal{K}_M}, \mathbf{p}_{\mathcal{U}}) := [\partial J_C(\mathbf{p}_{\mathcal{K}_M}, \mathbf{p}_{\mathcal{U}})/\partial \mathbf{p}_i]^\top \in \mathbb{R}^n$$

for each $i \in \mathcal{K}_M$, which yields the total gradient $\nabla J_C(\mathbf{p}_{\mathcal{K}_M}, \mathbf{p}_{\mathcal{U}}) = [\dots \nabla_i J_C^\top(\mathbf{p}_{\mathcal{K}_M}, \mathbf{p}_{\mathcal{U}}) \dots]^\top \in \mathbb{R}^{nK_M}$ for the set $\mathcal{K}_M$. The differentiation of the DFIM defined in (7.3), required to evaluate

the gradient of J_D with (7.8), gives

$$\frac{\partial \mathbf{F}_D}{\partial \xi_i} = \frac{1}{\sigma_i^2}\left(\frac{2(\xi - \xi_i)}{d_i^4}\mathbf{e}_i\mathbf{e}_i^\top + \frac{1}{d_i^2}\mathbf{D}_{\xi_i}\right), \tag{7.9}$$

denoting $\xi \in \{x, y, z\}$ the tag' coordinates. $\mathbf{D}_{\xi_i} \in \mathbb{R}^{n\times n}$ is obtained using elementary differentiation rules

$$D_{\xi_i}^{\eta,\zeta} = \begin{cases} 2(\xi_i - \xi), \text{ if } \eta = \zeta = \xi, \\ \zeta_i - \zeta, \text{ if } \eta = \xi \text{ and } \zeta \neq \xi, \\ 0, \text{ if } \eta \neq \xi \text{ and } \zeta \neq \xi, \end{cases}$$

and $D_{\xi_i}^{\zeta,\eta} = D_{\xi_i}^{\eta,\zeta}$, for all $\eta, \zeta \in \{x, y, z\}^2$.

7.4.2 An Example of Localizability Enhancement

We show an example that highlights the dependence between the localizability potential and the estimates' precision through a simple experiment. Consider a localization system made of two fixed anchors $\mathcal{K} = \{K_1, K_2\}$ and a tag, carried by a ground robot shown in Fig. 7.1. Here, the anchors and the tags are custom boards equipped with a Decawave `DW1000M` UWB module [Decawave, 2017]. The anchors are placed on tripods at the same height $z_1 = z_2 = 1.7$ m. We assume that the tag's height $z = 0.7$ m is a known parameter and so $\mathbf{p}_\mathcal{U} = [x, y]^\top$ has to be determined through ranging. Each anchor-tag pair $(i, T), i \in \mathcal{K}$ acquires a distance measurement $\tilde{d}_i$ thanks to the bias-compensated *Single-Sided Two-Way Ranging* (SSTWR) protocol described in [Cano et al., 2022b]. These estimates $\hat{\mathbf{p}}_\mathcal{U}$ are computed by solving the LS problem

$$\hat{\mathbf{p}}_\mathcal{U} = \underset{\mathbf{p}_\mathcal{U}\in\mathbb{R}^2}{\operatorname{argmin}} \sum_{i\in\mathcal{K}} \left(\tilde{d}_i - ||\mathbf{p}'_\mathcal{U} - \mathbf{p}'_i||\right)^2 \tag{7.10}$$

thanks to the Gauss-Newton algorithm [Bertsekas, 2016], where $\mathbf{p}'_\mathcal{U} := [\mathbf{p}_\mathcal{U}^\top, z]^\top$ and $\mathbf{p}'_i := [\mathbf{p}_i^\top, z_i]^\top$. Here, we assume that the information is modeled by the DFIM $\mathbf{F}_D$ introduced in (7.2) since we do not provide prior information to build $\hat{\mathbf{p}}_\mathcal{U}$. The measurement noise is modeled with a standard deviation of $\sigma = 2.5$ cm. We used a millimeter-accurate motion capture system, which provides a ground truth for $\mathbf{p}_\mathcal{U}$, to compute estimation errors.

As shown in Fig. 7.2, the tag's initial position $\hat{\mathbf{p}}_\mathcal{U}(0)$ is almost aligned with the anchors. This configuration has a poor localizability since Proposition 7.2 states that the DFIM is singular in the case of sensors alignment. To improve this configuration, the robot is deployed following

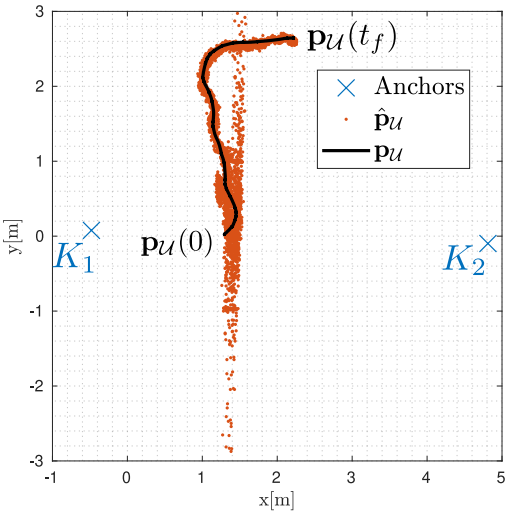

Figure 7.2 – Estimates $\hat{\mathbf{p}}_{\mathcal{U}}(t)$ and actual trajectory $\mathbf{p}_{\mathcal{U}}(t)$

a gradient descent scheme [Le Ny and Chauvière, 2018] using (7.8) and (7.9)

$$\mathbf{p}_{\mathcal{U}}^{k+1} = \mathbf{p}_{\mathcal{U}}^{k} - \gamma^k \nabla_T J_D(\mathbf{p}_{\mathcal{U}}^{k}),$$

with $\nabla_T J_D(\mathbf{p}_{\mathcal{U}}^{k}) = -\sum_{i\in\mathcal{K}} \nabla_i J_D(\mathbf{p}_{\mathcal{U}}^{k})$. The superscript k denotes time indices and $\gamma^k > 0$ is a normalized step-size [Bertsekas, 2016]. We provided the way-points generated by the scheme to a lower-level position controller [Lynch and Park, 2017, p.529] using the ground truth values as input. The trajectory is visible in Fig. 7.2 and superposed with the obtained estimates $\hat{\mathbf{p}}_{\mathcal{U}}$.

In Fig. 7.3 we plotted the time series of the localizability cost function $J_C(\mathbf{p}_{\mathcal{U}}^{k})$ alongside the empirical squared errors $SE^k := ||\hat{\mathbf{p}}_{\mathcal{U}} - \mathbf{p}_{\mathcal{U}}||^2$ for a trajectory realization. As seen in (7.6),

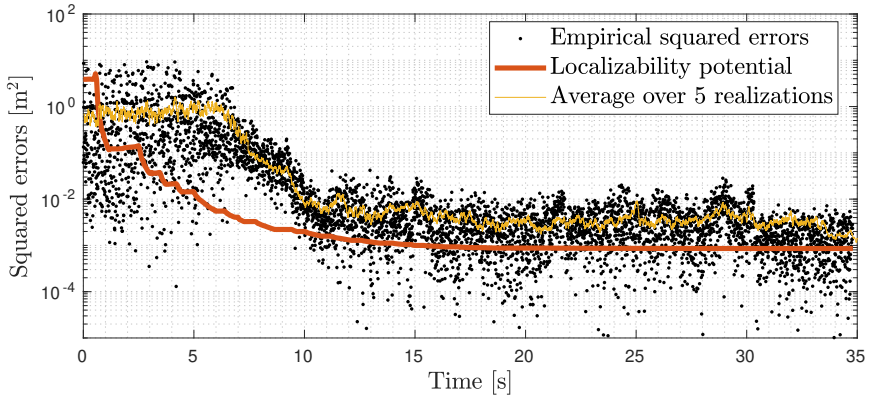

Figure 7.3 – Localizability function and squared errors

the potential J_D is a lower bound on the expectation of the squared error which seems to be empirically observed along the trajectory after 1 s. To highlight this remark, we plotted a 100-point sliding average curve over 5 trajectories in Fig. 7.3. This experiment stresses that the descent of the localizability potential has strongly enhanced (SE decreases of three orders of magnitude) the estimates' quality.

7.5 Motion Planners

In this section, we provide two methods to decrease the localizability potentials J_D and J_B with real-time position estimates.

7.5.1 Deterministic Motion Planner

In this subsection we suppose that we do not have access to prior information, *i.e.*, $\mathbf{p}_{\mathcal{U}}$ is treated as a deterministic parameter and J_D is considered as the potential. To decrease this function, we use the *Deterministic Motion Planner* (DMP) based on the approach presented in [Cano and Le Ny, 2023, V]. This motion planner uses the estimated gradient $\nabla_{\mathbf{p}_{\mathcal{K}_M}} J_c(\mathbf{p}_{\mathcal{K}_M}, \hat{\mathbf{p}}_{\mathcal{U}})$ of $J_c(\mathbf{p}_{\mathcal{K}_M}, \mathbf{p}_{\mathcal{U}})$ where $\mathbf{p}_{\mathcal{U}}$ is replaced by its estimate $\hat{\mathbf{p}}_{\mathcal{U}}$. At each time k, a local variable $\mathbf{q}^{l,k}$ is set to $\mathbf{q}^{0,k} = \mathbf{p}^k_{\mathcal{K}_M}$ in order to perform the following descent operation

$$\mathbf{q}^{l+1,k} = \mathbf{q}^{l,k} - \mathbf{\Gamma}^l \nabla J_D(\mathbf{q}^{l,k}, \hat{\mathbf{p}}^k_{\mathcal{U}}), \tag{7.11}$$

for $l \in [0, L-1]$ where L is the maximum iterations number. The localizability gradient is evaluated with the last available estimate $\hat{\mathbf{p}}^k_{\mathcal{U}}$. The step-size matrix $\mathbf{\Gamma}^k = \mathrm{diag}(\dots, \gamma_i^k \mathbf{I}_n, \dots)$ is parameterized with $\gamma^l = \gamma_0 \min\{1, \gamma_M ||\nabla_i J_D(\mathbf{q}^l, \hat{\mathbf{p}}^k_{\mathcal{U}})||^{-1}\}$ where $\gamma_0 > 0$ and γ_M is set order to limit the magnitude of the gradient [Bertsekas, 2016]. The DMP is stopped i) if $\max_i ||\nabla_i J_D(\mathbf{q}^{l,k}, \hat{\mathbf{p}}^k_{\mathcal{U}})|| < \epsilon$ where $\epsilon > 0$ is a given tolerance; or ii) if L iterations are computed and then yields $\mathbf{p}^{k,*}_{\mathcal{K}_M}$. Finally, $\mathbf{p}^{k,*}_{\mathcal{K}_M}$ is transmitted to the mobile anchors, setting $\mathbf{p}^{k+1}_{\mathcal{K}_M,\mathrm{ref}} := \mathbf{q}^{L,k}$ as the anchors' controller references at time $k+1$.

7.5.2 Bayesian Motion Planner

In the case of a Gaussian distribution prior $\mathcal{N}\left(\mathbf{p}^k_{\mathcal{U}}, \Sigma^k\right)$, the information is gathered in the BFIM $\mathbf{F}_B$ given by (7.1). Here we propose the *Bayesian Motion Planner* (BMP) that decreases an approximated gradient of J_B. We suppose that $\mathbf{\Sigma}^k$ and $\hat{\mathbf{p}}^k_{\mathcal{U}}$ are known by the motion planner at time k. First, the equation (7.8) used to compute the potential gradient involves the quantity $\mathbf{F}^k_B$ which must be estimated. To do so, we use the numerical

approximation (7.5), that yields $\hat{\mathbf{F}}_B^k$ computed thanks to $\{\hat{\mathbf{p}}_{\mathcal{U}}^k, \mathbf{\Sigma}^k\}$. Second, $\partial \mathbf{F}_B / \partial \xi_i^k$ computation is required for all $\xi_i^k \in \{x_i^k, y_i^k, z_i^k\}$ with $i \in \mathcal{K}_M$ at time k. The computation of $\partial \mathbf{F}_B(\mathbf{p}^k)/\partial \xi_i^k = \partial \mathbb{E}_{\mathbf{p}_\mathcal{U}} \left\{ \mathbf{F}_D(\mathbf{p}_\mathcal{U}^k, \mathbf{p}_\mathcal{K}^k) \right\} / \partial \xi_i^k$ involves an expectation over the prior PDF and cannot be analytically computed.

To address this issue, we implement a stochastic gradient algorithm [Bottou, 2012]. The BMP initializes the local variable $\mathbf{q}^{0,k} = \mathbf{p}_{\mathcal{K}_M}^k$ similarly to the DMP. At each iteration l of the algorithm, a random draw $\mathbf{r}^l$ with $\mathbf{r}^l \sim \mathcal{N}\left(\hat{\mathbf{p}}_\mathcal{U}^k, \Sigma^k\right)$ is realized. Then for each mobile tag $i \in \mathcal{K}_M$, we compute the following gradient descent step

$$\mathbf{q}_i^{l+1} = \mathbf{q}_i^l - \gamma^l \hat{\nabla}_i J_B^l, \tag{7.12}$$

where $\hat{\nabla}_i J_B^l = [\dots s_{\xi_i}^l \dots]^\top$, for $\xi \in \{x, y, z\}$ with

$$s_{\xi_i}^l = \mathrm{Tr}\left\{ \left(\hat{\mathbf{F}}_B^l\right)^{-2} \frac{\partial \mathbf{F}_D(\mathbf{q}^l, \mathbf{r}^l)}{\partial \xi_i} \right\}, \tag{7.13}$$

and $\mathbf{q}^l = [\dots \mathbf{q}_i^\top \dots]^\top$. In (7.12), for a sufficiently small step-size γ^l, we approximate $\partial \mathbb{E}_{\mathbf{p}_\mathcal{U}} \{\mathbf{F}_D(\mathbf{p}_\mathcal{K}, \mathbf{p}_\mathcal{U})\} / \partial \xi_i$ after repeating the iterations. Indeed, performing (7.12) with small moves empirically averages the gradient by successive draws and then estimates its expectation with a limited computational cost [Bottou, 2012]. We adjusted $\mathbf{\Gamma}^l$ with the rule presented in Section 7.5.1 in order to compute $\hat{\nabla}_{\mathbf{p}_{\mathcal{K}_M}} J_B(\mathbf{q}^l, \mathbf{r}^l) = [\dots, \hat{\nabla}_i J_B^l, \dots]^\top$, $i \in \mathcal{K}_M$. After L iterations of (7.12), the BMP transmits $\mathbf{q}^{L,k}$ to the anchors as new reference positions $\mathbf{p}_{\mathcal{K}_M,\mathrm{ref}}^{k+1}$. Algorithm 7.1 summarizes the procedure.

Algorithm 7.1: BMP algorithm.

Input: $\mathbf{p}_\mathcal{K}^k$,$\hat{\mathbf{p}}_\mathcal{U}^k$,$\mathbf{\Sigma}^k$

$\mathbf{q}^{0,k} = \mathbf{p}_{\mathcal{K}_M}^k$

for $l \in [0, L-1]$ **do**

  draw randomly $\mathbf{r}^l \sim \mathcal{N}\left(\hat{\mathbf{p}}_\mathcal{U}^k, \Sigma^k\right)$

  compute $\hat{\mathbf{F}}_B$ with (7.5)

  compute $\hat{\nabla}_{\mathbf{p}_{\mathcal{K}_M}} J_B(\mathbf{q}^l, \mathbf{r}^l)$ with (7.12)

  $\mathbf{q}^{l+1,k} = \mathbf{q}^{l,k} - \mathbf{\Gamma}^l \hat{\nabla}_{\mathbf{p}_{\mathcal{K}_M}} J_B(\mathbf{q}^l, \mathbf{r}^l)$

end

transmit $\mathbf{p}_{\mathcal{K}_M,\mathrm{ref}}^{k+1} := \mathbf{q}^{L,k}$ to $\mathcal{K}_M$.

7.6 Multi-Robot Deployment

We present two deployment experiments using the DMP and the BMP. We consider a system of three anchors $\mathcal{K} = \{K_1, K_2, K_3\}$, with two of them $\mathcal{K}_M = \{K_1, K_2\}$ carried by ground robots (where $z_1 = 43$ cm, $z_2 = 53$ cm) and the third fixed on a tripod ($z_3 = 1.60$ m). We aim to localize a tag T carried by a robot (where $z = 51$ cm is known), with $\mathbf{p}_\mathcal{U} \in \mathbb{R}^2$ unknown. The tag's location is determined thanks to range measurements provided by SSTWR performed by UWB sensors, as in Section 7.4.2. The three robots used in the experiments are shown in Fig. 7.1.

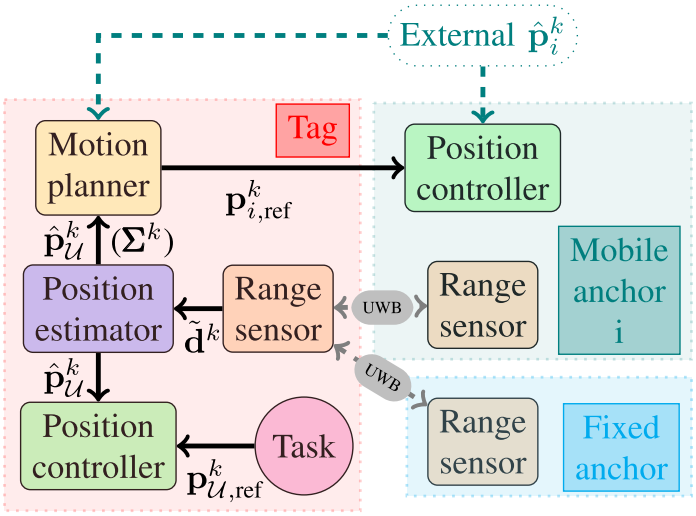

Figure 7.4 – System architecture

The tag has an assigned task that involves to follow a given trajectory $\{\mathbf{p}_{\mathcal{U},\text{ref}}^k\}$ along the x-axis of the workspace between the origin and $x(t_f) = 1.5$ m, where t_f is the final time of the experiment. The estimates $\hat{\mathbf{p}}_\mathcal{U}$ are used by the tag to perform its own trajectory and by the anchors to decrease the localizability potential. The architecture of the system is summarized in Fig. 7.4 and is implemented using the middleware `ROS Melodic`.

7.6.1 DMP implementation with LS estimator

First, we implemented the DMP using $\hat{\mathbf{p}}_\mathcal{U}^k$ obtained by the LS estimator (7.10) with the last available measurements. The initial positions $\mathbf{p}_j(0)$ of the robots $j \in \mathcal{K}_M \cup \{T\}$ with the fixed anchor's position $\mathbf{p}_3$ are shown in Fig. 7.5. The DMP computes an iteration when the reference position of the tag $\mathbf{p}_{\mathcal{U},\text{ref}}^k$ and the planed anchors' position $\mathbf{p}_{i,\text{ref}}^k$ are reached for K_1 and K_2 (with a tolerance of 20 cm). After convergence, the DMP sends to the anchors the

new reference positions $\mathbf{p}_{i,\mathrm{ref}}^{k+1}$ while $\mathbf{p}_{\mathcal{U},\mathrm{ref}}^{k+1}$ is independently sent to the tag. Then, they are transmitted to the anchors position controllers and processed. After a time of $t_f = 140$ s the robots reached their final positions $\mathbf{p}_j(t_f)$, $j \in \mathcal{K}_M \cup \{T\}$.

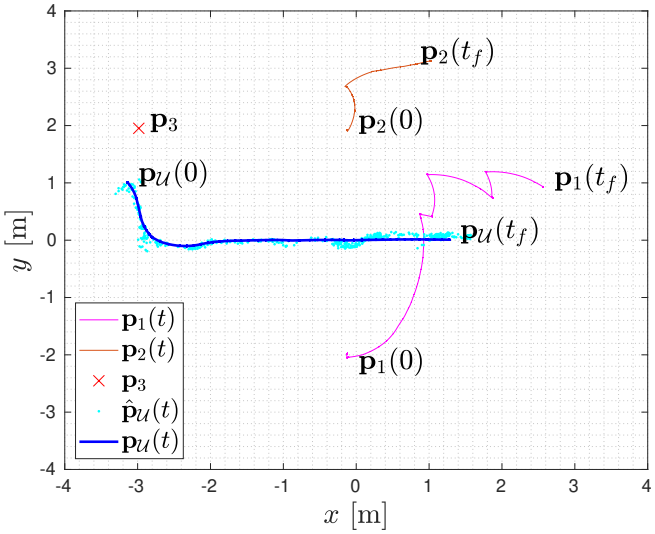

Figure 7.5 – Robots trajectory and estimates (DMP/LS)

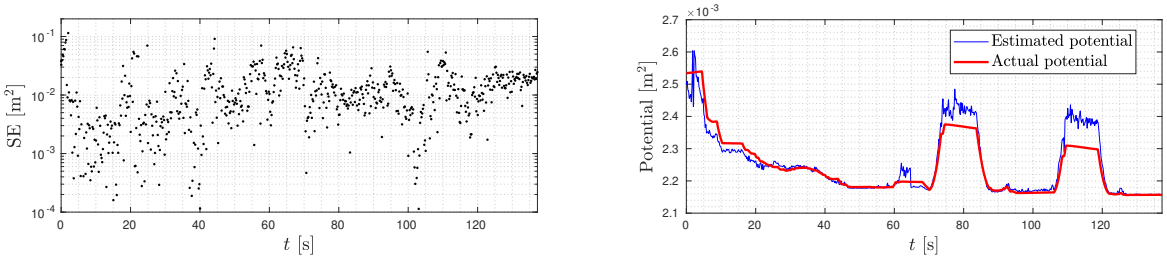

(a) Empirical squared errors

(b) Localizability potential

Figure 7.6 – Results with (DMP/LS)

The trajectories of each robot with the estimates $\hat{\mathbf{p}}_{\mathcal{U}}$ are plotted in Fig. 7.5 and their squared errors (SE) in Fig. 7.6a. During the trajectory, the average squared error on $\hat{\mathbf{p}}_{\mathcal{U}}$ is around $(0.11)^2$ m, which remains sufficient to follow the tag's reference trajectory. Nevertheless, we noticed some estimation issues due to measurement outliers, produced by nearby reflective surfaces such as the ground and the robots' bodies. This is a strong motivation to consider prior information (*i.e.*, filtering) in the estimation schemes to filter these unmodelized phenomena which can generate significant errors in the localizability gradient computation.

In Fig. 7.6b we plotted the localizability potential computed with the estimated $\hat{\mathbf{p}}_{\mathcal{U}}$ (*i.e.*, $J_D(\mathbf{p}_{\mathcal{K}_M}, \hat{\mathbf{p}}_{\mathcal{U}})$, in blue) and the reference $\mathbf{p}_{\mathcal{U}}$ (*i.e.*, $J_D(\mathbf{p}_{\mathcal{K}_M}, \mathbf{p}_{\mathcal{U}})$, in red) obtained by the motion capture reference system. The increases in the potential observable at $t = 70$ s and $t = 110$ s are due to the tag deploying faster than the anchors while it achieves its task. Indeed, gradient computations in (7.11) are based on the $k-1$-th tag's position. However, the potential is decreased after the anchors' deployment and maintained at low values during the trajectory. We remark that the potential values in Fig. 7.6b are lesser than the SE presented in Fig. 7.6a since (7.6) holds.

7.6.2 BMP implementation with EKF estimator

Here, we present the BMP-based deployment while an Extended Kalman Filter (EKF) [Kay, 1993] is used to compute $\hat{\mathbf{p}}_{\mathcal{U}}$. In order to implement the EKF, we consider the continuous-time kinematic state $\mathbf{x}(t) = [\mathbf{p}_{\mathcal{U}}, \mathbf{v}_{\mathcal{U}}]^\top$, where $\mathbf{v}_{\mathcal{U}} = [v_x, v_y]^\top$ is the tag velocity vector. We suppose the single-integrator dynamic model as follows for $\xi \in \{x, y\}$

$$\begin{cases} \dot{\xi} = v_\xi + \omega_\xi, \\ \dot{v}_\xi = \kappa_\xi \end{cases}$$

where ω_ξ are κ_ξ independent centered white Gaussian noises with power spectral densities $S_{\omega,\omega} = 10^{-2}$ and $S_{\kappa,\kappa} = 10^{-3}$. The observation model, at time l is given by $\tilde{\mathbf{d}}^l := \mathbf{d}^l + \boldsymbol{\nu}^l$ denoting $\mathbf{d}^l = [d_1, d_2, d_3]^\top$ and $\boldsymbol{\nu}^l \sim \mathcal{N}(\mathbf{0}, (0.05)^2\mathbf{I}_3)$.

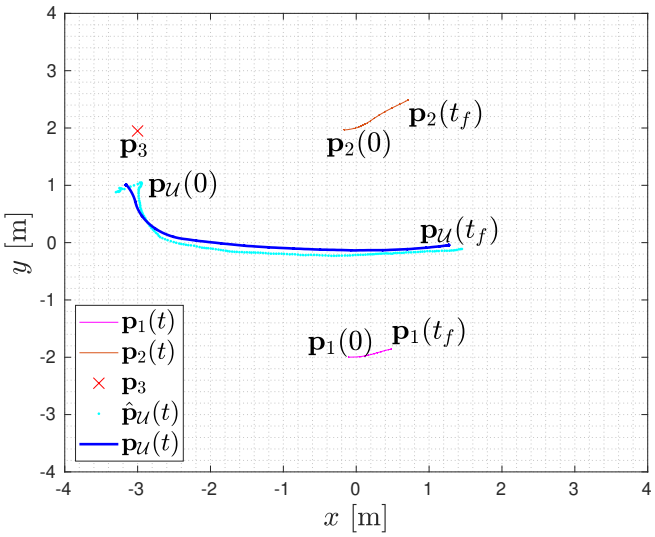

Figure 7.7 – Robots trajectory and estimates (BMP/EKF)

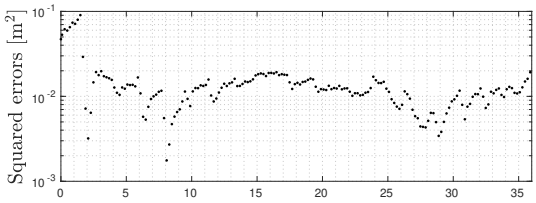

(a) Empirical squared errors

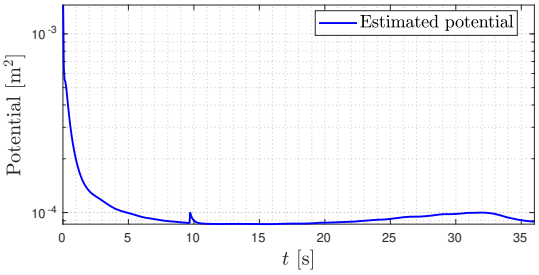

(b) Localizability potential

Figure 7.8 – Results with (BMP/EKF).

After careful discretization of the tag's kinematics model, we implemented the EKF in the corresponding robot. It allowed to compute estimates $\hat{\mathbf{x}}^l$ and their covariance matrices $\hat{\mathbf{\Sigma}}^l_{\mathbf{x}}$ with an average refresh rate of 20 Hz when new measurements $\mathbf{d}^l$ are available. We use as input of the BMP at step k the last available estimate $\hat{\mathbf{p}}^k_{\mathcal{U}}$ extracted from $\hat{\mathbf{x}}^k$ and $\mathbf{\Sigma}^k := \hat{\mathbf{\Sigma}}^k_{\mathbf{p}_{\mathcal{U}}}$ from the estimated covariance $\hat{\mathbf{\Sigma}}^k_{\mathbf{x}}$ provided by the EKF. Then, we repeated with the BMP the same experiment presented in 7.6.1.

For this experiment, the trajectories and the estimates are plotted in Fig. 7.7 while the SE are shown in Fig. 7.8a. At the beginning of the trajectory, we observe on Fig. 7.8a a quick decrease of the SE and the potential function on Fig. 7.8b. Indeed, the measurement, provided at a 20 Hz refresh rate allows the EKF to converge fast and $\mathrm{Tr}\left\{(\mathbf{\Sigma}^k)^{-1}\right\}$ increases as the state estimate's uncertainty decreases. Around $t = 30$ s, we notice a slight increase of the potential values, due to the temporary alignment of the three robots in the workspace. This slight raise yields an insufficient gradient norm to redeploy the anchors (the gradient is strongly weighted by $\mathbf{\Sigma}^k$, which remains low has the EKF has converged) while the estimates remains at tolerable precision. Moreover, in contrast to the experiment presented in Section 7.6.1, the EKF smoothed the errors generated by measurement outliers despite using a simple kinematic model.

In the BMP experiment, the tag's took $t_f = 36$ s to reach its destination. This difference with DMP is explained by the more restrained deployment of the anchors. Indeed, considering the prior information given by the EKF (which takes into account all measurement history [Kay, 1993]) the localizability is less dependent on the geometry than in the deterministic case. Despite transient effects at the beginning of the experiment due to the EKF convergence, the mean of the SE over the trajectory is $(0.11)^2$ m which yields a similar performance than DMP for a faster deployment time. Indeed, the DMP deploys the anchors at local optimal positions in terms of geometry at each time k irrespective of the prior information used to

build $\hat{\mathbf{p}}_k$, which can be time-costly. In contrast, the BMP is influenced dynamically by the prior on $\mathbf{p}_{\mathcal{U}}$ and redeploys the anchors if that information suddenly decreases, which makes it more operative.

7.7 Conclusion and Perspectives

In this paper, we showed a method to maintain the localizability of a robot performing relative distance measurements with known positions sensors, *i.e*, anchors. Thanks to covariance inequalities, we defined a novel localizability potential taking into account prior information on the robot's position. We proposed a methodology to compute and optimize this quantity by moving mobile anchors. Through experiment, we highlighted the relationship between the localizability cost function and actual positioning uncertainties. Finally, we validated existing and novel motion planners in multi-robot experiments. Future work will include leveraging tighter bounds capturing more realistic measurement models and prior dynamics.

Acknowledgment

The authors thank Louis Treton from ISAE for his availability and his assistance.

CHAPTER 8 BAYESIAN ANCHOR DEPLOYMENT

In this additional chapter, we are interested in the optimal deployment of static anchors to maximize the tags' localizability using distance measurements. This problem formulation is of interest when the likely operating area of the tags is known *a priori*. In fact, this information can be used by the position estimators of the tags. As a concrete example, the estimate may be constrained to be located inside the workspace, which can be seen as a kind of prior information.

The proposed approach requires a prior spatial statistical distribution of the tags within the workspace. We aim to design an anchor deployment algorithm that maximizes the localizability of the tags while taking into account their prior distribution. The BCRLB is particularly adapted to solve this problem, since it allows to incorporate prior information in the modeling of the estimation uncertainties. However, this notion of uncertainty is defined on average in the workspace, whereas we must also guarantee a minimum level of precision at all locations.

8.1 Related Work

Let us give a brief overview of how the anchor deployment problem is treated in the literature. The modeling of positioning uncertainty under Gaussian measurement is well studied in [Patwari et al., 2005], using the CRLB as a modeling of positioning uncertainty of multi-agent systems located by RMs. And it can be used to place agents to optimize the localizability of tags, *e.g.* as claimed throughout Chapter 5. As an alternative to this uncertainty model, the DoP can also be used to optimally place anchors to localize tags in a ranging context [Khalife and Kassas, 2019, Zhao et al., 2020].

In [Ash and Moses, 2008], the authors propose an approach to optimize the geometry of ranging networks in terms of a lower bound on the MSE using the trace of the CRLB. In this paper, a planar solution is found by optimizing an algebraic criterion on the subspace of the possible Euclidean transformations of the network's agent positions. In [Jourdan and Roy, 2008], a Position Error Bound (PEB) optimization, in fact also a bound on the MSE derived from a CRLB, is proposed for anchors located on an ellipse within the plane. In that work, the authors used a single-term path loss model that exploited range-deteriorated centered Gaussian noise with constant variance. In [Monica and Ferrari, 2015], another MSE lower bound optimization for anchor deployment is proposed in the UWB range-based navigation

context in a corridor. However, in practice, these indoor anchor deployment approaches are limited to the boundaries of the workspace. This can be a problem since it is known that MP outliers occur near reflective surfaces and could be exacerbated by placing the anchors near walls that bound a workspace.

The more recent study [Khalife and Kassas, 2019] uses the DoP to quantify the positioning uncertainty introduced by a given anchor geometry. In particular, the authors propose to place additional sensors for source localization and select signal of opportunity to correct vertical DoP in GNSS-based navigation solutions. The proposed approach uses both A and D optimal design strategies to solve the problem via constrained fractional programming. *Zhao et al.* in [Zhao et al., 2020] also use the DoP matrix to maximize the tags' localizability in UWB sensor deployment using Bayesian optimization to reduce a cost function based on the GDoP. Again, this approach remains two-dimensional and aims to place anchors at the boundary of the workspace. The preprint article [Panwar et al., 2022] aims to place static UWB anchors that perform hybrid source localization, *i.e.*, using ToA, RSS, and AoA fused data to locate a given source. This theoretical study assumes that the placement is performed knowing the location of the source, which is different from the problem addressed in this chapter.

In this chapter, we propose an anchor deployment method that takes into account both range deteriorated RMs and prior information on the location of the tags in order to maximize their localizability. The deployment algorithm takes advantage of the BCRLB to model the uncertainties, which is a novel approach in anchor deployment that allows a more realistic three-dimensional localizability optimization for a moderate computational cost. Another novelty of the proposed method is that the tags positions are probabilistic, allowing the geometry optimization for complex workspaces weighted by probability.

8.2 Problem Statement

We are interested in deploying static anchors performing distance measurements with tags in an *a priori* known operating area. This section gives the mathematical formalism of that problem. As a preliminary remark, we consider in the rest of this chapter that the tags are laying at unknown places and that their location is modeled by a PDF, assumed known.

8.2.1 Notation and Assumptions

We want to place the set $\mathcal{K}$ of $|\mathcal{K}| = K$ anchors in a n-dimensional space ($n \in \{2, 3\}$). The set $\mathcal{K}$ performs distance measurements with a set of tags $\mathcal{U}$ to position it. The positions of

the tags are assumed to be unknown, although their PDF $f_{\mathcal{U}} : \mathbb{R}^n \mapsto \mathbb{R}^+$ is known. We also assume that the tags are generally unable to perform RMs between themselves, as is typically the case when OWR protocols are implemented. For the sake of simplicity, in this chapter, we assume that there exists only a single probabilistic tag laying in the workspace. Then we model a tag's position by the random vector $\mathbf{p}_{\mathcal{U}} \in \mathbb{R}^n$ following the law given by $f_{\mathcal{U}}$.

Here we consider the Gaussian range-deteriorated measurement model (6.2) introduced in Chapter 6. Namely, we have the range measurement $\tilde{d}_k \sim \mathcal{N}\left(d_k, \sigma_k^2(d_k; \boldsymbol{\alpha})\right)$ captured by the anchor $k \in \mathcal{K}$, where $d_k = \|\mathbf{p}_{\mathcal{U}} - \mathbf{p}_k\|$. We recall that the general variance model $\sigma_k^2(d_k; \boldsymbol{\alpha})$ is given in the equation (6.3).

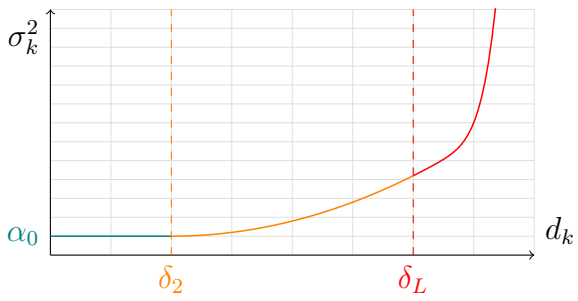

Figure 8.1 – Example of typical variance model

This model allows to capture soft communication losses (as emphasized in Remark 5.2 in Chapter 5) and power fading. In fact, a realistic anchor deployment scheme requires careful modeling of distortion at long range in order to best match the real-world performance of the localization system.

To give an illustration of such a model, in Figure 8.1 we have plotted a polynomial model of the variance $\sigma_k^2(d_k; \boldsymbol{\alpha})$. This model includes standard performance at short range (teal segment, with constant variance), then as d_l increases, degradation due to RxP fading (orange segment), and finally smooth communication losses (red segment) at long range. This variance map is given by

$$\sigma_k^2(d_k; \boldsymbol{\alpha}) = \alpha_0 + \alpha_2 (d_k - \delta_2)^2 \mathbf{1}_{d_k > \delta_2} + \alpha_L (d_k - \delta_L)^L \mathbf{1}_{d_k > \delta_L}, \tag{8.1}$$

where $0 < \delta_2 < \delta_L$, $\alpha_0, \alpha_2, \alpha_L \in \mathbb{R}_*^+$ and L is a high-order term (*e.g.*, we took $L = 6$ in Figure 8.1).

We assume that the tag has access to K Gaussian distance measurements $\tilde{d}_k$, collected in the vector $\tilde{\mathbf{d}} = [\dots \tilde{d}_k \dots] \in \mathbb{R}^K$. In fact, the model (8.1) makes it possible to "naively" consider the ranging graph to be fully connected by penalizing the quality of the measurements

captured by the remote tags. For the rest of the discussion, we denote the joint PDF of the K measurements as f_μ, as in Chapter 7.

8.2.2 Anchor Deployment Problem

We aim to place the set $\mathcal{K}$ knowing the PDF $f_\mathcal{U}$ of the tags in $\mathbb{R}^n$. In practice, the anchor deployment must satisfy several constraints. For example, they must be placed far enough away from RF-reflecting surfaces and the tags' operation zone to avoid interference with the robots' bodies. Therefore, to model these constraints, we assume that the anchors must satisfy $\mathbf{p}_\mathcal{K} \in \mathcal{P}^K$ where $\mathcal{P} \subset \mathbb{R}^n$, using the notation introduced in Chapter 5. On the other hand, we consider the subset $\mathcal{Z} \subset \mathbb{R}^n$, which models the robot's workspace, *i.e.*, where a minimum localizability must be ensured. We call the subset $\mathcal{P}$ the placement domain and $\mathcal{Z}$ the operation zone. Note that the above subsets and the PDF $f_\mathcal{U}$ are illustrated in the figure 8.2.

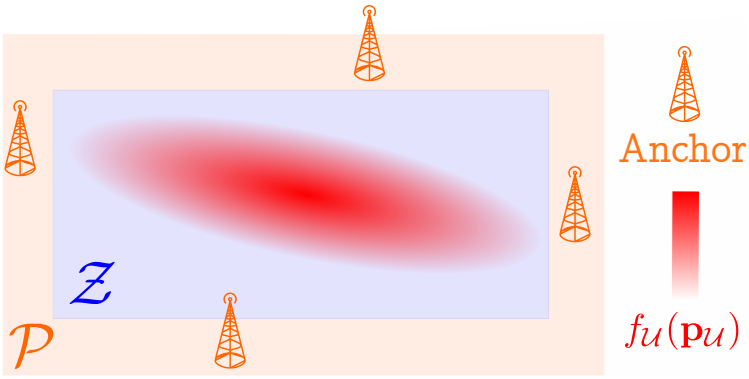

Figure 8.2 – Illustration of the placement and operation zones with the tag's position PDF

The deployment of the anchor set $\mathcal{K}$ can be seen as an average localizability optimization problem under the constraint that a minimum precision is ensured for all possible positions of the tag in $\mathcal{Z}$. For this, we define the localizability cost function $J(\mathbf{p}_\mathcal{U}; \mathbf{p}_\mathcal{K})$, which gives the expected positioning uncertainty for a given (deterministic) tag position $\mathbf{p}_\mathcal{U}$ and an anchor configuration $\mathbf{p}_\mathcal{K}$.

Therefore, we aim to solve the following constrained optimization problem

$$\begin{cases} \mathbf{p}_\mathcal{K}^* \in \underset{\mathbf{p}_\mathcal{K} \in \mathcal{P}^K}{\operatorname{argmin}} \; \mathbb{E}_{\mathbf{p}_\mathcal{U}} \left\{ J(\mathbf{p}_\mathcal{U}; \mathbf{p}_\mathcal{K}) \right\} \\ \text{s.t.} \; \underset{\mathbf{p}_\mathcal{U} \in \mathcal{Z}}{\max} \; J(\mathbf{p}_\mathcal{U}; \mathbf{p}_\mathcal{K}) < C_M, \end{cases} \tag{8.2}$$

where $C_M \in \mathbb{R}$, the maximum tolerated positioning uncertainty in the operation zone, is a

known parameter. We also assume that the number of anchors K is known or imposed. This fact implicitly allows a failure of (8.2) if the intended K is too small with respect to the expected minimum performance C_M, *i.e.*, K should be increased. (8.2) is typically a difficult combinatorial problem that cannot be solved optimally.

To approximate the optimal configuration $\mathbf{p}_{\mathcal{K}}^*$, we divide this problem into two parts. First, in Subsection 8.4.1, a coverage problem is proposed that ensures minimum localizability in the operation zone $\mathcal{Z}$ with respect to the cost function J, yielding an optimized coverage configuration $\mathbf{p}_{\mathcal{K}}^c$. Second, starting from $\mathbf{p}_{\mathcal{K}}^c$, a local policy minimizing J, based on a stochastic gradient descent using $f_{\mathcal{U}}$, is proposed in Subsection 8.4.2, with a stopping condition that includes the inequality constraint in (8.2). The design and computation of such a function is explained in Section 8.3.

8.3 Design of the Cost Function

Let us now construct the localizability cost function J that scores the uncertainty of a given estimator $\hat{\mathbf{p}}_{\mathcal{U}}$ that has access to the tag's distribution and the measurement PDFs, namely $f_{\mathcal{U}}$ and f_μ. Note that in this case, the PDF $f_{\mathcal{U}}$ can be used as a prior information to build $\hat{\mathbf{p}}_{\mathcal{U}}$. If we assume that the covariance $\mathbf{\Sigma}_{\hat{\mathbf{p}}_{\mathcal{U}}}$ is finite, then, using Theorem 7.1 presented in [Van Trees and Bell, 2007], the BCRLB $\mathbf{F}_B^{-1}$ satisfies

$$\mathbf{F}_B^{-1} \preceq \mathbf{\Sigma}_{\hat{\mathbf{p}}_{\mathcal{U}}}, \tag{8.3}$$

assuming that the Bayesian FIM, given by

$$\mathbf{F}_B(\mathbf{p}_{\mathcal{U}}; \mathbf{p}_{\mathcal{K}}) = -\mathbb{E}_{\tilde{\mathbf{d}}, \mathbf{p}_{\mathcal{U}}} \left\{ \frac{\partial^2 \ln f_\mu(\tilde{\mathbf{d}}; \mathbf{p}_{\mathcal{U}}, \mathbf{p}_{\mathcal{K}})}{\partial \mathbf{p}_{\mathcal{U}} \partial \mathbf{p}_{\mathcal{U}}^\top} \right\} - \mathbb{E}_{\mathbf{p}_{\mathcal{U}}} \left\{ \frac{\partial^2 \ln f_{\mathcal{U}}(\mathbf{p}_{\mathcal{U}})}{\partial \mathbf{p}_{\mathcal{U}} \partial \mathbf{p}_{\mathcal{U}}^\top} \right\}, \tag{8.4}$$

is invertible. This assumption is satisfied if there are at least $n+1$ unaligned anchors in $\mathcal{P}$ (see Proposition 7.2).

In order to solve (8.2), several assumptions have to be made on the uncertainty modeling. We assume that the localizability cost function can be computed with moderate computational cost for a given anchor configuration $\mathbf{p}_{\mathcal{K}}$, tag PDF $f_{\mathcal{U}}$ and measurement PDF f_μ. In fact, in general, criteria extracted from the Bayesian FIM are not analytic, *i.e.*, they are accessible only by numerical schemes.

Therefore, we restrict the tag's location PDF to be Gaussian in this chapter for computational reasons. Then the PDF f_u is assumed Gaussian, parameterized by $\bar{\mathbf{p}} \in \mathbb{R}^n$ and $\mathbf{\Sigma} \in \mathbb{R}^{n \times n}$,

i.e. $\mathbf{p}_{\mathcal{U}} \sim \mathcal{N}(\bar{\mathbf{p}}, \mathbf{\Sigma})$. In that case, one can express the following Bayesian FIM

$$\mathbf{F}_B(\mathbf{p}_{\mathcal{U}}; \mathbf{p}_{\mathcal{K}}) = \mathbb{E}_{\mathbf{p}_{\mathcal{U}}} \left\{ \sum_{k \in \mathcal{K}} \frac{w_k (\mathbf{p}_{\mathcal{U}} - \mathbf{p}_k)(\mathbf{p}_{\mathcal{U}} - \mathbf{p}_k)^\top}{\sigma_k^2 d_k^2} \right\} + \mathbf{\Sigma}^{-1}, \tag{8.5}$$

where $w_k := 1 + \frac{1}{2} \left(\partial \sigma_k^2 / \partial d_k \right)^2 \sigma_k^{-2}$, with σ_k defined in (8.1). The previous result is derived from the Slepian-Bangs formula [Kay, 1993, Section 3.9] and the demonstration is given in Chapter 6. To estimate the FIM, we use the method based on the *Unscented Transform* presented in Chapter 7, which leverages the scheme (7.5). Since this scheme has been used in that chapter for real-time optimization for an implementation in a MRS, the evaluation of the cost function is expected to be computationally affordable.

An application of the trace operator in (8.3) results in a MSE bound. Therefore, the following localizability cost function can be defined

$$J(\mathbf{p}_{\mathcal{U}}; \mathbf{p}_{\mathcal{K}}) = \mathrm{Tr} \left\{ \mathbf{F}_B^{-1} \right\} \preceq \mathbb{E}_{\hat{\mathbf{p}}_{\mathcal{U}}} \left\{ \| \hat{\mathbf{p}}_{\mathcal{U}} - \mathbf{p}_{\mathcal{U}} \|^2 \right\}. \tag{8.6}$$

This design choice is motivated by the fact that the inequality constraint parameter C_M in (8.2) is then directly related to a minimally achievable Root Mean Squared Error (RMSE). This criterion, widely used in positioning algorithm performance analysis, can be used to set an appropriate parameter C_M. For example, if UWB distance measurement is performed by TWR protocol to locate the tag, the order of magnitude of the expected precision, in terms of RMSE, is at best the decimeter [Decawave, 2018]. In this case, we can choose for instance $C_M = (5 \times 0.1)^2$ m^2, i.e., the maximal lower bound tolerated on the RMSE within the operation zone is 50 cm.

Nevertheless, the A-opt design used in (8.6) make the combinatorial problem difficult to solve in a greedy manner, *i.e.*, by placing the anchors one by one to decrease $\min_{\mathbf{p}_{\mathcal{U}}} J(\mathbf{p}_{\mathcal{U}}; \mathbf{p}_{\mathcal{K}})$. In fact, it is known that this type of function is generally not submodular [Krause et al., 2008], which implies that the greedy policy may produce results far from the global optimum [Bian et al., 2017]. In contrast, other cost functions, such as the D-opt design, allow for near-optimal results when greedy approaches are used [Sagnol, 2010, Section 7.2]. Therefore, for the design imposed by (8.6), we cannot use greedy policies to solve efficiently the combinatorial problem of anchor deployment.

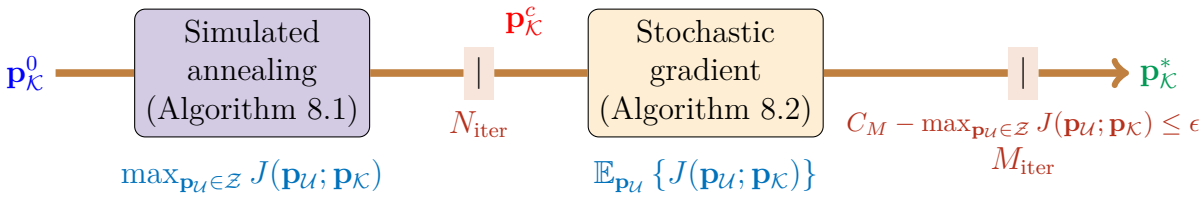

Figure 8.3 – Deployment strategy

8.4 Deployment Algorithm

In this Section, we propose a two-step strategy for solving the deployment problem (8.2). As shown in Figure 8.3, we first consider an initial configuration $\mathbf{p}^0_{\mathcal{K}} \in \mathcal{Z}^K$, which may be trivial (regular geometric form). Then, a simulated annealing heuristic is performed to coarsely cover the entire zone $\mathcal{Z}$ with a minimum localizability, regardless of the occurrence probability of the tags, represented by the PDF $f_{\mathcal{U}}$. Then, in a second time, the minimum of the coverage problem $\mathbf{p}^c_{\mathcal{K}}$ is refined with a local method (stochastic gradient descent) to minimize the expectation of the minimum MSE on tag location as written in the equation of the problem (8.2). The optimization terminates when the constraint is about to be violated, *i.e.*, when $C_M - \min_{\mathbf{p}_{\mathcal{U}} \in \mathcal{Z}} J(\mathbf{p}_{\mathcal{U}}; \mathbf{p}_{\mathcal{K}}) \leq \epsilon, \epsilon > 0$, or when the number of iterations M_{iter} is exceeded. In the same Figure 8.3, the cost functions minimized by the two algorithms are shown in blue.

The rest of this section explains the implementation of the algorithm, and an example of a standard use case is provided in Section 8.5. This solver has been implemented in Python, in our package `BAD` (Bayesian Anchor Deployment), which supports the main features of localizability, relying on the `Numpy` library.

8.4.1 Minimal Localizability Coverage Problem Algorithm

Here, we are interested in solving the following auxiliary problem of (8.2), defined as follows

$$\mathbf{p}^c_{\mathcal{K}} \in \underset{\mathbf{p}_{\mathcal{K}} \in \mathcal{P}^K}{\operatorname{argmin}} \max_{\mathcal{Z}} J(\mathbf{p}; \mathbf{p}_{\mathcal{K}}), \tag{8.7}$$

in order to respect the constraint in the main deployment problem and to obtain a compliant coarse initial anchor position $\mathbf{p}^c_{\mathcal{K}}$ before optimizing localizability. This formulation is largely inspired by the coverage problem, which is well known in the sensor networks literature [Cortes et al., 2004, Wang, 2011]. Since it is an NP-hard problem and not solvable by a greedy policy, we propose a simulated annealing approach, which is widely used in coverage

problem formulation due to its relative ease of implementation [Jourdan and Roy, 2008, Lin and Chiu, 2005].

First, we (coarsely) discretize the zone of operation $\mathcal{Z}$, which yields the set of finite points $\mathcal{Z}_D$. We assume an initial configuration $\mathbf{p}_{\mathcal{K}}^0$ at the start of the algorithm as well as an exploration step size $\eta > 0$.

At step l we start with the active configuration $\mathbf{p}_{\mathcal{K}}^a$ and evaluate a candidate configuration $\mathbf{p}_{\mathcal{K}}^l = \mathbf{p}_{\mathcal{K}}^a + \eta\mathbf{r}$ where $\mathbf{r} \in \mathbb{R}^{nK}$ is a random vector with components uniformly distributed between -1 and 1. We then constrain $\mathbf{p}_{\mathcal{K}}^l \in \mathcal{P}^K$ to stay in the placement zone. Then the selected configuration $\mathbf{p}_{\mathcal{K}}^l$ is compared to the best configuration found so far, and replaced if it appears to be better.

Algorithm 8.1: Simulated Annealing.

Data: $\mathbf{p}_{\mathcal{K}}^0, \theta_0, \beta, \eta, \mathcal{Z}_D$

$\theta^0 \leftarrow \theta_0$ $J^{\text{best}}, J^a \leftarrow \max_{\mathbf{p}\in\mathcal{Z}_\mathcal{D}} J(\mathbf{p}; \mathbf{p}_{\mathcal{K}}^0)$

$\mathbf{p}_{\mathcal{K}}^{\text{best}}, \mathbf{p}_{\mathcal{K}}^{\text{a}} \leftarrow \mathbf{p}_{\mathcal{K}}^0$.

for $l \in [1, N_{iter}]$ **do**

  draw $\mathbf{r} \sim \mathcal{U}_{[-\mathbf{1}_{nK}, \mathbf{1}_{nK}]}$ such that $\mathbf{p}_{\mathcal{K}}^l + \eta\mathbf{r} \in \mathcal{Z}^K$

  $\mathbf{p}_{\mathcal{K}}^l \leftarrow \mathbf{p}_{\mathcal{K}}^a + \eta\delta$

  $J^l \leftarrow \max_{\mathbf{p}\in\mathcal{Z}} J(\mathbf{p}; \mathbf{p}_{\mathcal{K}}^l)$

  if $J^{best} > J^l$ **then**

    $\mathbf{p}_{\mathcal{K}}^{\text{best}} \leftarrow \mathbf{p}_{\mathcal{K}}^l$

    $J^{\text{best}} \leftarrow J^l$

  end

  $\Delta^l \leftarrow J^l - J^a$

  $\theta^l \leftarrow \beta\theta^{l-1}$

  $s^l \leftarrow \exp(-\Delta^l/\theta^l)$

  draw $\rho \sim \mathcal{U}_{[0,1]}$

  if $\Delta^l < 0$ *or* $\rho < s^l$ **then**

    $J^a \leftarrow J^l$

    $\mathbf{p}_{\mathcal{K}}^{\text{a}} \leftarrow \mathbf{p}_{\mathcal{K}}^l$

  end

end

return $\mathbf{p}_{\mathcal{K}}^{best}$ *and* J_{best}

The simulated temperature θ, with the absorption factor $0 < \beta < 1$ which makes it "cool down" during the iterations, starts from the known initial θ_0 and conditions a Metropolis Hasting test. This test compares a random variable $\rho \sim \mathcal{U}_{[-1,1]}$ with the energy $s^l = \exp(-(J^l - J^a)/\theta^l)$ between the active and the local configuration based on their cost difference. If it succeeds, which is less and less likely over time as the system "cools down", then the local configuration l becomes the new active configuration a. In other words, this test

allows random exploration of the placement zone $\mathcal{P}^K$ with decreasing probability over time.

At the end of the optimization process, *i.e.*, when N_{iter} iterations have been performed, the best configuration result that solves (8.7), is kept in memory. The found position $\mathbf{p}_{\mathcal{K}}^{c} := \mathbf{p}_{\mathcal{K}}^{\text{best}}$ is transferred to the second level of our deployment strategy. The environment Algorithm 8.1 summarizes this process. If $J_{\text{best}} > C_M$, then the optimization process must be restarted, increasing the number of anchors to satisfy the constraint on the MSE.

8.4.2 Local Average Minimization Policy

Starting from $\mathbf{p}_{\mathcal{K}}^{c}$, we aim to solve locally the second auxiliary problem of (8.2), *i.e.*, find a local minimum of

$$\mathbf{p}_{\mathcal{K}}^{*} \in \underset{\mathbf{p}_{\mathcal{K}} \in \mathcal{P}^k}{\operatorname{argmin}} \, \mathbb{E}_{\mathbf{p}_{\mathcal{U}}} \left\{ J(\mathbf{p}_{\mathcal{U}}; \mathbf{p}_{\mathcal{K}}) \right\}. \tag{8.8}$$

To do so, we rely on a stochastic gradient algorithm similar to Algorithm 7.1 presented in Chapter 7. Indeed, we can perform the stochastic gradient iterations for $l \geq 0$, setting $\mathbf{p}_{\mathcal{K}}^{0} = \mathbf{p}_{\mathcal{K}}^{c}$, as follows

$$\mathbf{p}_{k}^{l+1} = \mathbf{p}_{k}^{l} - \alpha_k \left. \frac{\partial J}{\partial \mathbf{p}_{k}^{l}} \right|_{\mathbf{p}_{k}^{l}, \mathbf{p}_{\mathcal{U}}}^{\top} \tag{8.9}$$

for each anchor $k \in \mathcal{K}$ and a given random position $\mathbf{p}_{\mathcal{U}}$ drawn according to the PDF $f_{\mathcal{U}}$. However, the solution must satisfy the constraint $\mathbf{p}_{\mathcal{K}} \in \mathcal{P}^K$. To do so, we apply the following stepsize rule

$$\alpha_l = \begin{cases} \alpha_0, \text{ if } \mathbf{p}_{k}^{l} + \alpha_0 (\partial J / \partial \mathbf{p}_{k}^{l})^{\top} \in \mathcal{P}, \\ 0 \text{ otherwise,} \end{cases} \tag{8.10}$$

where $\alpha_0 > 0$ is a fixed stepsize. For the evaluation of the gradient, we took advantage of the closed form (7.13) given in Chapter 7, which relies on the element-wise differentiation of $\mathbb{E}\{\partial^2 \ln f_{\mu} / \left(\partial \mathbf{p}_{\mathcal{U}} \partial \mathbf{p}_{\mathcal{U}}^{\top} \right)\}$ given in (6.19). The optimizer program stops when M_{iter} has been computed or if $C_M - \max_{\mathbf{p}_{\mathcal{U}} \in \mathcal{Z}} J(\mathbf{p}_{\mathcal{U}}; \mathbf{p}_{\mathcal{K}}) < \epsilon$. The Algorithm 8.2 summarizes this minimization process.

Algorithm 8.2: Stochastic gradient descent

Data: $\mathbf{p}_{\mathcal{K}}^{c}, \alpha, \epsilon, C_M$

$\mathbf{p}_{\mathcal{K}}^{0} \leftarrow \mathbf{p}_{\mathcal{K}}^{c}$
for $l \in [1, M_{iter}]$ **do**
  Draw a position $\mathbf{p}_{\mathcal{U}}$ following the PDF $f_{\mathcal{U}}$
  for $k \in \mathcal{K}$ **do**
    Perform the gradient descent (8.9)
    if $C_M - \max_{\mathbf{p}_{\mathcal{U}} \in \mathcal{Z}} J(\mathbf{p}_{\mathcal{U}}; \mathbf{p}_{\mathcal{K}}) < \epsilon$ **then**
      return $\mathbf{p}_{\mathcal{K}}^{*} \leftarrow \mathbf{p}_{\mathcal{K}}^{l}$.
    end
  end
end
return $\mathbf{p}_{\mathcal{K}}^{*} \leftarrow \mathbf{p}_{\mathcal{K}}^{l}$.

8.5 Simulations

Consider $K = 10$ anchors to place in a three-dimensional space ($n = 3$) to locate UAVs. We assume that the workspace $\mathcal{W}$ is a $40 \times 40 \times 5$ m room, *i.e.*, $[x, y, z]^\top \in \mathcal{W}$ if $|x| \leq 20, |y| \leq 20$ and $0 \leq z \leq 5$. The anchors are placed on tripods (with a maximum height of 2 m) and must be placed inside the workspace but away from reflective surfaces. So we define the following placement zone for the anchors

$$\mathcal{P} = \{[x, y, z]^\top \in \mathbb{R}^3, |x| < 19.5, |y| < 19, 0.5 < z < 2\}.$$

The UAVs that carry tags are supposed to fly over $\mathcal{Z}$ and their distribution is Gaussian, namely $\mathbf{p}_{\mathcal{U}} \sim \mathcal{N}(\boldsymbol{\mu}, \boldsymbol{\Sigma})$ with the following variance and mean parameterization

$$\boldsymbol{\mu} = [0, 0, 2.5]^\top \ , \ \Sigma = \mathrm{diag}(\sigma_{xy}^2, \sigma_{xy}^2, \sigma_z^2),$$

where $\sigma_{xy} = 5$ m and $\sigma_z = 0.5$ m. Here, we aim to find a solution to the problem (8.2) with a constraint of $C_M = (0.5)^2$ m^2 on the maximum value of the MSE lower bound. The setup of the simulation is shown in the Figure 8.4.

Each anchor performs distance measurements with the Gaussian model described in Section 8.2.1, with $\alpha_0 = 3.8 \times 10^{-2}$ m^2 , $\alpha_2 = 5.0 \times 10^{-4}$, $\delta_2 = 4.5$ m and $\alpha_1 = \delta_1 = \alpha_L = 0$. These parameters are taken from the experiment of Chapter 6, modeling only power fading effects and not communication losses, since the dimensions of the workspace $\mathcal{W}$ are moderate. We also assume that the measurements are performed in LoS.

Each anchor $k \in \mathcal{K}$ is initially (and arbitrarily) placed around the origin, $\mathbf{p}_k^0 = [r_1, r_2, r_3]^\top$

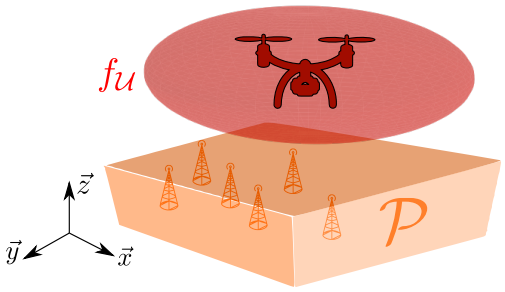

Figure 8.4 – Simulated scenario setup

with each $r_i \sim \mathcal{U}_{[-5\times10^{-2},5\times10^{-2}]}$, $i \in [1,3]$, is a small perturbation to avoid singularities in $\mathbf{F}_B$ (and thus in J). We chose such initial parameters to prove the efficiency of the simulated annealing algorithm explained in Section 8.4.1. The discrete operation zone $\mathcal{Z}_D$, defined to use Algorithm 8.1, is given by

$$\mathcal{Z}_D = \{[i\sigma_{xy}, j\sigma_{xy}, m\sigma_z] \in \mathbb{R}^3, \{i,j,m\} \in \{-2,-1,0,1,2\}^3\}.$$

The parameters for this scheme are as follows: the stepsize $\eta = 2$, the absorption factor $\beta = 99/100$, the initial temperature $\theta^0 = 200 \max_{\mathbf{p}_\mathcal{U} \in \mathcal{Z}_D} J(\mathbf{p}_\mathcal{U}, \mathbf{p}_\mathcal{K}^0)$ and the number of iterations is set to $N_{\text{iter}} = 200$. The result, obtained in 13 s on a standard off-the-shelf computer (with an `Intel Core i7` processor), is shown in Figure 8.5. It appears that simulated annealing successfully and rapidly decreases the coverage criterion $\max_{\mathbf{p}_\mathcal{U} \in \mathcal{Z}_D} J(\mathbf{p}_\mathcal{U}; \mathbf{p}_\mathcal{K})$ in Figure 8.5a. After 190 iterations, the value stabilizes around 0.16 m^2, which corresponds to a maximum RMSE lower bound of 0.40 m in $\mathcal{Z}$. The obtained solution $\mathbf{p}_\mathcal{K}^c$, shown in red in Figure 8.5b, satisfies the constraint set to $C_M = (0.5)^2$ m^2 in (8.2).

Then $\mathbf{p}_\mathcal{K}^c$ is provided as input to Algorithm 8.2, tuned with a $\alpha_0 = 0.7$ stepsize and $M_{\text{iter}} = 10^4$ iterations allowed. After a 63 s run, it successfully minimized $\mathbb{E}_{\mathbf{p}_\mathcal{U}} \{J(\mathbf{p}_\mathcal{U}, \mathbf{p}_\mathcal{K})\}$ without violating the constraint imposed by C_M, as highlighted in Figure 8.6a. In this figure, the cost function (expectation) of (8.2) is plotted in blue, while the constraint (maximum value on $\mathcal{Z}_D$) is plotted in red. Minimizing the average localizability yields a 26% gain on the MSE lower bound, which is significant for the number of agents involved. The final anchor geometry $\mathbf{p}_\mathcal{K}^*$ is shown in green in Figure 8.6b, alongside the intermediate one $\mathbf{p}_\mathcal{K}^c$ in red, provided by Algorithm 8.1. Overall, our strategy efficiently solved the deployment problem, *i.e.*, by obtaining an acceptable MSE while a minimal localizability is ensured in the workspace, for a moderate computational cost, despite the relative complexity of the proposed scenario.

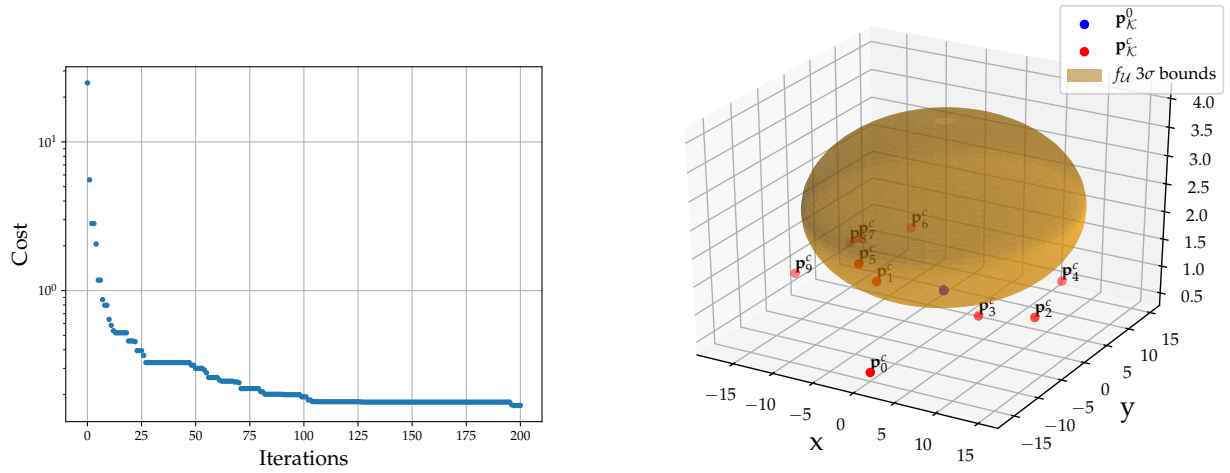

(a) Values of $\max_{\mathbf{p}_{\mathcal{U}}} J(\mathbf{p}_{\mathcal{U}}; \mathbf{p}_{\mathcal{K}})$

(b) Tags' PDF shape, initial and final position of the anchors.

Figure 8.5 – Simulated annealing algorithm results

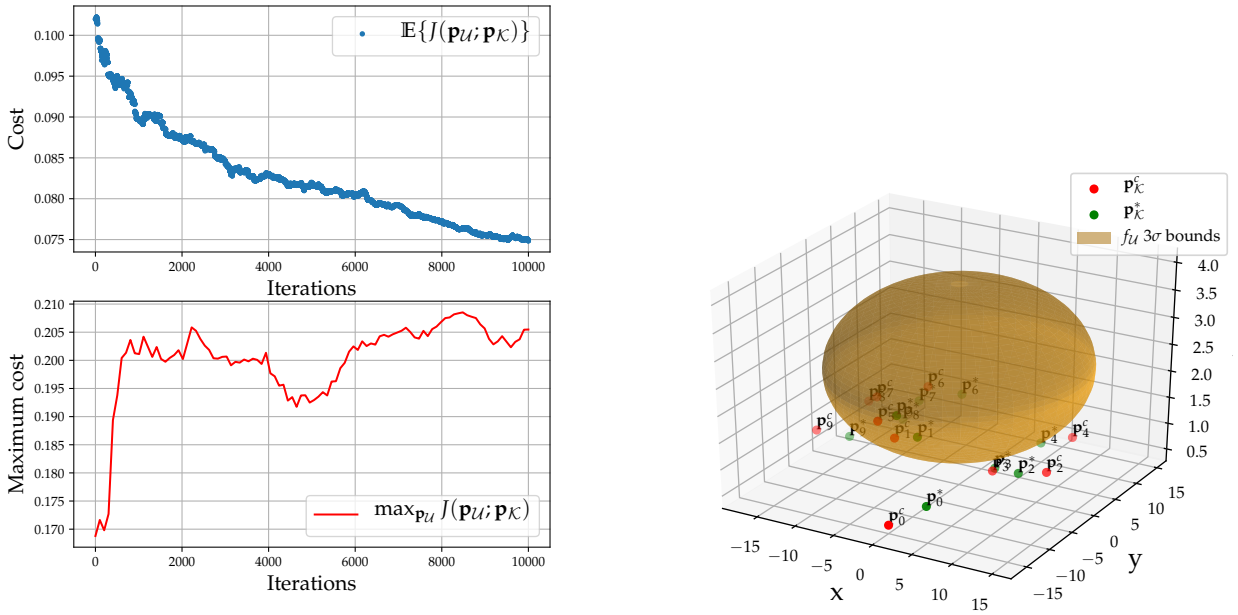

(a) Values of the localizability cost function $\mathbb{E}_{\mathbf{p}_{\mathcal{U}}}\{J(\mathbf{p}_{\mathcal{U}}; \mathbf{p}_{\mathcal{K}})\}$ (blue) and function $\max_{\mathbf{p}_{\mathcal{U}}} J(\mathbf{p}_{\mathcal{U}}; \mathbf{p}_{\mathcal{K}})$ (red).

(b) Tags' PDF shape, initial and final position of the anchors.

Figure 8.6 – Stochastic gradient algorithm results

8.6 Conclusion and Perspectives

In this Chapter, we have formulated a deployment problem for anchors that perform distance measurements with randomly located tags. The knowledge of their probability distribution allowed us to develop a strategy using a BCRLB-based localizability cost function. This model allows to capture both the prior information accessible to the tags, their probability density, and the information brought by the measurements. Subsequently, we proposed a two-step optimization strategy that allows first to solve a combinatorial problem of optimal localizability coverage and second to increase the average localizability of the tags. This strategy makes use of well-known optimization algorithms: the simulated annealing heuristic and the stochastic gradient descent. Finally, we simulated a practical three-dimensional deployment scenario where our method succeeded in efficiently decreasing the average localizability of the tags while guaranteeing a good positioning accuracy coverage in the zone of operation.

CHAPTER 9 GENERAL DISCUSSION

> "I have made this longer than usual because I have not had time to make it shorter."
>
> – Blaise Pascal (1623-1662)

This short chapter discusses the overall contributions made during this thesis project. Here we summarize both the main theoretical contributions and the validation processes which were undertaken.

Article 1 : First, in Chapter 4, we proposed a methodology to characterize the systematic bias in UWB ranging measurements under LoS conditions. A general methodology was proposed for ToF-based protocols to calibrate the errors due to both the clock offset and the RxP level. Indeed, since the LDE is used to determine the ToA and its performance depend on the RxP, this quantity influences the estimates' quality, independently of the protocol used. However, the synchronization bias is highly dependent on the measurement protocol used, which may include its estimation in the process, *e.g.*, TDoA. Once the synchronization was performed, we were able to build RxP calibration maps with a straightforward methodology, in contrast to existing deep learning-based methods. These obtained calibration maps have illustrated the repeatability of the results using a dozen UWB standard transceivers.

To highlight the duality of the bias calibration problem, induced by both synchronization and RxP-dependent factors, we proposed an extended version of DSTWR using our correction algorithm. This protocol has been implemented on a commercial UGV carrying UWB transceivers for validation purposes. To verify the repeatability of the experiments, they were performed in two different laboratories using the same calibration data.

First, these experiments allowed to validate Hypothesis 1 (bias removal) at a reasonable level for LoS scenarios. Indeed, it has been shown that the bias has been significantly removed by our calibration method, with an order of magnitude smaller than the variance of the SSTWR ranging protocol. Second, the Hypothesis 2 (Gaussian-centered model for distance measurements) has also been validated by these experiments in LoS. To obtain such measurements, masts have been used to move UWB transceivers away from the ground, which is a reflective surface that generates MP contamination. Note that in the supplementary article [Cano et al., 2023] a method is proposed to mitigate MP-contaminated scenarios

using the M-Robust EKF when SSTWR is performed. The results of this work tend to confirm the Hypothesis 2 once again.

Article 2 : In Chapter 5, we proposed a mathematical definition of MRS localizability for Gaussian and log-normal unbiased distance measurements (leveraging Hypotheses 1 and 2) using the CRLB. We also established a connection between the FIM leveraged to model localizability and the infinitesimal rigidity in order to take advantage of pre-existing results in this field of research. The structure of the FIM and in particular its rank has been carefully studied. Indeed, the fact that the FIM is non-degenerate allows to use the CRLB as a proxy to model the positioning uncertainties. Then, we proposed to build an MRS deployment scheme that improves the localizability of tags based on the artificial potentials method. The chosen cost functions are popular in the wireless sensor network literature and come from the theory of optimal design of experiments. To minimize these potentials on a large scale, we proposed decentralized gradient descent strategies, built on existing generalist algorithms.

In the same chapter, we presented an extension of localizability to the case where several tags are carried by the same robot. Two contributions were made considering both the inter-tag distances and their relative positions. These approaches leverage the CCRLB and primal-dual optimization scheme in order to respect the constraints in the tags' motion planning (since several are onboard the same vehicle). All of these extensions were tailored both for UAV and UGV use-cases.

For the validation of the decentralized and noisy gradient descent, we used a large-scale simulation. Then, we proposed a hardware experiment coupled with a simulation using the CCRLB-based motion planner for an MRS. This example highlighted the benefits of our planners and the realism of the localizability potential paradigm.

The results of both the experiments and the simulations presented in Chapter 5 or in the preliminary work [Cano and Le Ny, 2021] tended to validate Hypothesis 3, which stated that decreasing the localizability cost function brings an improvement in positioning accuracy. On the other hand, the results of the simulation part of Chapter 5 tended to prove that the decrease was feasible under noisy measurements and a complex MRS's topology, *i.e.*, validated Hypothesis 4. Furthermore, the real-time implementation presented in Chapter 5 tended to confirm this claim.

Article 3 : In Chapter 6, we extended the results of the previous work by modeling the deterioration of the RMs (including angle measurements) with distance. To do so, we proposed a polynomial variance model identification that solves a LS-based fitting problem. Then, we

derived the CRLB in this case and a localizability cost function. Since the FIM structure remains the same in this model, the decentralized policies presented in Chapter 5 are still applicable in this extension. Moreover, it allows to model smooth communication losses between agents at large distances. We compared the obtained result with the standard CRLB formulation (presented in chapter 5) in an experiment of a UGV in a workspace equipped with UWB fixed anchors. This validation allowed to emphasize that this CRLB is tighter than the original one.

Article 4 : Then, in Chapter 7, we presented an extension of the CRLB scheme using a Bayesian formulation (*i.e.*, the BCRLB). We proposed a method to numerically evaluate this new bound using a sigma points scheme for a Gaussian prior PDF. This model was designed to plan the motion of UGV while using an EKF, taking advantage of the posterior uncertainties given by the estimator. We proposed an optimization method for a localizability cost function extracted from the BCRLB, based on stochastic gradient descent. We validated this method in real time through a UGV deployment using both BCRLB and the original (deterministic) CRLB.

As expected, the refined localizability models presented in both Chapter 6 and 7 were closer to the estimator performance than the model presented in Chapter 5. In fact, the introduction of a more sophisticated and empirically identified measurement model in chapter 6 has yielded a MSE bound closer to reality than that of the constant variance model. On the other hand, the introduction of BCRLB in Chapter 7 allowed to obtain a better performance prediction for EKF, since this estimator relies heavily on prior information. These considerations tend to validate Hypothesis 5.

Additional Chapter : Finally, Chapter 8 presented some results on static anchor placement knowing a prior distribution of the tags. We developed an algorithm based on simulated annealing to initially deploy the anchors on a coarse mesh to cover the workspace with a minimum level of localizability. Then, a local policy based on stochastic gradient descent optimized an average localizability criterion based on BCRLB. This algorithm was tested on a three dimensional simulated scenario. The simulations presented in this last chapter have shown a strong improvement in the localizability of the tags for a moderate computational cost, which tends to validate the Hypothesis 6 in this use case.

In Table 9.1, we have summarized the different contributions of this thesis and their corresponding chapters. In this table, the research axes are highlighted with their respective colors, *i.e.*, 1 (red); 2 (green); 3 (blue).

Table 9.1 – Summary of the contributions made during the thesis with their respective validations

Chapter	Main Contributions	Validation
4	i. UWB Bias calibration using simple synchronization and RxP based method; ii. Enhancement of the SSTWR protocol.	Calibration maps taken in several locations; Measurement precision strongly enhanced.
5	i. Connection between localizability and rigidity theory; ii. FIM invertibility theorem; iii. Distributed localizability potential optimization schemes; iv. Extension of localizability for multi-sensor robots.	Large-scale simulation; Real-time implementation on a ground MRS.
6	i. CRLB formulation for RMs (angles and distances) with distance dependent variance.	Experiment with a UGV for a relative-position constrained CRLB (robot carrying multiple UWB sensors).
7	i. BCRLB formulation for Gaussian prior and measurement PDFs; ii. Real-time optimizer of the BCRLB.	Real-time optimization of both CRLB and BCRLB for an MRS with a fixed anchor.
8	i. Static anchor deployment algorithm optimizing the localizability of tags, having access to a prior PDF and range-deteriorated distance measurements.	Simulated scenario.

CHAPTER 10 CONCLUSION AND RECOMMENDATIONS

"*Un être qui pense c'est un être qui doute.*"

– René Descartes (1596-1650)

This chapter concludes the manuscript by summarizing the work done during this thesis. We then point out the limitations of our approach and recall the main assumptions made along our work. Finally, we suggest some avenues for future research.

10.1 Summary of Works

In this thesis, we mathematically quantified using CRLBs the localizability of MRS localized thanks to RMs. Then, we designed localizability cost functions based on the optimal design of experiments. Moreover, we made connections between the infinitesimal rigidity theory and the Fisher information for Gaussian or log-normal RMs. This allowed us to take advantage of the results of decentralized rigidity formation control, which are well known in the field of swarm robotics. Thanks to this, we proposed decentralized optimization schemes to provide scalable deployment algorithms for large MRS.

We then extended the theoretical results to robots carrying multiple sensors, using Lagrangian-based descent schemes and the CCRLB. We considered both known distances and known relative positions within the robots' frames. We also addressed realism issues of the Gaussian RMs model at long range, and proposed a version of the CRLB that accounts for distance degradation of the measurements. Finally, using the BCRLB, we proposed deployment policies knowing prior information about the tag positions. The latter result was applied both to place static anchors in a probabilistic MRS context and to maintain the localizability of a robot using an EKF to navigate.

Along this thesis, we experimentally applied this paradigm of localizability to UWB range measurements captured by ToF-based protocols. In order to provide an operational localization system, we studied the main sources of error in this type of protocol. We first focused on the calibration of systematic biases in LoS for ToF measurement, which violate a fundamental assumption of CRLB. Finally, we successfully adapted robust filtering techniques to mitigate MP outliers indoors in an additional article.

The contributions made during this thesis lead to two IEEE/RAS peer-reviewed journal articles in Robotics and four IEEE international conference papers (both in Robotics and Signal Processing).

10.2 Limitations

Here we describe the limitations of the work done during this thesis. First, its strongest limitation is also the main assumption made to model localizability: the fact that the CRLB is a proxy for the real estimator uncertainties. The CRLB is a theoretical minimum on the covariance and there is no guarantee that "decreasing" it would improve the localizability of the MRS if the probabilistic observation model being considered is not close enough to the true observations. We can make it tighter to fit reasonable estimator performances by adding constraints or prior information, but this fact harms the generalist nature of the localizability. In fact, additional information means making assumptions about the structure of the estimators. Our approach, however, aimed to design general pre-computable deployment criteria with a minimum assumption on the estimators.

In this thesis we mainly assumed that the measurements were Gaussian for the CRLB design, but this standard model may not be appropriate for some types of sensors. In particular, the clock drift was not modeled in the PDF of the RMs for ToF measurements, so the synchronization was assumed to be perfect. Another limitation of the model is that our extension focuses only on the range degradation of the measurements. In fact, even if the RMs captured by RF sensors generally deteriorate with RxP and thus with distance, outliers such as MP may occur at close range. For example, a wall next to a robot can distort the signal, highlighting the fact that distance modeling of degradation remains a coarse approximation.

Experimentally, our validation was limited by the thesis schedule and the equipment at our disposal. We essentially validated the results of this thesis on UWB commercial transceivers using the SSTWR protocol, which is a specific ranging method. Also, the UWB boards used to capture the RMs were not able to perform angle measurements, limiting our scope of protocols. We also used a UGV swarm to test the algorithms, leaving another implementation on UAVs for future research.

The deployment policies given in this thesis are computationally expensive, and this fact is exacerbated as the number of robots N involved in the MRS increases. In fact, the structure of the adjacency matrix, especially its sparsity, plays a crucial role in the complexity of the optimization program. However, these concerns are beyond the scope of this work and are left for future work.

10.3 Future Research

Future research will include trajectory planning under localizability constraint leveraging the RBCRLB. Indeed, this mathematical tool allows to predict state propagation and can be useful to compute paths between two points while maintaining localizability through dynamic programming based method. However, since this problem is computationally demanding, a practical implementation necessarily requires heuristics to spare operations. In addition, a research avenue including synchronization terms in the localizability could be of great interest, since the family of BCRLBs (including the RBCRLB) can track dynamic problems. It might also be interesting to map the MP perturbations in a robot workspace in real time (as in the *Simultaneous Location And Mapping*, SLAM protocol) in order to further output optimal localizability trajectories.

To complete the preliminary results of Chapter 8, future work will include static anchor deployment for other types of RMs, such as angle or RSS-based measurements. In addition, more challenging scenarios using more sophisticated PDFs will be performed, in particular for UGV navigation in environments with complex geometries such as logistic warehouses.

On the experimental side, a more comprehensive validation of the deployment schemes for UWB could be undertaken, including MRS involving UAVs, angle measurements (*e.g.* AoA), other ToF-based ranging protocols such as DSTWR, ToA or TDoA. In addition, future work on indoor deployment may include Bluetooth technology, which is promising for low-cost applications.

REFERENCES

[Alavi and Pahlavan, 2006] Alavi, B. and Pahlavan, K. (2006). Modeling of the TOA-based distance measurement error using UWB indoor radio measurements. *IEEE Communications Letters*, 10(4):275–277.

[Aldubaikhy, 2012] Aldubaikhy, K. (2012). Differential code-shifted reference impulse-radio ultra-wideband receiver: timing recovery and digital implementation. Master's thesis, Dalhousie University.

[Amanda Prorok, 2013] Amanda Prorok (2013). *Models and Algorithms for Ultra-Wideband Localization in Single- and Multi-Robot Systems*. PhD thesis, École Polytechnique Fédérale de Lausanne, Lausanne, Switzerland.

[Angelis et al., 2017] Angelis, A. D., Moschitta, A., and Comuniello, A. (2017). TDoA based positioning using ultrasound signals and wireless nodes. In *2017 IEEE International Instrumentation and Measurement Technology Conference (I2MTC)*, pages 1–6.

[Ash and Moses, 2008] Ash, J. N. and Moses, R. L. (2008). On optimal anchor node placement in sensor localization by optimization of subspace principal angles. In *2008 IEEE International Conference on Acoustics, Speech and Signal Processing*, pages 2289–2292. ISSN: 2379-190X.

[Aspnes et al., 2006] Aspnes, J., Eren, T., Goldenberg, D. K., Morse, A. S., Whiteley, W., Yang, Y. R., Anderson, B. D., and Belhumeur, P. N. (2006). A theory of network localization. *IEEE Transactions on Mobile Computing*, 5(12):1663–1678.

[Astolfi, 1999] Astolfi, A. (1999). Exponential Stabilization of a Wheeled Mobile Robot Via Discontinuous Control. *Journal of Dynamic Systems, Measurement, and Control*, 121(1):121–126. Publisher: American Society of Mechanical Engineers Digital Collection.

[Barfoot, 2017] Barfoot, T. D. (2017). *State estimation for robotics*. Cambridge University Press.

[Barrière et al., 2013] Barrière, L., Huemer, C., Mitsche, D., and Orden, D. (2013). On the Fiedler value of large planar graphs. *Linear Algebra and its Applications*, 439(7):2070–2084.

[Bell and Tian, 1968] Bell, H. and Tian, Z. (1968). Detection, estimation, and modulation theory part i.

[Bensky, 2016] Bensky, A. (2016). *Wireless positioning technologies and applications*. Artech House, 2 edition.

[Bertsekas, 2012] Bertsekas, D. (2012). *Dynamic programming and optimal control: Volume I*, volume 1. Athena scientific.

[Bertsekas and Tsitsiklis, 2015] Bertsekas, D. and Tsitsiklis, J. (2015). *Parallel and distributed computation: numerical methods*. Athena Scientific.

[Bertsekas, 2016] Bertsekas, D. P. (2016). *Nonlinear programming*. Athena Scientific, Belmont, MA, 3 edition.

[Bian et al., 2017] Bian, A. A., Buhmann, J. M., Krause, A., and Tschiatschek, S. (2017). Guarantees for Greedy Maximization of Non-submodular Functions with Applications. In *Proceedings of the 34 th International Conference on Machine Learning*, pages 498–507, Sydney, Australia.

[Bonnabel and Barrau, 2015] Bonnabel, S. and Barrau, A. (2015). An intrinsic Cramér-Rao bound on lie groups. In *Geometric Science of Information*, pages 664–672. Springer International Publishing.

[Bottou, 2012] Bottou, L. (2012). Stochastic gradient descent tricks. In *Neural networks: Tricks of the trade*, pages 421–436. Springer.

[Boumal et al., 2014] Boumal, N., Singer, A., Absil, P.-A., and Blondel, V. D. (2014). Cramér-Rao bounds for synchronization of rotations. *Information and Inference*, 3(1):1–39. arXiv: 1211.1621.

[Bregar and Mohorčič, 2018] Bregar, K. and Mohorčič, M. (2018). Improving indoor localization using convolutional neural networks on computationally restricted devices. *IEEE Access*, 6:17429–17441.

[Buehrer et al., 2018] Buehrer, R. M., Wymeersch, H., and Vaghefi, R. M. (2018). Collaborative sensor network localization: Algorithms and practical issues. *Proceedings of the IEEE*, 106(6):1089–1114.

[Bullo, 2019] Bullo, F. (2019). *Lectures on Network Systems*. Kindle Direct Publishing, 1 edition. `http://motion.me.ucsb.edu/book-lns`.

[Bullo et al., 2009] Bullo, F., Cortés, J., and Martinez, S. (2009). *Distributed control of robotic networks: a mathematical approach to motion coordination algorithms*. Princeton University Press.

[Cai et al., 2017] Cai, D., Wu, S., and Deng, J. (2017). Distributed Global Connectivity Maintenance and Control of Multi-Robot Networks. *IEEE Access*, 5:9398–9414.

[Cano, 2019] Cano, J. (2019). Synchronisation et positionnement simultanés d'un réseau ultra-large bande et applications en robotique mobile. Master's thesis, Polytechnique Montréal, Montreal, QC, Canada.

[Cano et al., 2022a] Cano, J., Chauffaut, C., Pages, G., Chaumette, E., and Le Ny, J. (2022a). Maintaining Robot Localizability With Bayesian Cramér-Rao Lower Bounds. In *Proceedings of the IEEE/RSJ International Conference on Intelligent Robots and Systems (IROS)*, Kyoto, Japan.

[Cano et al., 2019] Cano, J., Chidami, S., and Le Ny, J. (2019). A Kalman Filter-Based Algorithm for Simultaneous Time Synchronization and Localization in UWB Networks. In *Proceedings of the International Conference on Robotics and Automation (ICRA)*, Montreal, QC, Canada.

[Cano et al., 2023] Cano, J., Ding, Y., Pages, G., Chaumette, E., and Le Ny, J. (2023). A Robust Kalman Filter Based Approach for Indoor Robot Positionning with Multi-Path Contaminated UWB Data. In *2023 IEEE International Conference on Acoustics, Speech and Signal Processing*, Rhodes, Greece. (Accepted) `http://justincano.com/doc/icassp2023.pdf`.

[Cano and Le Ny, 2021] Cano, J. and Le Ny, J. (2021). Improving Ranging-Based Location Estimation with Rigidity-Constrained CRLB-Based Motion Planning. In *2021 IEEE International Conference on Robotics and Automation (ICRA)*, pages 5758–5764, Xi'An (China). ISSN: 2577-087X.

[Cano and Le Ny, 2023] Cano, J. and Le Ny, J. (2023). Ranging-Based Localizability-Optimization for Mobile Robotic Networks. *IEEE Transactions on Robotics*. (accepted, on press) arXiv: 2202.00756.

[Cano et al., 2022b] Cano, J., Pagès, G., Chaumette, E., and Le Ny, J. (2022b). Clock and power-induced bias correction for UWB time-of-flight measurements. *IEEE Robotics and Automation Letters*, 7(2):2431–2438.

[Cano et al., 2022c] Cano, J., Pages, G., Chaumette, E., and Le Ny, J. (2022c). Optimal localizability criterion for positioning with distance-deteriorated relative measurements. In *International Conference on Intelligent Robots and Systems (IROS)*, Kyoto, Japan.

[Cao et al., 2020] Cao, K., Han, Z., Li, X., and Xie, L. (2020). Ratio-of-Distance Rigidity Theory With Application to Similar Formation Control. *IEEE Transactions on Automatic Control*, 65(6):2598–2611.

[Carlino et al., 2019] Carlino, L., Jin, D., Muma, M., and Zoubir, M. (2019). Robust distributed cooperative RSS-based localization for directed graphs in mixed LoS/NLoS environments. *EURASIP Journal on Wireless Communications and Networking*, 2019.

[Carrillo et al., 2012] Carrillo, H., Reid, I., and Castellanos, J. A. (2012). On the comparison of uncertainty criteria for active SLAM. In *IEEE International Conference on Robotics and Automation (ICRA)*, pages 2080–2087, St Paul, MN, USA.

[Chirikjian, 2018] Chirikjian, G. S. (2018). From Wirtinger to Fisher information inequalities on spheres and rotation groups. In *IEEE International Conference on Information Fusion (FUSION)*, pages 730–736, Cambridge, United Kingdom.

[Cho et al., 2009] Cho, H., Jung, J., Cho, B., Jin, Y., Lee, S., and Baek, Y. (2009). Precision Time Synchronization Using IEEE 1588 for Wireless Sensor Networks. In *2009 International Conference on Computational Science and Engineering*, volume 2, pages 579–586.

[Choset et al., 2005] Choset, H., Lynch, K., Hutchinson, S., George, K., Burgard, W., Kavraki, L., and Thrun, S. (2005). *Principles of Robot Motion*, volume 1. The MIT Press, Cambridge, Massachusetts.

[Chui and Chen, 1999] Chui, C. K. and Chen, G. (1999). *Kalman filtering: with real-time applications*. Number 17 in Springer series in information sciences. Springer, Berlin ; New York, 3rd ed edition.

[Connelly, 2005] Connelly, R. (2005). Generic Global Rigidity. *Discrete & Computational Geometry*, 33(4):549–563.

[Corke, 2011] Corke, P. (2011). *Robotics, Vision and Control*, volume 73 of *Springer Tracts in Advanced Robotics*. Springer Berlin Heidelberg.

[Cortes et al., 2004] Cortes, J., Martinez, S., Karatas, T., and Bullo, F. (2004). Coverage Control for Mobile Sensing Networks. *IEEE Transactions on Robotics and Automation*, 10:243–255.

[Coulson et al., 1998] Coulson, A. J., Williamson, A. G., and Vaughan, R. G. (1998). A statistical basis for lognormal shadowing effects in multipath fading channels. *IEEE Transactions on Communications*, 46(4):494–502.

[Cramér, 1946] Cramér, H. (1946). *Mathematical Methods of Statistics*. Princeton University Press, USA.

[Decawave, 2017] Decawave (2017). DW1000 User manual, V2.18. `https://www.decawave.com/dw1000/usermanual/`.

[Decawave, 2018] Decawave (2018). APS011 : Sources of error in DW1000 based TWR schemes. Technical report, Qorvo.

[Dewberry and Einhorn, 2016] Dewberry, B. and Einhorn, M. (2016). Wideband Active Two-Way Ranging. *xponential 2016*, page 17.

[Ding et al., 2022] Ding, Y., Chauchat, P., Pages, G., and Asseman, P. (2022). Learning-Enhanced Adaptive Robust GNSS Navigation in Challenging Environments. *IEEE Robotics and Automation Letters*, 7(4):9905–9912.

[Dotlic et al., 2017] Dotlic, I., Connell, A., Ma, H., Clancy, J., and McLaughlin, M. (2017). Angle of arrival estimation using decawave DW1000 integrated circuits. In *2017 14th Workshop on Positioning, Navigation and Communications (WPNC)*, Bremen.

[Eldar, 2004] Eldar, Y. C. (2004). Minimum variance in biased estimation: bounds and asymptotically optimal estimators. *IEEE Transactions on Signal Processing*, 52(7):1915–1930.

[Eldar, 2007] Eldar, Y. C. (2007). Rethinking Biased Estimation: Improving Maximum Likelihood and the Cramér–Rao Bound. *Foundations and Trends® in Signal Processing*, 1(4):305–449.

[Etzlinger and Wymeersch, 2018] Etzlinger, B. and Wymeersch, H. (2018). Synchronization and Localization in Wireless Networks. *Foundations and Trends® in Signal Processing*, 12:1–106.

[Frerking, 1978] Frerking, M. (1978). *Crystal Oscillator Design and Temperature Compensation*. Springer.

[Fritsche et al., 2013] Fritsche, C., Klein, A., and Gustafsson, F. (2013). Bayesian Cramer-Rao Bound for Mobile Terminal Tracking in Mixed LOS/NLOS Environments. *IEEE Wireless Communications Letters*, 2(3):335–338.

[Gallego and Yezzi, 2015] Gallego, G. and Yezzi, A. (2015). A compact formula for the derivative of a 3-D rotation in exponential coordinates. *Journal of Mathematical Imaging and Vision*, 51(3):378–384.

[Galy et al., 2015] Galy, J., Renaux, A., Chaumette, E., Vincent, F., and Larzabal, P. (2015). Recursive hybrid CRB for Markovian systems with time-variant measurement parameters. In *2015 IEEE 6th International Workshop on Computational Advances in Multi-Sensor Adaptive Processing (CAMSAP)*, pages 473–476, Cancun, Mexico. IEEE.

[Gavin, 2019] Gavin, H. P. (2019). The Levenberg-Marquardt algorithm for nonlinear least squares curve-fitting problems. Technical report, Department of Civil and Environmental Engineering, Duke University.

[Giorgi and Narduzzi, 2011] Giorgi, G. and Narduzzi, C. (2011). Performance Analysis of Kalman-Filter-Based Clock Synchronization in IEEE 1588 Networks. *IEEE Transactions on Instrumentation and Measurement*, 60(8):2902–2909.

[Godsil and Royle, 2001] Godsil, C. and Royle, G. F. (2001). *Algebraic graph theory*. Springer.

[González et al., 2009] González, J., Blanco, J., Galindo, C., de Galisteo, A. O., Fernández-Madrigal, J., Moreno, F., and Martínez, J. (2009). Mobile robot localization based on ultra-wide-band ranging: A particle filter approach. *Robotics and Autonomous Systems*, 57(5):496–507.

[Gorman and Hero, 1990] Gorman, J. D. and Hero, A. O. (1990). Lower bounds for parametric estimation with constraints. *IEEE Transactions on Information Theory*, 36(6):1285–1301.

[Groves, 2013] Groves, P. D. (2013). *Principles of GNSS, inertial, and multisensor integrated navigation systems*. Artech House, 2nd edition.

[Gururaj et al., 2017] Gururaj, K., Rajendra, A. K., Song, Y., Law, C. L., and Cai, G. (2017). Real-time identification of NLOS range measurements for enhanced UWB localization. In *2017 International Conference on Indoor Positioning and Indoor Navigation (IPIN)*. ISSN: 2471-917X.

[Hamer and D'Andrea, 2018] Hamer, M. and D'Andrea, R. (2018). Self-calibrating ultra-wideband network supporting multi-robot localization. *IEEE Access*, 6:22292–22304.

[Harville, 1997] Harville, D. A. (1997). *Matrix Algebra from a Statisticians Perspective*. Springer, New York, NY, USA.

[Haug, 2012] Haug, A. J. (2012). *Bayesian estimation and tracking: a practical guide*. Wiley, Hoboken, N.J. OCLC: ocn767824937.

[Hero et al., 1996] Hero, A. O., Fessler, J., and Usmann, M. (1996). Exploring estimator bias-variance tradeoffs using the uniform CR bound. *IEEE Transactions on Signal Processing*, pages 2026–2041.

[Huber, 1964] Huber, P. J. (1964). Robust Estimation of a Location Parameter. *The Annals of Mathematical Statistics*, 35(1):73–101.

[Ikemoto et al., 2020] Ikemoto, Y., Nishimura, K., Mizutama, Y., Sasaki, T., and Jindai, M. (2020). Network Connectivity Control of Mobile Robots by Fast Position Estimations and Laplacian Kernel. *Journal of Robotics and Mechatronics*, 32(2):422–436.

[Irani et al., 2019] Irani, B., Wang, J., and Chen, W. (2019). A Localizability Constraint-Based Path Planning Method for Autonomous Vehicles. *IEEE Transactions on Intelligent Transportation Systems*, 20(7):2593–2604.

[Jiang et al., 2020] Jiang, C., Shen, J., Chen, S., Chen, Y., Liu, D., and Bo, Y. (2020). UWB NLOS/LOS Classification Using Deep Learning Method. *IEEE Communications Letters*, 24(10):2226–2230.

[Jiang and Leung, 2007] Jiang, Y. and Leung, V. C. (2007). An Asymmetric Double Sided Two-Way Ranging for Crystal Offset. In *2007 International Symposium on Signals, Systems and Electronics*, pages 525–528, Montreal, QC, Canada. IEEE.

[Jourdan and Roy, 2008] Jourdan, D. B. and Roy, N. (2008). Optimal sensor placement for agent localization. *ACM Transactions on Sensor Networks*, 4(3):13:1–13:40.

[Kay, 1993] Kay, S. M. (1993). *Fundamentals of Statistical Signal Processing: Estimation Theory*. Prentice-Hall, Englewood Cliffs, NJ, USA.

[Khalife and Kassas, 2019] Khalife, J. J. and Kassas, Z. Z. M. (2019). Optimal Sensor Placement for Dilution of Precision Minimization Via Quadratically Constrained Fractional Programming. *IEEE Transactions on Aerospace and Electronic Systems*, 55(4):2086–2096.

[Khatib, 1986] Khatib, O. (1986). Real-time obstacle avoidance for manipulators and mobile robots. In *Autonomous robot vehicles*, pages 396–404. Springer.

[Kia et al., 2019] Kia, S. S., Van Scoy, B., Cortes, J., Freeman, R. A., Lynch, K. M., and Martinez, S. (2019). Tutorial on dynamic average consensus: The problem, its applications, and the algorithms. *IEEE Control Systems Magazine*, 39(3):40–72.

[Kim, 2009] Kim, H. (2009). Double-sided two-way ranging algorithm to reduce ranging time. *IEEE Communications Letters*, 13(7):486–488.

[Kim and Mesbahi, 2006] Kim, Y. and Mesbahi, M. (2006). On maximizing the second smallest eigenvalue of a state-dependent graph Laplacian. *IEEE Transactions on Automatic Control*, 51(1):117.

[Kovvali et al., 2013] Kovvali, N., Banavar, M., and Spanias, A. (2013). *An Introduction to Kalman Filtering with MATLAB Examples*, volume 6. Morgan and Claypool.

[Krause et al., 2008] Krause, A., Singh, A., and Guestrin, C. (2008). Near-Optimal Sensor Placements in Gaussian Processes: Theory, Efficient Algorithms and Empirical Studies. *Journal of Machine Learning Research*, pages 235–284.

[Le Ny and Chauvière, 2018] Le Ny, J. and Chauvière, S. (2018). Localizability-constrained deployment of mobile robotic networks with noisy range measurements. In *Proceedings of the American Control Conference (ACC)*, pages 2788–2793.

[Le Ny and Pappas, 2009] Le Ny, J. and Pappas, G. J. (2009). On trajectory optimization for active sensing in Gaussian process models. In *IEEE Conference on Decision and Control (CDC)*, Shanghai, China.

[Ledergerber and D'Andrea, 2017] Ledergerber, A. and D'Andrea, R. (2017). Ultra-wideband range measurement model with Gaussian processes. In *2017 IEEE Conference on Control Technology and Applications (CCTA)*, pages 1929–1934.

[Ledergerber and D'Andrea, 2018] Ledergerber, A. and D'Andrea, R. (2018). Calibrating away inaccuracies in ultra wideband range measurements: A maximum likelihood approach. *IEEE Access*, 6:78719–78730.

[Ledergerber et al., 2015] Ledergerber, A., Hamer, M., and D'Andrea, R. (2015). A robot self-localization system using one-way ultra-wideband communication. In *Proceedings of the IEEE/RSJ International Conference on Intelligent Robots and Systems (IROS)*. IEEE.

[Li and Cao, 2014] Li, X. and Cao, F. (2014). Location Based TOA Algorithm for UWB Wireless Body Area Networks. In *2014 IEEE 12th International Conference on Dependable, Autonomic and Secure Computing*, pages 507–511.

[Li et al., 2018] Li, X., Wang, Y., and Khoshelham, K. (2018). UWB/PDR Tightly Coupled Navigation with Robust Extended Kalman Filter for NLOS Environments. *Mobile Information Systems*, 2018:e8019581. Publisher: Hindawi.

[Lin and Chiu, 2005] Lin, F. and Chiu, P. (2005). A near-optimal sensor placement algorithm to achieve complete coverage-discrimination in sensor networks. *IEEE Communications Letters*, 9(1):43–45.

[Liu et al., 2012] Liu, Z., Chen, W., Wang, Y., and Wang, J. (2012). Localizability estimation for mobile robots based on probabilistic grid map and its applications to localization. In *2012 IEEE International Conference on Multisensor Fusion and Integration for Intelligent Systems (MFI)*, pages 46–51.

[Lv et al., 2010] Lv, X., Liu, K., and Hu, P. (2010). Geometry Influence on GDOP in TOA and AOA Positioning Systems. In *2010 Second International Conference on Networks Security, Wireless Communications and Trusted Computing*, volume 2, pages 58–61.

[Lynch and Park, 2017] Lynch, K. M. and Park, F. C. (2017). *Modern robotics: mechanics, planning, and control*. Cambridge University Press, Cambridge, UK. OCLC: ocn983881868.

[Maceraudi et al., 2016] Maceraudi, J., Dehmas, F., Denis, B., and Uguen, B. (2016). Multipath components tracking adapted to integrated IR-UWB receivers for improved indoor navigation. In *2016 24th European Signal Processing Conference (EUSIPCO)*, pages 753–757.

[Mai et al., 2018] Mai, V., Kamel, M., Krebs, M., Schaffner, A., Meier, D., Paull, L., and Siegwart, R. (2018). Local positioning system using UWB range measurements for an unmanned blimp. *IEEE Robotics and Automation Letters*, 3(4):2971–2978.

[Marano et al., 2010] Marano, S., Gifford, W. M., Wymeersch, H., and Win, M. Z. (2010). NLOS identification and mitigation for localization based on UWB experimental data. *IEEE Journal on Selected Areas in Communications*, 28(7):1026–1035.

[McAulay and Hofstetter, 1971] McAulay, R. and Hofstetter, E. (1971). Barankin bounds on parameter estimation. *IEEE Transactions on Information Theory*, 17(6):669–676.

[Menni et al., 2014] Menni, T., Galy, J., Chaumette, E., and Larzabal, P. (2014). Versatility of constrained CRB for system analysis and design. *IEEE Transactions on Aerospace and Electronic Systems*, 50(3):1841–1863.

[Michael et al., 2009] Michael, N., Zavlanos, M. M., Kumar, V., and Pappas, G. J. (2009). Maintaining connectivity in mobile robot networks. In Siciliano, B., Khatib, O., Groen, F., Khatib, O., Kumar, V., and Pappas, G. J., editors, *Experimental Robotics*, volume 54, pages 117–126. Springer. Springer Tracts in Advanced Robotics.

[Michieletto et al., 2021] Michieletto, G., Cenedese, A., and Zelazo, D. (2021). A Unified Dissertation on Bearing Rigidity Theory. *IEEE Transactions on Control of Network Systems*, 8(4):1624–1636.

[Monica and Ferrari, 2015] Monica, S. and Ferrari, G. (2015). UWB-based localization in large indoor scenarios: optimized placement of anchor nodes. *IEEE Transactions on Aerospace and Electronic Systems*, 51(2):987–999.

[Moore et al., 2004] Moore, D., Leonard, J., Rus, D., and Teller, S. (2004). Robust distributed network localization with noisy range measurements. In *International Conference on Embedded Networked Sensor Systems*, page 50–61, Baltimore, MD, USA.

[Morales et al., 2016] Morales, J. J., Khalife, J. J., and Kassas, Z. M. (2016). GNSS Vertical Dilution of Precision Reduction using Terrestrial Signals of Opportunity. In *International Technical Meeting of The Institute of Navigation*, pages 664–669, Monterey, CA, USA. ISSN: 2330-3646.

[Mueller et al., 2015] Mueller, M. W., Hamer, M., and D'Andrea, R. (2015). Fusing ultra-wideband range measurements with accelerometers and rate gyroscopes for quadrocopter state estimation. In *IEEE International Conference on Robotics and Automation (ICRA)*, pages 1730–1736, Seattle, WA, USA.

[Naidu, 2009] Naidu, P. S. (2009). *Sensor Array Signal Processing*. CRC Press, Boca Raton, Florida, USA, 2 edition.

[NASA, 2010] NASA (2010). Ultra-Wideband Angle-of-Arrival Tracking Systems. Technical report, Lyndon B. Johnson Space Center, Houston, Texas, USA.

[Neirynck et al., 2016] Neirynck, D., Luk, E., and McLaughlin, M. (2016). An alternative double-sided two-way ranging method. In *2016 13th Workshop on Positioning, Naviation and Communications*, Bremen, Germany. IEEE.

[O'Connor and Robertson, 1999] O'Connor, J. J. and Robertson, E. F. (1999). *Al-Biruni Biography*. MacTutor History of Mathematics archive, University of St Andrews. `https://mathshistory.st-andrews.ac.uk/Biographies/Al-Biruni/`.

[Panwar et al., 2022] Panwar, K., Fatima, G., and Babu, P. (2022). Optimal Sensor Placement for Hybrid Source Localization Using Fused TOA-RSS-AOA Measurements. *arXiv:2204.06198 [eess]*. arXiv: 2204.06198.

[Papalia and Leonard, 2020] Papalia, A. and Leonard, J. (2020). Network Localization Based Planning for Autonomous Underwater Vehicles with Inter-Vehicle Ranging. In *2020 IEEE/OES Autonomous Underwater Vehicles Symposium (AUV)*, pages 1–6. ISSN: 2377-6536.

[Papalia et al., 2021] Papalia, A., Thumma, N., and Leonard, J. (2021). Prioritized Planning for Cooperative Range-Only Localization in Multi-Robot Networks. *arXiv:2109.05132 [cs]*.

[Patwari et al., 2005] Patwari, N., Ash, J. N., Kyperountas, S., Hero, A. O., Moses, R. L., and Correal, N. S. (2005). Locating the nodes: cooperative localization in wireless sensor networks. *IEEE Signal Processing Magazine*, 22(4):54–69.

[Paulin, 2017] Paulin, G. (2017). Multi-System GNSS Receiver Software. Technical report, Distributed Computing Group Computer Engineering and Networks Laboratory, ETHZ, Zurich, Switzerland.

[Peng and Sichitiu, 2006] Peng, R. and Sichitiu, M. L. (2006). Angle of Arrival Localization for Wireless Sensor Networks. In *2006 3rd Annual IEEE Communications Society on Sensor and Ad Hoc Communications and Networks*, volume 1, pages 374–382. ISSN: 2155-5494.

[Petersen and Pedersen, 2012] Petersen, K. B. and Pedersen, M. S. (2012). The Matrix Cookbook. Technical report, Technical University of Denmark.

[Png et al., 2008] Png, K.-B., Peng, X., Chattong, S., Francis, H. T., and Chin, F. (2008). Joint carrier and sampling frequency offset estimation for MB-OFDM UWB system. In *IEEE Radio and Wireless Symposium*, pages 29–32.

[Preter et al., 2019] Preter, A. D., Goysens, G., Anthonis, J., Swevers, J., and Pipeleers, G. (2019). Range Bias Modeling and Autocalibration of an UWB Positioning System. In *2019 International Conference on Indoor Positioning and Indoor Navigation (IPIN)*.

[Prorok, 2013] Prorok, A. (2013). *Models and Algorithms for Ultra-Wideband Localization in Single- and Multi-Robot Systems*. PhD Thesis, Ecole Polytechnique Federale de Lausanne (EPFL).

[Prorok et al., 2012a] Prorok, A., Bahr, A., and Martinoli, A. (2012a). Low-cost collaborative localization for large-scale multi-robot systems. In *Proceedings of the IEEE International Conference on Robotics and Automation (ICRA)*, Saint Paul, MN, USA.

[Prorok et al., 2012b] Prorok, A., Gonon, L., and Martinoli, A. (2012b). Online Model Estimation of Ultra-Wideband TDOA Measurements for Mobile Robot Localization. In *Proceedings of the IEEE International Conference on Robotics and Automation (ICRA)*, Saint Paul, MN, USA.

[Pukelsheim, 2006] Pukelsheim, F. (2006). *Optimal Design of Experiments*. SIAM.

[Qorvo, 2022] Qorvo (2022). *DWM1000 datasheet*. Qorvo Inc. (formerly Decawave). `https://www.qorvo.com/products/p/DWM1000`.

[Rao, 1945] Rao, C. R. (1945). Information and accuracy attainable in estimation of statistical parameters. *Bulletin of the Calcutta Mathematical Society*.

[Raol, 2016] Raol, J. (2016). *Data Fusion Mathematics / Theory and Practice*. CRC Press.

[Ren, 2015] Ren, C. (2015). *Caractérisation des performances minimales d'estimation pour des modèles d'observations non-standards*. PhD thesis, Université Paris-Sud, Paris.

[Ren et al., 2015] Ren, C., Galy, J., Chaumette, E., Vincent, F., Larzabal, P., and Renaux, A. (2015). Recursive Hybrid Cramér–Rao Bound for Discrete-Time Markovian Dynamic Systems. *IEEE Signal Processing Letters*, 22(10):1543–1547.

[Roumeliotis and Bekey, 2002] Roumeliotis, S. and Bekey, G. (2002). Distributed multirobot localization. *IEEE Transactions on Robotics and Automation*, 18(5):781–795.

[Sagnol, 2010] Sagnol, G. (2010). *Optimal design of experiments with application to the inference of traffic matrices in large networks: second order cone programming and submodularity*. PhD thesis, Mines Paris Tech.

[Sahinoglu and Gezici, 2006] Sahinoglu, Z. and Gezici, S. (2006). Ranging in the IEEE 802.15. 4a standard. In *Wireless and Microwave Technology Conference, 2006. WAMICON'06. IEEE Annual*, pages 1–5. IEEE.

[Sahinoglu et al., 2008] Sahinoglu, Z., Gezici, S., and Guvenc, I. (2008). *Ultra-wideband Positioning Systems: Theoretical Limits, Ranging Algorithms, and Protocols*. Cambridge University Press.

[Sarkka, 2013] Sarkka, S. (2013). *Bayesian Filtering and Smoothing*. Cambridge University Press, Cambridge.

[Savic et al., 2016] Savic, V., Larsson, E. G., Ferrer-Coll, J., and Stenumgaard, P. (2016). Kernel methods for accurate UWB-based ranging with reduced complexity. *IEEE Transactions on Wireless Communications*, 15(3):1783–1793.

[Shames et al., 2009] Shames, I., Fidan, B., and Anderson, B. D. (2009). Minimization of the effect of noisy measurements on localization of multi-agent autonomous formations. *Automatica*, 45(4):1058–1065.

[Sharp et al., 2009] Sharp, I., Yu, K., and Guo, Y. J. (2009). Peak and leading edge detection for time-of-arrival estimation in band-limited positioning systems. *IET communications*, 3(10):1616–1627.

[Shen et al., 2008] Shen, G., Zetik, R., and Thoma, R. S. (2008). Performance comparison of TOA and TDOA based location estimation algorithms in LOS environment. In *Navigation and Communication 2008 5th Workshop on Positioning*, pages 71–78.

[Sheu et al., 2010] Sheu, J., Hu, W., and Lin, J. (2010). Distributed localization scheme for mobile sensor networks. *IEEE Transactions on Mobile Computing*, 9(4):516–526.

[Shi et al., 2020] Shi, Q., Cui, X., Zhao, S., and Lu, M. (2020). Sequential TOA-Based Moving Target Localization in Multi-Agent Networks. *IEEE Communications Letters*, pages 1719 – 1723.

[Sun et al., 2015] Sun, Z., Yu, C., and Anderson, B. D. O. (2015). Distributed optimization on proximity network rigidity via robotic movements. In *Chinese Control Conference (CCC)*, pages 6954–6960, Hangzhou, China.

[Tay and Whiteley, 1985] Tay, T.-S. and Whiteley, W. (1985). Generating Isostatic Frameworks. *Struct. Topology*, 11.

[Tewes et al., 2017] Tewes, S., Schwoerer, L., and Bosselmann, P. (2017). Designing a Basic IR-UWB-RTLS - Raw-data position estimation utilizing TWR. In *Smart SysTech 2017; European Conference on Smart Objects, Systems and Technologies*.

[Tichavsky et al., 1998] Tichavsky, P., Muravchik, C., and Nehorai, A. (1998). Posterior Cramer-Rao bounds for discrete-time nonlinear filtering. *IEEE Transactions on Signal Processing*, 46(5):1386–1396.

[Tiemann et al., 2019] Tiemann, J., Elmasry, Y., Koring, L., and Wietfeld, C. (2019). ATLAS FaST: Fast and Simple Scheduled TDOA for Reliable Ultra-Wideband Localization. In *2019 International Conference on Robotics and Automation (ICRA)*, pages 2554–2560.

[Tron et al., 2016] Tron, R., Thomas, J., Loianno, G., Daniilidis, K., and Kumar, V. (2016). A Distributed Optimization Framework for Localization and Formation Control: Applications to Vision-Based Measurements. *IEEE Control Systems Magazine*, 36(4):22–44.

[Uciński, 2004] Uciński, D. (2004). *Optimal measurement methods for distributed parameter system identification*. CRC press.

[Van Herbruggen et al., 2019] Van Herbruggen, B., Jooris, B., Rossey, J., Ridolfi, M., Macoir, N., Van den Brande, Q., Lemey, S., and De Poorter, E. (2019). Wi-PoS: A low-cost, open source ultra-wideband (UWB) hardware platform with long range sub-GHz backbone. *Sensors*, 19(7):1548.

[Van Trees and Bell, 2007] Van Trees, H. L. and Bell, K. L. (2007). *Bayesian bounds for parameter estimation and nonlinear filtering/tracking*. Wiley.

[Vo and De, 2016] Vo, Q. D. and De, P. (2016). A Survey of Fingerprint-Based Outdoor Localization. *IEEE Communications Surveys Tutorials*, 18(1):491–506.

[Wang, 2011] Wang, B. (2011). Coverage problems in sensor networks: A survey. *ACM Computing Surveys*, 43(4):1–53.

[Wann et al., 2006] Wann, C.-D., Yeh, Y.-J., and Hsueh, C.-S. (2006). Hybrid TDOA/AOA Indoor Positioning and Tracking Using Extended Kalman Filters. In *2006 IEEE 63rd Vehicular Technology Conference*, volume 3, pages 1058–1062.

[Wei et al., 2015] Wei, M., Aragues, R., Sagues, C., and Calafiore, G. C. (2015). Noisy range network localization based on distributed multidimensional scaling. *IEEE Sensors*, 15(3):1872–1883.

[Whiteley, 1996] Whiteley, W. (1996). Some matroids from discrete applied geometry. In Bonin, J. E., Oxley, J. G., and Servatius, B., editors, *Contemporary Mathematics*, volume 197, pages 171–311. American Mathematical Society, Providence, Rhode Island.

[Wymeersch et al., 2012] Wymeersch, H., Marano, S., Gifford, W. M., and Win, M. Z. (2012). A machine learning approach to ranging error mitigation for UWB localization. *IEEE Transactions on Communications*, 60(6):1719–1728.

[Xu et al., 2008] Xu, J., Ma, M., and Law, C. L. (2008). AOA cooperative position localization. In *IEEE Global Telecommunications Conference (GLOBECOM)*, New Orleans, LA.

[Xu and Chou, 2017] Xu, S. and Chou, W. (2017). An Improved Indoor Localization Method for Mobile Robot Based on WiFi Fingerprint and AMCL. In *2017 10th International Symposium on Computational Intelligence and Design (ISCID)*, volume 1, pages 324–329. ISSN: 2473-3547.

[Xue and Yang, 2017] Xue, S. and Yang, Y. (2017). Understanding GDOP minimization in GNSS positioning: Infinite solutions, finite solutions and no solution. *Advances in Space Research*, 59(3):775–785.

[Yang et al., 2010] Yang, P., Freeman, R. A., Gordon, G. J., Lynch, K. M., Srinivasa, S. S., and Sukthankar, R. (2010). Decentralized estimation and control of graph connectivity for mobile sensor networks. *Automatica*, 46(2):390–396.

[Yu et al., 2019] Yu, K., Wen, K., Li, Y., Zhang, S., and Zhang, K. (2019). A Novel NLOS Mitigation Algorithm for UWB Localization in Harsh Indoor Environments. *IEEE Transactions on Vehicular Technology*, 68(1):686–699.

[Zelazo et al., 2012] Zelazo, D., Franchi, A., Allgöwer, P., Bülthoff, H., and Robuffo Giordano, P. (2012). Rigidity maintenance control for multi-robot systems. In *Robotics: Science and Systems VIII*.

[Zelazo et al., 2015] Zelazo, D., Franchi, A., Bülthoff, H. H., and Robuffo Giordano, P. (2015). Decentralized rigidity maintenance control with range measurements for multi-robot systems. *The International Journal of Robotics Research*, 34(1):105–128.

[Zhao and Zelazo, 2015] Zhao, S. and Zelazo, D. (2015). Bearing rigidity and almost global bearing-only formation stabilization. *IEEE Transactions on Automatic Control*, 61(5):1255–1268.

[Zhao and Zelazo, 2016] Zhao, S. and Zelazo, D. (2016). Bearing Rigidity and Almost Global Bearing-Only Formation Stabilization. *IEEE Transactions on Automatic Control*, 61(5):1255–1268.

[Zhao et al., 2021] Zhao, W., Panerati, J., and Schoellig, A. P. (2021). Learning-based bias correction for time difference of arrival ultra-wideband localization of resource-constrained mobile robots. *IEEE Robotics and Automation Letters*, 6(2):3639–3646.

[Zhao et al., 2020] Zhao, W., Vukosavljev, M., and Schoellig, A. P. (2020). Optimal Geometry for Ultra-wideband Localization using Bayesian Optimization. *IFAC-PapersOnLine*, 53(2):15481–15488.

[Zhu and Kia, 2019] Zhu, J. and Kia, S. S. (2019). Bias compensation for UWB ranging for pedestrian geolocation applications. *IEEE Sensors Letters*, 3(9).

[Zoubir et al., 2018] Zoubir, A. M., Koivunen, V., Ollila, E., and Muma, M. (2018). *Robust Statistics for Signal Processing*. Cambridge University Press.